

University of Alberta
Department of Civil Engineering



Structural Engineering Report No. 202

Deformational Behaviour of Line Pipe

by

Magdi E. Mohareb

A.E. Elwi

G.L. Kulak

and

D.W. Murray

1994

Structural Engineering Report No. 202

DEFORMATIONAL BEHAVIOR OF LINE PIPE

by

MAGDI E. MOHAREB,

A.E. ELWI,

G.L. KULAK

and

D.W. MURRAY

Department of Civil Engineering
University of Alberta
Edmonton, Alberta,
Canada T6G 2G7

1994

ACKNOWLEDGMENTS

This report is based upon the thesis of the junior author submitted to the University of Alberta in partial fulfillment of the requirements for the degree of Doctor of Philosophy in Structural Engineering.

The writers extend their thanks to Dr. S. D. B. Alexander for taking the time to develop and test the control program used in the experimental program of this research. The help of Dr. A. Peterson in obtaining the photogrammetric results presented in Chapter 3 and of Dr. T. L. Souza in the rendering representation of these results is acknowledged with thanks.

The assistance of the I. F. Morrison Structural Laboratory Technicians at the University of Alberta Richard Helfrich and Larry Burden is sincerely acknowledged.

Funding for this research was jointly provided by the sponsorship of Inter-Provincial Pipelines Inc. and the Department of Energy Mining and Resources of the Government of Canada, by scholarship funds from the government of the Province of Alberta and from Petro-Canada, and by research grants from the National Science and Engineering Research Council of Canada through Dr. D. W. Murray and Dr. G. L. Kulak.

ABSTRACT

Steel pipelines buried in cold regions are subject to thermally induced axial loads, hoop stresses caused by the action of the fluids they convey, and differential settlements caused by factors such as thaw settlements, frost heave, and land slides. Due to these loads, pipelines may experience localized deformations well into the plasticity range of the pipe material.

An experimental program consisting of seven tests was designed in order to investigate and document the deformational behaviour of full-scale pipes subjected to loads similar to those in the field. The specimens and loading conditions were carefully selected to match those in the field

A finite element model was developed using the finite element simulator ABAQUS in order to predict the local buckling behaviour of pipes. The finite element model was based on a large displacement-large rotation-finite membrane strain formulation and included material non-linearity effects. The comparison between the numerical and the experimental results demonstrates the ability of the analytical model to predict the local buckling behaviour of pipes when deformed well into the post-yield range.

The parameters that may influence the local buckling behaviour of the pipes are identified. The numerical model is used to perform a series of 27 parametric runs. The results of the parametric runs are integrated into equations for predicting deformation limits for pipelines based on a number of proposed deformation limiting criteria.

Table of Contents

List of Tables

List of Figures

List of Symbols

1. INTRODUCTION	1
1.1 BACKGROUND TO THE PROBLEM.....	1
1.2 DESIGN OF PIPELINES IN CURRENT PRACTICE	1
1.3 NEED TO LIMIT DEFORMATIONS.....	2
1.4 THEORETICAL CONCEPTS IN PIPE LOCAL BUCKLING.....	2
<i>1.4.1 Non-linear Collapse Buckling</i>	<i>2</i>
<i>1.4.2 Bifurcation Buckling</i>	<i>3</i>
1.5 CATEGORIES OF DEFORMATION LIMITS.....	4
<i>1.5.1 Longitudinal Compressive Strain</i>	<i>4</i>
1.5.1.1 Buckling Initiation Criterion.....	5
1.5.1.2 Rapid Wrinkle Growth Criterion	5
1.5.1.3 Peak Moment Criterion.....	6
<i>1.5.2 Cross-Sectional Deformation</i>	<i>6</i>
<i>1.5.3 Tensile Hoop Strain.....</i>	<i>8</i>
1.6 DEFORMATION LIMITS FOR UNPRESSURIZED PIPES	9
<i>1.6.1 Elastic theory.....</i>	<i>9</i>
<i>1.6.2 Inelasticity of the Pipe Material</i>	<i>9</i>
1.7 DEFORMATION LIMITS FOR PRESSURIZED PIPES	11
1.8 SCOPE OF RESEARCH	13
 2. DESIGN OF EXPERIMENTS	 16
2.1 SCOPE	16

2.2 SELECTION OF SPECIMEN DIMENSIONS	17
2.3 SELECTION OF PIPE MANUFACTURING PROCESSES.....	17
2.4 MODELING OF FIELD CONDITIONS	18
2.4.1 <i>Axial Loading</i>	18
2.4.1.1 Axial Load Caused by the Thermal Effects.....	18
2.4.1.2 Axial Load Resulting From the Poisson's Ratio Effect for Hoop Stresses ...	19
2.4.1.3 Axial Load Caused by Internal Pressure Acting on Closed Ends of Specimens	20
2.4.1.4 Total Axial Load.....	20
2.4.2 <i>Differential Settlement Effects</i>	21
2.4.2.1 Longitudinal Bending Strains	21
2.4.2.2 Catenary Action of Pipelines	21
2.4.3 <i>Internal Pressure</i>	22
2.5 LOADING COMBINATIONS	23
2.6 DESCRIPTION OF EXPERIMENTS.....	24
2.6.1 <i>Experimental Setup</i>	24
2.6.2 <i>Fabrication Sequence and Alignment Procedure</i>	25
2.6.3 <i>Application of Internal Pressure</i>	26
2.6.4 <i>Control of the Test</i>	26
2.7 INSTRUMENTATION AND MEASUREMENTS	27
2.7.1 <i>Strain Measuring Devices</i>	27
2.7.2 <i>Load and Axial Movement Measuring Devices</i>	28
2.7.3 <i>Rotation Meters</i>	28
2.7.4 <i>Deformation Response Measuring Techniques</i>	28
2.8 ANCILLARY TESTS	29
2.8.1 <i>Tension Tests</i>	29
2.8.1.1 Description of The Tests.....	29
2.8.1.2 Computation of Engineering Stresses and Engineering Strains	30

2.8.1.3 True Stress vs. True Strain Relationship	31
2.8.1.4 Ramberg-Osgood Fit of Stress-Strain Curve	32
2.8.2 <i>Stub Column Tests</i>	33
3. EXPERIMENTAL RESULTS	53
3.1 GENERAL	53
3.2 DEFORMATIONAL RESPONSE.....	53
3.2.1 <i>Deformation Measurement Techniques</i>	53
3.2.2 <i>Buckling Patterns</i>	54
3.2.2.1 Diamond Shape Buckling	55
3.2.2.2 Outward Bulge Buckling	55
3.2.2.3 Buckling Location.....	56
3.3 LONGITUDINAL STRAINS	56
3.3.1 <i>Importance of Strains</i>	56
3.3.2 <i>Strain Measurement Techniques</i>	57
3.3.3 <i>Demec Gages</i>	57
3.3.3.1 Importance of Demec Gage Readings	57
3.3.3.2 Demec Gage Results	58
3.3.4 <i>Strain Gages</i>	58
3.3.4.1 Alignment of Specimens.....	59
3.3.4.2 Strains on the Compression Side	59
3.3.4.3 Strains on Tension Side	59
3.4 END ROTATIONS	60
3.4.1 <i>Influence of End Rotations on Buckling Location</i>	60
3.4.2 <i>Comparison between Techniques Used in Measuring End Rotations</i>	60
3.5 LOAD MEASUREMENTS	61
3.6 MOMENT CURVATURE RELATIONSHIPS	61

3.6.1 Computation of Curvatures	62
3.6.2 Computation of End Moments	62
3.6.3 Moment Curvature Diagrams.....	63
3.6.3.1 Effect of Internal Pressure	63
3.6.3.2 Effect of Boundary Conditions	63
3.6.3.3 Effect of Axial Loads.....	64
3.7 MOMENT CAPACITY.....	64
3.7.1 Relevance of Moment Capacity to the Pipeline Problem	64
3.7.2 Estimates of Plastic Moment Capacity.....	64
3.7.2.1 Cross-sectional Distortion and Curvature.....	65
3.7.2.2 Idealized Stress vs. Strain Relationship.....	65
3.7.2.3 Yield Criterion	66
3.7.2.4 Plastic Moments.....	66
3.7.2.5 Computation of Plastic Moment Capacity	66
3.7.3 Interaction Diagrams.....	69
 4. ANALYSIS	 95
4.1 GENERAL	96
4.2 FINITE ELEMENT FORMULATION	97
4.3 SHELL ELEMENT FEATURES	99
4.4 MATERIAL MODEL IDEALIZATION.....	95
4.5 RESIDUAL STRESSES	100
4.6 MODELING OF CONFINING COLLARS	100
4.7 FINITE ELEMENT MESH.....	101
4.8 BOUNDARY CONDITIONS	102
4.9 SEQUENCE OF LOAD APPLICATION IN THE ANALYSIS	102
4.10 COMPUTER HARDWARE	103

4.11 MOMENT CURVATURE RELATIONSHIP	103
4.12 BUCKLED CONFIGURATIONS	104
4.13 CONCLUSION	105
 5. PARAMETRIC STUDY	119
5.1 PARAMETERS INFLUENCING PIPE BEHAVIOR.....	119
5.2 DIMENSIONAL ANALYSIS	120
5.2.1 <i>Non-Dimensional Parameters Studied</i>	122
5.2.2 <i>Scope of the Study</i>	122
5.2.3 <i>Notation for the Parametric Runs</i>	123
5.3 ANALYTICAL MODEL FOR THE PARAMETRIC STUDY	124
5.3.1 <i>Material Model</i>	124
5.3.2 <i>Finite Element Mesh</i>	124
5.3.3 <i>Loading Sequence</i>	124
5.3.4 <i>Boundary Conditions</i>	127
5.3.4.1 <i>Boundary Conditions of Pipes in the Field</i>	124
3.7.2.2 <i>Modeling of Boundary Conditions</i>	124
5.3.5 <i>Gage Length</i>	127
5.3.6 <i>Local Curvature</i>	128
5.3.7 <i>Computation of Internal Moments</i>	128
5.3.8 <i>Selection of a Longitudinal Strain Measure</i>	130
5.3.9 <i>Limiting Strain Criteria</i>	130
5.3.9.1 <i>Limit Point Strain</i>	130
5.3.9.2 <i>Strain Corresponding to 95% Peak Moment</i>	131
5.3.9.3 <i>Limitations of Strain Criteria Based on Moment Capacity</i>	131
5.3.9.4 <i>Strain Limit at 15% Ovalization</i>	132
5.3.9.5 <i>Modeling of Boundary Conditions</i>	133

5.3.10 Selection of a Design Limiting Strain.....	134
5.4 PLASTIC MOMENT CAPACITY.....	135
5.4.1 Interaction Diagrams.....	136
5.4.2 Non-Dimensional Interaction Diagram.....	136
5.4.3 Local Moment vs. Local Curvature Relationships	137
5.4.4 Non-Dimensional Moment vs. Curvature Relationships	137
5.4.5 Parametric Study for Moment Capacity.....	137
5.4.6 Moment Capacity for Elevated Pipelines	138
5.5 DEFORMATION LIMIT STATE EQUATIONS.....	141
5.5.1 Limit Point Strain Criterion	142
5.5.1.1 Limit Point Strain	142
5.5.1.2 Strain Corresponding to 95% Peak Moment	143
5.5.1.3 Range of Applicability	145
5.5.2 Strain at 95% Moment Capacity.....	146
5.5.2.1 Limit Point Strain	147
5.5.2.2 Strain Corresponding to 95% Peak Moment	146
5.5.3 Ovalization Criterion.....	147
5.5.4 Hoop Strain Criterion.....	148
5.5.5 Comparison between Different Deformation Criteria.....	150
5.6 DEFORMED CONFIGURATIONS.....	150
5.6.1 Buckled Length	150
5.7 EFFECT OF BOUNDARY CONDITIONS	151
5.8 SUMMARY AND CONCLUSIONS	152
 6. SUMMARY AND CONCLUSIONS	 187
6.1 SUMMARY OF RESEARCH.....	187
6.2 CRITIQUES AND RECOMMENDATIONS	188

6.2.1.1 Material Properties.....	189
6.2.1.2 Test Set-up.....	189
6.2.2 <i>Deformation Limiting Criteria</i>	191
6.2.3 PARAMETRIC STUDY.....	192
6.3 IMPACT OF RESEARCH.....	187

List of Tables

Table 2.1 Pipe Geometry and Loading Conditions.....	35
Table 2.2 Design Pressure and Axial Loads Magnitude for Test Specimens.....	36
Table 2.3 Stress vs. Strain Values for X56 and X52 Steels.....	37
Table 3.1 Strains at the Initiation of Buckling Based on Demec Gage Readings.....	71
Table 3.2 Estimated Plastic Moment Capacity for Test Specimens	72
Table 5.1 Moment Capacity Ratios	153
Table 5.2 Summary of Strain Values for Different Design Criteria	154
Table 5.3 Longitudinal Compressive Strains at Limit Point	155
Table 5.4 Longitudinal Compressive Strains at 95% of the Moment Capacity.....	156
Table 5.5 Longitudinal Compressive Strains at 15% Ovalization.....	157
Table 5.6 Longitudinal Compressive Strains at 8% Hoop Strain	157
Table 5.7 Buckled Lengths and Buckling Modes.....	158
Table 5.8 Limit Point Strains based on Experimental and Finite Element Results	158

List of Figures

Figure 1.1 Typical Load vs. Displacement Relationship for Cylinders	14
Figure 2.1 Longitudinal Forces along Pipeline Subject to Differential Settlement	38
Figure 2.2 Pressure Head along Pipeline	39
Figure 2.3 Experimental Setup	40
Figure 2.4 Plan View of End Plate	41
Figure 2.5 Fabrication Process of the Specimen.....	42
Figure 2.6 Free Body Diagram for Loads Acting on Specimen.....	43
Figure 2.7 Location of Strain Gages	44
Figure 2.8 Demec Gage Measurements	45
Figure 2.9 LVDTs Measuring Radial Displacements	46
Figure 2.10 Stress vs. Strain Relationship for X52 Material	47
Figure 2.11 Stress vs. Strain Relationship for X56 Material	48
Figure 2.12 Ramberg-Osgood Curves for Different Plasticity Exponent Magnitudes	49
Figure 2.13 True Stress vs. True Strain Relationship for X56 and X52 Materials.....	50
Figure 2.14 Stub Column Tests	51
Figure 2.15 Stress vs. Strain Curves for Axially Loaded Pipes.....	52
Figure 3.1 Buckling Progression for UGA324	73
Figure 3.2 Buckling Progression for DGA508	74
Figure 3.3 Buckled Configurations for 324 OD Specimens	75
Figure 3.4 Buckled Configurations for 508 mm OD Specimens.....	76
Figure 3.5 Radial Displacements on Maximum Compression Fiber for UGA508	77
Figure 3.6 Radial Displacements on Maximum Compression Fiber for UGR508.....	77
Figure 3.7 Radial Displacements on Maximum Compression Fiber for DGA508	78
Figure 3.8 Radial Displacement on Maximum Compression Fiber for DLR508.....	78
Figure 3.9 Radial Displacements on Maximum Compression Fiber for UGA324	79

Figure 3.10 Radial Displacements on Maximum Compression Fiber for HGA324	79
Figure 3.11 Radial Displacements on Maximum Compression Fiber for DGA324	80
Figure 3.12 Demec Strains on Maximum Compression Fiber for DGA508	80
Figure 3.13 Demec Strains on Maximum Compression Fiber for DLR508.....	81
Figure 3.14 Demec Strains on Maximum Compression Fiber for UGA324	81
Figure 3.15 Demec Strains on Maximum Compression Fiber for HGA324	82
Figure 3.16 Demec Strains on Maximum Compression Fiber for DGA324	82
Figure 3.17 Comparison Between End Rotation Measurement Techniques	83
Figure 3.18 Free Body Diagram for a Specimen in a Deformed State	84
Figure 3.19 Load vs. End Rotation for UGA508.....	85
Figure 3.20 Load vs. End Rotation for UGR508.....	85
Figure 3.21 Load vs. End Rotation for DGA508.....	86
Figure 3.22 Load vs. End Rotation for DLR508	86
Figure 3.23 Load vs. End Rotation for UGA324.....	87
Figure 3.24 Load vs. End Rotation for HGA324.....	87
Figure 3.25 Load vs. End Rotation for DGA324.....	88
Figure 3.26 Moment vs. Curvature Diagrams for 324 mm OD Specimens	89
Figure 3.27 Moment vs. Curvature Diagrams for 508 mm OD Specimens	90
Figure 3.28 Von Mises Yield Envelope.....	91
Figure 3.29 Idealized Stress Distribution	91
Figure 3.30 Interaction Diagram for 508 OD Pipes.....	92
Figure 3.31 Interaction Diagram for 508 OD Pipes.....	93
Figure 3.32 Non-Dimensional Interaction Diagram	94
Figure 4.1 Finite Element Meshes	106
Figure 4.2 Boundary Conditions for Test Specimens.....	107
Figure 4.3 Moment vs. Curvature Relationship for UGA508	108
Figure 4.4 Moment vs. Curvature Relationship for UGR508.....	108
Figure 4.5 Moment vs. Curvature Relationship for DGA508	109

Figure 4.6 Moment vs. Curvature Relationship for DLR508	109
Figure 4.7 Moment vs. Curvature Relationship for UGA324	110
Figure 4.8 Moment vs. Curvature Relationship for HGA324	110
Figure 4.9 Moment vs. Curvature Relationship for DGA324	111
Figure 4.10 Deformed Configuration for Specimen UGA508	112
Figure 4.11 Deformed Configuration for Specimen UGR508.....	113
Figure 4.12 Deformed Configuration for Specimen DGA508	114
Figure 4.13 Deformed Configuration for Specimen DLR508	115
Figure 4.14 Deformed Configuration for Specimen UGA324	116
Figure 4.15 Deformed Configuration for Specimen HGA324	117
Figure 4.16 Deformed Configuration for Specimen DGA324	118
Figure 5.1 Boundary Conditions.....	159
Figure 5.2 Interaction Diagrams for 324 mm OD × 6.35 mm Cross Section	160
Figure 5.3 Interaction Diagrams for 610 mm OD × 7.92 mm Cross Section.....	161
Figure 5.4 Interaction Diagrams for 711 mm OD × 7.11 mm Cross-Section.....	162
Figure 5.5 Non-Dimensional Interaction Diagram	163
Figure 5.6 Local Moment vs. Local Curvature	
for 324 mm OD × 6.35 mm Cross Section	164
Figure 5.7 Local Moment vs. Local Curvature	
for 610 mm OD × 7.92 mm Cross Section.....	165
Figure 5.8 Local Moment vs. Local Curvature	
for 711 mm OD × 7.11 mm Cross Section.....	166
Figure 5.9 Non-Dimensional Moment vs. Curvature Diagrams for xxC7.5H36	167
Figure 5.10 Non-Dimensional Moment vs. Curvature Diagrams for 77C7.5Hxx	168
Figure 5.11 Non-Dimensional Moment vs. Curvature Diagrams for 77XxxH36	169
Figure 5.12 Scatter of Predicted Plastic Moments	
in Relation to Finite Element Results.....	170
Figure 5.13 Limit Point Strains vs. Axial Load Ratios.....	171

Figure 5.14 Longitudinal Compressive Strain at Limit Point (Hoop Stress Ratio = 0.00).....	172
Figure 5.15 Longitudinal Compressive Strain at Limit Point (Hoop Stress Ratio = 0.80).....	173
Figure 5.16 Scatter of Limit Point Strains: Finite Element Results vs. Equation 5.44....	174
Figure 5.17 The 95% Moment Capacity Strains vs. Axial Load Ratios.....	175
Figure 5.18 Longitudinal Strains at 95% Moment Capacity (Hoop Stress Ratio = 0.00).....	176
Figure 5.19 Longitudinal Strains at 95% Moment Capacity (Hoop Stress Ratio = 0.80).....	177
Figure 5.20 Scatter of 95% Moment Capacity Strains: Finite Element Results vs. Equation 5.46	178
Figure 5.21 Longitudinal Strains at 15% Ovalization (Internal Pressure = 0.00).....	179
Figure 5.22 Scatter of 15% Ovalization Strains: Finite Element Results vs. Equation 5.48	180
Figure 5.23 Longitudinal Compressive Strain at 8% Hoop Strain	181
Figure 5.24 Scatter of Longitudinal Strains corresponding to 8% Hoop Strains: Element Results vs. Equation 5.50.....	182
Figure 5.25 Deformed Configurations for Parametric Runs ($OD/t = 51$).....	183
Figure 5.26 Deformed Configurations for Parametric Runs ($OD/t = 77$).....	184
Figure 5.27 Deformed Configurations for Parametric Runs ($OD/t = 100$).....	185

List of Symbols

Latin Characters

- a ovalization of the pipe wall at the maximum compression fiber of a pipe subjected to bending (Gresnigt formulation)
- A the cross-sectional area of the pipe
- A_{comp} the area of the pipe cross section subjected to longitudinal compressive stresses
- A_{tens} the area of the pipe cross section subjected to longitudinal tensile stresses
- A_o undeformed cross-sectional area of a tension coupon
- A_p cross-sectional area of a tension coupon in the deformed configuration
- C_i ($i=1,6$) constants to be determined by regression analysis
- C axial compressive force in the pipe that is to be maintained constant in an active test
- d distance (in the deformed configuration) between the centroids of two cross sections located at the ends of a pipe segment that is used to compute local curvature
- d_o distance (in the undeformed configuration) between the centroids of two cross sections located at the ends of a pipe segment that is used to compute local curvature
- D outside diameter of a pipe cross section
- D_{av} average diameter of a pipe cross section

D_d	pipe diametric differential = $(D_l - D_s)/D$
D_e	pipe diametric expansion = $(D_l + D_s)/D$
D_l	largest outside diameter of a pipe deformed cross section
D_s	smallest outside diameter of a pipe deformed cross section
e	eccentricity of the force F
E	modulus of elasticity of the pipe material
F	eccentric load applied to the specimen
F_H	horizontal frictional force acting on the knife edge
f_x, f_y, f_z	equivalent nodal forces of a finite element in the global directions
h	distance from the edge of the knife edge (the point of application of the concentric load P) to the end of the specimen
I	moment of inertia of the pipe cross section about the axis of bending
L	overall length of a pipe specimen
L_b	buckled length of a pipe specimen
L_d	distance (in the deformed configuration) between the two points on the pipe mid-surface at the intersection of the maximum compression fibre and each of the two end cross sections of a pipe segment. (Used to compute local curvature)
L_o	distance (in the undeformed configuration) between the two points on the pipe mid-surface at the intersection of the maximum compression fibre and each of the two end cross sections of a pipe segment. (Used to compute local curvature)
l_o	gage length in a tension test (= 50.8 mm)

l_d	deformed gage length in a tension test
M	end moment
M_{cap}	predicted moment capacity
M_{FEA}	internal moment as determined from finite element analysis
M_i	internal moment
$M_{\sigma_\theta, max}^p$	maximum plastic moment capacity assuming a hoop stress of σ_θ
M_{σ_θ, P_e}^p	plastic moment capacity assuming a hoop stress of σ_θ and an axial load of P_e
m_n	dimensionless plastic moment capacity
m_x, m_y, m_z	equivalent nodal moments acting on a finite element in the global directions
n	plasticity exponent in a Ramberg-Osgood stress vs. strain curve
OD	outside diameter of a pipe cross section
O_r	pipe cross section out of roundness = $(D - D_s)/D$
O_v	pipe cross section ovalization = $2(D_l - D_s)/(D_l + D_s)$
p	pressure acting on pipe
p_n	dimensionless axial force
P	concentric load applied to the specimen
P_t	thermally induced axial compressive force in the pipe
P_e	net axial force acting on a pipe cross section

P_p	axial force applied to the ends of laboratory specimen in order to compensate the closed end effect of the internal pressure
P_{st}	static axial load recorded in a tension test
P_T	total axial load to be applied to a pipe test specimen
P_{tot}	total axial load felt by the pipe specimen
P_μ	axial load in the pipe due to Poisson's ratio effect
R	average radius of curvature for longitudinal bending
r_{av}	average of the external and internal radii of pipe cross section
r_i	internal radius of the pipe cross section
r'	average radius of pipe cross section modified for ovalization
SMYS	specified minimum yield strength
t	thickness of a pipe cross section
T_a	the ambient temperature at the time the pipe is welded into the line
T_o	the pipe operating temperature
u_i	nodal displacement in the global i direction ($i=1, 2, \text{ and } 3$)
w	weighting function determined from the post-buckling slope of the moment curvature diagram
x	ratio of outside diameter to thickness of a pipe cross section = OD/t
y	ratio of axial load caused by temperature differential to axial yield load
z	ratio of hoop stress to yield strength

$(\bar{x}_{c.g.}, \bar{y}_{c.g.}, \bar{z}_{c.g.})$ coordinates of the centroid of a pipe cross section in the deformed configuration

(x_i, y_i, z_i) coordinates of node i of a given pipe cross section

(x_n^e, y_n^e, z_n^e) coordinates of node n in element e in the deformed configuration

\bar{y}_c distance between the centroid of the compression area of the pipe cross section and the centroid of the whole pipe cross section

\bar{y}_t distance between the centroid of the tension area of the pipe cross section and the centroid of the whole pipe cross section

Greek Characters

α coefficient of thermal expansion for the pipe material $= 11.7 \times 10^{-6} / ^\circ\text{C}$

β ratio of the hoop stress to the yield strength of a pipe

Δ_j jack extension

Δ_c compression of the specimen

Δ_F relative displacement between the jack ends

Δl elongation of gage length of 50.8 mm, as measured in a tension test

Δ_P movement of the compression head of the testing machine

ϵ longitudinal strain measure (defined in Section 5.3.8)

ϵ_e engineering tensile strain as obtained in a tension test

ϵ_{lim} longitudinal compressive strain associated with the limit point determined by Equation 5.44

ϵ_{lim}^{FEA}	longitudinal compressive strain associated with the limit point determined from finite element runs
$\epsilon_{0.95}$	longitudinal compressive strain associated with the 95% post-buckling moment capacity determined by Equation 5.46
$\epsilon_{0.95}^{FEA}$	longitudinal compressive strain associated with the 95% post-buckling moment capacity criterion determined from finite element runs
$\epsilon_{15\%}$	longitudinal compressive strain associated with 15% ovalization
$\epsilon_{0.08}$	longitudinal compressive strain associated with 8 % hoop strain
ϵ_t	engineering tensile strain as obtained in a tension test
ϵ_{cr}	critical (buckling) strain as determined from an eigenanalysis
θ	rotation of the top or bottom loading arm
θ_b	rotation of the bottom end of the tested specimen
θ_i	nodal rotation around the global i axis ($i=1, 2, \text{ and } 3$)
θ_l	angle between the normals of the two planes passing through the end cross sections of a pipe segment used in computing local curvature.
θ_t	rotation of the top end of the test specimen
θ_{tot}	sum of the top and bottom rotations = $\theta_b + \theta_t$
ψ	half of the angle subtending the area of the pipe cross section subjected to tension
ϕ_g	global curvature
ϕ_l	local curvature

Φ_{lim}	local curvature at the limit point
$\Phi_{10.95}$	local curvature at the point of 0.95% moment capacity in the post-buckling range of deformation
Ψ_s	ratio of the elastic modulus to secant modulus
Ψ_t	ratio of the elastic modulus to the tangent modulus
μ	Poisson's ratio
σ_{comp}	longitudinal compressive stress in the pipe wall that would cause the pipe material to yield according to the Von-Mises criterion
σ_e	engineering tensile stress as obtained in a tension test
σ_h	hoop stress in the pipe wall
σ_l	longitudinal stress
σ_p	longitudinal stress in the pipe due to the closed end condition
σ_t	true tensile stress
σ_{tens}	longitudinal tensile stress in the pipe wall that would cause the pipe material to yield according to the Von-Mises criterion
σ_y	yield stress of the pipe material (stress corresponding to 0.5% strain)
σ_θ	circumferential stress

1. Introduction

1.1 Background to the Problem

Buried pipelines are subject to a number of loading conditions. These include internal pressure caused by the action of the fluids they convey, axial forces due to thermal effects, and bending induced by differential settlements. The latter type of deformation might be caused by factors such as slope movements, frost heave, and thaw settlements. Consequently, differential soil movement can represent a major design consideration in the design of buried pipelines.

1.2 Design of Pipelines in Current Practice

Clauses 5.2.3 and 5.3.2.1 of the Canadian code for oil pipeline systems, CAN/CSA-Z183-M90 (Canadian Standard Association, 1990), limit the maximum internal pressure acting on a pipe to that which will produce a hoop stress of 80% of the Specified Minimum Yield Strength (SMYS) of the pipe material. According to Clause 5.6.2.1 of the code, axial forces caused by temperature differentials are limited to values that do not cause the pipe steel to yield according to the Tresca criterion.

Potential causes of imposed deformations on buried pipelines are recognized by the code (Clause 5.1.4). These are slope movements, fault movements, seismic related movements, frost heave and thaw settlements. Clause 5.2.1.3 requires the designer to set criteria for pipe denting and wrinkling that limit excessive deformations resulting from these factors, based on non-linear modeling of pipe. The nature of the deformation criteria to be used, as well as the selection of the method of analysis, are left to the judgment of the designer.

1.3 Need to Limit Deformations

Excessive deformations can lead to one of at least two modes of failure in a pipeline. The first mode can occur when the pipe cross section undergoes ovalization under imposed deformation. If the least diameter of a deformed pipe cross section becomes too small, it can prevent the passage of pigging devices used in the monitoring of the pipeline, leading to an operational failure of the pipeline. In addition, the deformation of the cross section in the manner described can affect the flow capacity of the pipeline significantly, affecting the functionality of the pipeline. The second mode can occur when the pipe cross section exhibits an outward bulging. If the cross section becomes too inflated at an outward bulge buckle, high tensile hoop stresses occur in the pipe wall and may reach a level where rupture of the pipe material may can place.

1.4 Theoretical Concepts in Pipe Local Buckling

Two types of local buckling can occur in a pipe. These are non-linear collapse buckling and bifurcation buckling. The two types of local buckling are explained in the following sub-sections.

1.4.1 Non-linear Collapse Buckling

As a loading system is applied to a pipe made of an elasto-plastic material, the pipe undergoes deformation. At the beginning of the deformation response, the slope of the load vs. deformation curve corresponds to that of the elastic stiffness of the pipe. Due to geometric and material non-linearities, the slope of the curve becomes flatter as the pipe undergoes further deformation (see Figure 1.1). Eventually, the applied load vs. deformation curve reaches a point of zero slope. The point where the slope of the applied load vs. deformation curve is zero is referred to as the limit point. If the pipe is subjected to further imposed deformation, the load vs. deformation curve exhibits a drop in the load carrying capacity of the pipe, characterized by a negative slope of the applied load vs.

deformation curve. The non-linear load deformation path can be predicted by means of a non-linear incremental analysis.

Non-linear collapse occurs when the stiffness of the structure is zero or negative and the loading acting on the pipe is maintained constant (active system of loading) as the pipe deforms. The cylinder undergoes sudden collapse, characterized by very large deformations in an almost instantaneous manner.

1.4.2 Bifurcation Buckling

Bifurcation buckling is a different type of instability. Structures with no imperfections are susceptible to this kind of behaviour. At the beginning of the load vs. deformation response, the pipe response follows the initial equilibrium path (called the primary path) until it reaches a point in the load deformation response where the pipe may possess two (or more) different possible equilibrium paths (see Figure 1.1). Starting from this point, the pipe may follow a new deformation pattern, referred to as the secondary path. In the case of a cylinder, the slope of the secondary path of the load vs. deformation curve is typically negative. The point where a primary path intersects with a secondary path is referred to as a bifurcation point. The detection of bifurcation points, as well as the corresponding deformation patterns, can be accomplished through eigenvalue analyses. Bifurcation points may occur either before or after the limit point.

In a real structure, imperfections caused by geometric irregularity, material non-uniformity, and residual stresses induced during manufacturing and transportation processes can take place. These imperfections contain or result in components of both the pre-buckling and post-buckling deformation patterns. Therefore, bifurcation buckling cannot occur in a real structure. For the case of a cylinder with imperfections, the load vs. deformation curve does not exhibit the kinks as observed in the case of a perfect cylinder at points of bifurcation (see Figure 1.1). However, the load vs. deformation curve of a real cylinder approaches that of a perfect cylinder as the magnitude of imperfections in the real cylinder decreases.

The pre-buckling range of deformation is the range of deformation preceding a bifurcation or limit point. The post-buckling range of deformation is the range of deformation occurring after a bifurcation or limit point.

1.5 Categories of Deformation Limits

1.5.1 Longitudinal Compressive Strain

Among other researchers, Bouwkamp (1973), Workman (1981), and Kim and Velasco (1988) suggest the use of the extreme fiber compressive strain as a measure upon which to establish local inelastic buckling criteria. The selection of strain rather than stress in limiting deformations of pipes under buckling is based on two reasons. On the one hand, strains are easier to measure or estimate in the field. On the other hand, the stress vs. strain relationship is generally flat in the plastic range of deformation of the material, and a small variation in stresses corresponds to a large variation in strains. Therefore, stress is a poor measure upon which to base post-yield buckling criteria.

In the pre-buckling range of deformation, longitudinal compressive strain magnitudes do not depend on the gage length, as confirmed by the measurements of Bouwkamp (1974). After the strains become non-uniform, (i.e., develop regions of strain localization) they become dependent on the gage length used for strain measurements. In the post-buckling range of deformation, for the same local buckle the longitudinal compressive strain averaged over a small length of a buckled pipe segment is higher than that based on a bigger length of the same pipe. It is important therefore, in the post-buckling range of deformation, to mention the gage length used for the evaluation of strain measurements of a deformed pipe segment in order to fully describe its state of deformation.

Limits for longitudinal compressive strains can be based on a number of criteria. Some of the criteria adopted by researchers are presented in the following sub-sections.

1.5.1.1 Buckling Initiation Criterion

Longitudinal compressive strains at which the initiation of buckling of the pipe wall was observed were measured and documented in the full-scale tests performed by Bouwkamp and Stephen (1973, 1974). A rigorous measure in determining the initiation of buckling during the test was not reported by the authors, and one may assume that buckling initiation was visually determined. No records of strains after the initiation of buckling were taken. However, from the shape of the moment vs. curvature curves reported, it may be inferred that all the reported strains were all in the pre-buckling range of deformation.

The longitudinal strains were measured using strain gages and clip-gages. The gross strains based on clip-gage measurements were averaged over the whole length (3048 mm or 10 ft.) of pipe section. Strains as determined by clip-gage and strain gage measurements agreed within 5% in some of the specimens tested. The greatest difference between the two methods of strain measurement was 30% .

As described following, Lara (1987) used the measurements from the Bouwkamp and Stephen (1973, 1974) tests in order to set limits for compressive longitudinal strains for the pipes tested.

1.5.1.2 Rapid Wrinkle Growth Criterion

Lara (1987) performed analyses on pipe segment geometries and conditions of the Bouwkamp tests (1973). The analyses were based on the elbow elements of the finite element program ABAQUS. He suggested adopting the longitudinal compressive strain after which a rapid wrinkle growth is detected as rational deformation limiting criterion. An exact definition of rapid wrinkling growth was not explicitly stated in Lara's paper (Lara, 1987). However, it is inferred that rapid wrinkle growth was associated with a rapid change in wrinkling curvature on the compression side of the specimen with respect to the change in the overall curvature of the specimen.

According to Lara (1987), the rapid wrinkle growth criterion yielded higher limits on longitudinal compressive strains than those based on buckling initiation. For a pressure of 0.17 MPa, the strain based on rapid wrinkle growth criterion was 0.40% versus 0.30% for the initiation of buckling criterion. For a pressure of 6.35 MPa, significantly higher strains were obtained. The rapid wrinkle growth criterion yielded values in the 2.5% to 3.0% range versus a value of 0.55% at the initiation of buckling as determined by Bouwkamp and Stephen (1973 and 1974) for identical pipe geometry and loading conditions.

1.5.1.3 Peak Moment Criterion

Murphey and Langner (1985) observed that buckling deformations grow rapidly in thin cylinders after the point of maximum moment. Therefore, they adopted the compressive strain corresponding to the maximum moment as a deformation limit. This limit state definition is suited for cases where abrupt drops in the bending moment take place, i. e., for unpressurized pipes. An example for the use of the peak moment criterion in determining of longitudinal compressive strain limits is given in the experimental work of Prion and Birkemoe (1988).

Reddy (1979), following a series of tests on aluminum pipes, realized that curvatures (or strains) are more adequate measures of local buckling than are moment capacities. This was due to the fact that the moment vs. curvature diagram of the tests exhibited a flat plateau. Where the moment vs. curvature relationship of a pipe exhibits a flat plateau, as is the case for highly pressurized pipes in general, the point of significant softening in a moment curvature diagram (Zhou and Murray, 1993) becomes a more precise description of a deformation limit state.

1.5.2 Cross-Sectional Deformation

Ovalization of a pipe cross section occurs when a thin pipe undergoes curvature under flexural stresses. This phenomenon was described and studied by Gresnigt (1986). The

hoop stresses in the neighborhood of the extreme compression and tension fibers of a pipe subject to curvature have components that force the pipe wall at these region to move towards the centroid of the pipe cross section. Gresnigt (1986) suggests limiting pipe out-of-roundness O_r to 0.15, where

$$O_r = \frac{(D - D_s)}{D} \quad (1.1)$$

The symbol D denotes the original outside diameter of the pipe and D_s is the smallest outside diameter of the deformed cross section. Price and Barnette (1987) suggest adopting the same expression as a deformation limit state for buried pipelines. In a later paper, Price and Anderson (1991) give arbitrary limiting values for out-of-roundness (or ovalization) of 15% for unpressurized pipes and 6% for fully pressurized ones. The out-of-roundness expression was originally intended to limit cross section ovalization. However, the criterion may be extended to complex deformation patterns of pipe cross sections such as diamond shape buckling.

Row et al. (1987) defined another limit on ovalization O_v expressed as

$$O_v = \frac{2(D_l - D_s)}{(D_l + D_s)} \quad (1.2)$$

where D_l is the largest outside diameter of the deformed cross-section. In the same paper the authors suggested limiting the magnitude of O_v to 7.5% for pipes subjected to deformation controlled loads where it can be demonstrated based upon detailed inelastic analyses that sectional collapse will not occur as a result of excessive deformation.

The pipe diametric differential D_d is a slightly different expression proposed by Zhou and Murray (1993), and defined as

$$D_d = \frac{(D_l - D_s)}{D} \quad (1.3)$$

in which D_l is the largest diameter. Since the passage of pigging devices through a pipeline can be hindered only by the smallest diameter of the deformed cross section, it seems more appropriate to adopt Gresnigt's expression as a deformation limit state for this purpose. Consequently, Equation (1.1) will be used in computing the deformation limits based on ovalization presented in Chapter 5.

1.5.3 Tensile Hoop Strain

Zhou and Murray (1993), introduced a pipe cross section deformation descriptor intended for outward bulge type of buckles. This measure, called the diametric expansion, D_e , is defined as

$$D_d = \frac{(D_l + D_s)}{D} \quad (1.4)$$

Imposing limits on the diametric expansion for a given pipe indirectly limits the circumferential hoop stresses at the crest of the buckle and prevents it from rupturing under high pressure. It may, therefore, constitute a deformation limit state for pipes.

A more direct approach of tackling the problem is to limit the tensile hoop strain at the crest of outward bulges to the strain at the ductility limit of the pipe material. Limits on ductility for longitudinally welded steel pipes in the transverse direction are given in Clause 8.2.1.1 of the Canadian code for steel line pipe, (Canadian Standard Association, 1993). This approach will be used in setting one of the deformation limit states criteria in this research.

1.6 Deformation Limits for Unpressurized Pipes

1.6.1 Elastic theory

The buckling strain for an axially loaded elastic cylinder, as determined by eigenvalue analysis based on an elastic small strain theory, is presented by Timoshenko and Gere (1961). For a steel pipe with a Poisson ratio of 0.30, the critical strain is

$$\epsilon_{cr} = 1.21 \frac{t}{D_{av}} \quad (1.5)$$

where ϵ_{cr} = critical strain; t = thickness; and D_{av} = mean diameter. This value of strain is for the case of no bending and no internal pressure. The buckling configuration, as determined from eigenanalysis, follows a series of sinusoidal waves over the length of the cylinder.

It was found by Seide and Weingarten (1961), that critical strains based on bifurcation buckling for elastic cylinders subjected to bending are practically equal to those for cylinders of the same cross-sectional geometry subjected to uniform axial loading (Timoshenko and Gere, 1961). This finding was conservatively extended by Workmans (1981) and Kim (1992) in the computation of critical strains for pipes made of elasto-plastic material and subjected to bending.

1.6.2 Inelasticity of the Pipe Material

Batterman (1965) accommodated material plasticity in a procedure similar to that followed by Timoshenko and Gere (1961) in determining critical elastic buckling strains. The analysis of Batterman was accomplished through the use of reduced and tangent moduli of elasticity. Both the deformation theory and the incremental theory of plasticity were used in the analysis. Comparison with experimental results showed good agreement with the results obtained using the deformation theory of plasticity. The elastic-plastic buckling strain was expressed as

$$\epsilon_{cr} = \frac{4\psi_s}{\sqrt{3[(5-4\mu)\psi_t - (1-2\mu)^2]}} \times \frac{t}{D_{av}} \quad (1.6)$$

for the incremental theory of plasticity, if no unloading is allowed to take place, and

$$\epsilon_{cr} = \frac{4\psi_s}{\sqrt{(3\psi_s + 2 - 4\mu)\psi_t - (1-2\mu)^2}} \times \frac{t}{D_{av}} \quad (1.7)$$

for the deformation theory of plasticity. In equations (1.6) and (1.7), ψ_s = ratio of the elastic modulus to secant modulus, ψ_t = ratio of the elastic modulus to the tangent modulus, and μ = Poisson's ratio.

Expressions for buckling strain based on the point of maximum bending moment are given by Langner (1984) as

$$\epsilon_{cr} = 0.50 \frac{t}{D_{av}} \quad (1.8)$$

This equation was suggested so as to provide a lower bound of limiting strains for pipe of a diameter to thickness ratio of less than 50. Another equation given in the same paper is

$$\epsilon_{cr} = \left(4 \frac{t}{D_{av}} \right)^2 \quad (1.9)$$

Both Equations 1.8 and 1.9 are based on the experimental results of 40 tests. Ellinas et al. (1987) proposed an empirical equation of the same form as Equation (1.5) for inelastic bifurcation buckling strain and based on the experimental results of Reddy (1979) and Gellins (1980). The equation is

$$\epsilon_{cr} = 0.60 \frac{t}{D_{av}} \quad (1.10)$$

Equation 1.10 is valid for cylinders made of steel with a low strain hardening modulus and when subjected to pure bending.

Prion and Birkemoe (1988), conducted a series of twenty two tests on 450 mm OD specimens and diameter to thickness ratios between 51 and 100 with yield stresses of 250 to 450 MPa. Specimens were subjected to various combinations of axial forces and bending. One of the useful outcomes of this series of tests was the recording of longitudinal compressive strains corresponding to maximum moments.

1.7 Deformation Limits for Pressurized Pipes

Bouwkamp and Stephen (1973, 1974) performed a series of seven tests on full scale pipes. The tests were conducted on 1219 mm. (48 in.) diameter pipes, with an 11.7 mm (0.462 in.) wall thickness. The pipe material was grade X60 steel. The pipes were subjected to an axial load corresponding to a temperature differential of 75 C° (135° F) and internal pressure magnitudes of 0.172 MPa (25 psi) and 6.35 MPa (917 psi). Longitudinal compressive strains were recorded at the point of initiation of buckling. Lara (1987) used these test results to set limits for longitudinal compressive strains based on the measured values. For internal pressure magnitudes of 0.172 and 6.35 MPa (25 and 917 psi, respectively), the suggested limiting strains were 0.30 % and 0.55%, respectively.

These results were verified by an approximate method of analysis proposed by Popov (1973, 1974). The analysis consisted of two steps. First, an axi-symmetric analysis is performed in order to obtain the buckling characteristics of a pipe under the action of axial loading and internal pressure. A relationship is obtained between the axial stress and the average axial strain. This relationship is subsequently used as a material model in the modeling of the specimen under bending deformation. The pipe cross section is assumed to remain circular in the bending analysis. This approach was criticized by Lara (1987). The first criticism is that the axi-symmetric relation inadequately models diamond shape

buckling that is characteristic in the cases of low internal pressure. The second is that the assumption that pipe cross section remains circular is inadequate for large deformations in the post-buckling range of pipe deformation. The third is that the material constitutive model obtained in the first step of the analysis is dependent on the length of the specimen considered.

Workman (1981) suggested limiting the longitudinal compressive strain at the extreme fiber of a pipe segment subjected to axial loading, internal pressure, and bending to that of the strain at buckling of an axi-symmetric case of the pipe subjected to the same internal pressure. This approach is judged by the writer to be overly conservative since it neglects the effect of the compressive strain gradient that takes place in a pipe subjected to bending. The analysis was based on the deformation theory of plasticity and the mathematical formulation of Vol'mir (1966). Kim (1992) performed a parametric study based on the axi-symmetric assumption, using a different formulation than that derived by Vol'mir. The parameters investigated included the diameter-to-thickness ratio, the internal pressure effect (hoop stresses), and the material properties.

Gresnigt (1986), conducted an experimental program on pipes subjected to bending. He developed an analytical model based on an elasto-plastic material representation in order to model the behaviour of pipes subjected to axial force, bending moment, and to internal pressure. The analytical model accommodated ovalization of the pipe cross section due to bending. The solution was based on an idealized elastic-perfectly plastic stress vs. strain representation. Expressions for the critical strains were obtained as

$$\epsilon_{cr} = 0.25 \frac{t}{r^I} - 0.0025 + 3000 \left(\frac{pr}{EI} \right)^2 \frac{|p|}{p} \quad (1.11)$$

which is valid for $\frac{r^I}{t} < 60$, and in which

$$r^I = \frac{r_{av}}{1 - \frac{3a}{r_{av}}} \quad (1.12)$$

and a is the ovalization at the maximum compression fiber and r_{av} is the average radius of the pipe cross section. In Equation 1.11, E is the modulus of elasticity of the pipe; I is the moment of inertia; and p is the pressure acting on the pipe. It is positive for internal pressure. For $\frac{r^I}{t} > 60$, the following expression is suggested

$$\epsilon_r = 0.10 \frac{t}{r^I} + 3000 \left(\frac{pr_{av}}{EI} \right) \frac{|p|}{p} \quad (1.13)$$

Unlike the solution of Workman (1981), and Kim (1992), The Gresnigt solution addresses bending deformation of pipes under both internal and external pressure. However, two important design factors remain unaccounted for in the solution, namely, the influence of local buckling and the magnitude of the axial load to which the pipe may be subjected. Furthermore, no geometric non-linearity was accounted for in the analysis.

1.8 Scope of Research

This research is concerned with the deformational behaviour of buried pipelines under the action of axial loads, internal pressure, and deformation-controlled imposed bending. The research objectives are:

1. To provide an experimental data base for the deformational response of pipelines subjected to the combined action of axial loading, internal pressure, and deformation-controlled imposed deformation.
2. To select and establish the validity of an analytical tool to reliably predict the deformational behaviour of pipelines.

3. To perform a parametric study in order to determine the effects of factors such as axial loads, internal pressure, and diameter-to-thickness ratio on the deformational behaviour of pipelines.
4. To define and select deformation-limiting criteria suitable for design purposes.
5. To integrate the findings of the parametric study into design equations that include major factors influencing the deformational behaviour of pipes.

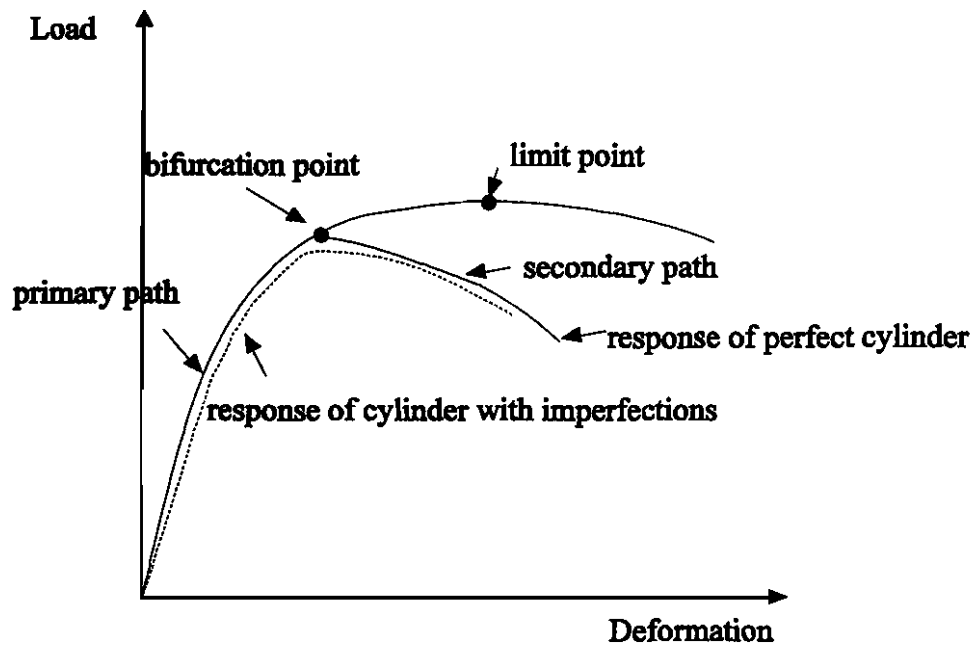


Figure 1.1 Typical Load vs. Displacement Relationship for Cylinders

2. DESIGN OF EXPERIMENTS

2.1 Scope

As reported in the literature, numerous experiments have been carried out in order to determine the structural response of pipes. However, only a very limited number of these tests were performed in order to investigate pipeline deformational behaviour. This project focuses on establishing the deformational behaviour of pipelines. It is economically prohibitive to try to cover the entire range of pipeline geometries, material properties, and loading conditions that might exist in the field in an experimental program. Therefore, it was the goal of the project to establish an experimental database of realistic benchmark problems against which the ability of selected analytical models for the prediction of pipeline deformational response could be tested. Once the validity of a predictive model is established, it can subsequently be utilized to perform a series of analyses in order to predict deformation limits for pipelines for design purposes.

The experimental program consisted of testing seven specimens. The testing conditions were carefully selected to represent limiting conditions achievable in the field, thereby providing experimental information at the bounds of the range of interest of major field variables. If the model is capable of reliably modeling these limiting conditions, it is judged to be capable of modeling any intermediate conditions with a comparable degree of confidence.

2.2 Selection of Specimen Dimensions

Full scale testing is needed in order to experimentally determine the deformational behaviour of pipes in the field. The size of pipes tested had to be representative of the pipes typically used in the pipeline industry. The selected diameters were to lie in the range of pipe diameters supplied by major suppliers of steel pipes in the Canadian market.

Two sizes of pipe were selected: 508 mm outside diameter (OD), and a 324 mm OD. The former is representative of pipes currently used in the oil pipeline industry and the latter was selected to match the size of the Norman Wells Line, operated by one of the sponsors of this project. In the Norman Wells pipeline, strains approaching those normally allowed in the current pipeline practice have been recorded, and were of concern to the line operators.

The diameter to thickness ratio (D/t) has been recognized by many researchers to be an influential factor in the local buckling behaviour of pipes (see Section 1.6). Most of the pipelines in current practice have a (D/t) ratio ranging from 30 to 100. The thicknesses of the test specimens were selected so that their diameter to thickness ratio falls in this range. The two sizes of pipes selected and their wall thicknesses gave (D/t) ratios of 64 and 51. Table 2.1 gives a summary of pipe geometry and loading conditions for test specimens.

The local buckling deformational behaviour of a pipe segment under axial load is generally independent of the specimen length. The validity of this statement will be subsequently verified (refer to Section 2.8.2 on stub column test). Therefore, specimen length was not considered as a parameter to be varied in the experimental program. However, an important consideration concerning specimen lengths is that they should be long enough to allow local buckling to develop in regions that are not influenced by the boundary condition disturbances. This consideration led to the selection of a specimen length in the neighborhood of three diameters of the large pipe. All specimens were 1690 mm long in order to be compatible with the designed experimental setup.

2.3 Selection of Pipe Manufacturing Processes

The behaviour of pipes under large deformation can depend upon fabrication techniques since these influence material properties, residual stress patterns, and initial imperfections. Two methods of pipe manufacturing were represented in the experimental

program, namely: (a) the double submerged arc-welded technique (DSAW), as used for the 508 mm OD diameter pipes , and (b) the electrical resistance welded technique (ERW), as used for the 324 mm OD diameter pipes. Both methods are used in current pipe manufacturing practice by major suppliers of pipes in Canada.

2.4 Modeling of Field Conditions

2.4.1 Axial Loading

The axial load to be applied to a test specimen in order to simulate the axial force in an operating pipeline is evaluated by superimposing the effects of temperature, Poisson's ratio, and internal pressure, as described below.

2.4.1.1 Axial Load Caused by the Thermal Effects

When a pipe segment is welded into a line of pipe at an ambient temperature less than the pipe operating temperature, it subsequently attempts to expand longitudinally because of the differential thermal effect between the operating temperature and the tie-in temperature. However, its longitudinal movement is restrained by the presence of anchors, adjacent pipe segments and fittings, as well as by the friction provided by the surrounding soil. Under full restraint, the thermally induced axial compressive load to which the pipe is subjected during operating conditions is

$$P_t = A E \alpha (T_o - T_a) \quad (2.1)$$

where P_t = the thermally induced axial compressive force in the pipe; A = the cross sectional area of the pipe; E = the elasticity modulus of the pipe material = 200 000 MPa; α = the coefficient of thermal expansion for the pipe material = 11.7×10^{-6} 1 / °C. T_o = the pipe operating temperature and T_a = the ambient temperature at the time the pipe is welded into the line. An operating temperature of 0 °C is maintained in oil

pipeline crossing regions of permafrost and, consequently, this temperature has been adopted in the design of this series of experiments. Practical considerations put a lower limit of -45°C for the value of T_a .

The maximum temperature differential $(T_o - T_a)$ would not normally exceed 45°C . This magnitude was used in the design of six out the seven tests in this program. Table 2.1 summarizes the design temperature differentials for all test specimens. In some instances, the tie-in temperature, T_a , may be higher than the operating temperature, T_o , subjecting the pipe to an initial tensile axial force instead. This case is less critical for buckling and was not considered in the experimental study. One of the seven tests was designed for a zero temperature differential.

2.4.1.2 Axial Load Resulting From the Poisson's Ratio Effect for Hoop Stresses

When internal pressure is applied to a pipe segment, that segment will attempt to shorten longitudinally because of the Poisson's ratio effect arising from circumferential stresses. In the field, this shortening is prevented, for a longitudinally restrained pipe, because of the presence of adjacent pipe and the surrounding soil. For a laboratory specimen, this restraint is not present and axial shortening is, therefore, not prevented. Thus, in order to simulate field conditions, an additional axial tensile force, P_{μ} , has to be applied to the ends of the specimen. This force is described by

$$P_{\mu} = -A\mu \sigma_h \quad (2.2)$$

where P_{μ} = axial load in the pipe due to the Poisson ratio effect; μ = Poisson's ratio; and σ_h = the hoop stress. The minus sign in Equation (2.2) denotes a tensile force acting on the specimen.

2.4.1.3 Axial Load Caused by Internal Pressure Acting on Closed Ends of Specimens

For laboratory specimens, both ends of the pipe must be closed and the internal pressure acting on the closed ends of the pipe results in an axial tensile force acting on the specimen. Such a force does not exist in the case of an open-ended pipe in the field. In order to properly simulate field conditions, it is therefore necessary to apply a compensating compressive axial force P_p to the ends of the laboratory specimen that has the value

$$P_p = \pi r_i^2 p \quad (2.3)$$

where r_i = the internal radius of the pipe and p = the internal pressure of the fluid in the pipe. The longitudinal stress in the pipe, σ_p , as the result of the closed end condition, is obtained by dividing both sides of Equation (2.3) by the cross-sectional area of the pipe.

$$\sigma_p = \frac{P_p}{A} = \frac{\pi r_i^2 p}{2\pi r_{av} t} \quad (2.4)$$

where r_{av} = the average radius and t = the thickness of the pipe wall. Considering that r_i is approximately equal to r_{av} , Equation 2.4 reduces to

$$\sigma_p = \frac{r_{av} p}{2t} \quad (2.5)$$

2.4.1.4 Total Axial Load

The total axial load to be applied to a test specimen, P_T , is given by superposition of the individual effects of P_t , P_μ , and P_p . Thus,

$$P_T = P_t + P_\mu + P_p \quad (2.6)$$

Table (2.2) gives the magnitudes of the design values of P_T , P_I , P_μ , and P_p for all seven tests in the experimental program.

2.4.2 Differential Settlement Effects

When differential settlement takes place, pipelines undergo longitudinal strains as a result of bending deformation and the catenary action of the pipeline. The effects of these two mechanisms of deformation are discussed in the two following sub-sections.

2.4.2.1 Longitudinal Bending Strains

Curvature imposed by differential settlements induces compressive longitudinal strains on the concave side of the bends. These strains, superimposed on the longitudinal compressive strains produced by axial loading make pipes susceptible to local buckling. In the experimental program, settlement-imposed curvatures are simulated by applying monotonically increasing rotations at both ends of the specimens.

2.4.2.2 Catenary Action of Pipelines

When a segment of a pipeline is subject to differential settlement, the difference between the slope length and the projected length causes the pipe to stretch. This attempt to elongate will be called the catenary effect of the pipe in the deformed state. Such action is apparent in Segment B of Figure 2.1. Adjacent portions of the pipe, Segments A and C, also attempt to elongate in order to relieve a portion of the axial stress to which they are subjected. This action is counteracted, in part, by longitudinal frictional forces between the soil and the pipe.

The following two extreme cases are identified:

a) **Constant Projected Length for Segment B:** When the friction forces distributed along the length of the pipe (F_1 and F_2) are of high enough magnitude, and are concentrated in the areas immediately adjacent to Segment B, the elongation of Segments A and C are negligible ($\Delta_1=\Delta_2=0$). In this case, the ends of segment B are fully restrained from moving

in the axial direction. Therefore, if segment B is initially subjected to a compressive thermal force, a decrease in the magnitude of this force will take place in Segment B as the segment is deformed by the action of differential settlement. For large differential settlements, the axial force at the center of the segment may eventually become tensile. The axial end forces on Segment B act as reactive forces. This case will be referred to as a reactive case. It is considered to be the least critical boundary condition with respect to local buckling.

b) Constant Forces on Ends of Segment B: If the longitudinal friction forces along Segments A and C are negligible, these portions become free to elongate. The ends of Segment B move inwards (i.e., Δ_1 and Δ_2 have non-zero values). If Segments A and C are long, the axial load acting on Segment B could remain approximately constant throughout the deformation history of the pipe. The axial forces at the end of segment B then act as active forces. This case will be referred to as an active case. This condition is considered to give the most critical case for local buckling in the pipe.

Real field loading conditions will lie between the active and reactive cases. In the experimental program, both limiting cases were investigated: there were five active tests and two reactive ones. (See Table 2.2)

2.4.3 Internal Pressure

Under working conditions, pipelines are subject to internal pressure caused by the pressure head of the fluid being conveyed. The magnitude of the internal pressure is a function of the location of the pipe segment relative to the pumping station. Immediately downstream of the pumping station, the internal pressure is at its maximum value. This magnitude drops as one moves downstream in the pipe because of the frictional resistance between the pipe and the fluid, as illustrated in Figure 2.2. A pressure magnitude in the neighborhood of zero is expected immediately upstream of the next pumping station.

The maximum design internal pressure is specified indirectly in the Canadian design code (CAN/CSA-Z183 Oil Pipeline Systems). The code limits the hoop stress produced by internal pressure to a fraction β of the specified minimum yield stress of the pipe material. The current code (CAN/CSA-Z183-M90) allows a maximum magnitude for hoop stress of 80% of the specified minimum yield strength ($\beta = 0.80$) while previous codes specified a maximum value of the magnitude of β of 0.72. A hoop stress magnitude of 0.80 (SMYS) represents the working conditions immediately downstream of the pumping station for pipelines now under construction and is of importance for design purposes. A hoop stress of 0.72 (SMYS) represents the working condition hoop stress of many existing pipeline networks. Its importance lies in assessment of existing lines. Maximum internal pressures corresponding to each of the above magnitudes of hoop stress were included in the experimental program. Three tests represented the upstream pressure condition, three simulated the downstream condition, and one test modeled a condition halfway between these extreme conditions (see Table 2.2).

2.5 Loading Combinations

A summary of the selected load combinations of all tests is given in Table 2.1. Each of the seven tests is designated by a descriptor of the form XYZnnn, where X designates the internal pressure condition, Y the thermal effect, Z the boundary condition of the pipe in the axial direction (i. e., whether it is active or reactive), and nnn designates the outside diameter of the pipe in mm.

The internal pressure indicator, X, is given the symbol U when the test is designed to model a pipe immediately upstream of a pumping station in the field (i.e., nearly zero internal pressure), D for a pipe segment immediately downstream of a pumping station (i.e., fully pressurized), or H for a pipe segment half-way between these two locations (i.e., medium pressure).

The thermal effect indicator, Y, is given the symbol G to represent the greatest possible compressive thermal effect (corresponding to a 45 C⁰ temperature differential), or L to represent the least compressive thermal effect (for zero temperature differential).

The axial boundary condition indicator, Z, is designated as A to represent an active type of boundary, or R to represent a reactive type of boundary. The pipe size indicator, nnn, is the outside diameter in mm. It has the values 508 for the 20 in. diameter pipe and 324 for the 12.75 in. diameter pipe.

2.6 Description of Experiments

2.6.1 Experimental Setup

The experimental program was carried out in the Morrison Structural Engineering Laboratory at the University of Alberta. The test setup for the program is shown in Figure 2.3. Each of the 1690 mm long specimens was placed vertically under the head of the universal testing machine. The 6000 kN capacity machine was used to provide a concentric axial load to the tested specimen. Each end of the specimen was welded to a 64 mm thick plate in order to maintain the pipe end cross sections planar throughout the test. Each end plate was bolted to an extremity of a 2080 mm long steel arm. The centerlines of the two arms were positioned such that they fell in a vertical plane containing the pipe center-line. A 600 kN capacity jack was pin-connected to the far ends of the loading arms in order to be able to provide an eccentric axial force to the tested specimen. The plane passing through the centerline of the pipe segment, loading arm, and jack centerline will be called the bending plane.

Normal to the bending plane, two knife edges were placed, one on the top of the upper arm, and the other at the bottom of the lower one (see Figure 2.3). Each knife edge was able to provide a rotation capacity of about seven degrees in the plane of the arms. In order to preserve the stability of the loading frame, the head of the compression machine

was locked so as to prevent its rotation. No out-of-plane deformations or rotations of the specimens were anticipated during the tests. However, a small lateral rotation capacity had to be provided to the testing frame in order to provide full contact between the compression head of the machine and the loading frame. This rotation capacity also accounted for any asymmetric behaviour of the specimen due to the variation in the specimen material properties and geometry, and to account for slight alignment errors. The rotation capacity needed was provided by placing an additional knife edge in the bending plane between the testing machine compression head and the top arm (see Figure 2.3).

In order to avoid potential end effects on the local buckling behaviour of the tested pipes, the ends of the specimen were confined by means of 150 mm wide steel collars made from a short length of the same pipe. No physical connection was provided between the collars and the pipe. The confining action was provided solely by contact between the two components. The collars prevented local buckling from occurring in the immediate vicinity of the specimen end plates.

2.6.2 Fabrication Sequence and Alignment Procedure

The loading arms consisted of a closed built-up section having two 10 mm thick webs and two 25 mm thick flanges. Each of the 660 x 540 x 64 mm steel end plates was bolted to a flange end of a loading arm using five ASTM A490 bolts on the tension side of the pipe and two on the compression side (see Figure 2.4). The other end of the loading arms was bolted to the jack fittings. The distance between the pipe and the location of the line of application of the eccentric force could be adjusted from test to test by changing the position of the jack fittings along the loading arms. Stiffening arrangements were provided to the loading arms at the loading points.

For each of the seven tests, the specimen was first flame-cut and its edges were beveled at angles between 50 and 60 degrees. The confining collars were placed around the specimen ends. The upper loading arm was placed on the laboratory floor in its inverted

position. The pipe was then welded to the end plate by means of three welding passes. The resulting L-shaped frame was then inverted and moved into the testing machine where it was suspended under the loading head (see Figure 2.5). The bottom arm was placed under the pipe in the same vertical plane as the top arm and then leveled. The bottom end of the pipe was then welded to the bottom end plate.

If the test was to model a pressurized case, the pipe interior was filled with water (refer to Section 2.6.3). After the test was completed, the specimen was emptied, flame cut at the top and bottom ends, and removed. The surface of the end-plates was ground and smoothed and the same process was repeated for the next specimen.

2.6.3 Application of Internal Pressure

A hole was provided through each end plate in order to connect the interior of the pipe to the pump and the bleeding hoses. The hole in the bottom plate served to fill the pipe with water and the hole on the top was used to bleed the pipe of air as the pipe was filled. Internal pressure was provided by filling the interior of the specimen with water. The water was pressurized by means of a manually regulated pneumatically-powered pump. The pressure was monitored with a pressure transducer installed in the supply line to the tube.

2.6.4 Control of the Test

The testing machine load, P , and eccentric jack load, F , shown in Figure 2.6, were regulated through a computer program written in Labview 2 language. The program ran on a Mac IICI computer equipped with a card that provided two analog output and eight analog input channels.

Six of the input channels were used to provide the program with analog signals of: (1) the concentric load, P ; (2) the movement of the compression head of the testing machine, Δ_P ; (3) the eccentric load, F ; (4) the movement between the jack ends, Δ_F ; and (5) two other LVDTs that monitored the axial extension of the pipe. Because of deformations in the

arms, knife edges, and testing frame, the quantity Δ_P was not equal to the deformation of the pipe.

The output channels were used to send analog signal outputs to control the position of the rams of the two applied loads, P and F .

Two types of control corresponding to the active and reactive schemes of loading were provided by the same program module. In the former type of control, the axial force in the pipe was maintained constant ($P - F = C_{set}$), while the latter maintained the length of the test section constant. In both cases, the end rotations of the specimen were monotonically increased by ramping the stroke of the jack at the end of the loading arms.

In order to preserve the overall stability of the testing frame between the knife edges, a minimum value of the concentric load P had to be maintained throughout the test. The control program had the capability of imposing this condition if the load P were to drop below a certain specified value P_{min} during the testing process.

2.7 Instrumentation and Measurements

Several categories of measurement devices were installed. These were strain gages, Demec points, rotation meters, LVDTs, load cells, and photogrammetric equipment. These are detailed in the following subsections.

2.7.1 Strain Measuring Devices

Thirty-six longitudinal strain gages were mounted on each specimen, as shown in Figure 2.7. Eighteen of them were placed near the maximum compression fiber and along the length of the specimen in order to get measurements for the buckling strains. Three rings of strain gages, one near the top, one at mid-height, and one near the bottom of the specimen, were mounted in order to check the alignment of the specimen. Each ring

consisted of eight strain gages and they were placed equidistantly around the circumference of the pipe. In addition, for five of the tested specimens, strains based on Demec gage readings were recorded. Figure 2.7 shows the location of strain gages for a typical specimen and Figure 2.8 shows the Demec gage reading process for one of the specimens.

2.7.2 Load and Axial Movement Measuring Devices

The load and the compression head movement of the testing machine were recorded by the data acquisition system. LVDTs were installed along the length of the specimen in order to measure its shortening and the jack piston change of position. A special load cell connecting the jack piston and the pin connection to the loading arm was installed to measure the jack load (see Figure 2.3).

2.7.3 Rotation Meters

Two electronic rotation meters were installed, one on the top arm and the other on the bottom arm, in order to measure the end rotations of the specimen. In addition, the rotation of the specimen ends could be estimated from the geometry of the deformed configuration of the loading frame, i.e., the jack stroke reading and the specimen shortening. These measurements provided relative displacements between points on the loading arms and from which the relative rotations were computed. This provided redundancy in the measurements of the end rotations and overall curvatures.

2.7.4 Deformation Response Measuring Techniques

Two methods were employed to monitor the local buckling of the pipe wall as load and deformation were imposed on the pipe. The first consisted of measuring the radial displacements of selected points on the surface of the pipe. In order to do this, a frame with a circular hole concentric with the test specimen was constructed as shown in Figure 2.9. The frame carried a series of eight LVDTs pointed in a direction perpendicular to the

initial surface of the pipe (i. e., the radial direction). The frame was able to slide up and down along the posts of the testing machine and this enabled the measurement of radial displacements at pre-selected heights. For a given deformed configuration of the pipe, radial displacement readings were taken at up to thirteen stations along the length of the specimen. The deformed configuration of the pipe could then be mapped relative to the pipe initial configuration, also obtained using measured radial displacements.

The second method used to monitor local buckling consisted of taking photographs of the specimen simultaneously with two different cameras from two different angles. The intention was that coordinates of any point on the specimen could then be determined from the photogrametric processing of the resulting pairs of photographs.

2.8 Ancillary Tests

2.8.1 Tension Tests

2.8.1.1 Description of The Tests

Coupons were cut from the pipe material in the longitudinal direction. The tension coupons and testing procedures conformed to the ASTM specifications. One of the purposes of these tests was to get a description of the material properties well into the large deformation range. This information is a vital input in the finite element analysis needed to corroborate the experimental analysis. Accordingly, the tension tests were carried out using displacement control and under a slow rate of deformation. For a given strain, the test was stopped for a few minutes before the magnitude of the load was recorded so that the loads recorded and, subsequently, the stresses computed were static values and, would not be influenced by rate effects in the test. The load versus deformation response was recorded throughout the range of deformation and until rupture occurred.

An extensometer of 50.8 mm gage length was mounted on the tension coupon to measure the longitudinal strain in the middle portion of the coupon. Longitudinal strain gages were used as another measure of longitudinal strains, providing a measurement redundancy in order to check the quality of the measurements. The strain readings from both methods agreed well in the initial state of the tests, discrepancies in the readings were detected after the coupons were deformed well into the plastic range. This was probably due to the detachment of the strain gages from the surface of the specimen at high strains. The strain readings of the extensometer were judged to be reliable until necking occurred and were therefore selected to determine the longitudinal strain response. The extensometer was removed before the longitudinal engineering strain reached a 20% value. After necking, the strain field along the coupon loses its uniformity and different locations of the extensometer with relative to the neck would yield different strain readings.

Transverse strains were measured by strain gages mounted transversally on the central portion of the coupon. One strain gage was mounted on each large face of the coupon. The average of the two readings was taken, and the initial ratio of the transverse to the longitudinal strain determined the Poisson ratio to be used in the analysis. As expected, the coupons exhibited significant ductility. Engineering longitudinal strains were estimated to attain values in excess of 20%.

2.8.1.2 Computation of Engineering Stresses and Engineering Strains

The engineering stress σ_e is computed as the recorded static load P_{st} divided by the undeformed area of the coupon A_o

$$\sigma_e = \frac{P_{st}}{A_o} \quad (2.7)$$

The engineering strain was calculated as the ratio of measured elongation to the initial gage length

$$\varepsilon_e = \frac{\Delta l}{l_o} \quad (2.8)$$

where ε_e is the engineering strain and Δl is the elongation of the gage length l_o . Figures 2.10 and 2.11 show the engineering stress vs. engineering strain relationships for X56 material (508 mm OD pipes) and the X52 material (324 mm OD pipes). The stress vs. strain curves presented are based on the average stress values (at arbitrarily selected strains) obtained in the three coupon tests performed for each of the X52 and X56 materials.

2.8.1.3 True Stress vs. True Strain Relationship

The engineering stress vs. engineering strain relationship is a satisfactory representation of the material behaviour for a small strain analysis. However, for a finite strain analysis, such as for the kind of problems investigated in this research, a true stress vs. true strain relationship is a more adequate description of material behaviour. The true stress is the measured load per unit cross-sectional area in the deformed configuration. It is not practical to measure the area of a tension coupon for every load increment in a tension test. However, knowing that the volume of the specimen remains constant when it undergoes plastic deformation, i.e.,

$$A_o l_o = A_d l_d \quad (2.9)$$

where A_d is the coupon cross-sectional area in the deformed state, l_d is the deformed length of the gage length l_o . The true stress, σ_t , can be calculated by

$$\sigma_t = \frac{P_{st}}{A_d} = \frac{P_{st}}{A_o} \times \frac{A_o}{A_d} = \sigma_e \times \frac{l_d}{l_o} \quad (2.10)$$

The true strain is defined by the integral

$$\varepsilon_t = \int_{l_0}^{l_d} \frac{dl}{l} = \ln\left(\frac{l_d}{l_0}\right) = \ln\left(\frac{l_0 + \Delta l}{l_0}\right) = \ln(1 + \varepsilon_e) \quad (2.11)$$

Figures 2.10 and 2.11 show the true stress-true strain relationships as computed from Equations 2.10 and 2.11 for X52 and X56 materials, respectively.

2.8.1.4 Ramberg-Osgood Fit of Stress-Strain Curve

The Ramberg-Osgood fit (1946) is an analytical description that is specially suited to represent the true stress-true strain relationship of metals not exhibiting a flat yield plateau. It takes the form

$$\varepsilon_t = \frac{\sigma_t}{E} + c \left(\frac{\sigma_t}{\sigma_y} \right)^n \quad (2.12)$$

where σ_y is the stress corresponding to 0.005 strain and constant c and plasticity exponent n are parameters determined from regression analysis. The magnitude of n determines the slope of the plastic region, as illustrated in Figure 2.12. As exponent n increases, the slope of the stress vs. strain curve in the post-yielding range decreases.

This stress idealization has been used by other researchers (e.g., Workman, 1981) in order to derive solutions to elasto-plastic analyses for steel structures exhibiting gradual yielding, based on the assumptions of the deformation theory of plasticity. No such formulations are used or derived in this work. However, the idealization is provided here since it provides an adequate description of the stress vs. strain relationship throughout the whole range of deformation with only four parameters. The deformational behaviour of pipelines should be particularly dependent on the stress vs. strain slope in the plastic range, and, consequently, on the magnitude of the exponent n .

Linear regression analyses of the data give value of n in the proximity of about 15 for the X56 material and 12 for the X52 material. Table 2.3 gives the magnitude of the constants

E and σ_y as determined from tension tests and the constants c and n as determined from regression analyses. The same table provides magnitudes of true stresses and corresponding true strains as measured from tests and as determined from the Ramberg-Osgood idealization. A comparison between the X52 and X56 material true stress vs. true strain relationship is depicted in Figure 2.13.

2.8.2 Stub Column Tests

Four axially loaded stub-column tests were carried out on the 508 mm diameter pipe. The length to diameter ratios L/D were 0.5, 1.0, 2.36, and 3.0. Stub column tests are standard tests used in structural engineering to provide the basic material response of the material including the effect of residual stresses and imperfections. For a pipe, the stub column relationship between stress and average strain (over the whole length of the specimen) is dependent on the length of the specimen and hence is not representative of the material behaviour after the peak load is reached. This is explained by the fact that in all cases local buckling is developed in a single wave (see Figure 2.14) and the ratio of the buckled length to the overall length L_b/L varies for different L/D ratios. Figure 2.15 shows the stress vs. average strain relations for all stub column tests performed. The greater the length is, the closer the pre-buckling curve is to the curve obtained from a tension test. After the peak load is reached, all curves exhibit softening due to local buckling. The steepest negative slope is obtained for the highest L/D ratio. This is explained by the fact that although the observed buckled length L_b is the same for all tested stub-columns, the ratio L_b/L decreases as the length of the tested stub-column L increases. As the axial capacity of the column decreases (depicted by the descending branches of the stress vs. strain curves in Figure 2.15), the buckled portion L_b of the specimen undergoes further axial shortening, while the unbuckled portion, $L - L_b$, subjected to elastic unloading, undergoes elongation. The elastic elongation of the unbuckled segment follows Hooke's law and is proportional to the length $L - L_b$. The overall shortening of the stub-column is obtained by superimposing the shortening of Segment L_b to the elongation of Segment $L -$

L_b . Therefore, in the post-peak range of deformation, as the length $L-L_b$ increases, the overall shortening of the specimen at a given axial load decreases.

In the elastic regime, the through-wall average strain in the axial direction is uniformly distributed along the length of the specimen. However, lateral deformations produced by the presence of circumferential strains exist non-uniformly throughout the length of the pipes in the regions of discontinuity adjacent to the loading patterns. This gives rise to bending of the pipe walls in the proximity of the loading pattern and local buckling takes place in the neighborhood of this region.

Table 2.1 Pipe Geometry and Loading Conditions

Test Descriptor	Outside Diameter D (mm)	Thickness t (mm)	D/t	End Conditions	Pressure Condition	Thermal Effect Corresponding to a Temperature Differential of
UGA508	508	7.90	64	Active (A)	No pressure (U)	45 C (G)
UGR508	508	7.90	64	Reactive (R)	No pressure (U)	45 C (G)
DGA508	508	7.90	64	Active (A)	Full pressure (D)	45 C (G)
DLR508	508	7.90	64	Reactive (R)	Full pressure (D)	0 C (L)
UGA324	324	6.35	51	Active (A)	No pressure (U)	45 C (G)
HGA324	324	6.35	51	Active (A)	Half pressure (H)	45 C (G)
DGA324	324	6.35	51	Active (A)	Full pressure (D)	45 C (G)

Notation

1. Pressure Condition (location from pumping station)

U = immediately upstream (Unpressurized)

H = halfway between pumping stations (Half Pressurized)

D = immediately downstream (Pressurized)

2. Thermal Effect

G = greatest compressive thermal effect

L = least compressive thermal effect

3. End Conditions

A = Active

R = Reactive

Table 2.2 Design Pressure and Axial Load Magnitudes for Test Specimens

Test Descriptor	Hoop Stress Ratio $b = \sigma_h / \sigma_y$ ⁽¹⁾	Design Pressure (MPa) ⁽²⁾	Temperature Differential Δt ($^{\circ}\text{C}$)	Axial Load Arising From				Load Constant During Test ?	Load Felt by Pipe P_{pipe} (kN) ⁽⁷⁾	P_{pipe}/P_y
UGA508	0.00	0.00	45	P_t (kN) ⁽³⁾	P_{μ} (kN) ⁽⁴⁾	P_p (kN) ⁽⁵⁾	P_T (kN) ⁽⁶⁾	yes	1311	0.27
UGR508	0.00	0.00	45	1311	0	0	1311	no	1311	0.27
DGA508	0.80	9.91	45	1311	-1153	1886	2043	yes	158	0.03
DLR508	0.80	9.91	0	0	-1153	1886	732	no	-1153	-0.24
UGA324	0.00	0.00	45	644	0	0	644	yes	644	0.29
HGA324	0.36	5.16	45	644	-237	393	800	yes	407	0.19
DGA324	0.72	10.33	45	644	-475	786	956	yes	170	0.08

Notes keyed to superscripts in Table

⁽¹⁾ maximum value for $\beta = 0.80$ in CAN/CSA Z183-M90 and 0.72 in CAN/CSA Z183-M84

⁽²⁾ Design Pressure computed by $p = 2t \beta \sigma_y / (D - 2t)$. Example: for DGA324, $p = 2(6.35)(0.72)(359)(324 - 2 \times 6.35) = 10.33$ MPa

⁽³⁾ P_t computed from Equation 2.1. Example: for DGA324, $P_t = (200,000)(6120)(11.7 \times 10^{-6})(45)/1,000,000 = 644$ kN

⁽⁴⁾ P_{μ} computed from Equation 2.2

⁽⁵⁾ $P_p = \pi(D - 2t)^2 p / 4$

⁽⁶⁾ P_T computed from Equation 2.3

⁽⁷⁾ P_{pipe} = computed from Equation 2.4

Table 2.3 Stress vs. Strain Values for X56 and X52 Steels

Grade X56 Steel				Grade X52 Steel			
Engineering Strain (Micro-strains)	Stress (Mpa)	True Strain (Micro-strains)	True Stress (Mpa)	Engineering Strain (Micro-strains)	Stress (Mpa)	True Strain (Micro-strains)	True Stress (Mpa)
0	0	0	0	0	0	0	0
1,000	204	1,000	204	1,000	200	1,000	200
2,000	329	1,998	329	2,000	314	1,998	315
3,000	373	2,996	374	3,000	356	2,996	357
4,000	382	3,992	384	5,000	378	4,988	380
5,000	391	4,988	393	10,000	384	9,950	388
10,000	402	9,950	406	20,000	397	19,803	405
20,000	410	19,803	418	40,000	420	39,221	436
40,000	419	39,221	435	60,000	434	58,269	460
60,000	425	58,269	450	80,000	442	76,961	477
80,000	429	76,961	463	140,000	454	131,028	518
200,000	433	182,322	520	200,000	456	182,322	547
Elasticity Modulus			203,704 MPa	Elasticity Modulus			199,754 MPa
Yield Strength			391 MPa	Yield Strength			378 MPa
Plasticity Exponent			15	Plasticity Exponent			12
c			0.00447	c			0.00446

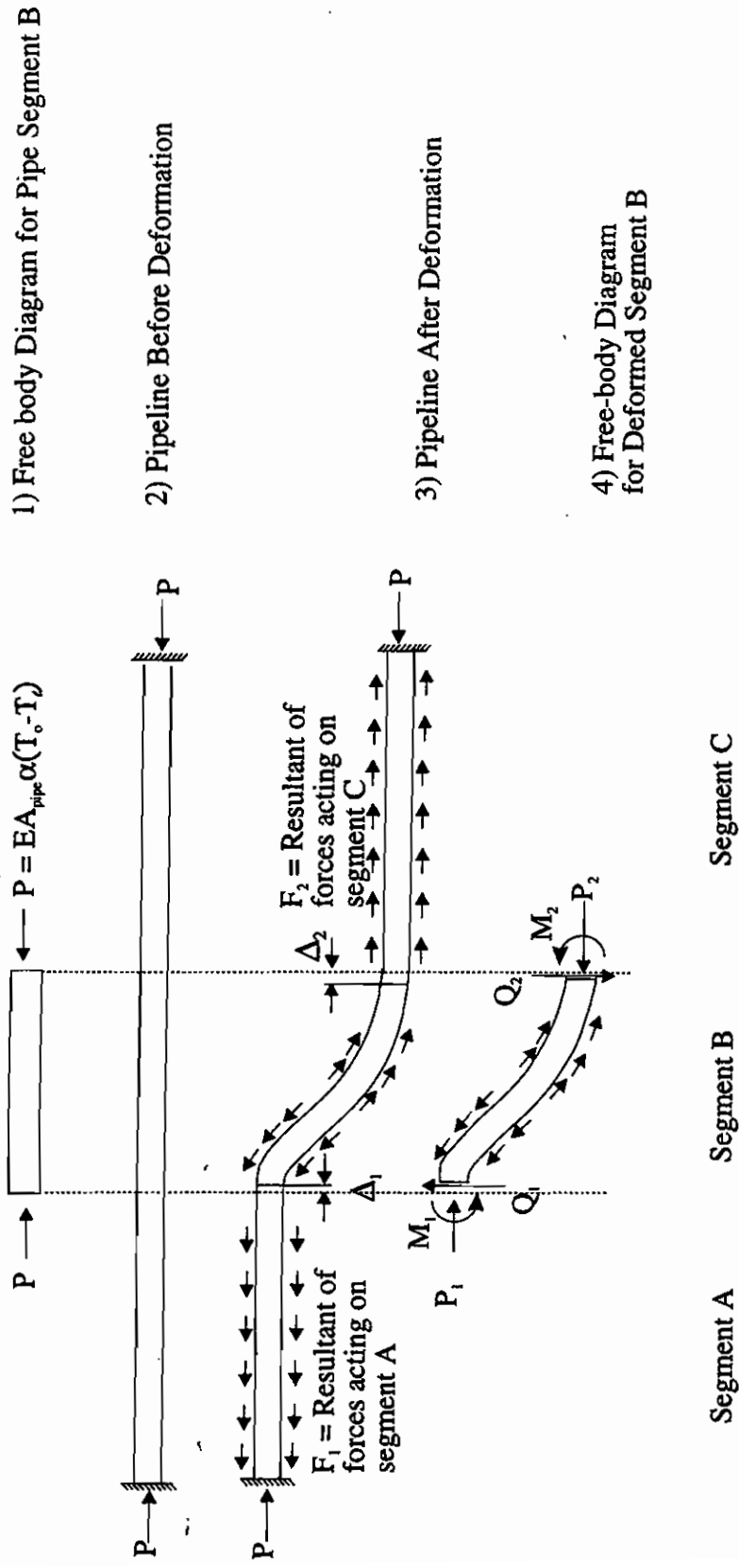


Figure 2.1 Longitudinal Forces along Pipeline Subject to Differential Settlement

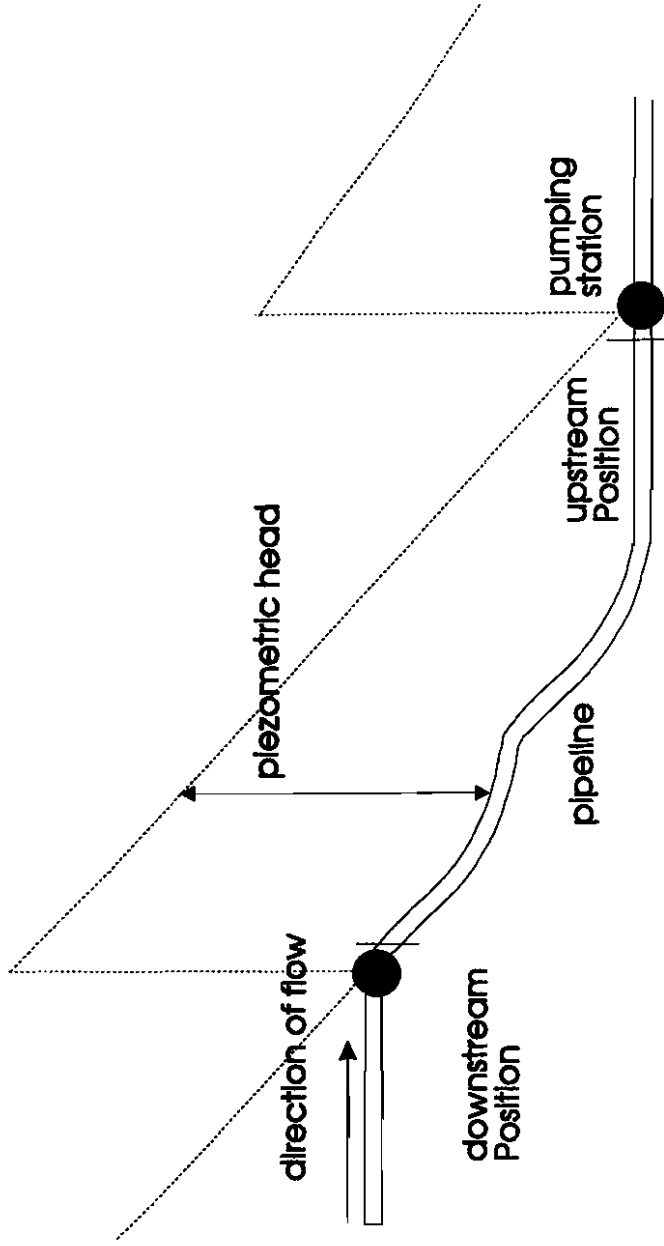


Figure 2.2 Pressure Head along Pipeline

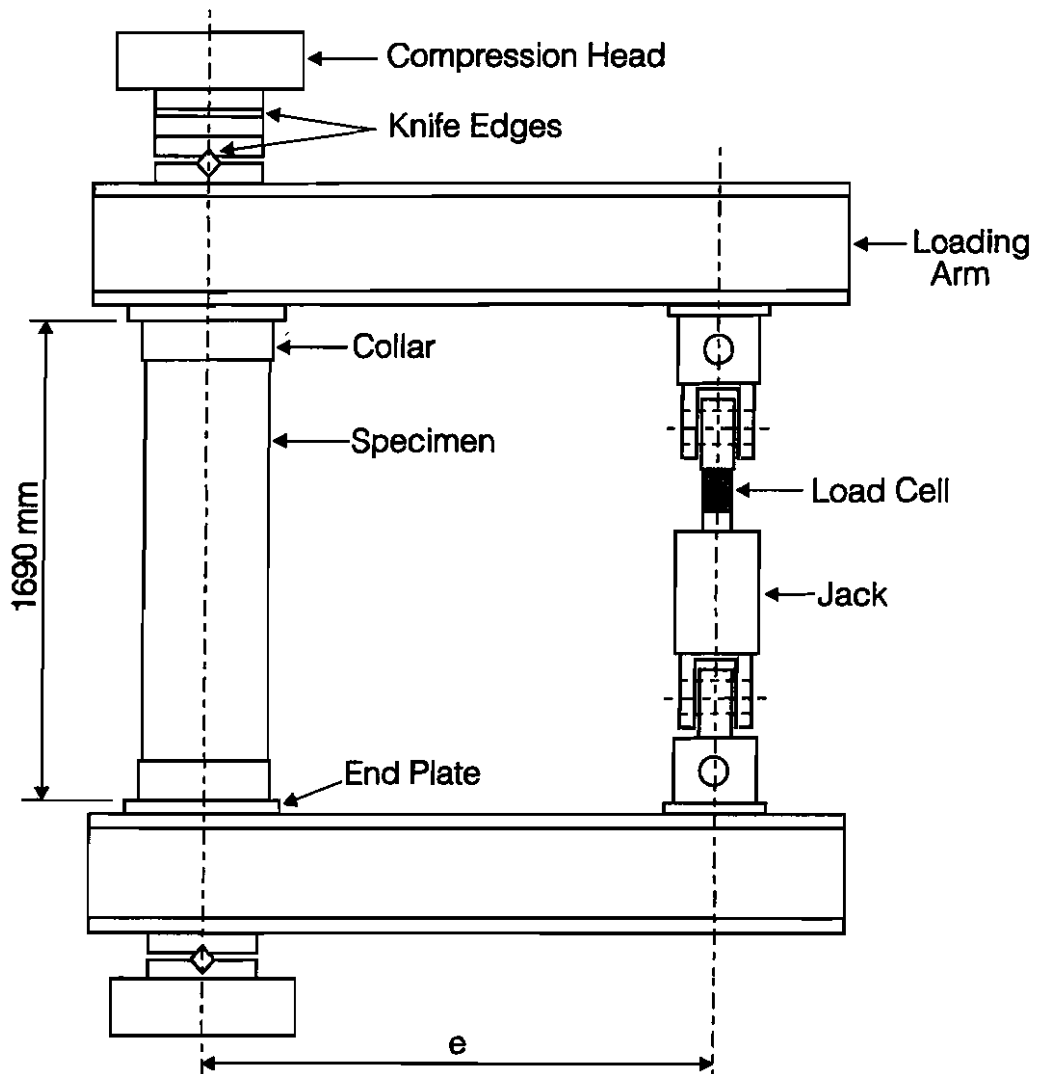


Figure 2.3 Experimental Setup

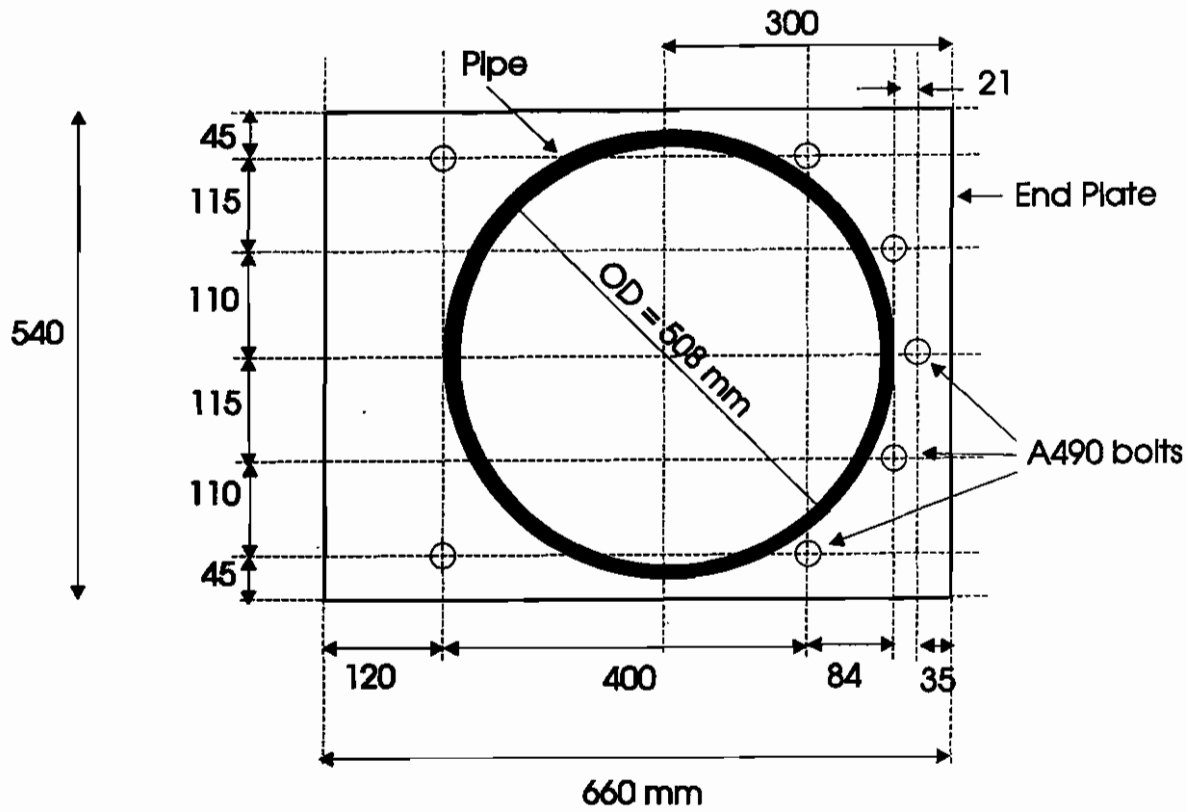


Figure 2.4 Plan View of End Plate



Figure 2.5 Fabrication Process of the Specimen

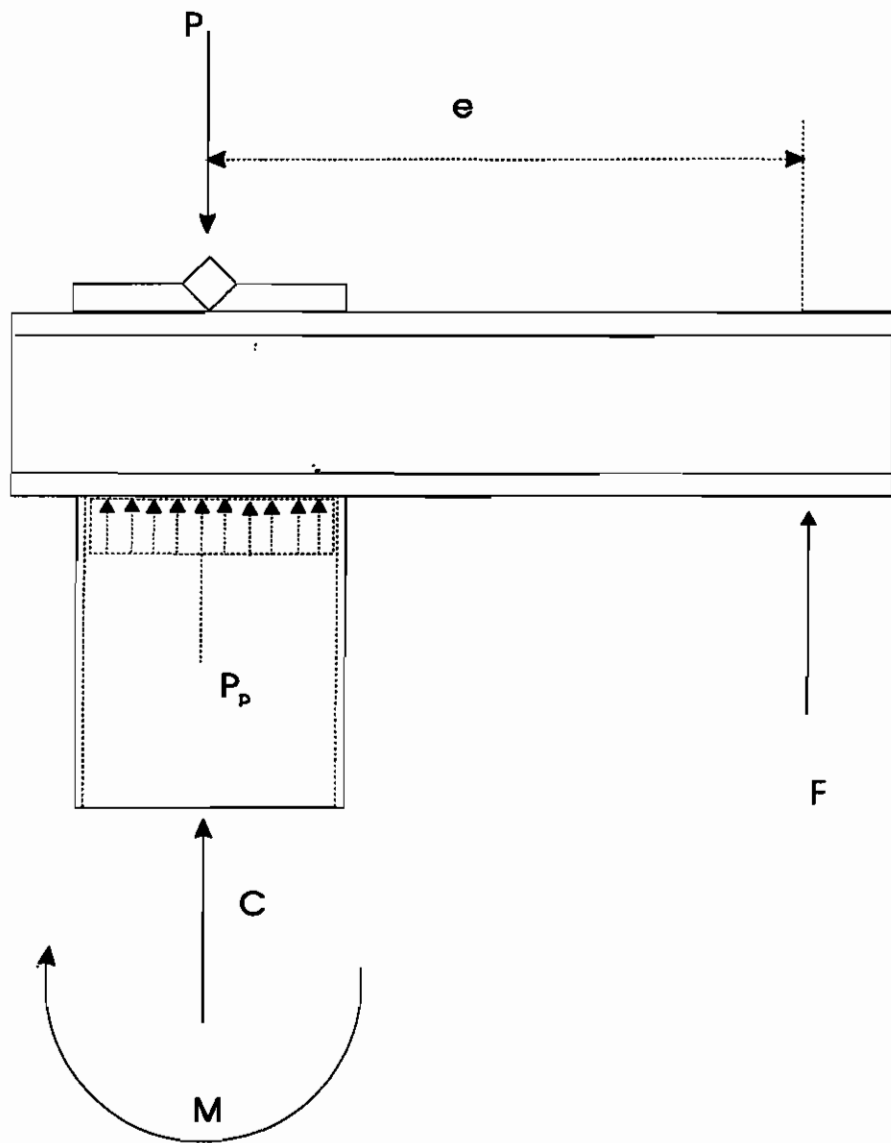


Figure 2.6 Free Body Diagram for Loads Acting on Specimen

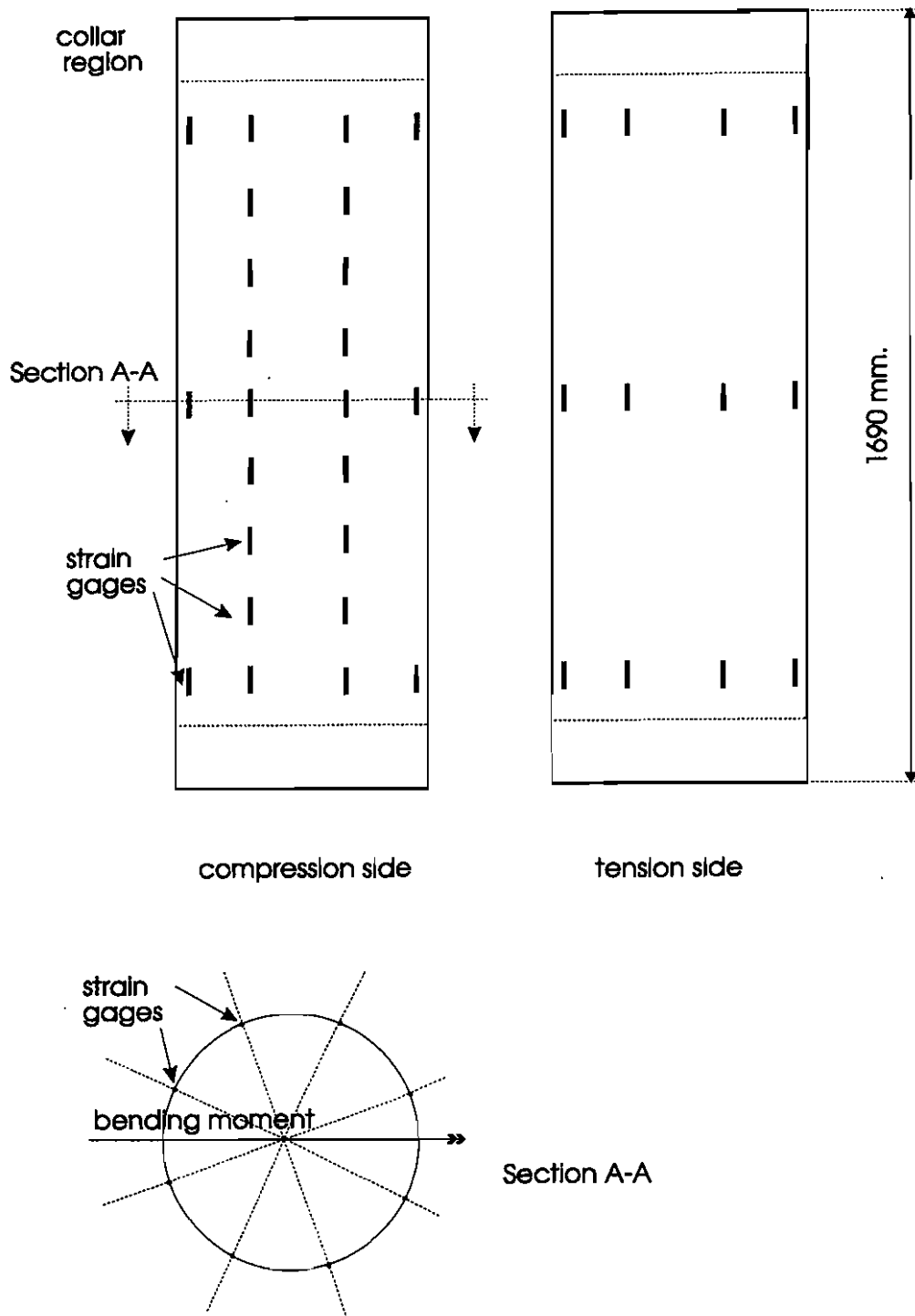


Figure 2.7 Location of Strain Gages



Figure 2.8 Demec Gage Measurements

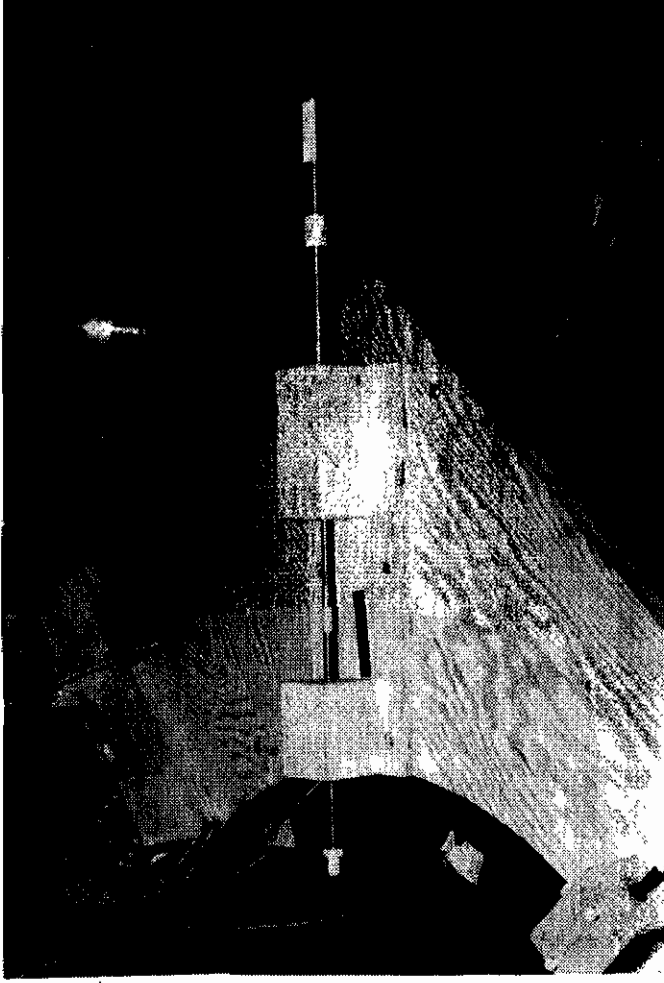


Figure 2.9 LVDTs Measuring Radial Displacements

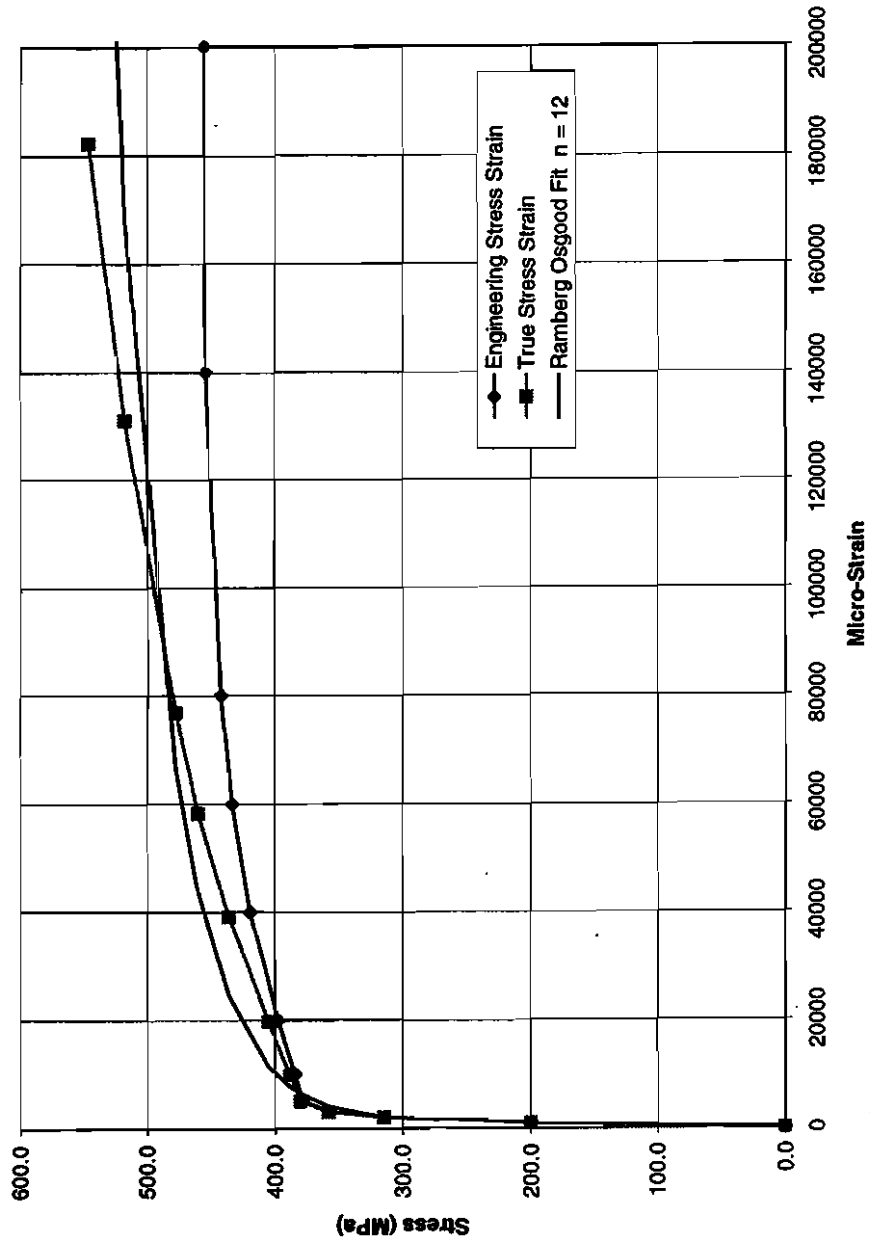


Figure 2.10 Stress vs. Strain Relationship for X52 Material

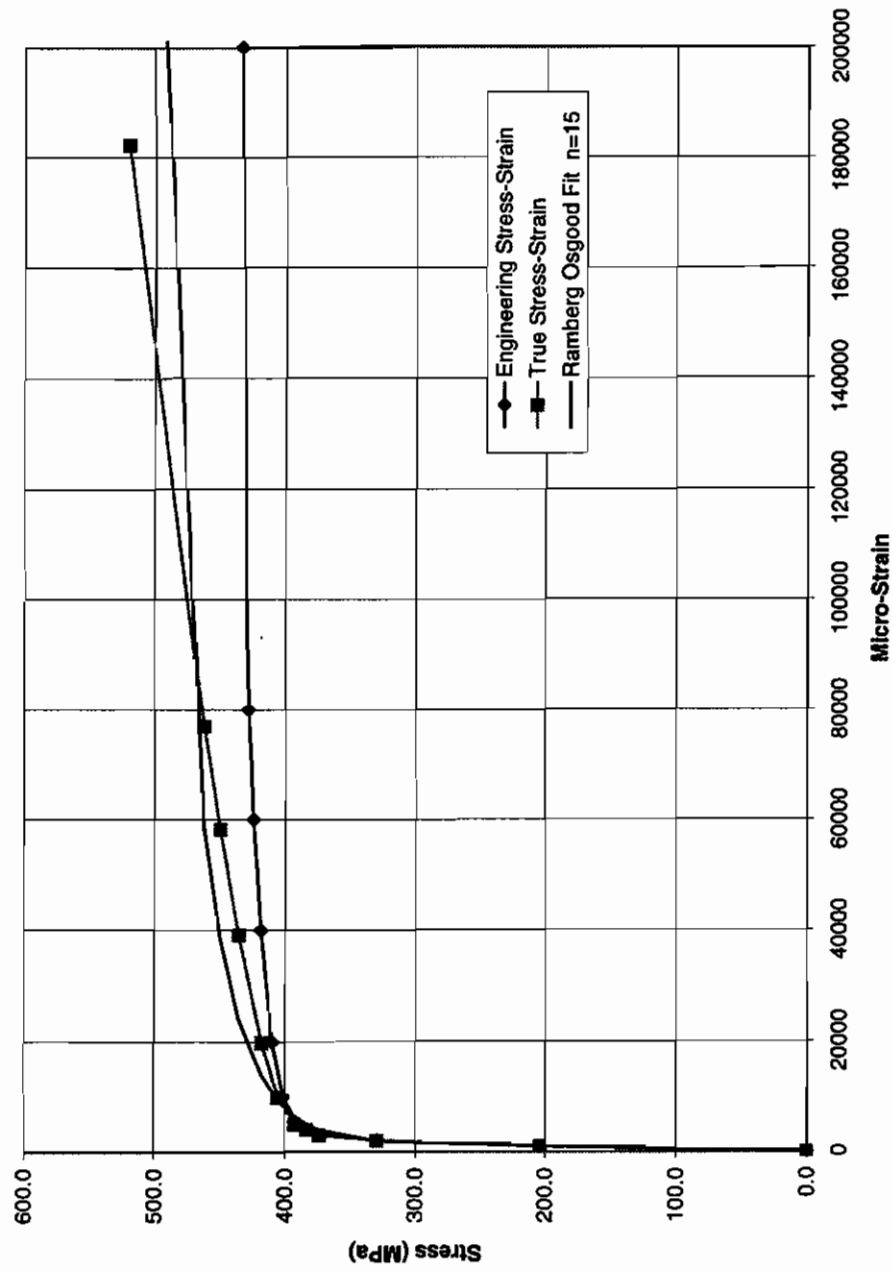


Figure 2.11 Stress vs. Strain Relationship for X56 Material

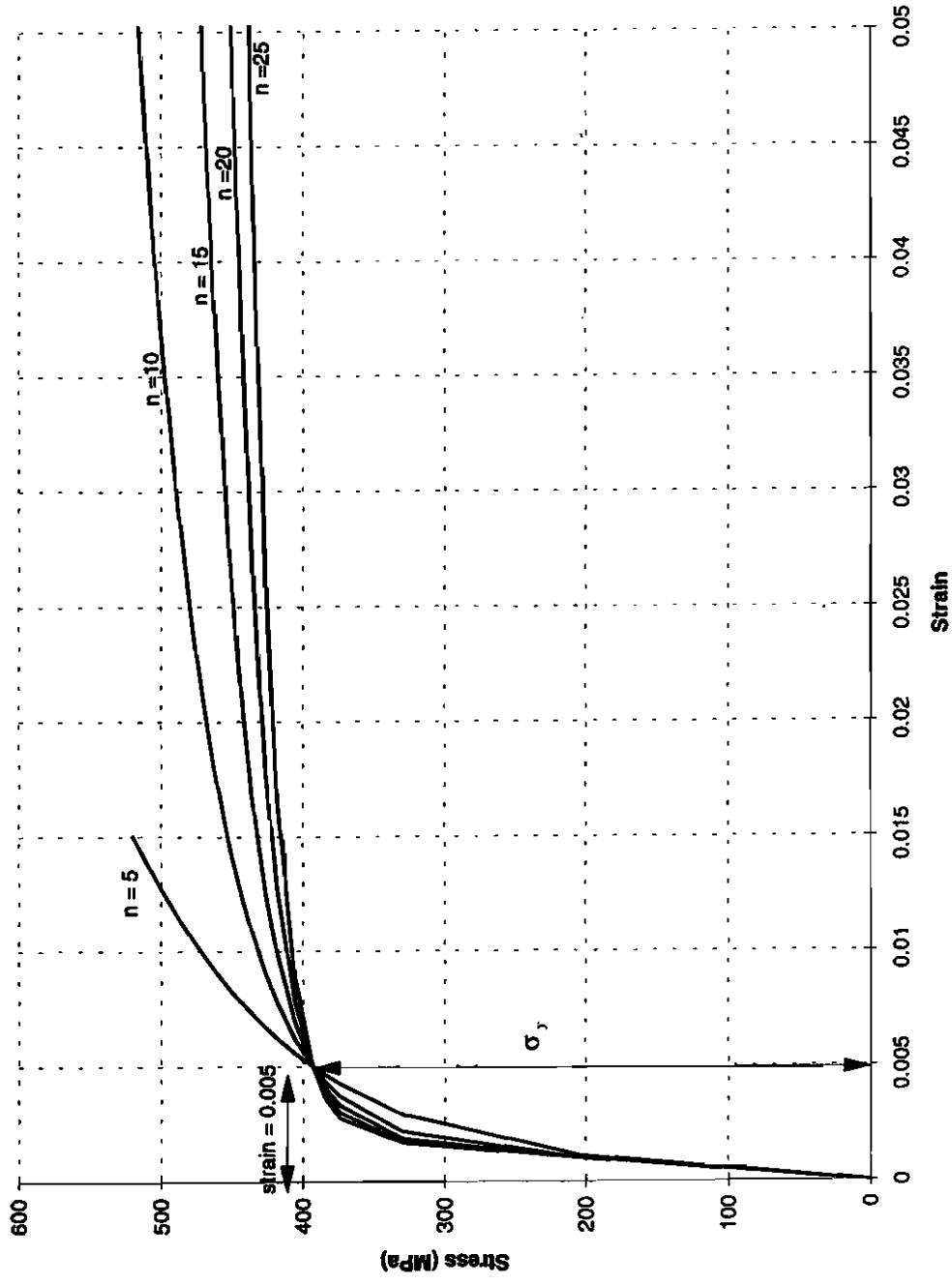


Figure 2.12 Ramberg-Osgood Curves for Different Plasticity Exponent Magnitudes

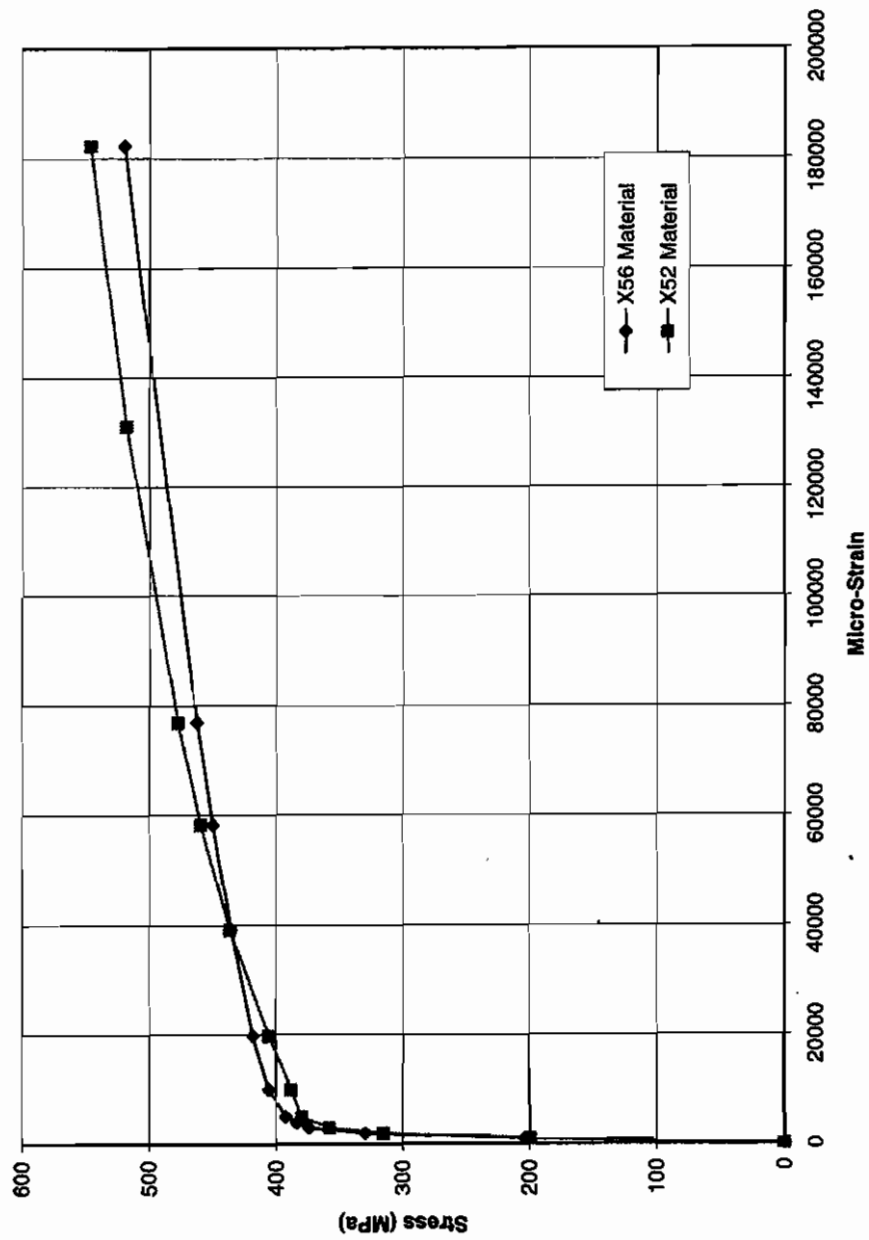


Figure 2.13 True Stress vs. True Strain Relationship for X56 and X52 materials

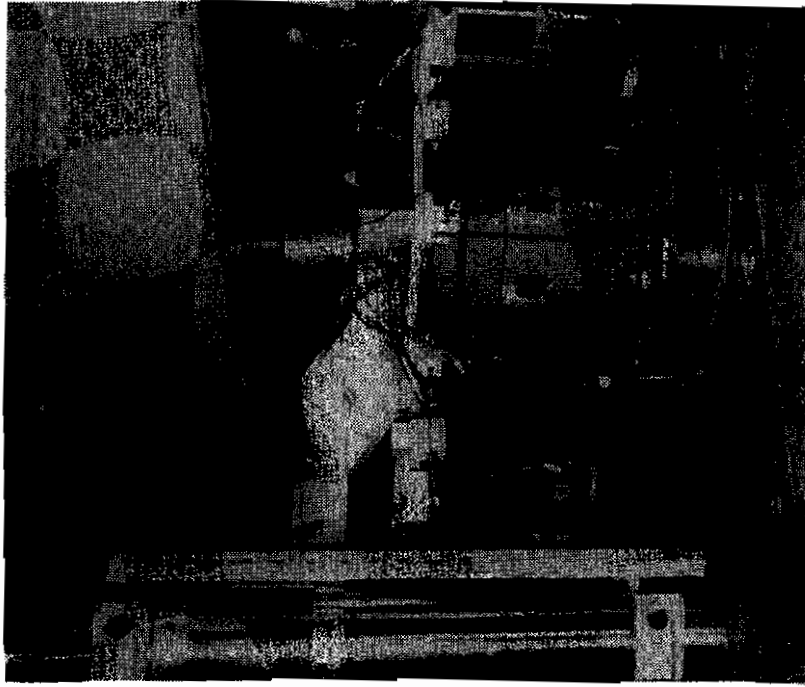
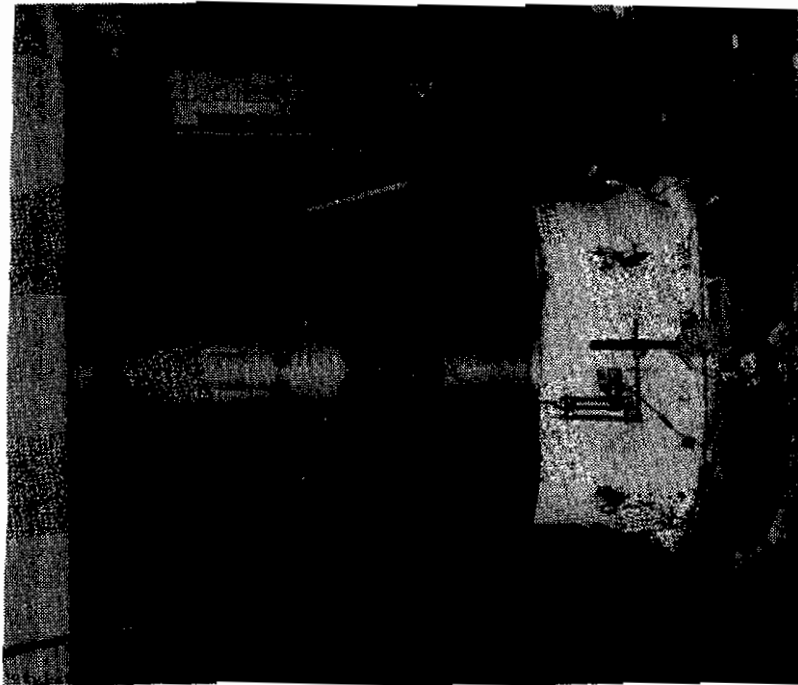


Figure 2.14 Stub Column Tests

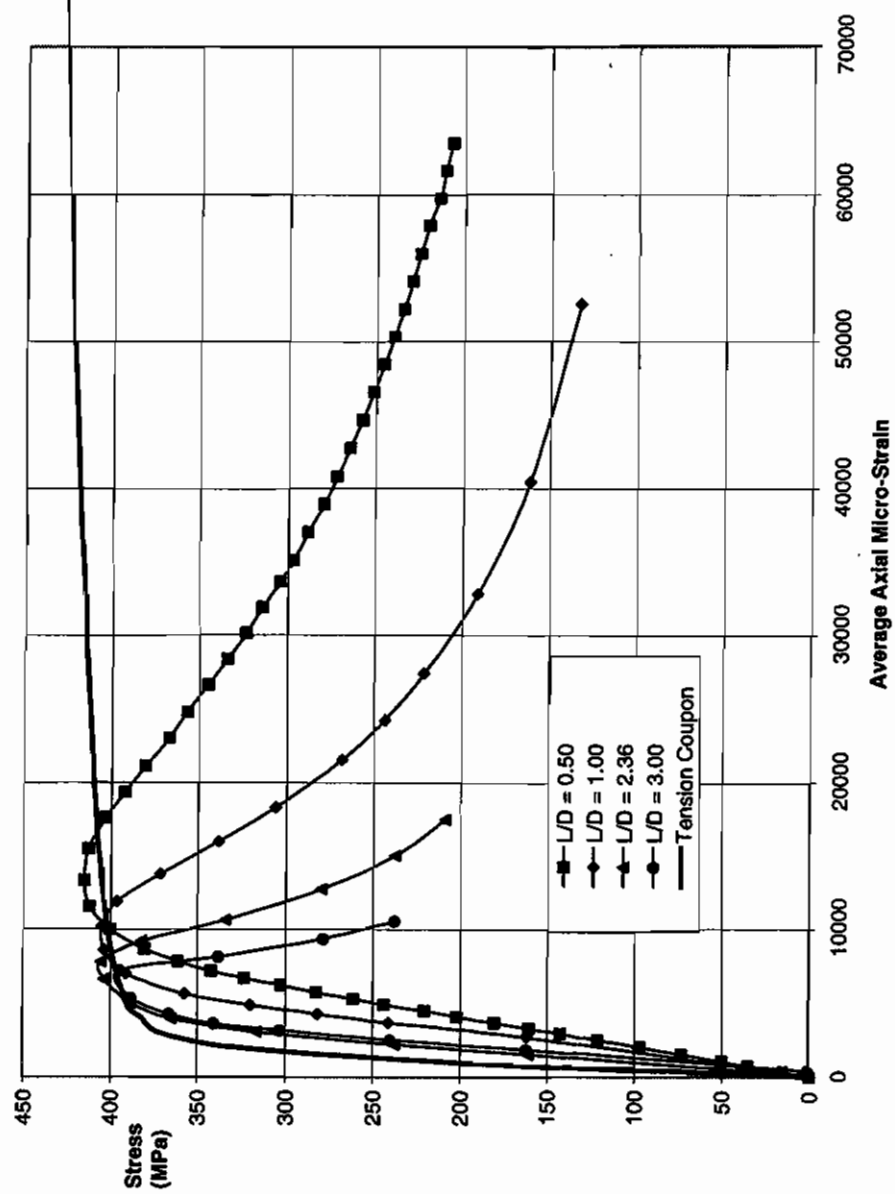


Figure 2.15 Stress vs. Strain Curves for Axially Loaded Pipes

3. EXPERIMENTAL RESULTS

3.1 General

The purpose of this chapter is to present the results obtained in the experimental program described in Chapter 2. The results include the recorded radial displacements, longitudinal strains, end rotations, moment vs. curvature relationships, and moment capacities for the tested specimens. A simplified formulation for the calculation of plastic moment capacities is derived and a comparison between the moments predicted by the formulation and those obtained from the tests is presented.

3.2 Deformational Response

One of the major goals of the experimental program was to develop a data-base on the deformational response of the specimens tested. The following sub-sections describe the deformation measurement techniques employed in the test program as well as the deformation responses obtained.

3.2.1 Deformation Measurement Techniques

The progression of local buckles was recorded at arbitrarily selected times during the tests using both photogrametric techniques and LVDT radial displacement measurements.

Figures 3.1 and 3.2 show the histories of buckles for Specimens UGA324 and DGA508 occurring on the compression side as determined from photogrametric results. The three components of displacement of arbitrarily selected points on five initially vertical lines on the compression face of the specimen were obtained through photogrametric processing. The process of obtaining the coordinates of the points selected, together with an error analysis of the process, are described by Peterson (1992). Using the photogrametric results obtained, the pipe surface was reconstructed using bi-cubic B-spline surface

patches (Souza, 1995). The photo-realistic renderings in Figures 3.1 and 3.2 were produced by L. T. Souza. Figure 3.1 shows the development of a diamond shape buckle occurring near mid-height of Specimen UGA324 while Figure 3.2 shows the progression of an outward bulge occurring at the bottom of Specimen DGA508. Photographs of the 324 mm OD and 508 mm OD tests are given in Figures 3.3 and 3.4. Comparison of Figures 3.1 and 3.2 with Specimens UGA324 and DGA508 in Figures 3.3 and 3.4, shows that the photogrametric technique was successful in recording the deformed configurations of the specimens, especially for outward bulge type of buckling. Because of the complexity of diamond shaped buckles, a greater number of generators is needed to produce a closer resemblance between the real shape of specimen (Figure 3.4) and the processed photogrametric results (Figure 3.2).

The cylindrical coordinates of eight points around the pipe circumference at selected heights were obtained from LVDT radial measurements taken throughout the test. Figures 3.5 through 3.11 give the progression of the radial displacements near the maximum compressive fiber for the seven specimens tested in this program. In the initial stages of all tests, the maximum compressive fiber exhibits smooth curvature along the specimen length. An exception to this observation is for the third set of readings for Specimen DGA508 (Fig. 3.7), where the radial LVDT close to the maximum compression fiber of the specimen seems to give erroneous results for the top three readings. As the tests progress, the greatest deformations become localized over a limited length of the specimen, which is characterized on the maximum compression fiber by inward depressions for diamond buckles and by an external bulge for outward buckling modes. The localized deformations continue to increase significantly as the end rotations of the specimen increase.

3.2.2 Buckling Patterns

Figures 3.1 through 3.4 show the buckled shapes for Specimens DGA508 and UGA324. They exhibit two distinct modes of local buckling, namely, a diamond shape mode (for

UGA324) and an outward bulge mode (for DGA508). In all tests, local buckling took place over a length of the specimen ranging from about 250 mm to 350 mm. For tests in which the internal pressure was present, four to five small amplitude waves occurred on the compression side of the specimens. As deformation progressed, the amplitude of one of the buckles progressed while the amplitude of the other buckles decreased in magnitude. For unpressurized specimens, only one buckle occurred. At the initiation of local buckling, the shape of the buckle seemed similar to an outward bulge. However, as the end rotations of the specimens were increased the buckle transformed gradually into a diamond shape pattern. In all of the tests, no additional local buckles were formed as the specimens were subjected to large end rotations.

3.2.2.1 Diamond Shape Buckling

Diamond shaped buckling, illustrated in Figures 3.4, 3.5 3.6 and 3.9, occurred in all the non-pressurized tests. At the initiation of buckling, the specimens exhibited a single outward bulge of a shape similar to that depicted in Figure 3.3. The buckles were located in the middle third of the specimen. As the specimens continued to deform, the localization took a more complex configuration. It consisted of one large depression with two small side depressions adjacent to it (see Figure 3.4). Each of the three depressions was shaped like a diamond. The diamond buckles were symmetric with respect to the plane of bending of the specimen.

3.2.2.2 Outward Bulge Buckling

This mode of buckling occurred for all of the pressurized specimens in the testing program. For the highly pressurized specimens, a deformation pattern consisting of four to five buckles took place on the compression side of the pipe and extended over the whole length of specimen at the initiation of local buckling. As deformations increased, only one of the bulges progressed while the other bulges decreased in amplitude and gradually disappeared as the moment carrying capacity of the specimen dropped. Figure

3.2 shows a sequence of photogrametrically processed results giving the progression of the outward bulge for Specimen DGA508.

3.2.2.3 Buckling Location

For a given specimen, the location of the buckle is influenced by two factors. One factor is the $P-\delta$ effect of the axial loading applied by the testing machine. For a compressive net axial load and a specimen of reasonable length, the $P-\delta$ effect predisposes local buckling at the mid-height of the specimen. The other factor is the end effect. This effect attempts to trigger buckling in the neighborhood of the end plates because the restraint of these plates disrupts the uniform stress distribution along the pipe. The effect of residual stresses induced by welds connecting the pipe ends to the end plates is also present. It is difficult to quantify. However, in order to minimize the influence of the end effects on local buckling, the confining steel collars described in Chapter 2 were provided to force buckles to occur at a distance of at least 150 mm away from the end plates. If the second-order effects of the axial load ($P-\delta$ effect) is more predominant than the end effects, the buckle occurs near the middle of the specimen. If, on the other hand, the end effects are more predominant, local buckling takes place near the end of the specimen.

In five out of the seven tests, local buckling occurred in the central third of the specimen. For the remaining two tests (DGA508 and DLR508), the buckle formed near the bottom end of the specimen.

3.3 Longitudinal Strains

3.3.1 Importance of Strains

In current pipeline practice, limiting the longitudinal compressive strain on the pipeline wall to a prescribed value seems to be the most accepted design criterion for bending of buried pipelines. It was, therefore, important to record the longitudinal compressive strain histories for the tested specimens.

3.3.2 Strain Measurement Techniques

Strain gages were used to measure longitudinal strains at selected locations on the exterior wall of the specimens (see Figure 2.6). However, since strain gages have a small gage length, their readings in the compression zone of the pipe were highly sensitive to their position with respect to the location of the local buckle. In the neighborhood of local buckles, they do not yield readings for the through-wall average strains. After the occurrence of local buckling, one has to rely on strain readings based on longer gage lengths. Demec gage points provided an ideal strain measurement tool for this purpose.

3.3.3 Demec Gages

Demec gage readings were taken on the compression side for five of the seven specimens tested. The Demec gage lengths selected were roughly equal to half of the diameter of the specimen tested (refer to Table 3.1). Demec points were mounted on the extreme compression fiber of the specimen and the distances between Demec points were accurately measured by an electronic caliper at the beginning of the test. As the test progressed, new distances between the Demec points were measured at selected times. The change in the distance between the Demec points divided by the original distance between them gives a measure of the average longitudinal compressive strain over the Demec gage length.

3.3.3.1 Importance of Demec Gage Readings

The importance of Demec gage readings lies in the fact that they provide average compressive strain readings over a relatively long gage length. Strains based on Demec gage readings are less dependent on the location of Demec points with respect to the location of local buckle, or with respect to bends caused by end effects, than strains based on strain gage measurements.

3.3.3.2 Demec Gage Results

Figures 3.12 through 3.16 give the progression of strains along the maximum compression fibers based on Demec gage results for Specimens DGA508, DLR508, UGA324, HGA324, and DGA324, respectively. Highly localized strains at the location of the buckles are apparent in Figure 3.12 and Figures 3.14 through 3.16. All pressurized specimens were capable of sustaining the applied internal pressure until the end of the test, where they reached compressive strains as high as 12% in some cases. For Specimen DLR508, several strain localizations of comparable magnitudes occurred along the length of the specimen as is apparent in Figure 3.13. Unlike other specimens, the longitudinal compressive strains recorded for DLR508 did not exceed 4%. When the specimen reached the maximum rotational capacity of the test setup, there was only a small outward bulge occurring near the bottom end of the specimen. Because of the high tensile load to which the specimen was subjected, a rotation capacity beyond that provided by the knife edges used in the test setup was needed to localize the longitudinal compressive strains at the bottom of the specimen up to a level comparable to that of Specimen DGA508. Table 3.1 gives a lower bound of longitudinal compressive strains based on Demec gage readings at the last set of readings recorded prior to the visual detection of local buckling. The exact strains when the buckles were initiated were not measured. Table 3.1 also gives the gage lengths used in strain measurements as well as the end rotations corresponding to the reported lower bound of the longitudinal compressive strain.

3.3.4 Strain Gages

Strain gages mounted on the specimens (Section 2.7.1) had three purposes: (a) to check the alignment of the specimen; (b) to detect the location of local buckles in their initiation stage on the compression side; and (c) to provide strain measurements on the tension side.

3.3.4.1 Alignment of Specimens

The three rings of longitudinal strain gages (Figure 2.7) mounted on each of the specimens were used to check the alignment of the pipes under the testing machine. A small concentric axial load was applied to the specimen before the start of the main test and the longitudinal strain readings were monitored. In all tests, longitudinal strain readings along the circumference could be brought to agree within 10%, giving confidence in the alignment of the specimen under the center of the loading head of the compression machine.

3.3.4.2 Strains on the Compression Side

The eighteen strain gages mounted on the compression face of the specimens (Figure 2.7) provided longitudinal compressive strain measurements and allowed the early detection and monitoring of the location of local buckling along the height of the specimen. These measurements were reliable only before local buckling took place. After buckling, the readings became inaccurate as they detached from the surface of the pipe at strains in the neighborhood of 3%. Also, the strain readings based on strain gage measurements were highly dependent upon the bending of the pipe wall and, consequently, on the location of the strain gages with respect to the local buckle. The magnitude of the tensile strains monitored were much lower than the strains corresponding to the ductility limits of the pipe material. Therefore, it was concluded that fracture due to high longitudinal strains on the tension side of the pipes is an unlikely mode of failure. This result is consistent with the findings of Bouwkamp and Stephen (1974) and Zhou and Murray (1993).

3.3.4.3 Strains on Tension Side

No significant variability is expected in the strain magnitudes along the maximum tensile fiber of the specimens and the strain gages on the tension side yielded reliable strain readings. The importance of these longitudinal tensile strains lies in the fact that they could be used for the calculation of curvatures based on segments of the specimen.

3.4 End Rotations

Electronic rotation meters (see Section 2.7.3) placed on the loading arms at the top and bottom of the specimen, provided accurate measures of the end rotations of the specimens. The sum of the two end rotations can be estimated from the jack extension Δ_j , the specimen compression Δ_c , and the geometry of the loading frame. The relative rotation is:

$$\theta_{tot} = \theta_b + \theta_t = 2 \arctan(\Delta_j + \Delta_c) / 2e \quad (3.1)$$

where θ_{tot} = the sum of the top and bottom rotations, θ_b and θ_t , and e = the length of the loading arm. The displacements Δ_j and Δ_c are of the same sign when they occur in opposite directions. Equation 3.1 is approximate since it assumes that the loading arms are infinitely stiff. Therefore, Equation 3.1 gives an upper bound to the magnitude of θ_{tot} . The calculation of θ_{tot} based on Equation 3.1 provides a means of checking the magnitudes of the end rotations obtained using the electronic rotation meter measurements.

3.4.1 Influence of End Rotations on Buckling Location

No particular attempt was made during testing to impose equal (and opposite) end rotations at the top and bottom ends of the specimen throughout the test. The end rotations were, in general, unequal and they were recorded in order to be subsequently modeled in the numerical simulation of the test results. The inequality of the end rotations is compatible with local buckles that are offset from the middle of the specimen in some of the tests, as for Specimens DGA508 and DLR508.

3.4.2 Comparison between Techniques Used in Measuring End Rotations

Figure 3.17 gives a comparison between the end rotations as measured by electronic rotation meters and as computed from the jack extension for three of the specimens

tested. Rotation meters based on electronic rotation meters consistently give higher values than rotations computed based on jack extension. This is explained by the fact that the loading arms, having some flexibility, undergo bending deformations under the action of the eccentric jack load. The values obtained from rotation meters are, therefore, considered to be more accurate than those estimated from jack extensions and were used in all subsequent computations.

3.5 Load Measurements

As described in Section 2.6.1, two external loads were applied to the specimen in addition to the internal pressure. As shown in Figure 3.18, the load, P , was initially applied concentrically to the specimen and the load, F , was applied by an eccentric jack at a distance e from the pipe. In addition to these loads, the action of the internal pressure on the end plates P_p contributed to the magnitude of the internal axial force in the pipe wall. From the free body diagram in Figure 2.6, the internal axial force C in the pipe wall is given by

$$C = P - F - P_p \quad (3.2)$$

Equation 3.2 is approximate since it is based on the undeformed configuration of the specimen. For active tests, the magnitudes of P and F are controlled such that the load in the pipe, C , is maintained constant. For reactive tests, the magnitude of internal axial force C is a variable reactive force because the length of the specimen is maintained constant. Figures 3.19 through 3.25 give the loads P , F , and C versus total end rotation (sum of top and bottom rotations) for the seven specimens tested.

3.6 Moment Curvature Relationships

The applied moment vs. curvature averaged over the whole length of the specimens for 508 mm and 324 mm OD pipes are presented in Figures 3.26 and 3.27, respectively. The

way global curvatures and the end moments were computed for these plots is described in the following sub-sections.

3.6.1 Computation of Curvatures

If the internal moment along the length of a pipe were uniform, average curvatures would be independent of the length of the segment of pipe considered, as long as no local buckling takes place. When local buckling occurs, curvatures for a segment of pipe become length dependent. A curvature based on a small length containing a local buckle will be higher than that computed over a greater length containing the same local buckle. The length of pipe upon which a curvature is calculated has to be specified in order to fully describe a given state of deformation. In Figures 3.26 and 3.27, the average curvature, φ_g , also referred to as the global curvature, is based on the whole length of the specimen and is evaluated as

$$\varphi_g = \frac{\theta_i + \theta_b}{L} \quad (3.3)$$

where L , the length of the specimen, is 1690 mm.

3.6.2 Computation of End Moments

The end moment M applied to one of the ends of the specimen (see Figure 3.18) is given by

$$M = F \times e \times \cos(\theta) + P \times h \times \sin(\theta) - F_H \times h \times \cos(\theta) \quad (3.4)$$

where h is the distance from the knife edge (the point of application of the concentric load P) to the end of the specimen and θ is the rotation of the loading arm. The force F_H is a frictional force acting on the knife edge. No attempts were made to measure the force F_H during the tests. The end moments computed were based on F_H values as determined from the finite element analyses described in Chapter 4. The second term on the right

hand side of Equation 3.4 accounts for the second order effect of the concentric load, P . At a given location along the length of a pipe, second order effects caused by internal pressure and pipe bending will, in general, affect the magnitude of bending moments in the wall of the pipe. However, at both ends of the pipe, the internal pressure induces zero net moment about the centroid of the pipe (Figure 3.18). Therefore, no terms involving the internal pressure second order effects appear in the computation of internal end moments in Equation 3.4. The relationship between end moments, as defined by Equation 3.4, and curvature, as defined by Equation 3.3, give a basis for comparison between tests and analytical procedures (described in Chapter 4). However, because of their dependency on the length of the specimens tested, they cannot be used as pipe properties.

3.6.3 Moment Curvature Diagrams

3.6.3.1 *Effect of Internal Pressure*

Figure 3.26 shows the average end moment vs. the global curvature relationships for the three 324 mm. OD pipes tested. The highest moment capacity is obtained for an unpressurized specimen, UGA324. The least moment capacity obtained is that of a fully pressurized specimen, DGA324. The moment capacity for HGA324 lies between the other two values. Conversely, the longest plateau observed is that of the highly pressurized specimen. The length of the plateau decreases as the internal pressure decreases. The same observation is confirmed in Figure 3.27 where Specimen DGA508 is capable of retaining its moment capacity for a bigger deformation range than is Specimen UGA508.

3.6.3.2 *Effect of Boundary Conditions*

Figure 3.27 allows a comparison of the moment vs. curvature between Specimens UGA508 and UGR508, where the only difference lies in the type of axial boundary condition imposed (active versus reactive). It is observed that the reactive type of axial

boundary conditions results in a higher moment capacity along with a greater ability to retain the moment capacity as the specimens undergo further deformations.

3.6.3.3 Effect of Axial Loads

Specimen DLR508 was subjected to a net axial tensile load (See Figure 3.22). All other specimens were subjected to a net axial compressive force. In addition, Specimen DLR508 had a reactive type of axial boundary condition that allowed an increase in the net axial tensile force in the specimen as deformation progressed. Unlike all other six specimens tested, Specimen DLR508 retained all its moment capacity until the end of the test.

3.7 Moment Capacity

3.7.1 Relevance of Moment Capacity to the Pipeline Problem

The maximum moment carrying capacity of pipelines is not a limiting value for the design of buried pipelines subjected to imposed deformational loading. This is because the moments from deformational imposed loads are self limiting in nature. The moment carrying capacity of a buried pipeline does not, in general, affect its capacity to withstand the internal pressure to which it is subjected. However, the moment carrying capacity may be of importance in the design of elevated pipelines.

3.7.2 Estimates of Plastic Moment Capacity

The plastic moment capacity of a pipe depends upon the magnitude of the internal pressure and on the axial load to which it is subjected. In this section, an equation is derived for the prediction of the plastic moment capacity for pipes. It is based on some simplifying assumptions. A more rigorous analysis based on finite element modeling (see Chapter 4) will provide better prediction of the moment capacity values for the tested

specimens. The assumptions upon which the moment capacity formulation is based are discussed in the following sub-sections.

3.7.2.1 Cross-sectional Distortion and Curvature

The cross section of the pipe is assumed to remain circular throughout deformation. This assumption is justifiable near the ends of the test specimen where the weld connection between the end plate and the pipe forces the pipe to remain circular. However, this assumption is not valid for the portion of pipe lying in the middle region of the specimen length, where the pipe cross section is free to undergo ovalization when subjected to high applied moments, nor in the region of local buckling where the pipe cross section is free to take on complex configurations. These cross-sectional distortion effects are neglected in the formulation presented in this section, but they will be accounted for in the finite element analyses.

High curvatures will be assumed to occur, so that the whole section becomes plastified. This assumption gives a limiting maximum value of the pipe moment capacity.

3.7.2.2 Idealized Stress vs. Strain Relationship

The stress vs. strain curves obtained from coupon testing (Figures 2.10 and 2.11) exhibit strain hardening behaviour without a yield plateau. Strain hardening will be carefully modeled in the finite element modeling since it significantly affects the deformational response of pipes. However, an idealized elastic-perfectly plastic relationship is adopted in this section for the computation of plastic moment capacities. The idealized stress vs. strain relationship consists of a bi-linear relationship. The first line passes through the origin and has the same slope as the initial slope of tension coupon tests. The second line has zero slope (strain hardening is neglected) and passes through the yield point (defined as the stress corresponding to a 0.5% strain). This idealization should not significantly affect the magnitude of the estimated plastic moment, since the measured slopes of the material stress vs. strain curves are small after yielding.

3.7.2.3 Yield Criterion

Pressurized pipes are subject to hoop stresses caused by internal pressure and longitudinal stresses caused by the action of axial forces and bending moments. The longitudinal stress that the pipe material can withstand depends on the magnitude of the hoop stress to which it is subjected. Neglecting any additional stress components that might arise as the result of pressure and local buckling, the Von-Mises yield criterion can be expressed as

$$\sigma_l^2 - \sigma_l \sigma_\theta + \sigma_\theta^2 = \sigma_y^2 \quad (3.5)$$

where σ_l = longitudinal stress, σ_θ = circumferential stress, and σ_y = yield stress. The graphical representation of Equation 3.5 is given in Figure 3.28. Solving for σ_l , one obtains

$$\frac{\sigma_l}{\sigma_y} = 0.5 \frac{\sigma_\theta}{\sigma_y} \pm \sqrt{1 - \frac{3}{4} \left(\frac{\sigma_\theta}{\sigma_y} \right)^2} \quad (3.6)$$

3.7.2.4 Plastic Moments

In all of the tests conducted in this program, the internal pressure was kept at a constant value throughout the deformation history of the specimen. In addition, for active tests the magnitude of the applied axial load remained constant. Knowing the magnitudes of both the internal pressure and the axial force for a given test, the plastic moment capacity can be determined according to Section 3.7.2.5.

3.7.2.5 Computation of Plastic Moment Capacity

The location of the fully plastic neutral axis (see Figure 3.29) is determined by

$$2\psi r_{av} t \sigma_{tens} + 2 r_{av} t (\pi - \psi) \sigma_{comp} = P_e \quad (3.7)$$

where P = the externally applied axial force acting on the cross section, ψ = half the angle subtending the area of the cross section subjected to tension (see Figure 3.29); and r_{av} = the average of the interior and exterior radii of the pipe. The magnitude of σ_{comp} is equal to the longitudinal compressive stress in the pipe wall that would cause the pipe material to yield according to the Von-Mises criterion. It is equal to σ_t , as determined from Equation (3.6) with the negative sign before the square root. Note that σ_{comp} has a negative value because it is a compressive stresses. The value for σ_{tens} is equal to σ_t , as determined from Equation (3.6), with the positive sign before the square root. The force P_e has a positive value when the load is tensile. Solving Equation 3.7 for ψ yields

$$2\psi = \frac{P_e - 2\pi r_{av} t \sigma_{comp}}{r_{av} t (\sigma_{tens} - \sigma_{comp})} \quad (3.8)$$

Knowing the value of ψ , the plastic moment capacity M_{σ_θ, P_e}^P for a given hoop stress σ_θ and a given axial force P_e is computed by

$$M_{\sigma_\theta, P_e}^P = -\sigma_{comp} A_{comp} \bar{y}_c + \sigma_{tens} A_{tens} \bar{y}_t \quad (3.9)$$

where A_{comp} = the area of the pipe cross section subjected to longitudinal compressive stresses [$A_{comp} = 2\psi t r_{av}$]; \bar{y}_c = distance between the centroid of the compression area of the pipe cross section and the centroid of the whole cross section of the pipe; [$\bar{y}_c = r_{av} \sin(\psi)/\psi$]; A_{tens} = the area of the pipe cross section subjected to longitudinal tensile stresses [$A_{tens} = 2(\pi - \psi) t r_{av}$]; and \bar{y}_t = distance between the centroid of the tension area of the pipe cross section and the centroid of the whole cross section of the pipe [$\bar{y}_t = r_{av} \sin(\pi - \psi)/(\pi - \psi)$].

After the substitutions have been made in Equation 3.9, the plastic moment capacity can be expressed in the non-dimensional interaction equation

$$\frac{M_{\sigma_\theta, P_e}^P}{2r_{av}^2 t \sigma_y} = \pm \sqrt{4 - 3 \left(\frac{\sigma_\theta}{\sigma_y} \right)^2} \cos \left[\frac{\pi \left[\frac{P_e}{P_y} - \frac{1}{2} \left(\frac{\sigma_\theta}{\sigma_y} \right) \right]}{\sqrt{4 - 3 \left(\frac{\sigma_\theta}{\sigma_y} \right)^2}} \right] \quad (3.10)$$

where $P_y = A \sigma_y$. The range of variables for which Equation (3.10) is valid is

$$\frac{-2}{\sqrt{3}} \leq \frac{\sigma_\theta}{\sigma_y} \leq \frac{2}{\sqrt{3}}$$

and

$$\frac{1}{2} \left(\frac{\sigma_\theta}{\sigma_y} \right) - \frac{1}{2} \sqrt{4 - 3 \left(\frac{\sigma_\theta}{\sigma_y} \right)^2} \leq \frac{P_e}{P_y} \leq \frac{1}{2} \left(\frac{\sigma_\theta}{\sigma_y} \right) + \frac{1}{2} \sqrt{4 - 3 \left(\frac{\sigma_\theta}{\sigma_y} \right)^2}$$

For a given hoop stress value σ_θ , the maximum plastic moment capacity $M_{\sigma_\theta, max}^P$ of a

pipe cross section occurs when $\frac{P_e}{P_y} = \frac{1}{2} \left(\frac{\sigma_\theta}{\sigma_y} \right)$ and its magnitude is given by

$$\frac{M_{\sigma_\theta, max}^P}{2r_{av}^2 t \sigma_y} = \sqrt{4 - 3 \left(\frac{\sigma_\theta}{\sigma_y} \right)^2} \quad (3.11)$$

From Equation 3.11, substituting in Equation 3.10 for the expression

$2r_{av}^2 t \sigma_y \sqrt{4 - 3 \left(\frac{\sigma_\theta}{\sigma_y} \right)^2}$, one obtains the following non-dimensional form

$$m_n = \pm \cos(\pi p_n) \quad (3.12)$$

where

$$m_n = \frac{M_{\sigma_\theta, P_e}^P}{M_{\sigma_\theta, max}^P} \quad (3.13)$$

and

$$p_n = \left\{ \frac{\left[\frac{P_e}{P_y} - \frac{1}{2} \left(\frac{\sigma_\theta}{\sigma_y} \right) \right]}{\sqrt{4 - 3 \left(\frac{\sigma_\theta}{\sigma_y} \right)^2}} \right\} \quad (3.14)$$

3.7.3 Interaction Diagrams

Interaction diagrams provide an envelope for all possible combinations of applied moment and axial load for a given internal pressure (see Figures 3.30 and 3.31). Figure 3.30 gives the interaction diagrams for a 508 mm OD by 7.91 mm thickness cross section of a pipe made out of grade X56 steel. The two interaction diagrams correspond to hoop stress ratios of 0 and 80%. Figure 3.31 gives the interaction diagrams for a 324 mm OD by 6.35 mm thickness cross section a pipe made out of grade X52 steel. Three interaction diagrams are plotted corresponding to hoop stress ratios of 0%, 36% and 72%. Superimposed on the interaction diagrams are the loading paths of the seven tests conducted.

For active tests (Specimens UGA508, DGA508, UGA324, HGA324, and DGA324), the axial load to which the specimen is subjected remains constant throughout the test. Therefore, the loading path for these tests is represented by a vertical line in Figures 3.30 and 3.31.

For reactive tests, the axial load to which the specimen is subjected is deformation dependent. The plastic moment capacity is a function of the axial load applied. Therefore, it is not possible to predict the plastic moment capacity for a reactive test as a single

value. Therefore, the axial load to which the specimen is subjected is obtained from test measurements, and the corresponding predicted plastic moment capacity of the specimen at this stage is determined from the interaction diagrams. The moment capacity thus obtained provides a limiting value that should not be exceeded by the moments as measured in the tests. If assumptions of Sections 3.7.2.1 through 3.7.2.3 hold true, then the loading paths for UGR508 and DLR508 should remain inside the interaction diagram envelopes.

Excellent agreement between measured moment capacities and those predicted by Equation 3.10 is obtained for unpressurized specimens. For highly pressurized tests, Equation 3.10 is found to underestimate the plastic moment capacity. This is due to the fact that higher strains take place in these cases. Therefore, the effect of strain hardening becomes more pronounced for pressurized cases.

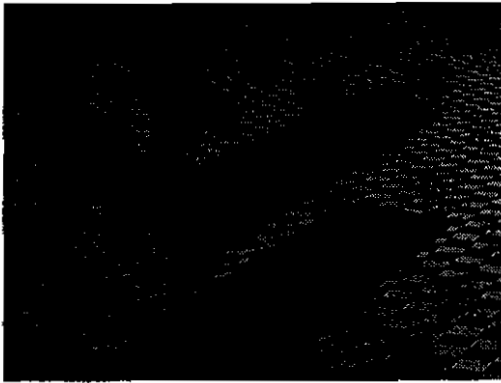
It is possible (and desirable from a design viewpoint) to combine the interaction diagrams for all possible combinations of cross-sectional geometries, yield strength, and internal pressure into a single non-dimensional interaction diagram that would be valid for all these cases. This is done in Figure 3.32, where a unique relationship between the non-dimensional moment m_n as defined by Equation 3.13 and the non-dimensional axial load p_n as defined by Equation 3.14 is presented.

Table 3.1 Strains at the Initiation of Buckling Based on Demec Gage Readings

Test Identifier	Lower Limit of Strain at Buckling	Corresponding End Rotation (Degrees)	Gage Length (mm)
DGA508	2.81%	3.37	256
DLR508	2.00%	5.33	224
UGA324	2.20%	4.40	167
HGA324	2.36%	6.89	167
DGA324	3.24%	6.12	167

Table 3.2 Estimated Plastic Moment Capacity for Test Specimens

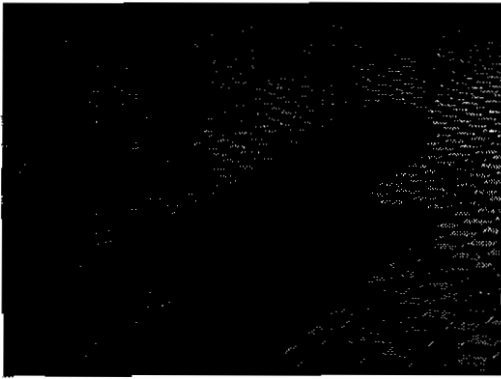
Test Descriptor	$\sigma_{hoop}/\sigma_{yield}$	$\gamma = \sigma_{tension}/\sigma_{yield}$	$\delta = \sigma_{comp}/\sigma_{yield}$	Average Radius (mm)	Thickness (mm)	Yield Stress (MPa)	Initial Axial Force (kN)	Axial Force Constant During Test?	Estimated Moment Capacity (kNm)	Measured Moment Capacity (kNm)
UGA508	0.00	1.00	-1.00	250.05	7.90	386	1303	yes	694	685
UGR508	0.00	1.00	-1.00	250.05	7.90	386	1303	no	694 - 762	769
DGA508	0.80	1.12	-0.32	250.05	7.90	386	216	yes	311	416
DLR508	0.80	1.12	-0.32	250.05	7.90	386	-1153	no	517 - 549	579
UGA324	0.00	1.00	-1.00	158.8	6.35	359	644	yes	208	211
HGA324	0.36	1.13	-0.77	158.8	6.35	359	409	yes	181	192
DGA324	0.72	1.14	-0.42	158.8	6.35	359	184	yes	114	146



End Rotation = 3.12°



End Rotation = 7.30°



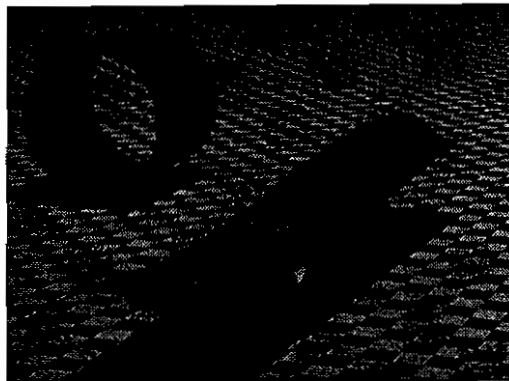
End Rotation = 5.87°



End Rotation = 8.10°

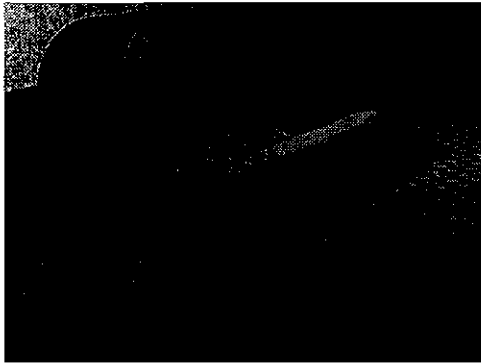


End Rotation = 6.86°



End Rotation = 9.17°

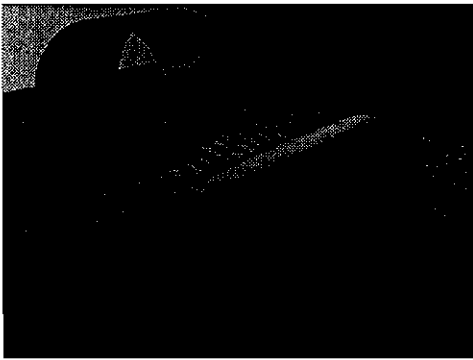
Figure 3.1 Buckling Progression for UGA324



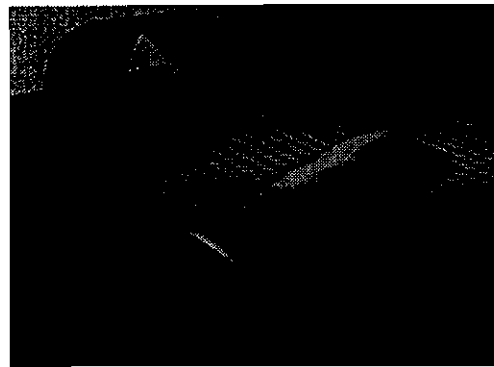
End Rotation = 0.00°



End Rotation = 4.27°



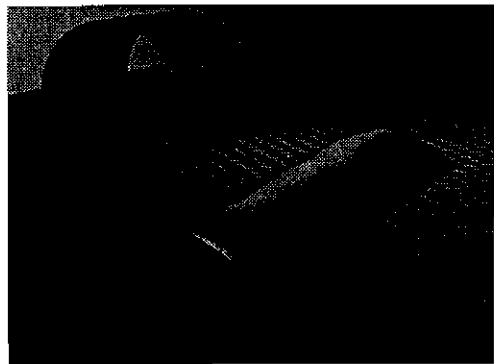
End Rotation = 0.83°



End Rotation = 5.50°



End Rotation = 1.94°



End Rotation = 7.40°

Figure 3.2 Buckling Progression for DGA508



Figure 3.3 Buckled Configurations for 324 OD Specimens (from left to right DGA324, HGA324, and UGA324)

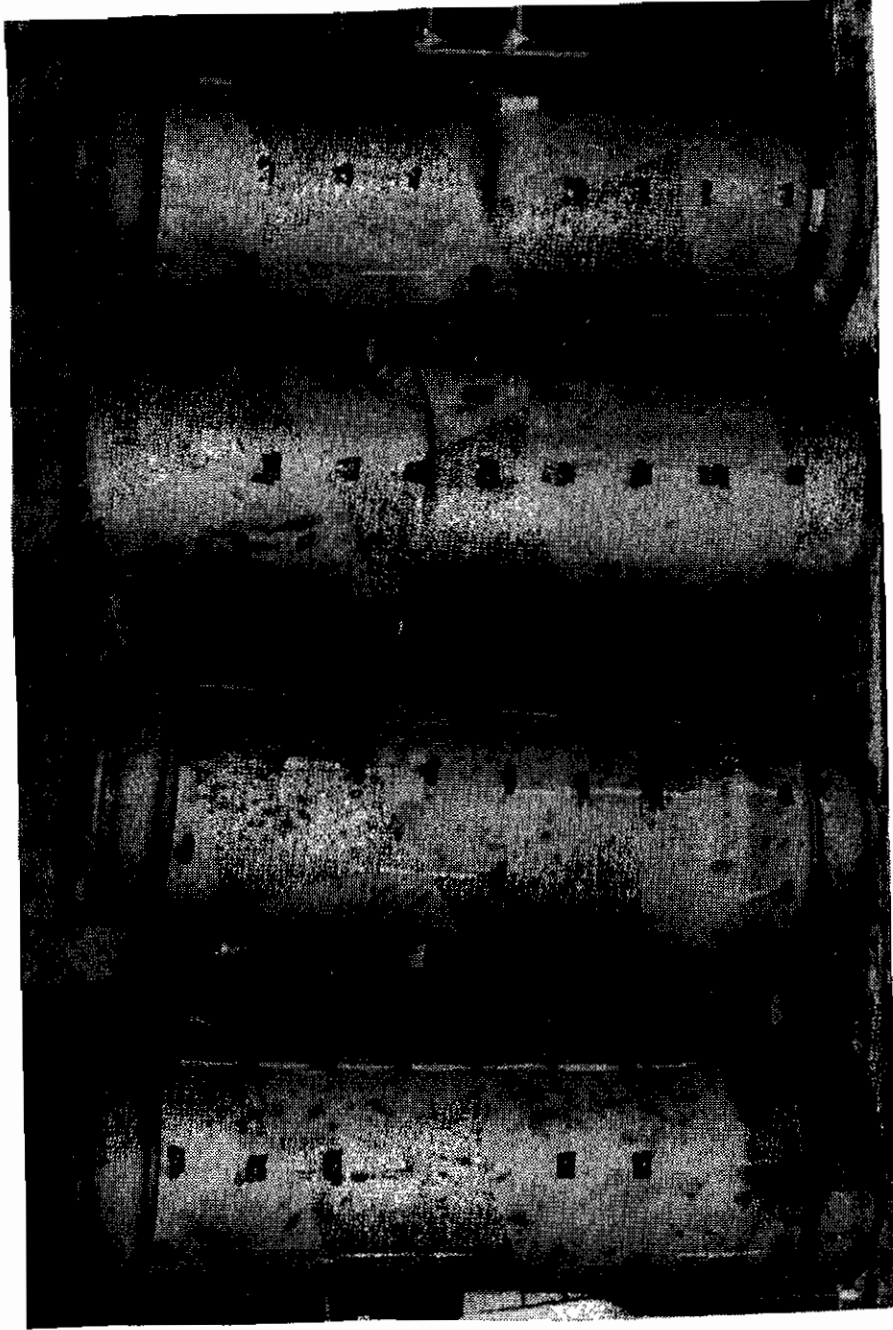


Figure 3.4 Buckled Configurations for 508 mm OD Specimens (from left to right DLR508, DGA508, UGA508, and UGR508)

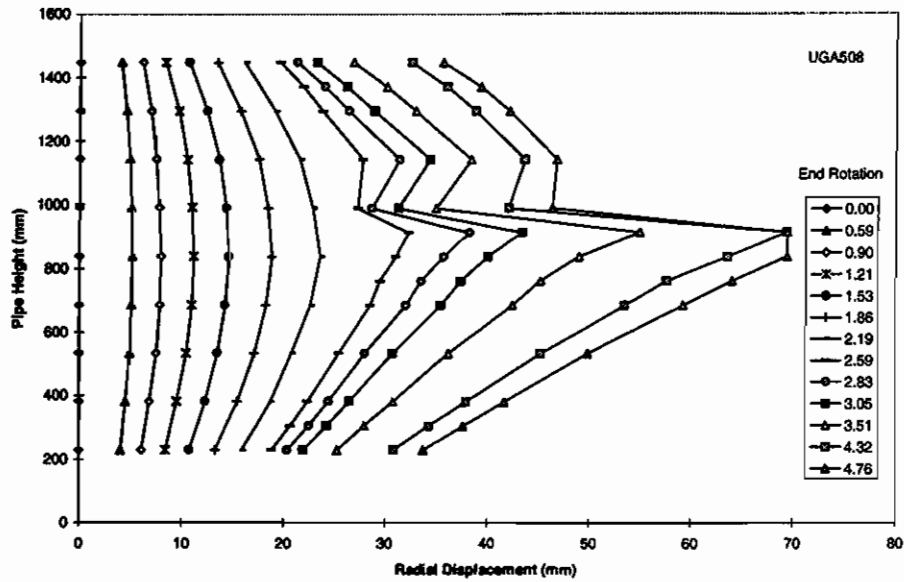


Figure 3.5 Radial Displacements on Maximum Compression Fiber for UGA508

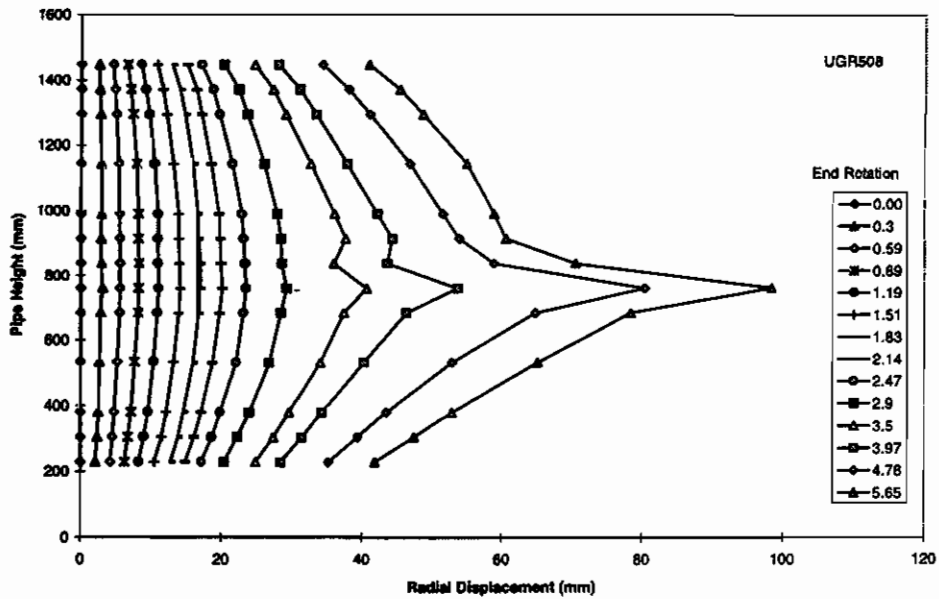


Figure 3.6 Radial Displacements on Maximum Compression Fiber for UGR508

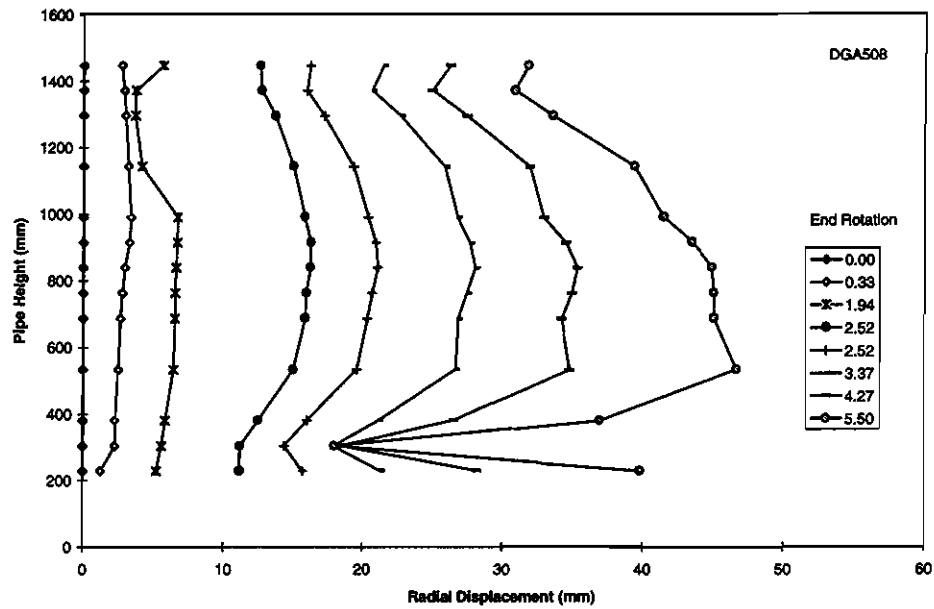


Figure 3.7 Radial Displacements on Maximum Compression Fiber for DGA508

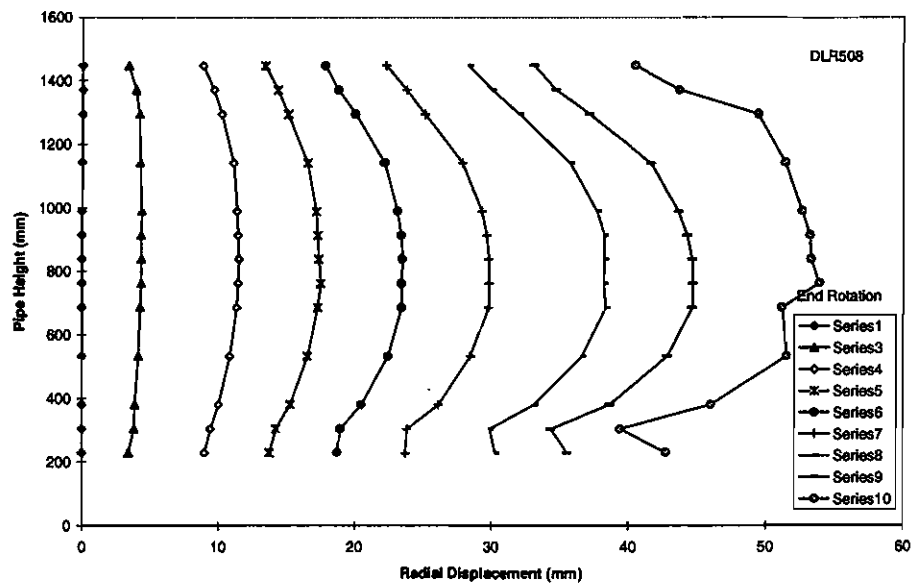


Figure 3.8 Radial Displacement on Maximum Compression Fiber for DLR508

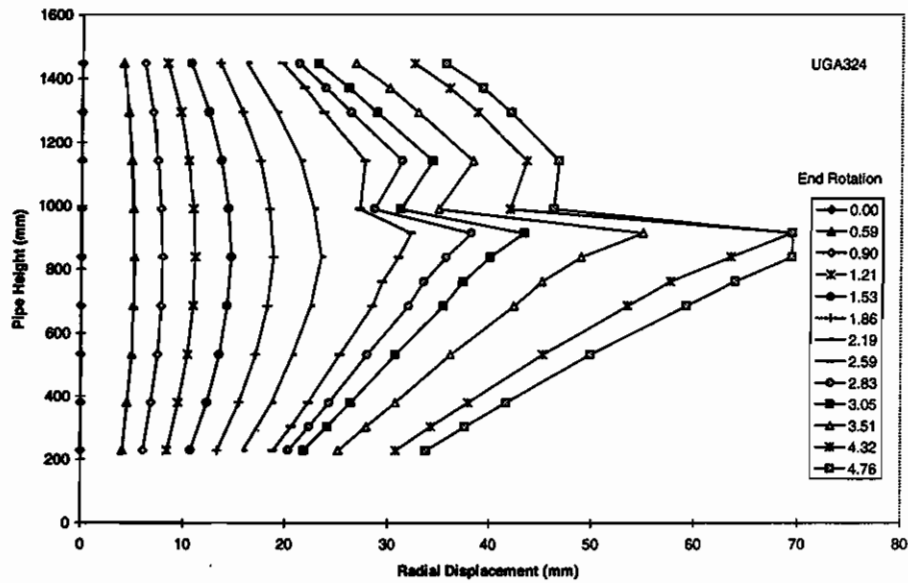


Figure 3.9 Radial Displacements on Maximum Compression Fiber for UGA324

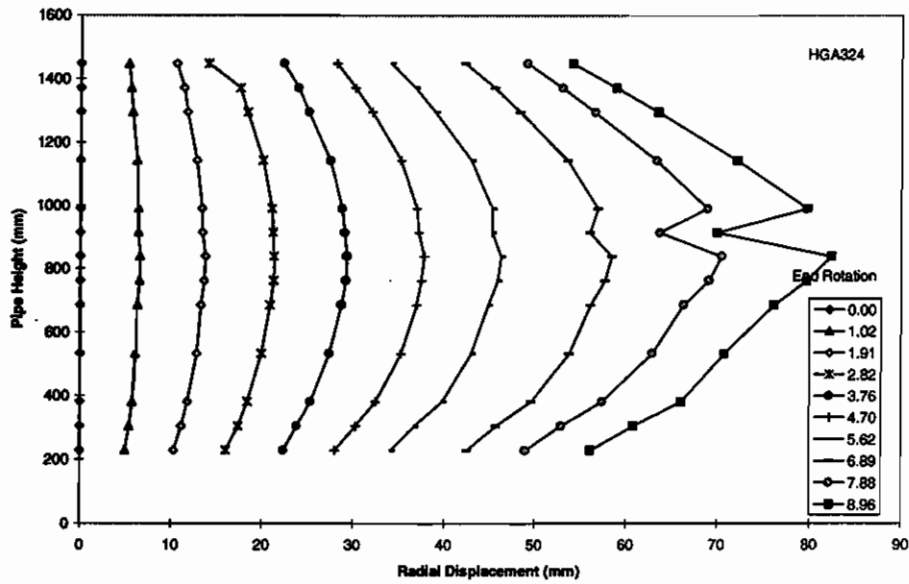


Figure 3.10 Radial Displacements on Maximum Compression Fiber for HGA324

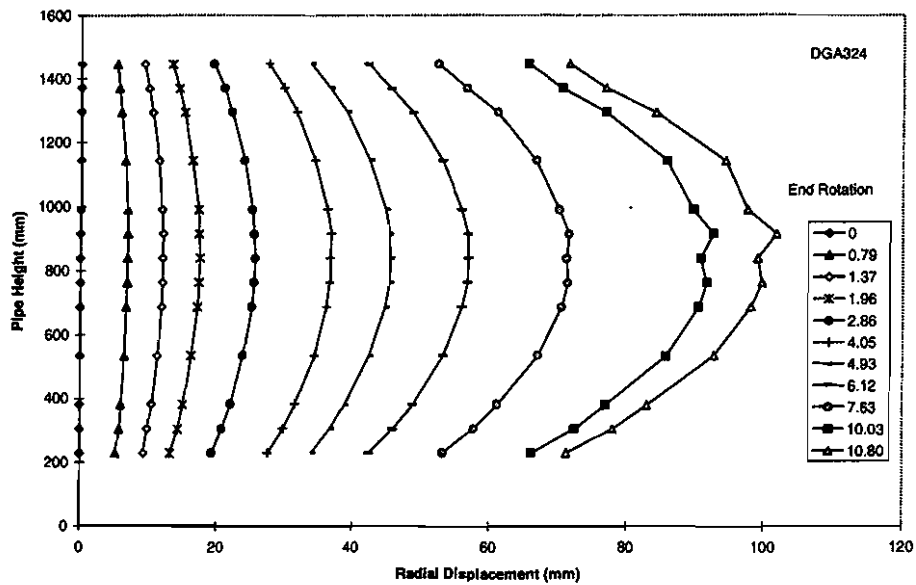


Figure 3.11 Radial Displacements on Maximum Compression Fiber for DGA324

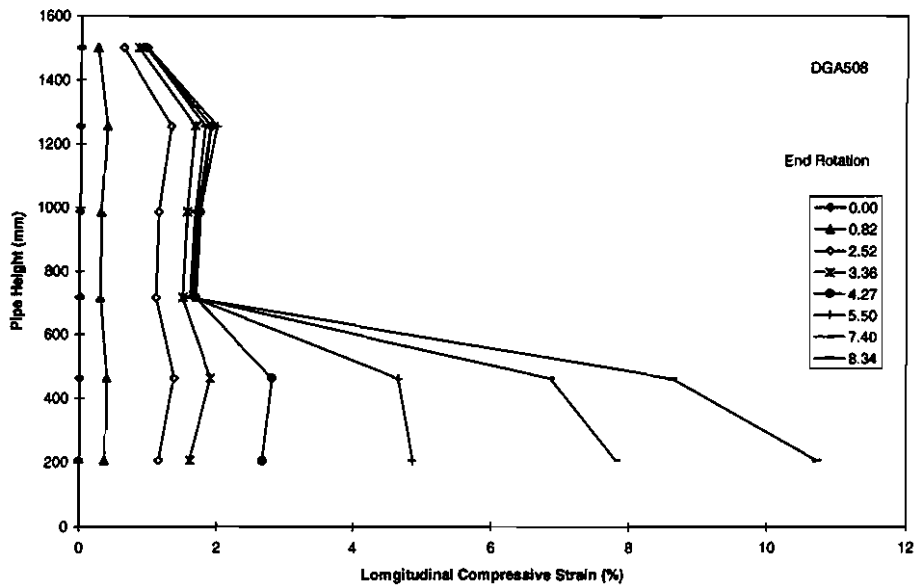


Figure 3.12 Demec Strains on Maximum Compression Fiber for DGA508

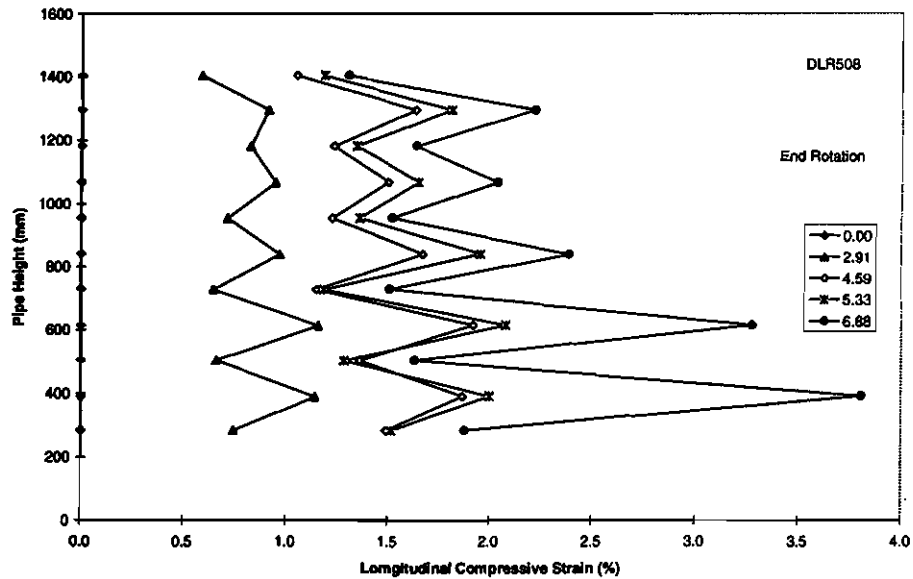


Figure 3.13 Demec Strains on Maximum Compression Fiber for DLR508

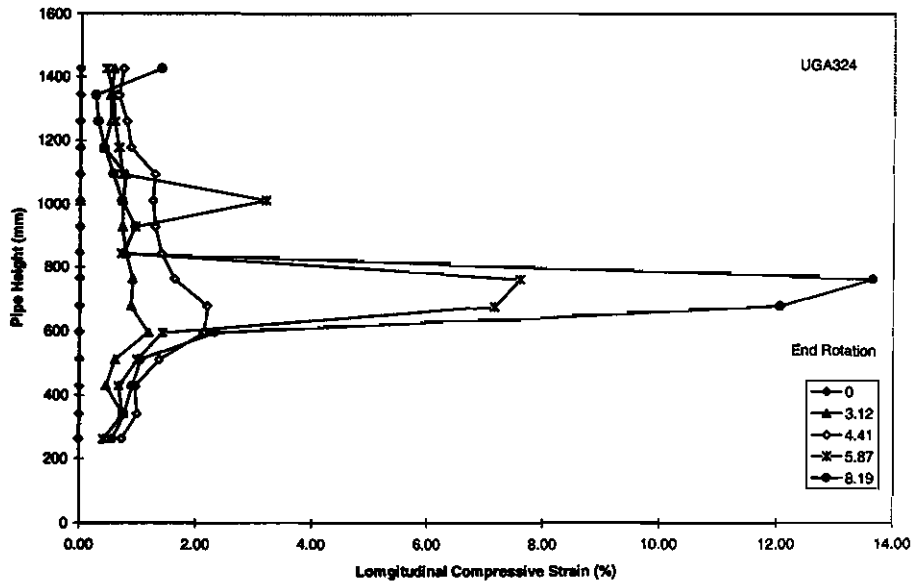


Figure 3.14 Demec Strains on Maximum Compression Fiber for UGA324

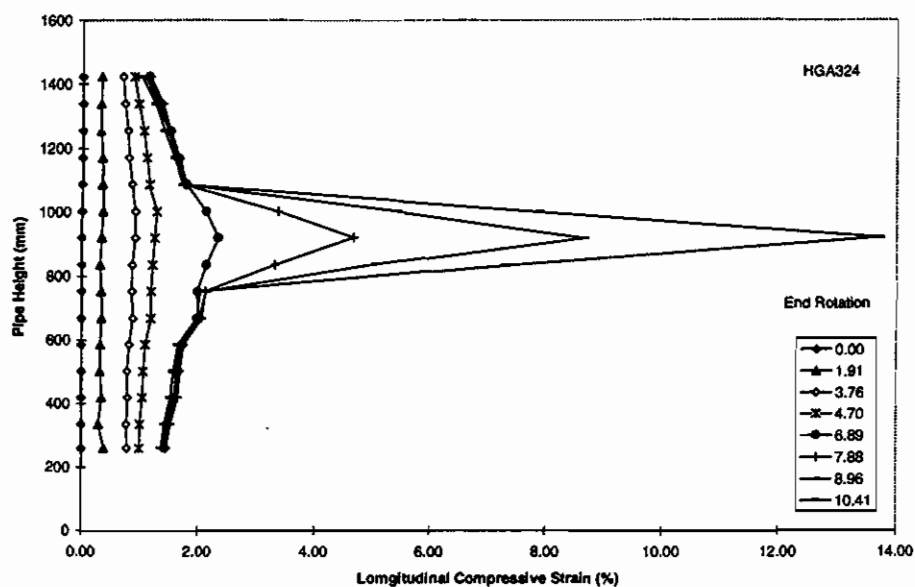


Figure 3.15 Demec Strains on Maximum Compression Fiber for HGA324

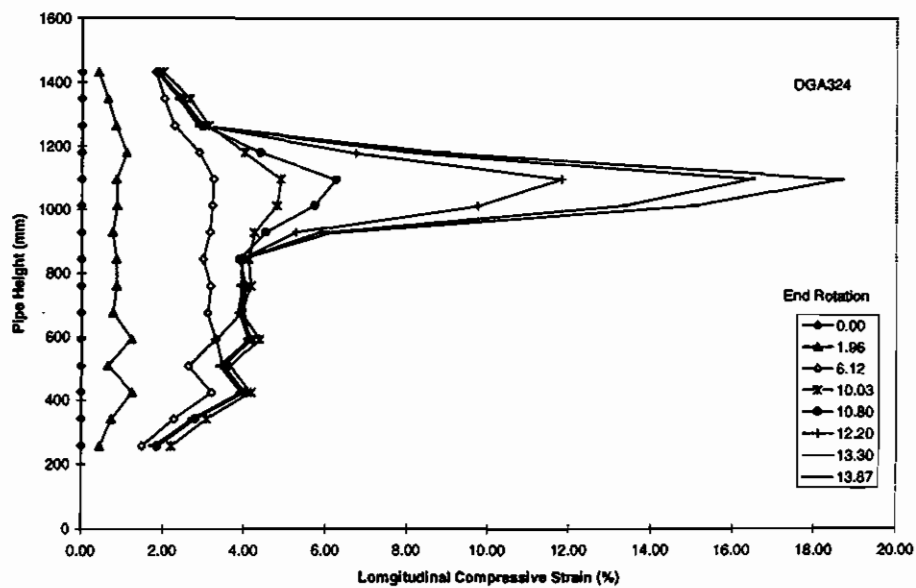


Figure 3.16 Demec Strains on Maximum Compression Fiber for DGA324

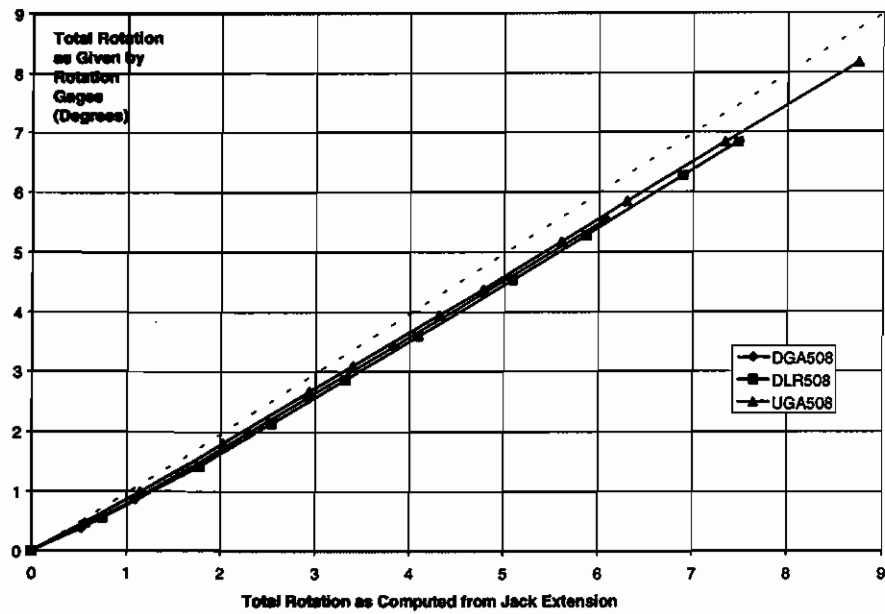


Figure 3.17 Comparison Between End Rotation Measurement Techniques

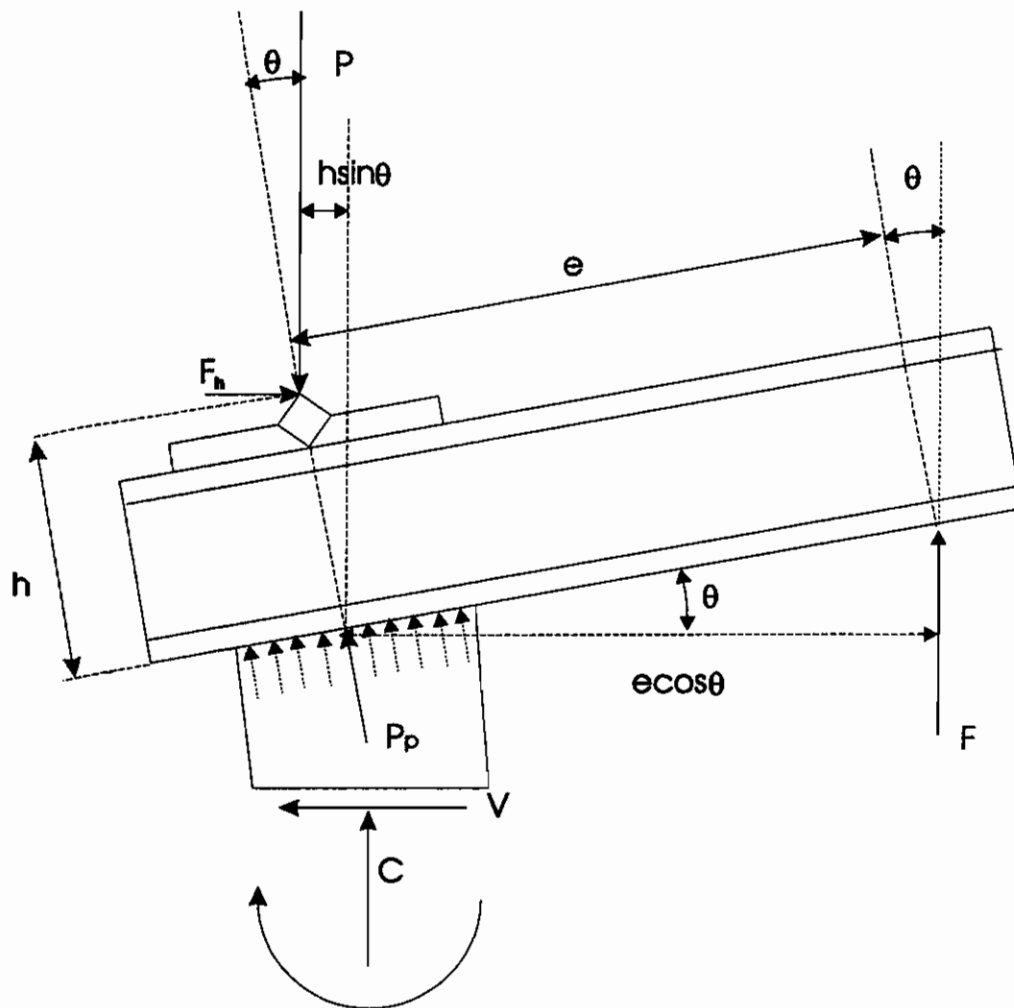


Figure 3.18 Free Body Diagram for a Specimen in a Deformed State

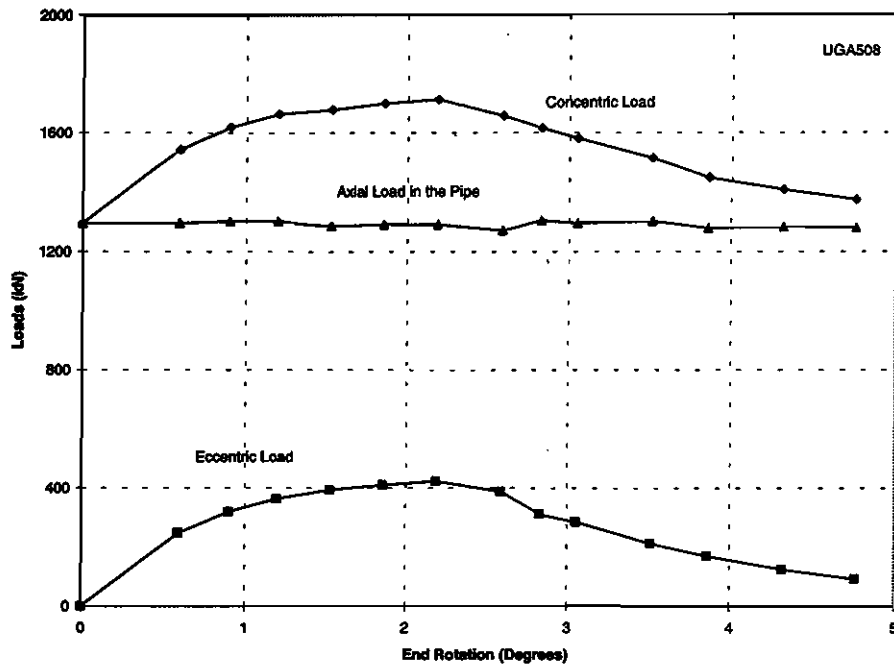


Figure 3.19 Load vs. End Rotation for UGA508

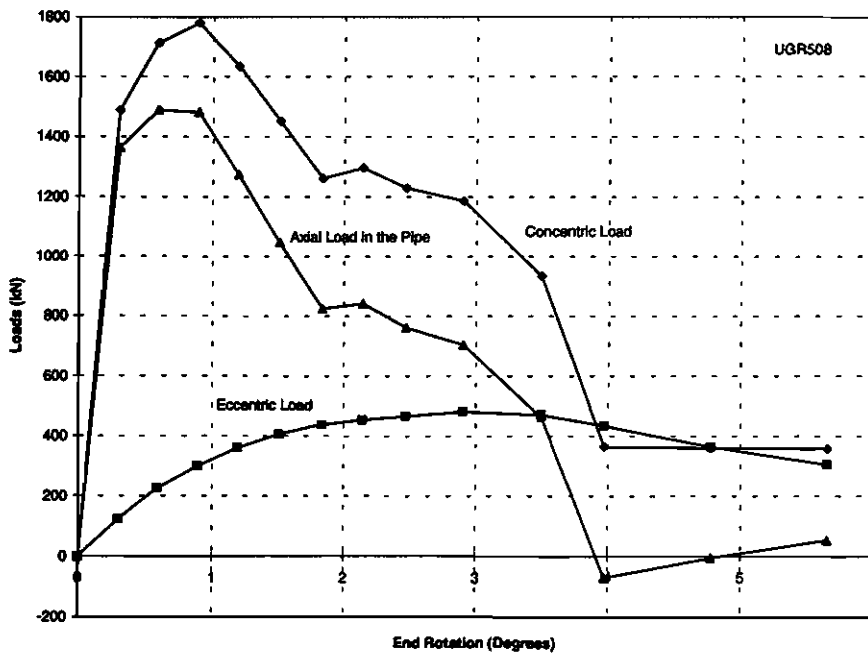


Figure 3.20 Load vs. End Rotation for UGR508

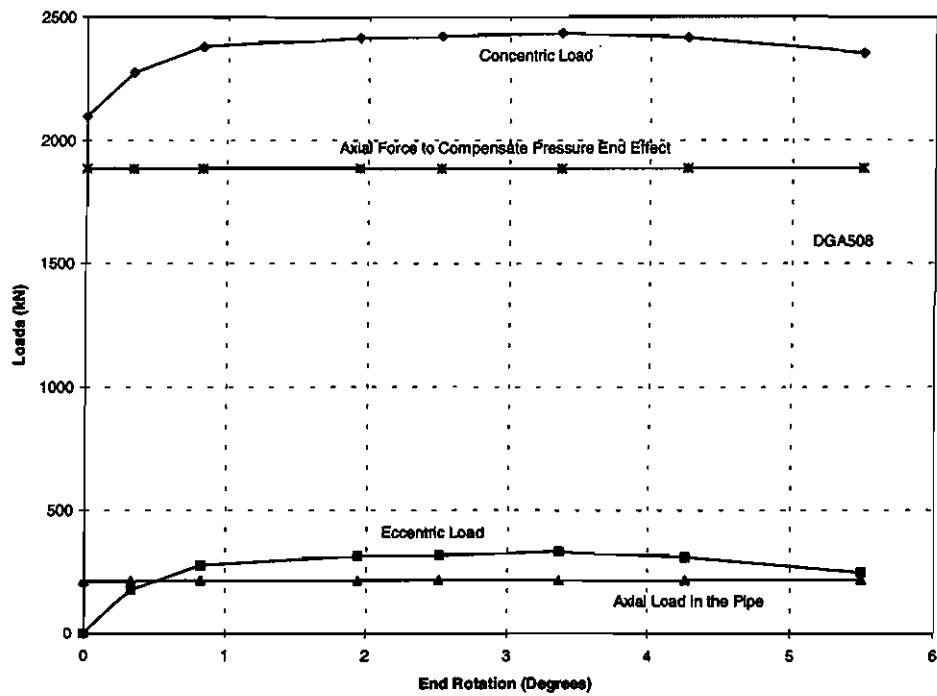


Figure 3.21 Load vs. End Rotation for DGA508

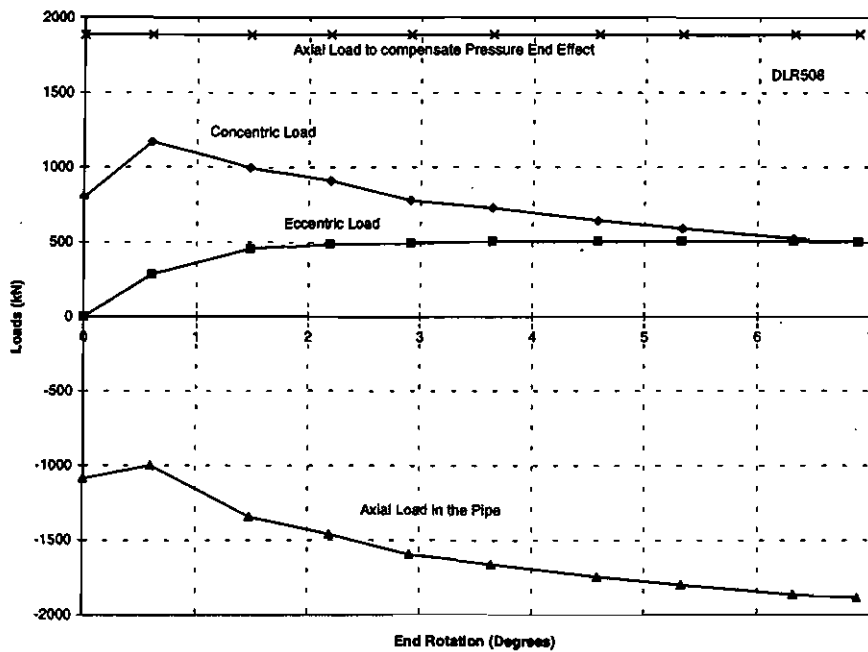


Figure 3.22 Load vs. End Rotation for DLR508

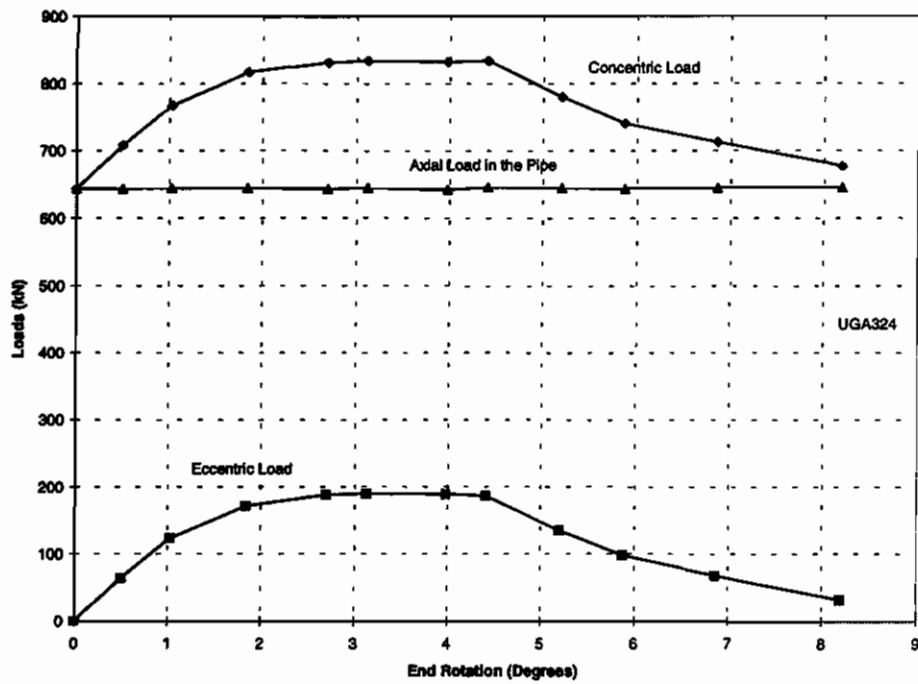


Figure 3.23 Load vs. End Rotation for UGA324

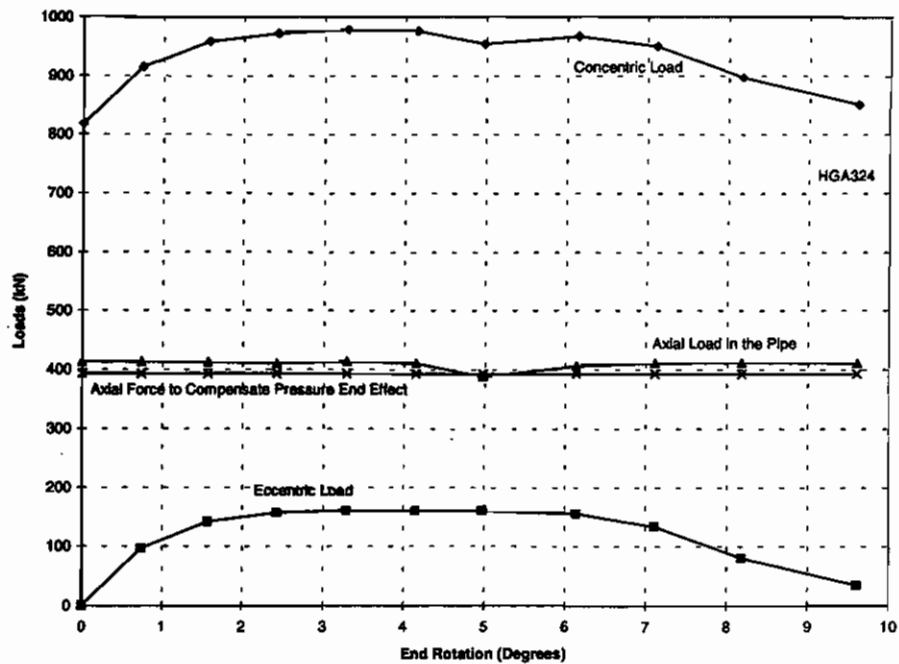


Figure 3.24 Load vs. End Rotation for HGA324

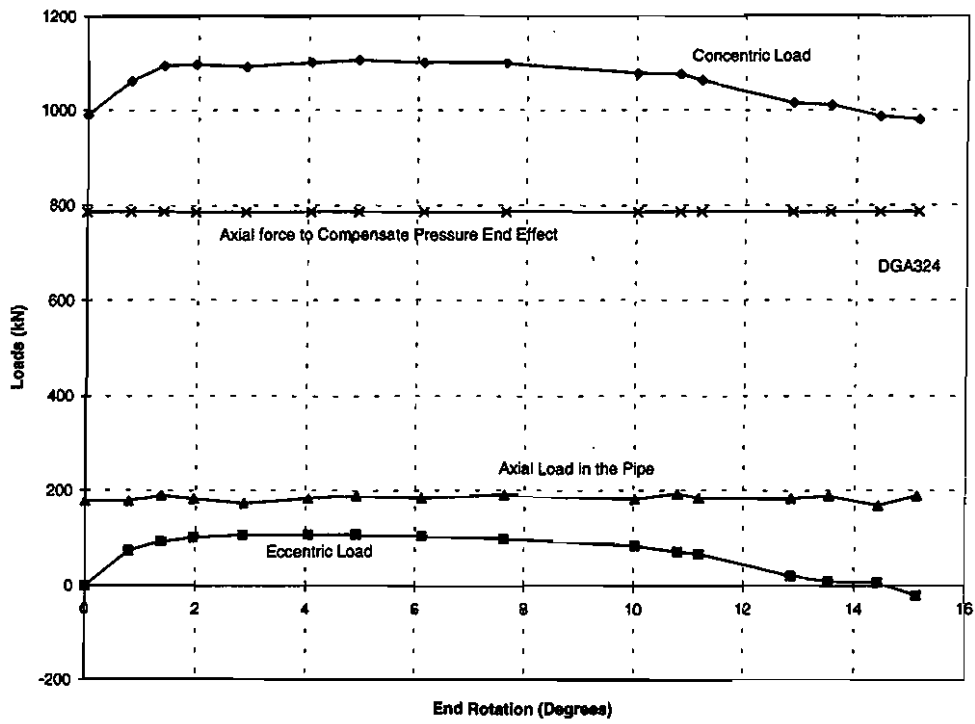


Figure 3.25 Load vs. End Rotation for DGA324

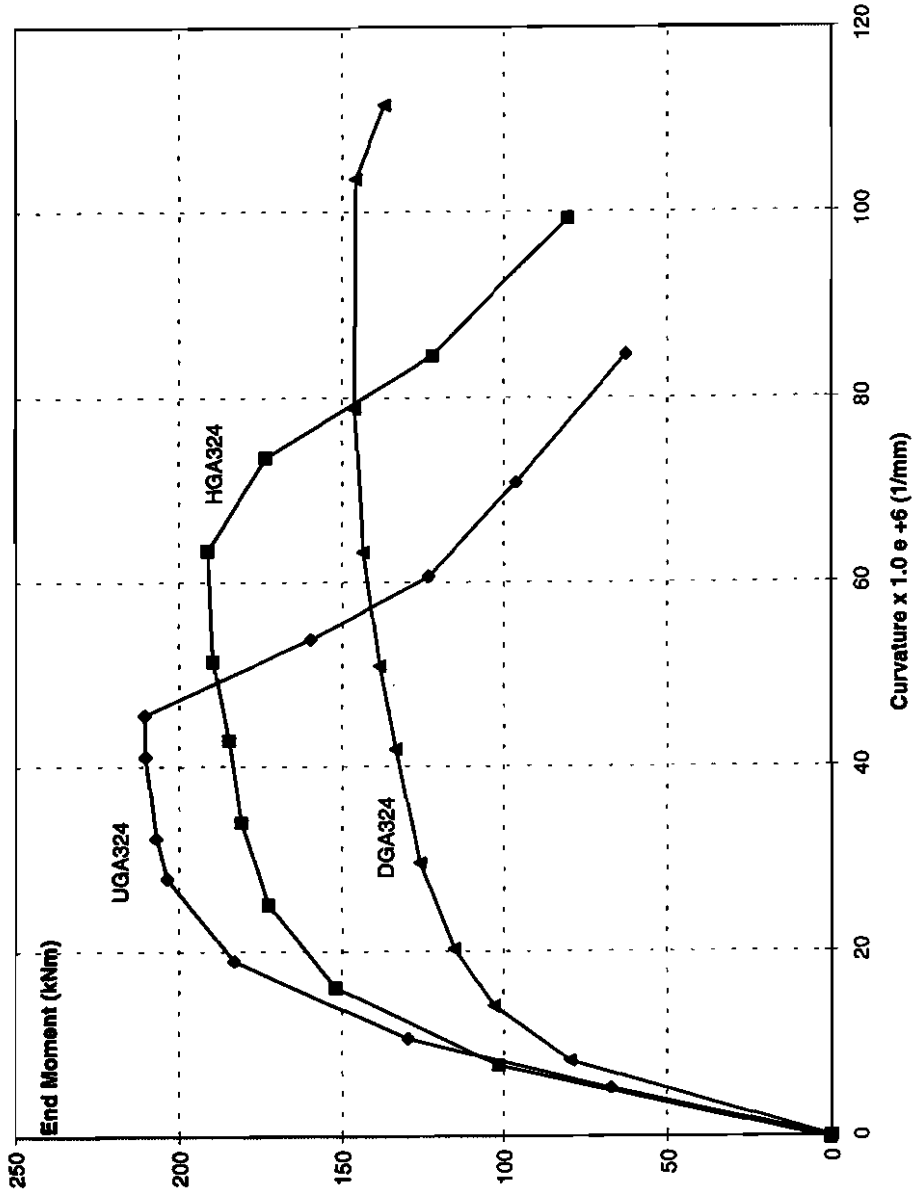


Figure 3.26 Moment vs. Curvature Diagrams for 324 mm OD Specimens

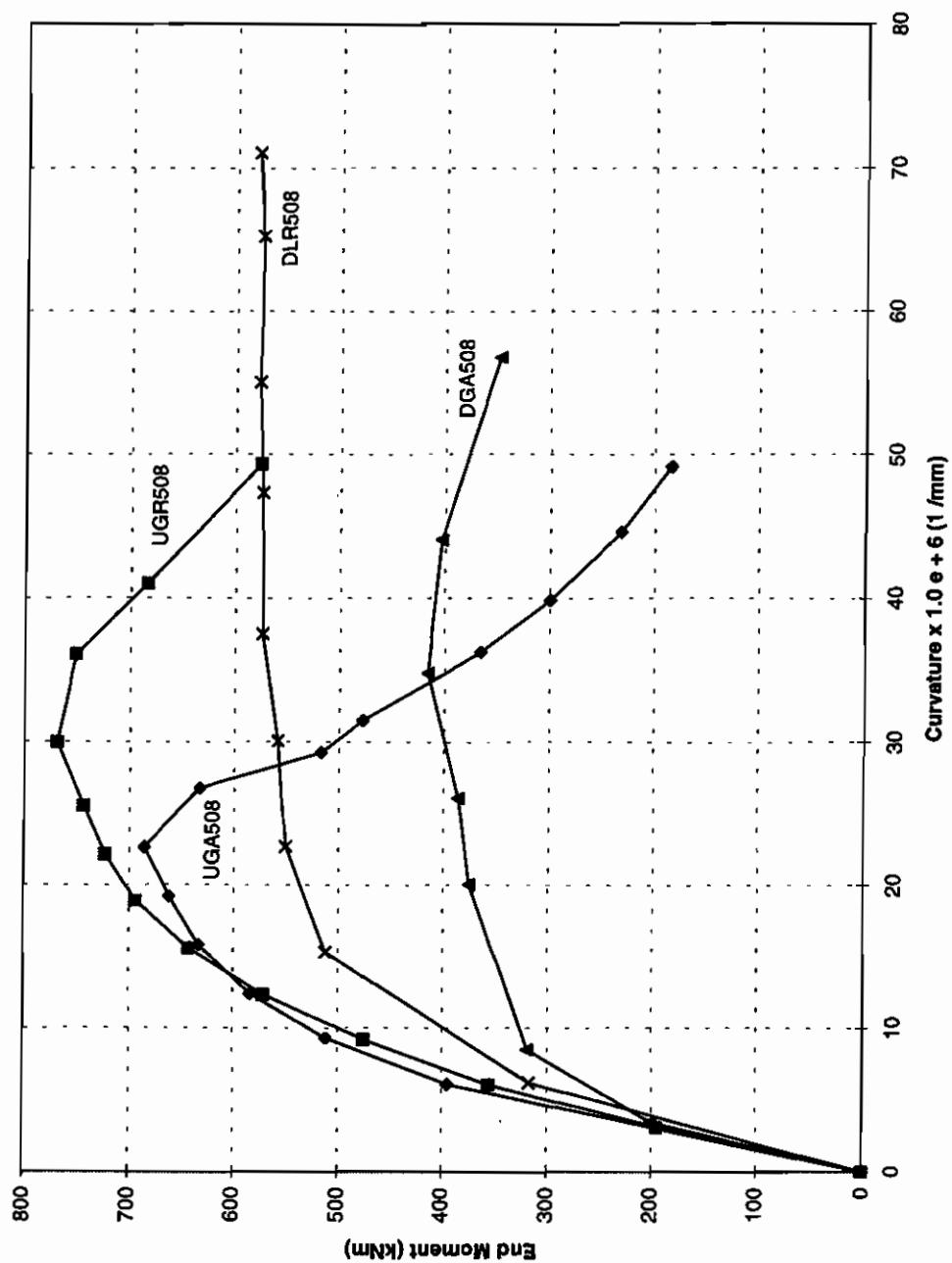


Figure 3.27 Moment vs. Curvature Diagrams for 508 mm OD Specimens

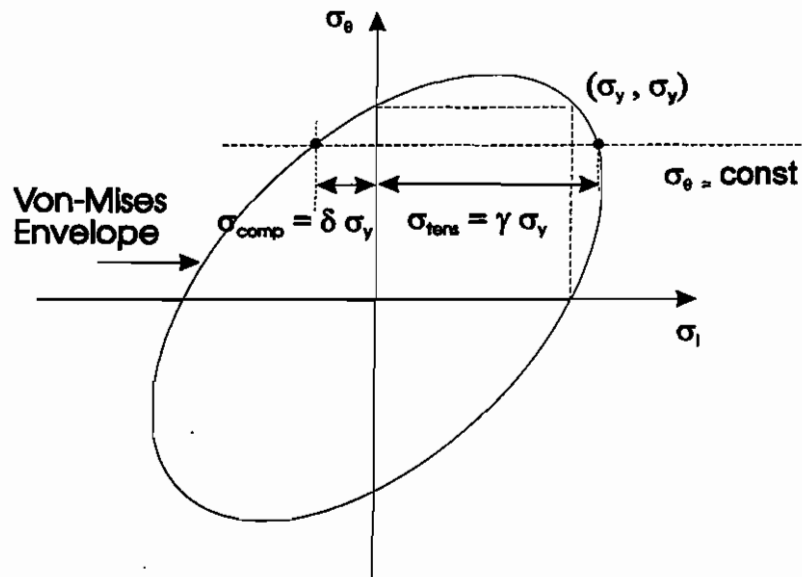


Figure 3.28 Von Mises Yield Envelope

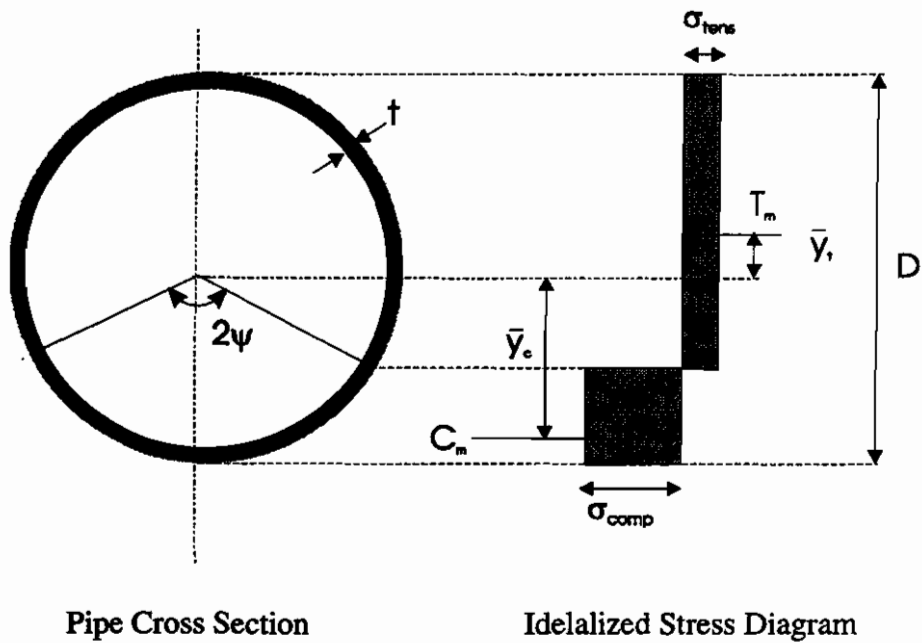


Figure 3.29 Idealized Stress Distribution

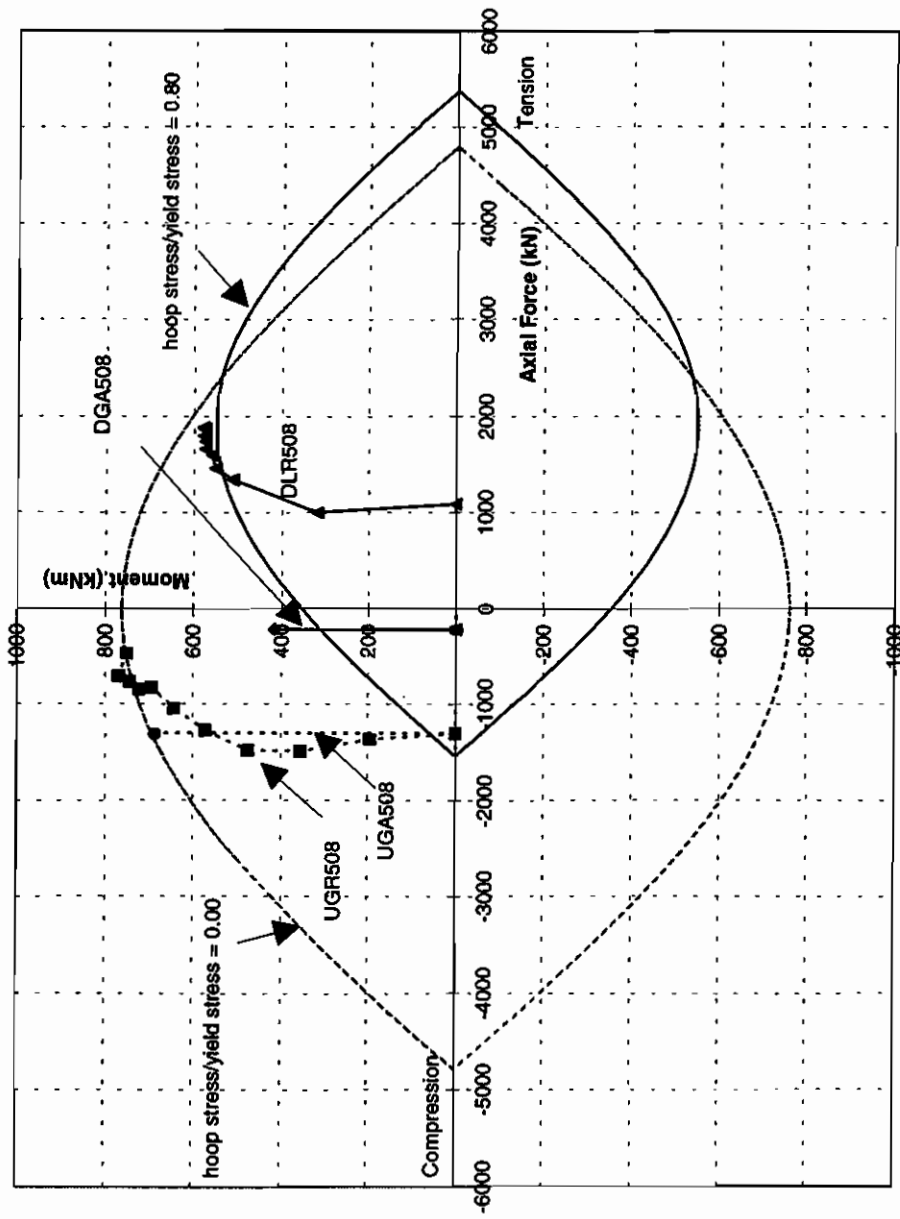


Figure 3.30 Interaction Diagram for 508 OD Pipes

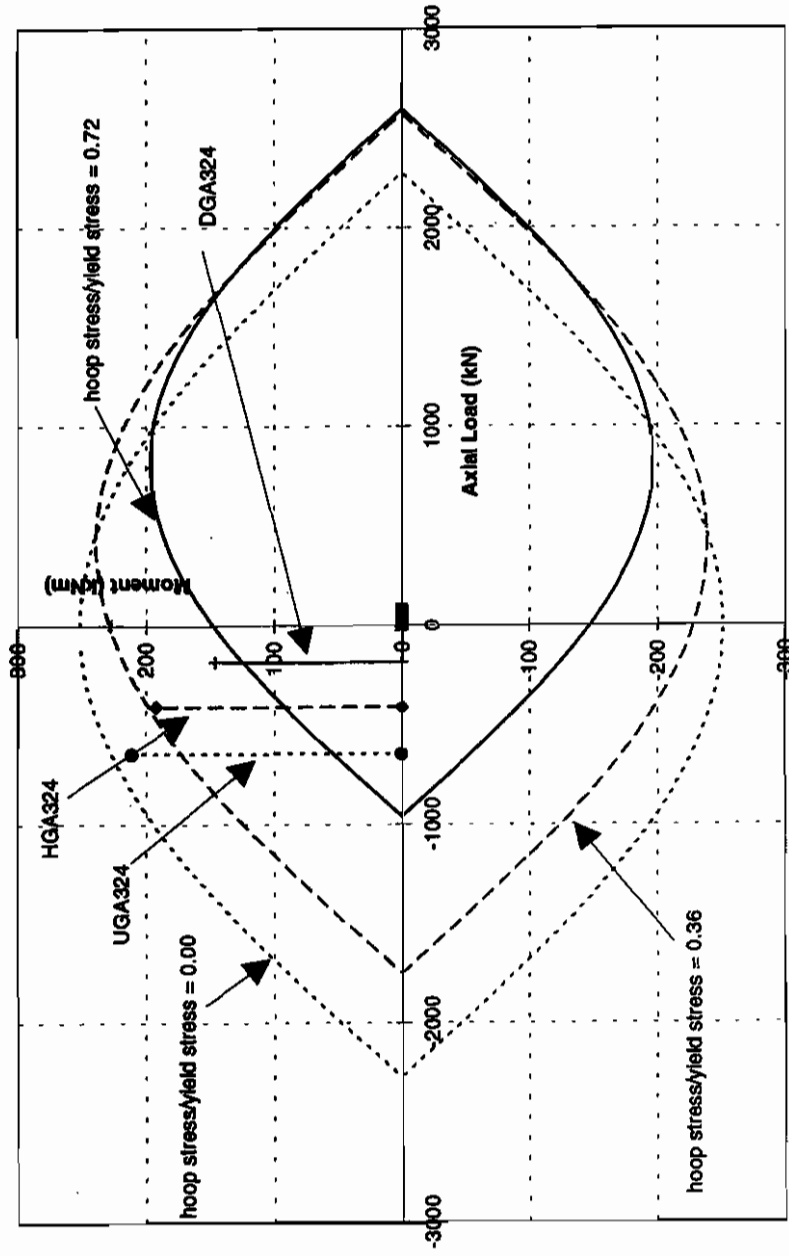


Figure 3.31 Interaction Diagram for 324 OD Pipes

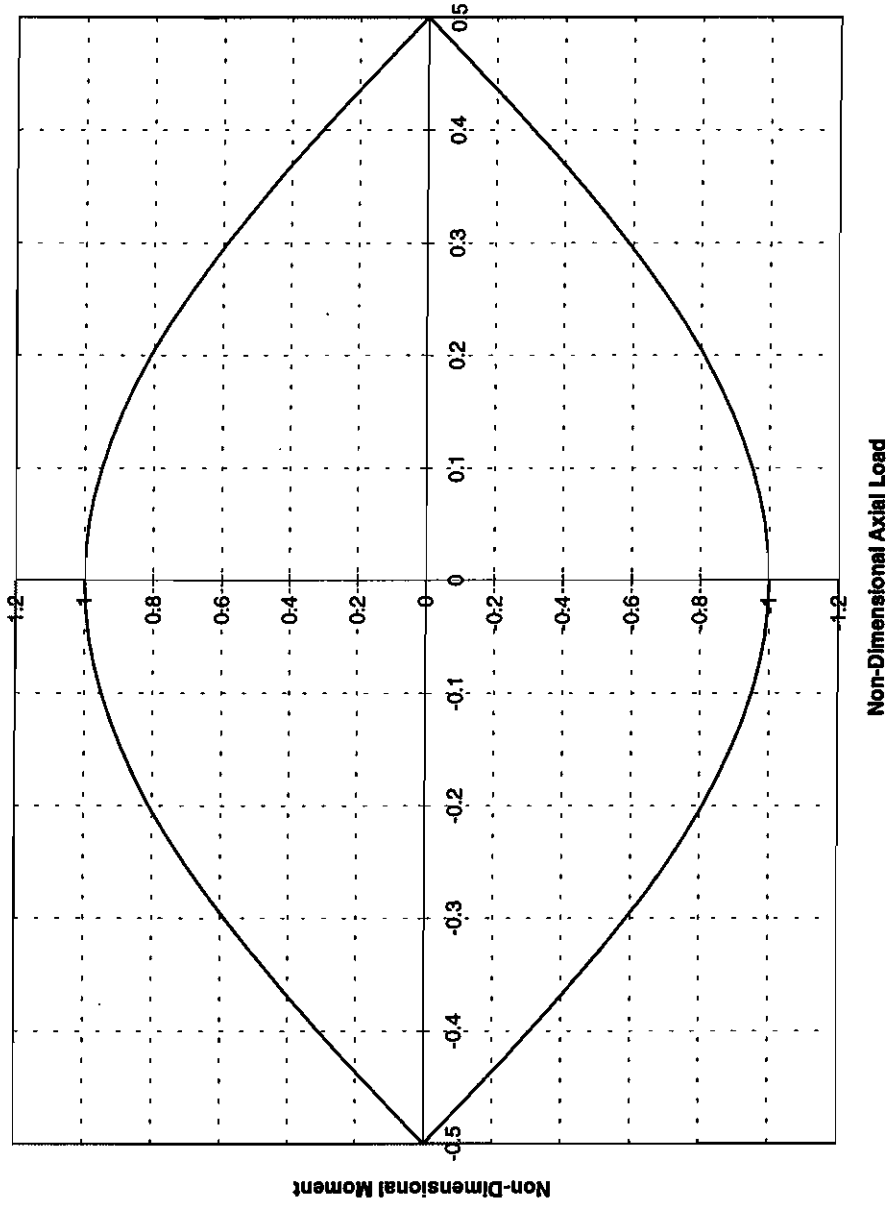


Figure 3.32 Non-Dimensional Interaction Diagram

4. ANALYSIS

4.1 General

The purpose of this chapter is to devise a numerical model that will be verified against the the results of the experimental program detailed in Chapter 3.

The comparison between the analytical predictions and the experimental results focuses on both the strength and the deformational behaviour of the specimens. In structural analysis problems, researchers primarily focus on strength comparisons (moment capacity), and less interest is given to the deformed structural configuration. This is justified for those cases where the structural strength of the element constitutes the primary design limit state. For buried pipelines, however, moment capacity is not the primary limit state because the moments induced in pipelines are self-limiting in nature. Therefore, emphasis is placed on an analytical and experimental comparison of the deformational behaviour of the pipe segments tested. Excessive deformation might affect the operation and maintenance of pipelines and this aspect is therefore a design limit state.

The verification of analytical techniques to predict the deformational behaviour of pipe segments includes the moment vs. curvature relationships, the buckling configurations, and the location of the buckles along the specimens.

A reliable prediction of the deformational behaviour of pipelines under the combined action of axial load, internal pressure, and imposed curvatures requires that a number of factors must be taken into account. These include: (a) a proper representation of the constitutive law of the pipe material, (b) a proper representation of the boundary conditions, and (c) the ability to address large deformations, large rotations, and finite strains. The complexities arising from these factors make a mathematical closed form solution unobtainable. Instead, a numerical solution to the problem is sought through the

finite element technique. The finite element analysis is a well established numerical tool that can be used to predict behaviour of complex problems in the area of mechanics.

In this research, the commercial finite element analysis package ABAQUS was used to predict the pipe behaviour. The selection of this package was based on the following features.

1. It has a built-in elasto-plastic isotropic hardening material model, suitable for modeling pipe material.
2. It includes an element type (S4RF) that is an efficient and reliable large displacement, large rotation and membrane finite strain shell element.
3. It is capable of accurately modeling both test and field boundary conditions, either through built-in multi-point constraints or through a user-written subroutine appended to the main program.
4. It has a built-in feature capable of modeling the internal pressure as a follower force.
5. It includes both the load control and the deformation control capabilities needed to simulate the test loads.
6. It includes post-processing capabilities that allow the user to view deformed configurations, contour lines of a variety of variables, and plots relating variables. The user has the flexibility of appending his own post-processing routines to the main program in order to perform problem-dependent analyses. This feature was used extensively in obtaining the results presented in Chapter 5.

4.2 Finite Element Formulation

In the finite element formulation, the principle of virtual work, together with assumed shape functions, are used to transform the differential equations of equilibrium into

algebraic equations. An incremental updated Lagrangian formulation is used in the solution.

Several shell formulations are available in the finite element analysis literature (and in ABAQUS). These include formulations for small strain problems, and large displacement–large rotation–small strain problems, and large displacement–large rotation–finite strain problems. The latter is the most general and therefore the most elaborate formulation.

4.3 Shell Element Features

Since local buckling of pipes involves large displacements and rotations, a large displacement–large rotation formulation needs to be adopted. In addition, Bathe (1982) suggests the use of finite strain formulation if the total equivalent plastic strains exceed 2% anywhere in the structure. After experimenting with the problems in hand, total equivalent plastic strains as high as 20% were found to be present at points lying in the mid-surface in some cases. This necessitates the use of a membrane finite strain formulation.

The shell element selected, S4RF, is a four-noded shell element and each node has five independent degrees of freedom. These are three translations in the direction of the global axes and the change in two independent components of a vector normal to the mid-surface of the shell from the original to the deformed configuration. The third component of the normal vector is obtained from the condition that the length of the normal vector is equal to unity.

The membrane strains on the reference surface are obtained from the derivatives of the position vector of a point in the reference surface in the deformed configuration with respect to the position on the surface. For the S4RF element, the membrane strains follow a finite strain formulation (Hibbit et al., 1993). The bending strains are derived from the

derivatives of the normal to mid-surface. Unlike membrane strains, strains due to bending are assumed to be small.

A direct implication of a membrane finite strain formulation is that the thickness of the shell element in the deformed configuration will differ from its value in the undeformed configuration. A further simplifying assumption used in S4RF is that the strain in the direction of the normal to the shell at the reference surface remains constant throughout the shell thickness.

The element has an iso-parametric formulation, (i. e., the same interpolation functions are used to interpolate both displacements and position vectors). The interpolation functions have C_0 continuity. The components of the vector normal to the surface are interpolated independently from the translational degrees of freedom.

In the S4RF element, transverse shear strain is measured as the change in the projection of a vector initially normal to the reference surface onto the tangent to the reference surface of the shell. The transverse shear acts as a penalty function imposing a constraint that enforces approximately that a material line originally normal to the shell reference surface remains normal to the surface throughout deformation. This is known as the Kirchhoff assumption in classic plate and shell literature. The Kirchhoff assumption is thus satisfied in an approximate sense. The transverse shear strain components are calculated at mid-points of element edges. The selection of these locations prevents the occurrence of the hourglass mode of deformation (Hibbit et al., 1993).

Seven points for through-thickness integration are selected. The integration through the element thickness follows the Simpson Rule of numeric integration.

4.4 Material Model Idealization

The average true stress-true strain curves observed in tension tests for both X52 and X56 materials are shown in Figure 2.11. They exhibit an initial elastic behaviour followed by gradual softening characterized by plastic flow with hardening.

The tensile coupons were taken in the longitudinal direction of the pipe. Since no material tests were performed to measure the stress vs. strain relationship of the pipe material in compression, the compressive stress vs. strain behaviour is assumed to be identical to the tensile behaviour. No attempts were made to determine the pipe material properties in the circumferential direction. In general, the properties of the pipe material in the longitudinal and circumferential directions are different, as observed by Workman (1988). For the scope of this work, the orthotropy of the material was neglected and material was assumed to be isotropic and to follow the observed longitudinal tensile stress vs. strain relationship as determined from coupon testing.

Strictly speaking, kinematic hardening is more representative of steel behaviour than isotropic hardening. However, the kinematic hardening models available in ABAQUS provided only a bi-linear representation of the stress vs. strain relationship. An accurate representation of the yield surface expansion as measured in the tension tests (see Chapter 2) necessitates the use of a multi-linear stress vs. strain relationship. Therefore, the advantage of using of a kinematic hardening model was offset by the disadvantage of modeling the yield surface through a bi-linear representation. On the other hand, since the analysis did not involve cyclic loading, the difference between the predicted behaviour of the pipes based on a kinematic model and that based on an isotropic model should not be significantly different. A multi-linear isotropic hardening stress strain model was therefore selected for the analysis. The material model obeyed the von Mises yield criterion, with an associative flow rule.

4.5 Residual Stresses

Residual stresses exist in the pipes tested. These are:

1. The through-thickness residual stresses in the pipe material, both in the longitudinal and hoop directions, that are created during the forming process. These were not measured, and therefore no attempt has been made to include their effect in the analysis.
2. The residual stresses caused by seam welding. Since longitudinal welds were intentionally kept at the extreme tension fiber of the pipes during testing, it was judged that these residual stresses would not significantly affect local buckles occurring in the compression zone.
3. The residual stresses caused by the welding process of the pipe edges to the end plates. Since the buckles were forced by the collars to occur at least 200 mm away from the end plates, these residual stresses were judged that these did not significantly affect the local buckling behaviour of the test specimens and they were not modeled in the analysis.

4.6 Modeling of Confining Collars

In the full-scale tests, the two confining collars described in Section 2.6.1 and shown in Fig. 2.3 were successful in preventing the pipe from buckling locally at the ends of the specimen. A perfect representation of the problem would necessitate the modeling of the collar-pipe interaction as a contact problem. However, in order to avoid the complications of such a model, the top and bottom 150 mm of the specimen length (the region confined by the collars) was modeled as perfectly-elastic and with the same properties (elasticity modulus and Poisson's ratio) as that of the pipe steel. The top and bottom parts of the specimens were, therefore, prevented from deforming plastically. This forced the local buckle away from the specimen ends in the same way that the confining

collars affected the location of the buckle in the tests. This modeling simplification was, therefore, judged not to compromise the integrity of the analytical model.

4.7 Finite Element Mesh

In order to take advantage of the symmetry of the problem with respect to the plane of bending, only one longitudinal half of the specimen is analyzed.

In order to minimize the number of degrees of freedom, attempts were made to use a refined mesh in the circumferential direction in the location where the local buckle was expected to occur (as observed in the test). A coarser mesh was used to model the rest of the specimen. A triangular element transition zone was used to connect the two groups of rectangular elements. It was noticed, however, that the transition mesh forced the local buckle to occur in the transition zone. Therefore, this type of mesh was abandoned.

Another alternative mesh investigated was to make finer elements in the longitudinal direction in the location where the buckle was expected to occur, and to use relatively coarser elements in the rest of the specimen. It was found that the location of the buckle was initiated within the boundary separating the two groups of elements. Therefore, a regular mesh has been used to model the test specimens.

Experimenting with the number of elements along both the circumferential and longitudinal directions indicated that the number of elements need not exceed 18 elements along half of the pipe circumference and 60 elements along the specimen height (see Figure 4.1) for specimens exhibiting diamond shape buckling patterns. For specimens with outward bulging patterns, 18 by 40 elements were used. Any further refinements did not yield any significantly different results from the meshes selected.

4.8 Boundary Conditions

The kinematics of the tests is such that each of the end rings of the pipe remains perfectly circular after deformation because the specimens are welded to end-plates having “infinite” in-plane rigidity. Also, all points of the end rings remain in one plane after deformation. This plane undergoes a rigid body rotation (θ_x) around the pivot of the knife edge (Figure 4.2) as the specimen is deformed. The pivot of the bottom knife edge is stationary whereas the top one is only free to move in the vertical direction as the pipe deforms. The boundary conditions described were carefully modeled and tested by combining the built-in ABAQUS capabilities with model boundary conditions.

4.9 Sequence of Load Application in the Analysis

For active tests (as defined in Section 2.4.2.2), the axial load was first applied to the model and then maintained constant in subsequent loading steps. Secondly, the internal pressure, if any, was applied and kept constant throughout the subsequent loading steps. Finally, the two end rotations as measured in the tests were incrementally imposed within the analytical model. The incrementing process followed the same path as the one recorded in the test.

For the reactive tests (as defined in Section 2.4.2.2), the internal pressure was applied first. Then the following steps were performed for each increment:

1. The axial load recorded in the test at the increment considered was applied to the specimen.
2. The end rotations were applied, while maintaining the axial load for this step constant.
3. Go to the next loading increment.

Attempts to impose the end moments as measured from tests were successful only in modeling the pre-buckling response of the specimens. In order to trace the post-buckling response of the specimens deformation-controlled loading had to be used instead. The two end rotations (see Figure 4.2) were used as deformation controlling parameters for this purpose.

4.10 Computer Hardware

The ABAQUS finite element runs were performed on IPC and IPX Sun Workstations that had 16 MB of RAM. The workstations use the UNIX operating system. Computer runs took from a few hours to a few days of computing time. The running time was problem-dependent in some aspects (number of degrees of freedom, number of increments, number of iterations required for convergence per increment, number of the through-thickness integration points selected) and system-dependent in some other aspects (number of jobs simultaneously run on a machine, amount of RAM available, availability of temporary space, machine speed in performing floating point operations, etc.). ABAQUS Version 5.2 was used to perform the runs presented in this chapter while the upgraded ABAQUS Version 5.3 was used to perform the runs of the parametric study presented in Chapter 5.

4.11 Moment vs. Curvature Relationship

Figures 4.3 through 4.9 show a comparison between the moment vs. curvature relationships for the seven specimens tested. The experimental moments obtained in the tests and by the analysis are the average of the moments at the top end and the bottom end of the specimens. The curvature values are those based on the whole length of the specimen. Experimental moment and curvature calculations were based on Equations 3.3 and 3.4, respectively. The analytical moments (designated as FEA in Figures 4.3 through

4.9) are those obtained from averaging the two end moment reactions resulting from the finite element analyses.

For unpressurized tests (UGA508, UGR508, and UGA324), the analytical moment vs. curvature curves exhibit the same trend as do the experimental curves and good agreement between analysis and tests is obtained in these cases. Excellent agreement is obtained for pressurized tests, DGA508, DLR508, and HGA324. The agreement between the analysis and test results for DGA324 is adequate. For DGA324, the maximum difference between the experimental and analytical moments is in the neighborhood of 30 kNm. However, due to the fact that the moment capacity of Specimen DGA324 is only 120 kNm, the 30 kNm moment capacity difference corresponds to the largest relative error of the seven specimens tested.

4.12 Buckled Configurations

Figures 4.10 through 4.16 present the deformed configuration of the seven specimens tested. Each figure consists of two parts. The first part is a photograph of the tested specimen in the deformed configuration. The second part consists of a wire mesh in the deformed configuration of the same specimen as predicted by finite element analysis. The finite element analysis model was capable of predicting the correct mode of buckling in all but one case.

Both the analyses and the test results give outward bulge buckles for pressurized specimens and inward buckles for unpressurized specimens. The buckled configuration of Specimen UGA324 (Figure 4.14) as predicted by the finite element model consisted of one depression (Brazier mode). In contrast, the same specimen exhibited one large depression with two small side depressions adjacent to it (diamond shape buckling) during the test. The finite element model was unable to reproduce the two small side depressions.

All pressurized specimens exhibited an outward bulging mode and all unpressurized tests exhibited a diamond shape pattern. According to both the physical tests and the analysis, only one local buckle occurred in each specimen. The buckle covered a length ranging from 0.25 OD to 0.50 OD for outward bulges and a length of 0.60 to 0.80 OD for inward buckles.

In most cases, reasonable agreement is obtained between the predictions of the analytical model of the location of the local buckles along the specimen length and the location of the buckles as obtained in the tests (Figure 4.10 to 4.16). The best agreement is obtained in pressurized specimens.

4.13 Conclusion

The agreement between analytical and experimental results, as demonstrated in this chapter, gives confidence that the analytical model devised is able to predict the physical test in a reasonable way. The analytical model can therefore be used in order to perform the parametric studies that will be used to a reliably predict deformation limit states for design purposes. It is within the scope of Chapter 5 to present these findings.

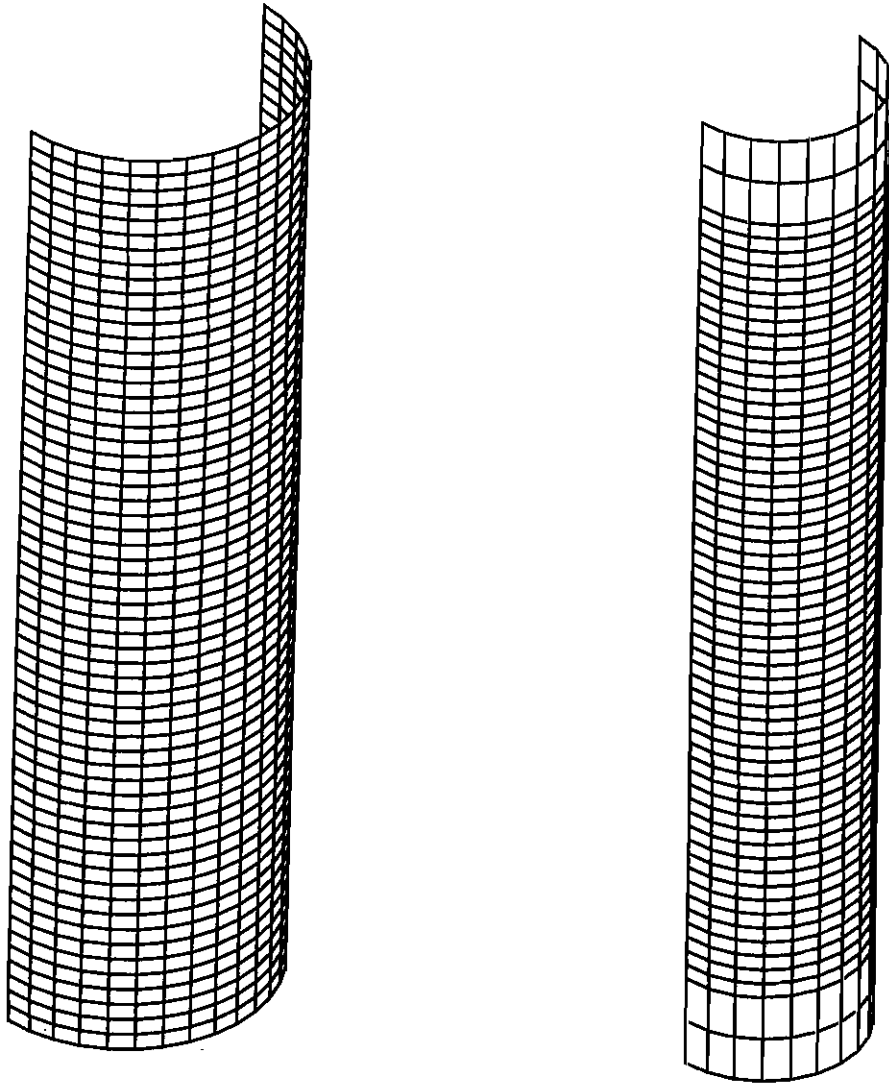


Figure 4.1 Finite Element Meshes

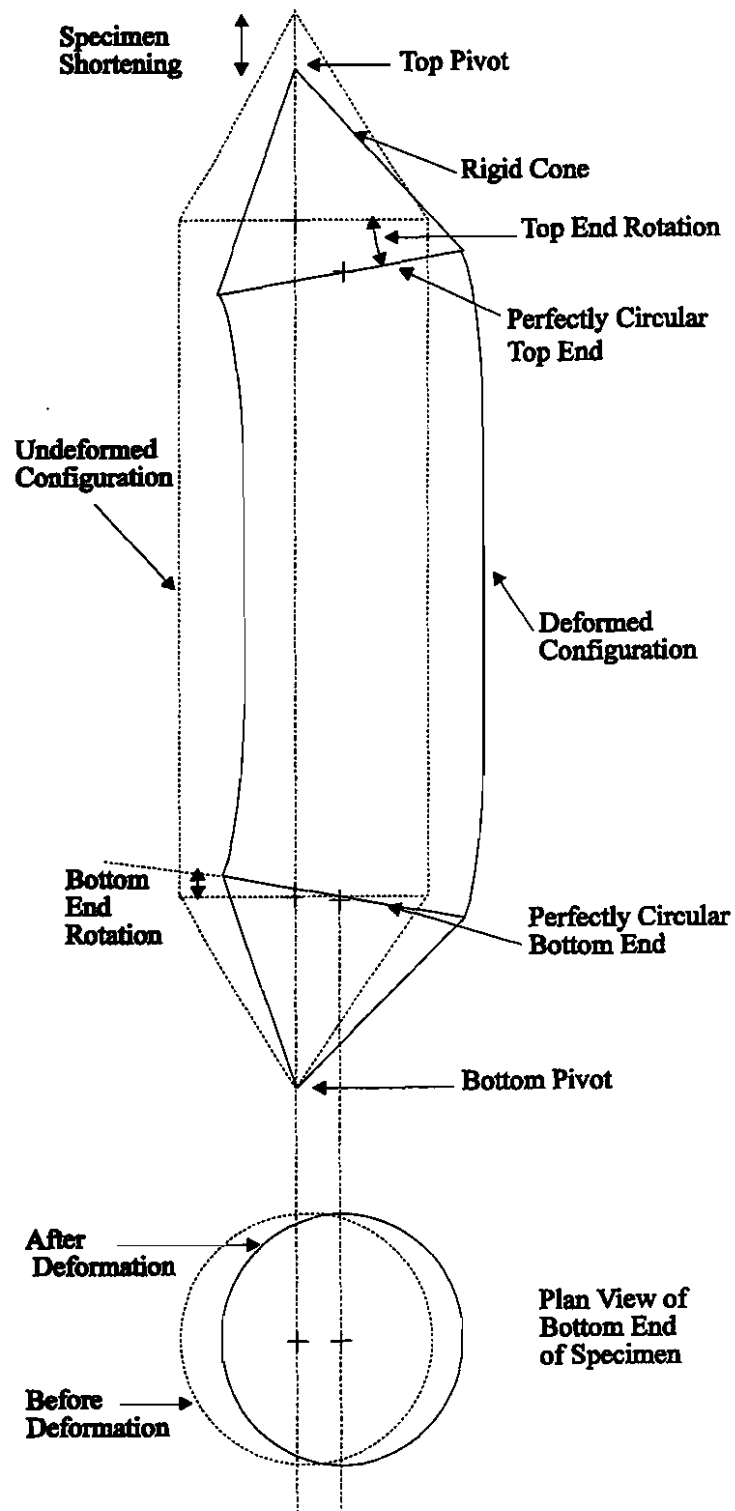


Figure 4.2 Boundary Conditions for Test Specimens

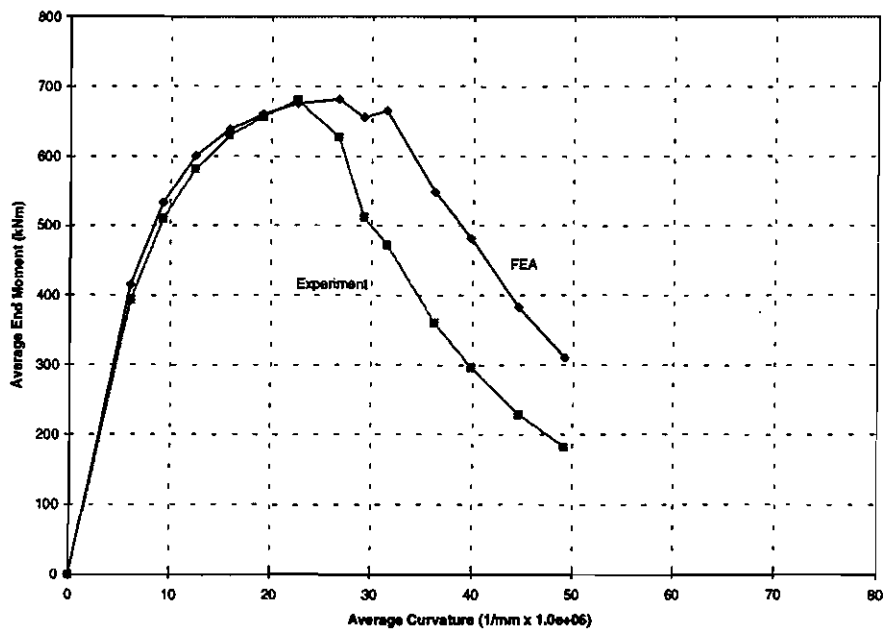


Figure 4.3 Moment vs. Curvature Relationship for UGA508

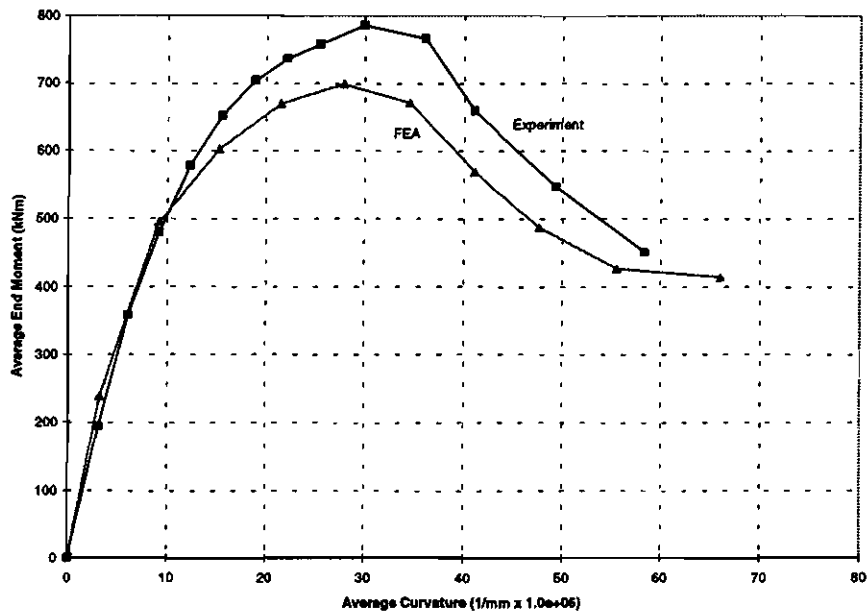


Figure 4.4 Moment vs. Curvature Relationship for UGR508

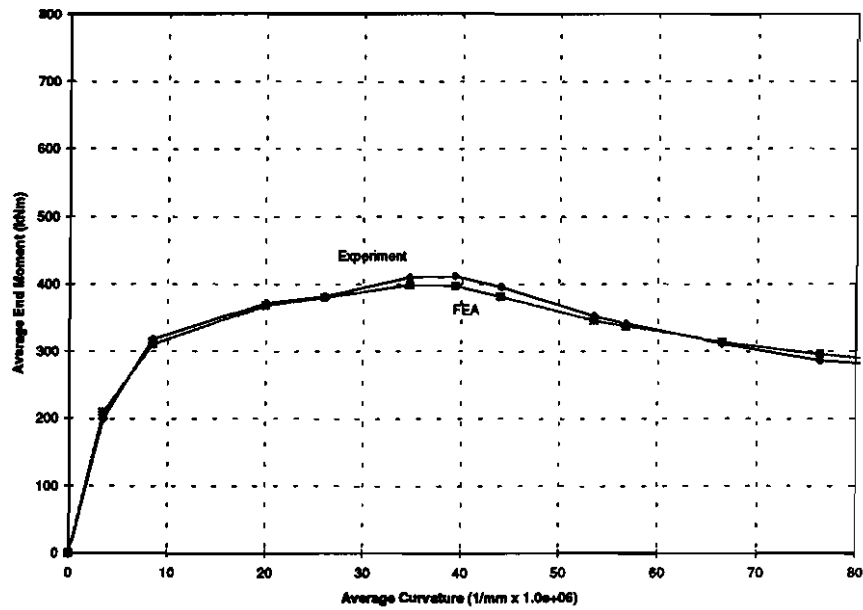


Figure 4.5 Moment vs. Curvature Relationship for DGA508

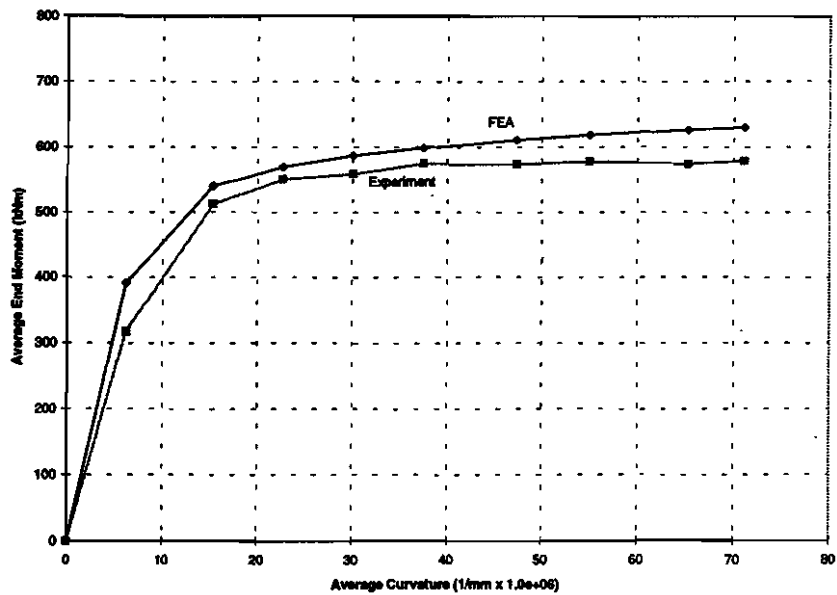


Figure 4.6 Moment vs. Curvature Relationship for DLR508

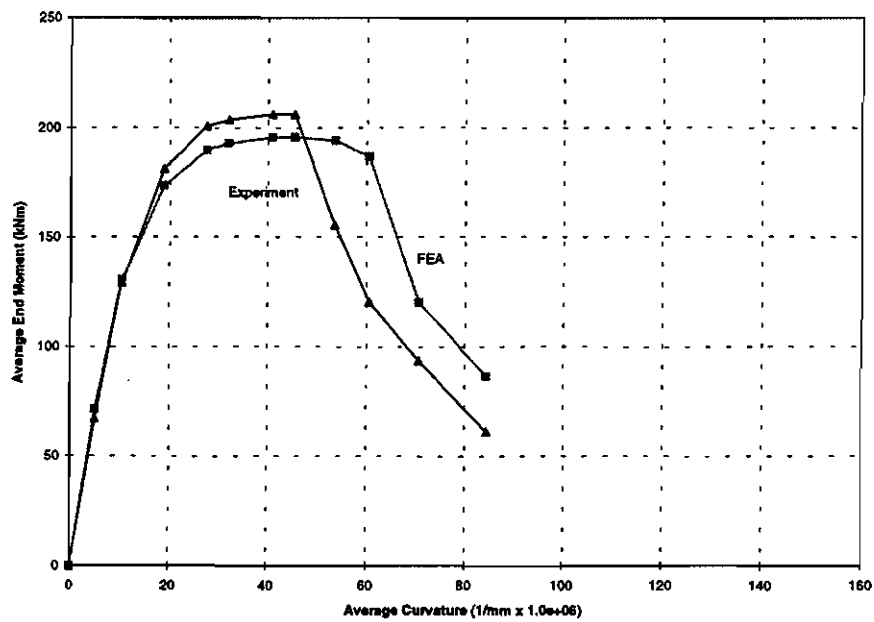


Figure 4.7 Moment vs. Curvature Relationship for UGA324

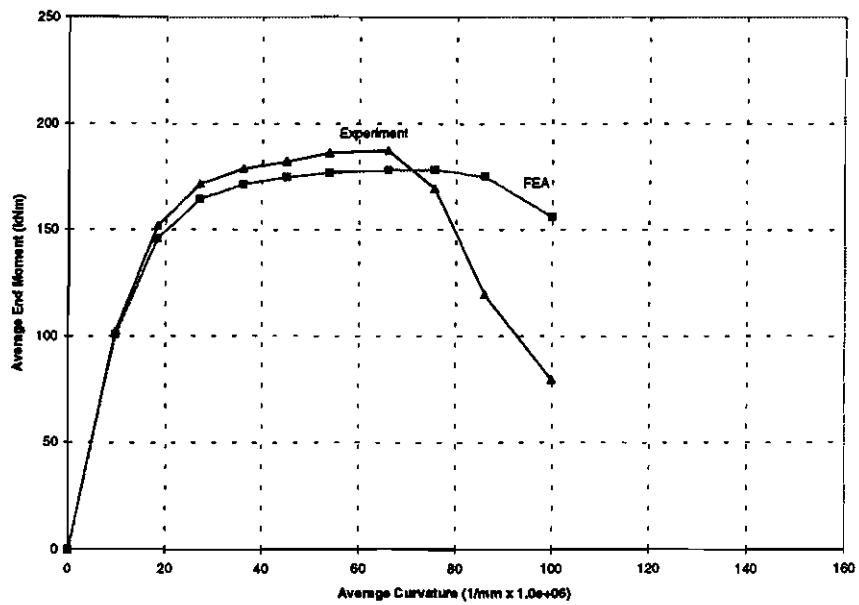


Figure 4.8 Moment vs. Curvature Relationship for HGA324

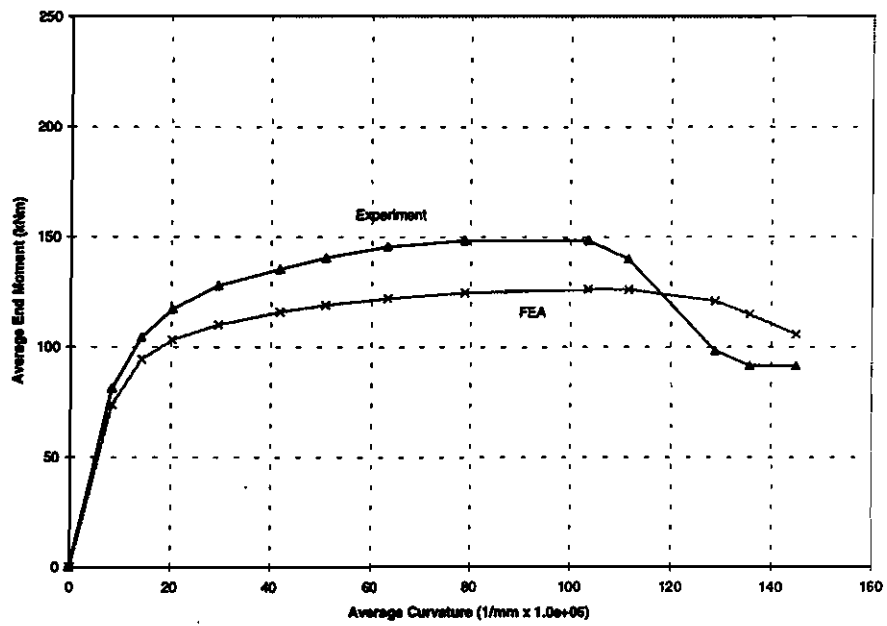


Figure 4.9 Moment vs. Curvature Relationship for DGA324

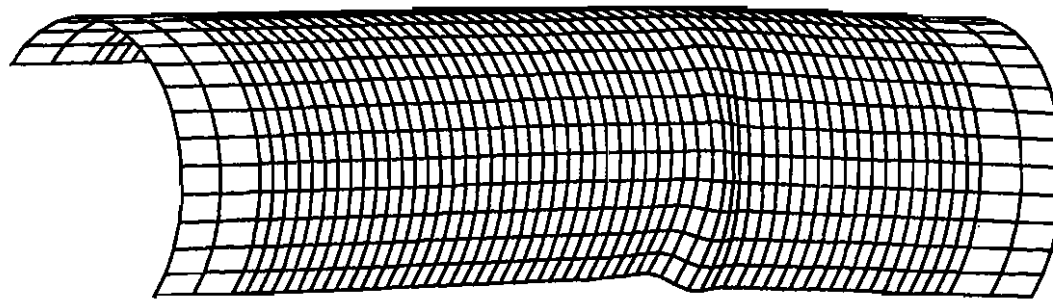
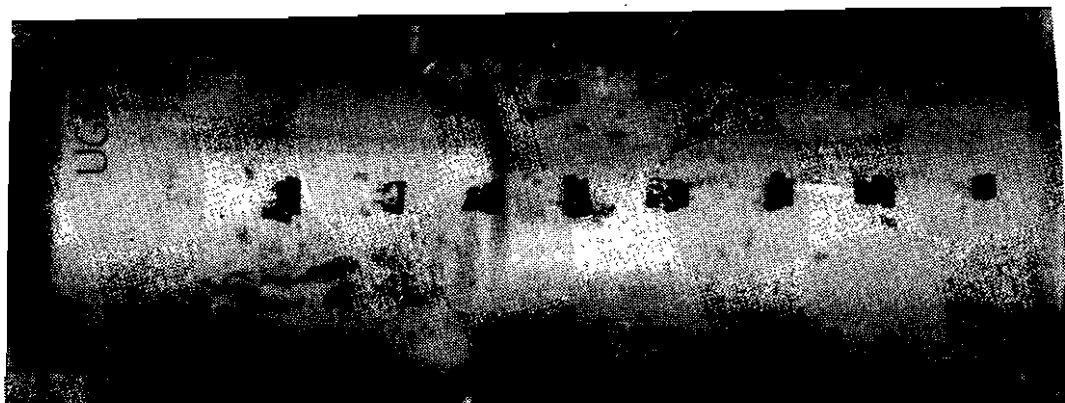


Figure 4.10 Deformed Configuration for Specimen UGA508

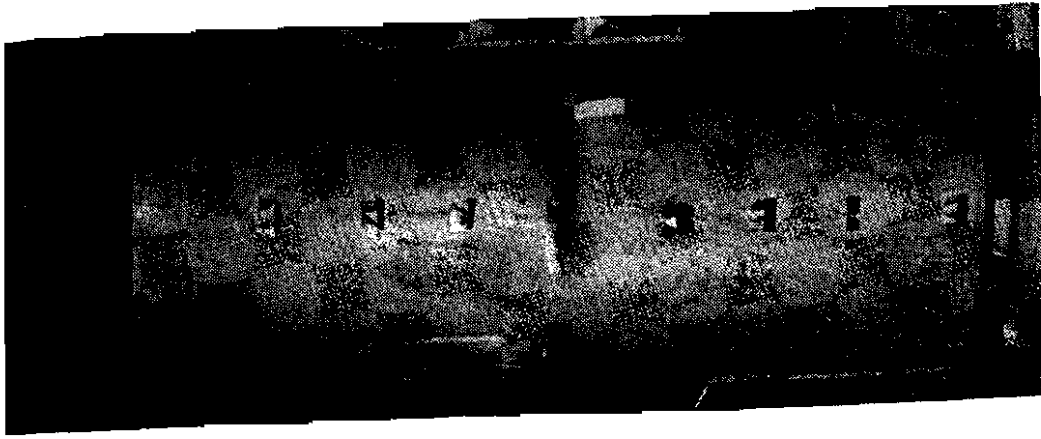
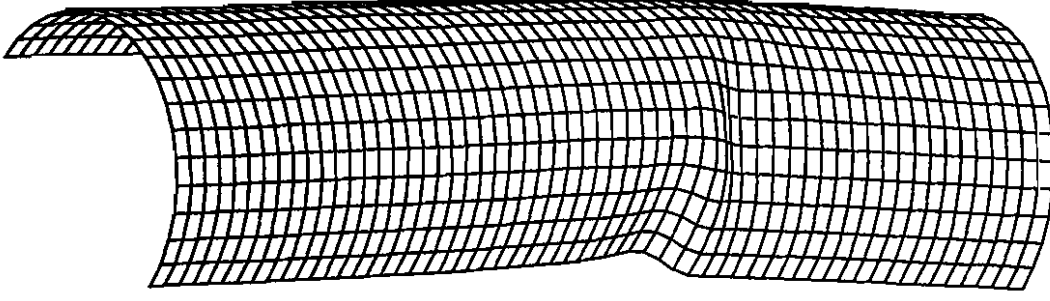


Figure 4.11 Deformed Configuration for Specimen UGR508

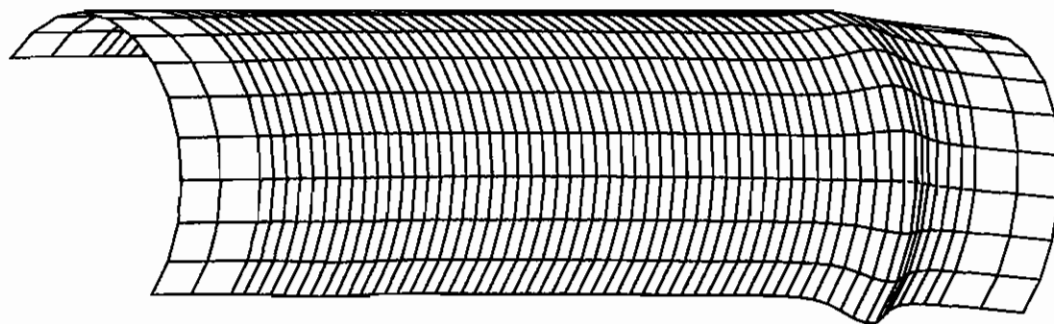


Figure 4.12 Deformed Configuration for Specimen DGA508

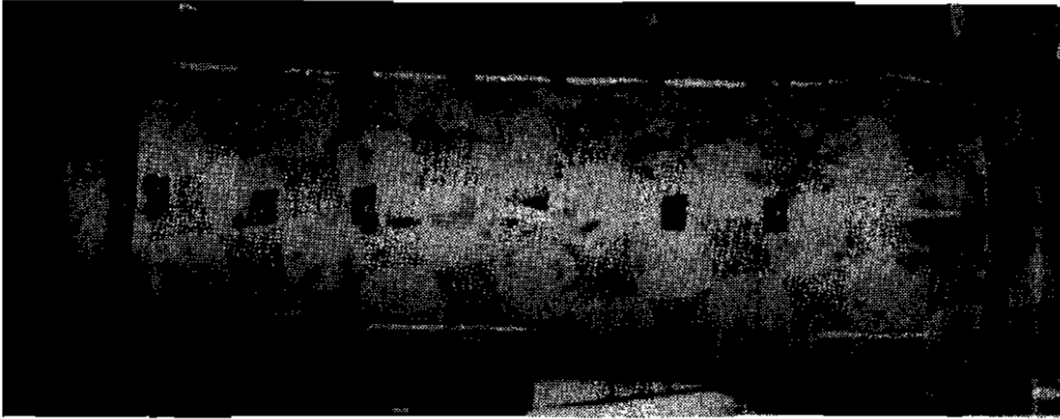
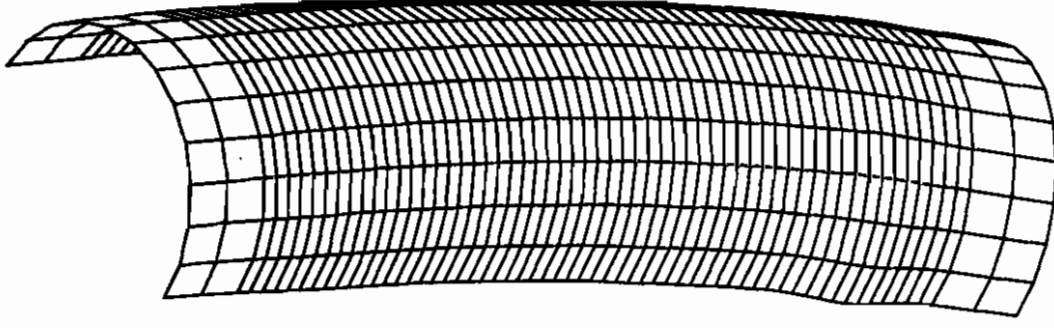


Figure 4.13 Deformed Configuration for Specimen DLR508

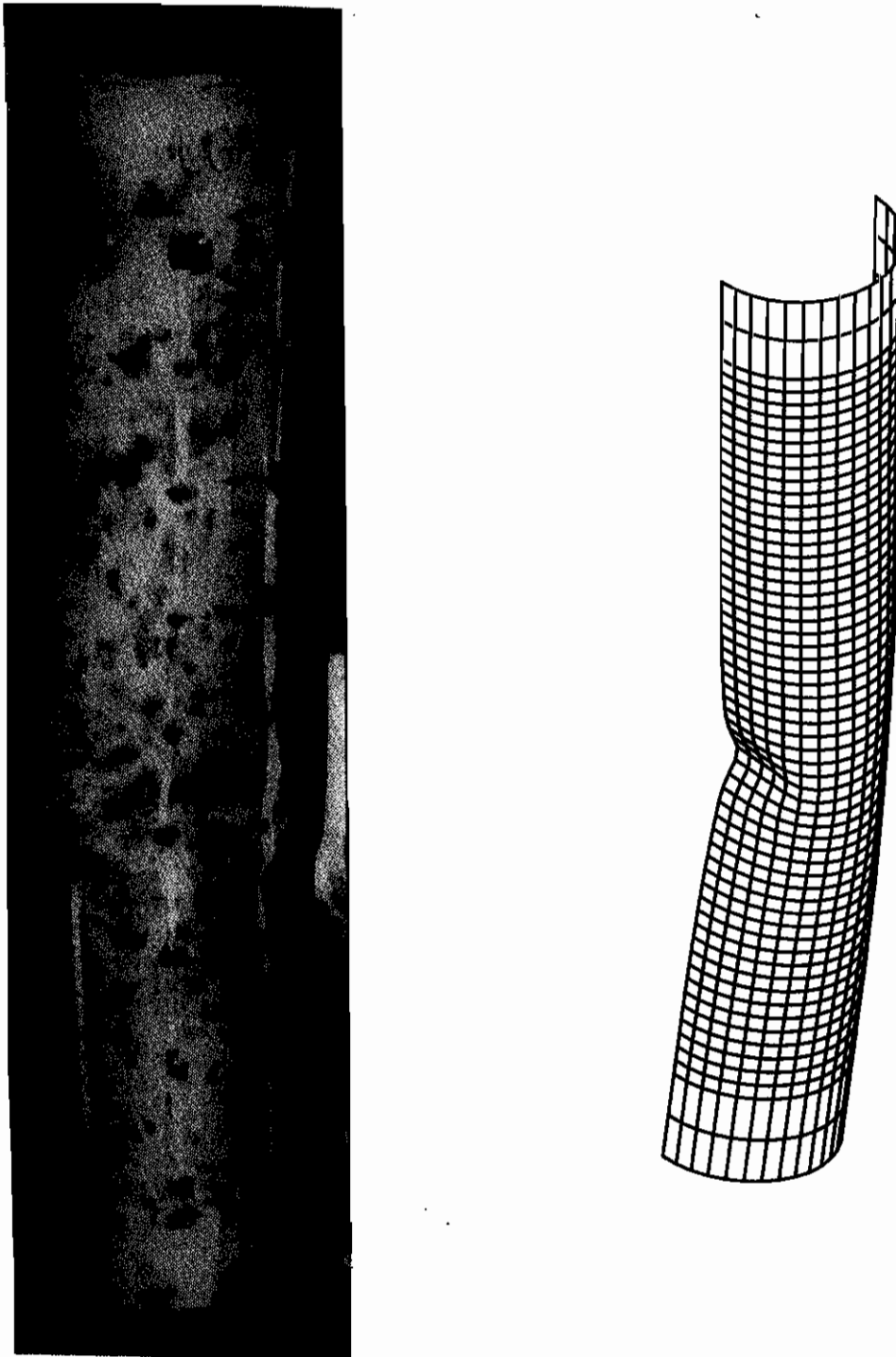


Figure 4.14 Deformed Configuration for Specimen UGA324

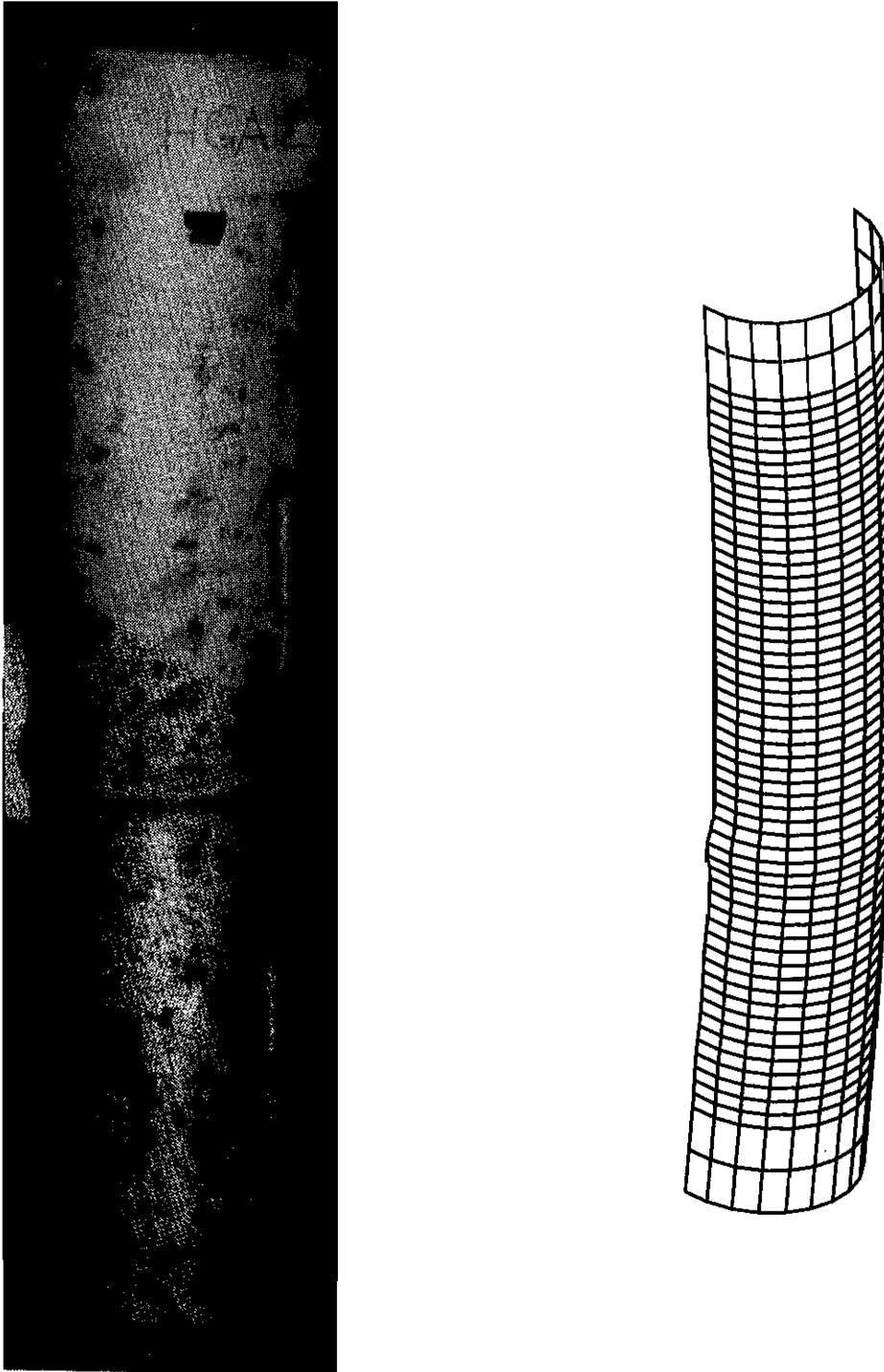


Figure 4.15 Deformed Configuration for Specimen HGA324

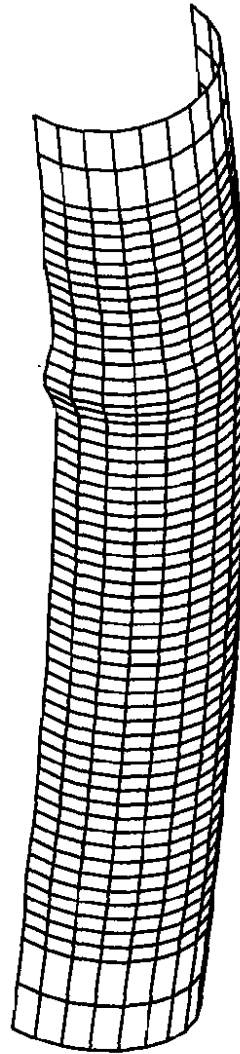
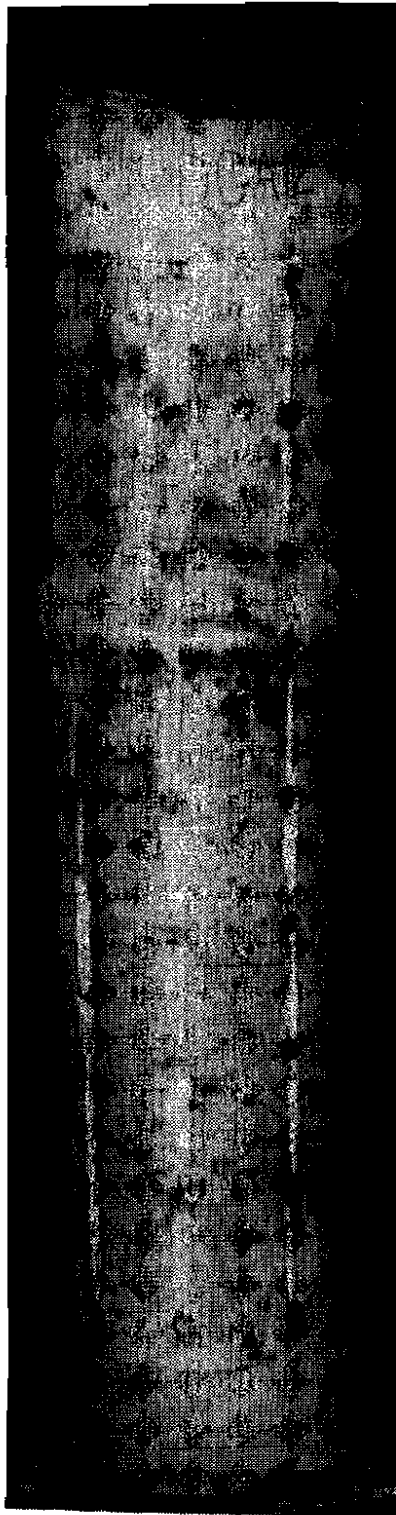


Figure 4.16 Deformed Configuration for Specimen DGA324

5. Parametric Study

5.1 Parameters Influencing Pipe Behavior

In this section, the parameters that are likely to influence the deformational behaviour of pipeline segments are presented. Three categories of parameters are identified; those describing pipe geometry, those defining the material constitutive law, and those describing pipe loading history.

The parameters defining the pipe geometry are the pipe length (L), the outside diameter (OD), and the thickness (t). Parameters pertaining to the weld geometry (longitudinal, helical, or circumferential) are outside the scope of this research, and will not be considered.

An adequate representation of the material model of a pipe requires at least four parameters; the elasticity modulus (E), the Poisson's ratio (μ), the plasticity exponent (n) (see Chapter 2), and the yield strength (σ_y). A more accurate description of the material model could include a multi-linear representation of the expansion of the yield surface instead of using only using one parameter, the plasticity exponent, for this purpose.

During the operation of a buried pipeline, a pipe segment is subjected to an axial load due to the temperature differential (P_t) and an internal pressure that induces a hoop stress (σ_h) in the wall of the pipe, in addition to imposed rotations caused by differential settlement or slope movement. An additional action to which a pipe segment may be subjected is the change of the axial force caused by pipe extension due to the catenary action as the pipe is deformed. A description of the histories of the axial forces and those of the rotations at the ends of the pipe segment are necessary to accurately predict the pipe response.

Any chosen measure of deformation (e.g., longitudinal strain) becomes a function of a number of variables. Consequently one may write

$$\varepsilon = \varepsilon [OD, t, L, E, \mu, n, \sigma_y, P_t, \sigma_h, h_1(\theta_1), h_2(\theta_2), h_3(P_1), h_4(P_2)] \quad (5.1)$$

where $h_1(\theta_1)$ is the history of the imposed rotation at end 1 of the segment under examination, $h_2(\theta_2)$ is the history of the imposed rotation at end 2 of the segment, $h_3(P_1)$ is the history of the axial load at end 1, and $h_4(P_2)$ is the history of the axial load at end 2.

For pipeline steel, the elasticity modulus is assumed not to vary significantly from the nominal value of 207,000 MPa for all grades of steel. The Poisson's ratio does not vary significantly from 0.3. Therefore, these two parameters are not varied in the parametric study. For practical purposes, the list of variables reduces to

$$\varepsilon = \varepsilon [OD, t, L, n, \sigma_y, P_t, \sigma_h, h_1(\theta_1), h_2(\theta_2), h_3(P_1), h_4(P_2)] \quad (5.2)$$

For a given segment of pipe, the end rotation and axial load histories are problem dependent, and may be obtained from a soil-structure interaction modeling of the problem for any given differential settlement or landslide scenario (see Zhou, 1993). They depend on a number of factors, and will not be addressed in this study. Instead, the axial load in the pipe will be assumed constant (and equal to the combined effects of the temperature differential and Poisson's ratio effects) throughout the loading process. The end rotations will be applied monotonically and equally at both ends of the analyzed segment. These assumptions allow further simplification of Equation 5.2 to

$$\varepsilon = \varepsilon (OD, t, L, n, \sigma_y, P_t, \sigma_h) \quad (5.3)$$

5.2 Dimensional Analysis

Applying the Buckingham π theorem (Langhaar 1951), the eight terms of Equation 5.3 lead to six possible independent non-dimensional terms (π -terms). These are

$$\varepsilon, \frac{OD}{t}, \frac{L}{OD}, n, \frac{P_t}{\pi (OD-t)t\sigma_y}, \text{ and } \frac{\sigma_h}{\sigma_y}$$

where the combination of terms was carefully selected to give meaningful non-dimensional variables for use in current pipeline practice. For instance, the second term, the outside diameter to thickness ratio, is frequently used in the literature and often considered as a major descriptor of the local buckling behaviour of a cylinder. The fifth term is the ratio of the axial load corresponding to a given temperature differential, in a fully restrained pipe, to the axial yield load. The sixth term is the ratio of the hoop stress induced in the pipe wall as a result of the internal pressure to the yield strength.

Using the non-dimensional parameters thus defined, the number of variables involved in Equation 5.3 can be reduced to

$$\varepsilon = \varepsilon \left(\frac{OD}{t}, \frac{L}{OD}, n, \frac{P_t}{\pi (OD-t)t\sigma_y}, \frac{\sigma_h}{\sigma_y} \right) \quad (5.4)$$

Since this study is only concerned with local buckling and not with overall buckling or any possible interaction between the two buckling modes, the length of pipe segment analyzed will be maintained constant and equal to three diameters for the finite element runs in the parametric study. A length of three diameter is chosen so as to provide enough length for local buckles to fully develop away from the ends of the specimens.

The plasticity exponent varies according to the grade of steel used. Its magnitude may be determined from curve-fitting of tension coupon test results for different grades of steel. This factor may influence the deformational behaviour of pipelines, and it should play a part in a comprehensive parametric study. However, in order to keep the parametric study to a manageable size, only the value of the plasticity exponent as obtained from the stress vs. strain curves of X52 materials (see Chapter 2) will be used in the finite element runs in this parametric study. These two simplifications lead to the following relationship

$$\varepsilon = \varepsilon \left(\frac{OD}{t}, \frac{P_t}{P_y}, \frac{\sigma_h}{\sigma_y} \right) \quad (5.5)$$

in which P_y is the axial yield load of the pipe.

5.2.1 Non-Dimensional Parameters Studied

The parametric study presented in this chapter focuses on the effect of the three non-dimensional parameters in the right hand side of Equation 5.5 upon deformation limits for buried pipelines. The non-dimensional parameter OD/t will be given one of three values that lie in the practical range of pipe geometries: these are 51, 77 and 100.

In practice, temperature differentials lie between 30 C° (inducing tensile force in the pipe) and -45 C° (inducing compressive force). Therefore, the values of P_t/P_y were selected to correspond to those associated with these differential temperature bounds, along with a third value corresponding to a temperature differential at mid-range. These temperature differentials correspond to values of P_t/P_y of 0.195, -0.049, and -0.293 for an X52 material, where the minus sign identifies compressive axial forces.

The term σ_h/σ_y is given the values 0.0, 0.36, and 0.72. These correspond to the extreme pressure magnitudes (and a mid-range value) as allowed in pipelines according to the Canadian code for oil pipeline systems CAN/CSA Z183-M84 (Canadian Standard Association, 1984).

5.2.2 Scope of the Study

The results of this study are not intended to be applicable for all grades of steel. They are applicable only for steel grades possessing a plasticity exponent close to that of an X52 material pipe, as measured in the experimental component of this study.

5.2.3 Notation for the Parametric Runs

Each finite element run in the parametric study is denoted by an identifier of the form nnXttHhh. The term nn denotes the diameter to thickness ratio and takes the values 51, 77, and 100. The character group Xtt denotes the temperature differential for the run. The letter X is either C (if the temperature differential induces a compressive force in the pipe) or T (if the force is tensile). The number tt takes on the values of 45, 7.5, and 30, denoting the magnitude of the temperature differentials in degrees Celsius. The character group Hhh takes on one of the values H00, H36, or H72. The last two digits denote the magnitude of the hoop stress as a percentage of the specified minimum yield strength. The actual pipe sizes were selected based on the geometry of the pipes currently produced by manufacturers in Canada. The three cross section geometries selected were 324 mm OD x 6.35 mm, 610 mm OD x 7.92 mm, and 711 mm OD x 7.11 mm.

5.3 Analytical Model for the Parametric Study

5.3.1 Material Model

All the specimen models are assumed to be of X52 grade steel. In order to force the buckle to occur away from the ends of the pipe segment, a length of 0.23 OD at each of the ends of the specimen is assumed to remain elastic. The elastic properties of the end portions of the model are identical to the elastic properties of the X52 material.

5.3.2 Finite Element Mesh

The element used in the parametric study is ABAQUS' S4RF, the same as that used in the verification runs presented in Chapter 4. The mesh consists of 18 elements around half of the circumference and 40 elements in the longitudinal direction. Only a longitudinal half of the specimen is modeled, thereby taking advantage of symmetry. Every node has five degrees of freedom, as described in Chapter 4. (The deformed meshes are shown in Figures 5.26 to 5.28).

5.3.3 Loading Sequence

The axial load is applied first and maintained constant. Then, if applicable, the internal pressure is introduced and kept constant throughout deformation. Finally, equal and opposite rotations at both ends are applied, such that the specimen is subjected to monotonically increasing single curvature.

5.3.4 Boundary Conditions

5.3.4.1 *Boundary Conditions of Pipes in the Field*

In Chapter 4, the finite element runs were performed with boundary conditions such that the ends of pipe segments remained perfectly circular throughout deformation. While this assumption accurately describes the kinematics of the tested specimens, it is not necessarily representative of a typical pipe deformation condition in the field. In the field, the end cross sections of a buckled segment of pipe have some freedom to undergo in-plane deformations (ovalization). Also, at a distance far enough from the location of a buckle in the field, the pipe cross section would remain plane throughout deformation and would be expected to behave in an elastic manner. These latter boundary conditions have been adopted for the parametric study. The way these boundary conditions are mathematically expressed is outlined in the next section.

5.3.4.2 *Modeling of Boundary Conditions*

The boundary conditions on the end of the specimens are modeled as follows. The reader should refer to Figure 5.1 for the notation and reference axes

- (a) The boundary conditions on the longitudinal vertical plane of symmetry of the specimens are such that, for all nodes on the extreme compression fiber and extreme tension fiber, the following conditions hold true:

$$u_2^{EX} = 0 \quad (5.6)$$

$$\theta_1^{EX} = 0 \quad (5.7)$$

$$\theta_3^{EX} = 0 \quad (5.8)$$

where the superscript *EX* denotes all the nodes on the extreme compression and extreme tension fibers (see Figure 5.1). Subscripts 1, 2, and 3 denote the global directions of displacements *u* and the finite rotations θ .

- (b) It is convenient to relate the nodal displacements and rotations at the top end of the specimen to the displacements and rotations of a fictitious point *CT*, originally located at the geometric centroid of the top cross section of the specimen (see Figure 5.1). Point *CT* is free to move in the vertical direction (global-3 direction) and rotate about the axis of bending (global-1 direction). The other components of displacement and rotation at point *CT* are restrained, as expressed in the following the relations:

$$u_1^{CT} = 0 \quad (5.9)$$

$$u_2^{CT} = 0 \quad (5.10)$$

$$\theta_1^{CT} = 0 \quad (5.11)$$

$$\theta_3^{CT} = 0 \quad (5.12)$$

where the superscript in Equations 5.9 through 5.12 denote quantities pertaining to fictitious point *CT*.

The nodes at the top edge of the specimen remain in one plane throughout deformation. Their displacement and rotation components are related to the degrees of freedom of point *CT* through the following constraints:

$$\theta_2^{ni} = \theta_2^{CT} \quad (5.13)$$

$$u_3^{nt} = u_3^{CT} + d^{nt} \sin(\theta_2^{CT}) \quad (5.14)$$

where superscript nt denotes any of the nodal points at the top edge of the specimen. Distance d^{nt} is the projection of a vector joining point CT and nodal point nt , as depicted in Figure 5.1. Expressing d^{nt} in Equation 5.14 in terms of the undeformed coordinates and nodal displacements of points CT and nt , the following relation is obtained:

$$u_3^{nt} = u_3^{CT} + \sqrt{\left[(X_1^{nt} + u_1^{nt}) - X_1^{CT}\right]^2 + \left[(X_3^{nt} + u_3^{nt}) - X_3^{CT}\right]^2} \sin(\theta_2^{CT}) \quad (5.15)$$

where symbols X_1^{nt} and X_3^{nt} denote the coordinates of nodes nt in the undeformed configuration in the global-1 and global-3 directions, respectively.

- (c) In a similar fashion, it is convenient to relate the nodal displacements and rotations at the bottom edge of the specimen to the displacements and rotations of a fictitious point CB , originally located at the geometric centroid of the bottom cross section of the specimen. Point CB is free to rotate about the axis of bending (global-1 direction). The other components of displacement and rotation at point CB are restrained as expressed in the following the relations.

$$u_1^{CB} = 0 \quad (5.16)$$

$$u_2^{CB} = 0 \quad (5.17)$$

$$u_3^{CB} = 0 \quad (5.18)$$

$$\theta_1^{CB} = 0 \quad (5.19)$$

$$\theta_3^{CB} = 0 \quad (5.20)$$

where superscript CB denotes the centroid of the bottom cross section. End rotation θ_2^{CB} is assigned a monotonically increasing imposed rotation equal to θ_2^{CT} with an opposite sign.

The nodes at the bottom edge of the specimen remain in one plane throughout deformation. Their displacement and rotation components are related to the degrees of freedom of point CB through the following constraints:

$$\theta_2^{nb} = \theta_2^{CB} \quad (5.21)$$

$$u_3^{nb} = -\sqrt{\left[\left(X_1^{nb} + u_1^{nb}\right) - X_1^{CB}\right]^2 + \left[\left(X_3^{nb} + u_3^{nb}\right) - X_3^{CB}\right]^2} \sin(\theta_2^{CB}) \quad (5.22)$$

where superscript nb denotes all the nodes at the bottom edge of the specimen. The distances X_1^{nb} and X_3^{nb} are the coordinates of nodes nb in the undeformed configuration in the global-1 and global-3 directions, respectively.

The boundary conditions described in Sub-Section 5.3.4.2 were coded into a FORTRAN subroutine and appended to ABAQUS, where they were enforced using Lagrangian multipliers.

5.3.5 Gage Length

The magnitude of the average moment, average curvature, and average compressive strain of a pipe segment in the post-buckling range of deformation are dependent on the length of the segment considered (Yoosef-Ghods et al., 1995). It is therefore important to specify the length of pipe considered in the computation of these quantities. In order to contain the complete strain localization, the length of pipe chosen must be equal to or exceed the length of buckle in the pipe. For all loading conditions investigated in this research, the length of local buckle in the pipe did not exceed one diameter in length.

Therefore, a gage length of one diameter that includes the entire local buckle was adopted in the computations of the results presented in this chapter.

5.3.6 Local Curvature

For a given gage length of a pipe segment, of length d_o in the undeformed configuration, the average curvature is computed using the following procedure. A plane is fitted through the position of nodes in the deformed configuration of each of the end cross sections (originally spaced at a distance d_o) through linear regression analysis. The direction cosines of the normals to the planes are determined. The coordinates of the geometric centroid of the end cross sections are determined as described in Section 5.3.7, and the straight line distance d between the two centroids is calculated. The average curvature can be computed approximately as:

$$\varphi_l = \frac{1}{R} = \frac{2 \sin(\theta_l / 2)}{d} \quad (5.23)$$

where φ_l is the local curvature, R is the average radius of curvature, and θ_l is the angle between the two normals at the planes passing through the end cross sections of the segment.

The average global curvature is the curvature based on the whole length of the specimen considered (based on a three-diameter length).

5.3.7 Computation of Internal Moments

At any stage of deformation, the internal bending moment acting on a pipe cross section lying at the transverse boundary of two adjacent layers of finite elements is computed according to the following procedure. The coordinates of the geometric centroid of the cross section in the deformed state are computed as:

$$\bar{x}_{c.g.} = \sum_{i=1}^{i=n} \frac{x_i}{n} \quad (5.24)$$

$$\bar{y}_{c.g.} = 0 \quad (5.25)$$

$$\bar{z}_{c.g.} = \sum_{i=1}^{i=n} \frac{z_i}{n} \quad (5.26)$$

where the summations are performed for all the nodes at the cross section considered, n is the number of nodes at the cross section, terms $\bar{x}_{c.g.}$, $\bar{y}_{c.g.}$, $\bar{z}_{c.g.}$ are the coordinates of the geometric centroid in the deformed configuration, and terms x_i , y_i , z_i are the coordinates of point i of the cross section. The coordinates x , y , and z correspond to the 1, 2, and 3 directions, respectively, in Figure 5.1.

The equivalent nodal forces and moments f_x , f_y , f_z , m_x , m_y and m_z at the nodes of each finite element are output by the program, where subscripts x , y and z denote the global directions. The internal moment M_i at a given cross section is computed as:

$$M_i = \sum_e \sum_n \left[m_{y_n}^e + f_{z_n}^e (x_n^e - \bar{x}_{c.g.}) - f_{x_n}^e (z_n^e - \bar{z}_{c.g.}) \right] \quad (5.27)$$

where the first summation is over all the elements (denoted by the identifier e) on one side of the cross section, the second summation is over each node n that lies on the cross section (nodes 1 and 2, or 3 and 4 depending on the location of the cross section with respect to the layer of elements), and x_n^e and z_n^e are the coordinates of node n of element e in the deformed configuration.

The average value of the local internal moments computed from the element nodal forces acting at nodes located on the transverse lines of element boundaries over a length of pipe of one diameter, including the buckled segment, will be referred to as the average local

moment. This moment will be used in the local moment vs. local curvature relationships in the moment diagrams to be presented in Section 5.5.3.

The end moments of the specimens are obtained as reactive quantities output by the analyses.

5.3.8 Selection of a Longitudinal Strain Measure

Several definitions of compressive strains are possible. The strain definition is length dependent. The compressive strain measure adopted is based on fibers with an initial length of one diameter. The longitudinal strain expression used is

$$\varepsilon = \frac{L_d - L_o}{L_o} \quad (5.28)$$

where L_o is the distance between the end points of the extreme compression fiber, at mid-surface. (For a segment length of one diameter, this distance would be equal to a diameter). The length L_d is the distance on a straight line between the same two points, in the deformed configuration.

5.3.9 Limiting Strain Criteria

No industry consensus on the definition of deformation limit state criteria seems to exist currently. However, it seems desirable to relate any proposed deformation criterion to a measure of longitudinal strain. The longitudinal compressive strains corresponding to different criteria are used in this research. These criteria are defined in the following sections.

5.3.9.1 Limit Point Strain

The limit point (the peak point in a moment vs. curvature relationship) is a limit state that has been used by a number of researchers as a deformation limiting point. Although there is little justification for the selection of this point as a deformation limit for a buried pipe,

it seems to be the most widely accepted deformation limit criterion in current pipeline practice (see Section 1.5.1.3). The limit point is dependent on the length of the pipe segment. Therefore, the length of the pipe segment has to be specified for a complete definition of a deformation limit state. Defining the longitudinal compressive strain as in Section 5.3.8, the local moment as in Section 5.3.7, and the local curvature as in Section 5.3.6, the limit point strain is defined as *the longitudinal compressive strain corresponding to the peak point in an average local moment vs. average local curvature curve based on a gage length of pipe of one diameter that includes one complete wave of local buckling.*

5.3.9.2 Strain Corresponding to 95% Peak Moment

In all the cases studied in this chapter, the local moment vs. local curvature exhibits a peak value of moment after which the slope of the curve becomes negative. The steeper the negative slope, the more susceptible is the buckled segment to undergo large local deformations for small increases of imposed curvature.

One of the shortcomings of the limit point strain criterion is that it does not take into consideration the effect of the moment curvature slope in the post-buckling range of deformation in determining the critical strains. Defining the longitudinal compressive strain as in Section 5.3.8, the local moment as in Section 5.3.7, and the local curvature as in Section 5.3.6, we define the longitudinal compressive strain corresponding to 95% moment capacity as *the longitudinal compressive strain corresponding to a moment in the post-buckling range of deformation equal to 95% of the peak moment in an average local moment vs. average local curvature relationship, based on a gage length of pipe of one diameter that includes one complete wave of local buckling.*

5.3.9.3 Limitations of Strain Criteria Based on Moment Capacity

The two deformation criteria defined in Sub-Sections 5.4.9.1 and 5.4.9.2 were based on the fact that moment vs. curvature diagrams possess a peak moment value, after which

the pipe segment exhibits softening. Although this assumption appears to be valid for cases in which the axial load is maintained constant throughout deformation, it is not necessarily true when the axial load decreases as the specimen is deformed. An example illustrating this case is Specimen DLR508 (Figure 4.6). The specimen does not reach the limiting strains according to the criteria suggested in Sub-Sections 5.3.9.1 and 5.3.9.2. However, an outward bulge was observed at the bottom of the specimen around the end of the test (Figure 4.13). More general criteria for limiting deformation are needed. Such deformation criteria should be solely based on the deformational behaviour of the specimen, regardless of its moment carrying capacity (Zhou and Murray, 1993). Two local conditions that may hinder the functionality of the pipeline are excessive ovalization and excessive hoop strains. Limits for these conditions are suggested in the following sub-sections.

5.3.9.4 Strain Limit at 15% Ovalization

The ovalization of a pipe cross section was defined in Chapter 1 as $(D - D_{min})/D$. The need for limiting the ovalization of a pipe cross section arises because excessive inward buckling may prevent the passage of inspection devices through the interior of the pipeline, thereby causing operational problems. Acceptable limits for ovalization are dependent upon pipe and inspection device geometries, and are case dependent. However, in the absence of particular information for specific cases, the present limits of ovalization in the current pipeline practice (see Section 1.5.2) are adopted here as a deformation limit state. For inward and outward buckles, these are

$$\frac{D - D_{min}}{D} \leq 0.15 \quad (5.29)$$

$$\frac{D - D_{min}}{D} \leq 0.06 \quad (5.30)$$

respectively.

For all 18 pressurized cases in this parametric study, local buckling took place in the form of outward bulges and in no case did ovalization exceeded 0.03. Therefore, for pressurized pipes, the 0.06 limit does not seem to be attainable in practical situations.

For all nine unpressurized cases of the study inward buckles were formed, however, and the 0.15 limit was attained within the range of deformation analyzed. Therefore, the 0.15 limit can be considered as a limiting value of ovalization for inward buckling. Defining the longitudinal compressive strain as in Section 5.3.8, the strain limit at 15% ovalization is defined as *the longitudinal compressive strain corresponding to an ovalization of the pipe cross section of 0.15 at the point of maximum distortion, when the pipe cross section exhibits inward buckling.*

5.3.9.5 Strain Limit at 8 % Hoop Strain

For an outward bulging mode of buckling, a deformation limit condition can take place when the hoop strains at the crest of a wrinkle reach limiting values of steel ductility as specified in the Canadian code for steel line pipe CAN/CSA -Z245.1- M90 (Canadian Standard Association, 1990).

Clause 8.2.2.5 of the code states that, "*For tests of longitudinal, helical, and skelp end welds of submerged arc welded pipe, the elongation in 50.8 mm shall be a minimum of 10%.*" The gage length must include the weld and the necking region.

Clause 8.2.1.1 specifies the required transverse ductility of the pipe material for welded pipes 219.1 mm OD or larger, in accordance with the grade of the steel and the cross-sectional area of the coupon, as

$$E_l = 1940 \frac{A_c^{0.20}}{\sigma_y^{0.90}} \quad (5.31)$$

where E_l is the elongation as a percentage of a 50.8 mm gage length of the tension coupon, σ_y is the specified yield strength, and A_c the cross sectional area of the tension coupon.

For a combination of $\sigma_y = 550$ MPa and $A_c = 30 \text{ mm}^2$, the required value of E_l as determined by Equation 5.31 is 12%. Therefore, the ductility limit of a welded pipe material appears to be governed by the requirement of Clause 8.2.2.5.

The percentage elongation from tension coupon tests is measured after fracture. A safe design necessitates that necking be prevented, and it is assumed that the material can undergo 80% of the minimum ductility specified at fracture without experiencing necking. Thus, for all grades of steel and pipe thicknesses, hoop strains can reach a value of 8% without the pipe material exhibiting necking.

In all the runs of this parametric study, it has been found that values of transverse tensile strain in the neighborhood of the 8% are attained only for outward bulge cases. Defining the longitudinal compressive strain as in Section 5.3.8, the strain corresponding to an 8% hoop strain is defined as *the longitudinal compressive strain corresponding to a transverse hoop strain of 8% at the crest of the buckle when the pipe cross section exhibits outward bulging.*

5.3.10 Selection of a Design Limiting Strain

One of the purposes of this research is to propose design limits based on finite element runs for each of the previously defined limiting strains. The selection of particular deformation limit criteria for design purposes is left to the designer. However, it is the opinion of the writer that, for buried pipelines, the strain corresponding to 0.15 ovalization (for diamond shape buckles) and that corresponding to a 0.08 hoop strain (for outward bulge buckles) provide a more justifiable rationale than that based on local moment vs. curvature diagrams.

5.4 Plastic Moment Capacity

The attainment of the maximum moment in a pipe cross section does not necessarily produce failure in a buried pipeline. However, in many situations, fully plastic moment capacity is a good approximation of the maximum moment that the pipe can sustain. Furthermore, if it can be shown that, within specific ranges of the parametric variables, the fully plastic moment is a good approximation of the limit point moment for a pipe that buckles locally, then the maximum moment capacity of the pipe can be estimated satisfactorily by Equation 3.10. This would eliminate the need to carry out complex finite element analyses in order to establish the limit point moment for the pipe.

A number of possible applications might then be possible. Some of these are:

1. For elevated pipe, the limit point represents a failure condition that can trigger collapse of the line.
2. A lower bound on the curvatures at the limit moment can be established quickly and easily by assuming elastic response up to the fully plastic moment capacity. This bound may be sufficient to eliminate the cause for concern associated with observed curvatures on buried pipelines in field situations.
3. Non-dimensionalized moment vs. curvature curves in which the fully plastic moment and the associated elastic curvature at this value are used as non-dimensionalizing values, are a common way of synthesizing behavioral characteristics of structural elements. Examination of such relationships over a range of pipe parameters may permit the limit point curvatures (i.e., those for the initiation of softening) to be estimated in a simple manner.

The following developments are intended to facilitate the exploration of such possibilities.

5.4.1 Interaction Diagrams

Figures 5.2 through 5.4 give the interaction diagrams for the 324 mm OD x 6.35 mm, the 610 mm OD x 7.92 mm, and the 711 mm OD x 7.11 mm pipe cross sections that were used with the parametric finite element runs. The material was grade X52 steel ($\sigma_y = 377.4 \text{ MPa}$). Each plot has three interaction curves, one for each of three different values of the internal pressure used, i.e., $\sigma_h/\sigma_y = 0.0, 0.36, \text{ and } 0.72$.

The curves are evaluated using Equation 3.10. Superimposed on each curve are three points based on the results of the runs of the finite element parametric study. The closeness of the points to the appropriate curve gives an indication of the agreement between the plastic moment of the cross section predicted by Equation 3.10 and the moment at the limit point from the finite element results. For the three cross sections studied, the best agreement is obtained for half-pressurized conditions. In general, finite element analyses yielded slightly higher values of plastic moments for fully pressurized cases and slightly lower values for unpressurized cases. This may be explained by the fact that the strain values at the limit points for pressurized cases are higher than unpressurized ones. Therefore, the effect of strain hardening is more pronounced in the case of fully pressurized pipes. The overestimation of moment capacity by the interaction curves (as compared to finite element results) is always less than 15% (for 77C45H72).

5.4.2 Non-Dimensional Interaction Diagram

It is possible to consolidate all of the curves in Figures 5.2 to 5.4 onto one non-dimensional interaction diagram that will be valid for all cross section geometries, internal pressures, and axial load combinations. The non-dimensional form of this interaction equation is given by Equations 3.12 through 3.14 and is plotted in Figure 5.5. The non-dimensional axial forces and corresponding non-dimensional moments obtained from the 27 runs of the parametric study are superimposed on the interaction curve.

The closeness between the points representing the finite element runs and the curve indicates sufficiently good agreement between the limit moments predicted by the finite element analysis and the fully plastic capacities predicted by Equation 3.12 to 3.14. Thus, these equations may be considered satisfactory for the purpose of estimating maximum moment capacities for design.

5.4.3 Local Moment vs. Local Curvature Relationships

Figures 5.6 through 5.8 give the local moment (as defined in Section 5.4.4) vs. local curvature (as defined in Section 5.4.2) for the runs having a diameter to thickness ratio of 51, 77, and 100, respectively. For all three cross section geometries studied, pipe segments exhibit more rotation capacity as the magnitudes of both the internal pressure and the axial tensile force acting on the pipe increase.

5.4.4 Non-Dimensional Moment vs. Curvature Relationships

At a given ratio of hoop stress, local moments can be normalized with respect to the fully plastic moment capacity, $M_{\sigma_h, max}^p$, as predicted by Equation 3.11. The elastic curvature corresponding to $M_{\sigma_h, max}^p$ is given by $M_{\sigma_h, max}^p / EI$, where E is the elasticity modulus and I the moment of inertia of the pipe cross section. Moments and curvatures in Section 5.4.5 are normalized with respect to $M_{\sigma_h, max}^p$ and $M_{\sigma_h, max}^p / EI$, respectively.

5.4.5 Parametric Study for Moment Capacity

Nine non-dimensional local moment vs. local curvature diagrams are presented in Figures 5.9 through 5.11. The grouping of the diagrams is such that only one of the three non-dimensional parameters OD/t , P_t/P_y , and σ_h/σ_y is varied, the two others being held constant in the figure.

The initial slope is the same for all cases, since the stiffness of the pipe segment is the elastic stiffness. As deformation progresses, the slope of the moment vs. curvature

deviates from the original slope and lessens until it reaches the limit point (the point of zero slope), after which the curve exhibits a negative slope.

The non-dimensional moment vs. curvature diagrams of the pipe segment exhibit a lesser slope in the post-buckling range as the diameter to thickness ratio decreases (Figure 5.9). Consistent with the results presented in Section 5.4.3, the ability of a pipe to retain its peak moment capacity increases as the tensile axial force increases, i.e., as the compressive axial force decreases (Figure 5.10) and as the hoop stress ratio increases (Figure 5.11).

In all cases, the limit point takes place at curvatures larger than the elastic curvature corresponding to $M_{\sigma_0, max}^p$. This is due in part to the gradual yielding in accordance with the pipe material behaviour (Figures 2.10 to 2.13) but primarily the result of the penetration of the yielding into the cross section as the specimen is subjected to monotonically increasing imposed curvature.

The magnitude of the non-dimensionalized curvature corresponding to the limit point increases as the diameter to thickness ratio decreases (Figure 5.9). Also, it increases with the increase in tensile axial load (Figure 5.10) and with the increase of the hoop stress ratios (Figure 5.11).

The ratio of the finite element moment capacity to that predicted by Equation 3.10 increases as the D/t ratio decreases (Figure 5.9). It increases as the tensile axial force to the yield axial load increases (Figure 5.10), and as the hoop stress ratio increases (Figures 5.2, 5.3, 5.4 and 5.11). The latter factor seems to be the most significant one.

5.4.6 Moment Capacity for Elevated Pipelines

Table 5.1 gives the ratio of the moment capacities as predicted by the finite element runs to those predicted by Equation 3.10. Overall, both values are equal since the average value of $M/M_{\sigma_0, p_e}^p$ is unity. However, there is a scatter in the agreement of the two

values depending on the load combinations considered. For the runs performed in this study, the $M_{FEA}/M_{\sigma_0, p}^p$ ratio ranged from 0.85 to 1.29 with a standard deviation of 0.09. Graphical representations of these results are given in Figure 5.5 and in Figure 5.12.

A closer prediction of the actual moment capacity M_{cap} can be obtained by introducing a function f such that

$$\frac{M_{cap}}{M_{\sigma_0, p}^p} = f\left(\frac{OD}{t}, \frac{P_{tot}}{P_y}, \frac{\sigma_h}{\sigma_y}\right) \frac{M_{FEA}}{M_{\sigma_0, p}^p} = 1 \quad (5.32)$$

where f is a correction function, P_{tot} is the total internal axial force in the pipe wall

$$P_{tot} = P_{imp} + P_{\mu} \quad (5.33)$$

and P_{μ} is the axial load resulting from the Poisson's ratio effect for hoop stresses as defined in Equation (2.2). The moment capacity M_{cap} is given by

$$M_{cap} = M_{\sigma_0, p}^p f\left(\frac{OD}{t}, \frac{P_{tot}}{P_y}, \frac{\sigma_h}{\sigma_y}\right) \quad (5.34)$$

In order to satisfy Equation (5.32) at all the points corresponding to all the finite element parametric runs, a twenty-seven constant function f is needed. Using the findings of Section 5.4.5 on the effect of OD/t , P_{tot}/P_y , σ_h/σ_y on $M/M_{\sigma_0, p}^p$, a simplified form for the function f may be assumed as:

$$f\left(\frac{OD}{t}, \frac{P_{tot}}{P_y}, \frac{\sigma_h}{\sigma_y}\right) = f_1\left(\frac{t}{OD}\right) \times f_2\left(\frac{P_{tot}}{P_y}\right) \times f_3\left(\frac{\sigma_h}{\sigma_y}\right) \quad (5.35)$$

The functions f_1, f_2 , and f_3 are assumed to take on the simplest possible form i.e., to have a linear variation with the variables $t/OD, P_{tot}/P_y, \sigma_h/\sigma_y$, respectively. This leads to the following form of the function f

$$f = C_1 \left[1 + C_2 \left(\frac{t}{OD} \right) \right] \left[1 + C_3 \left(\frac{P_{tot}}{P_y} \right) \right] \left[1 + C_4 \left(\frac{\sigma_h}{\sigma_y} \right) \right] \quad (5.36)$$

where C_1, C_2, C_3 and C_4 are constants to be determined by regression analysis. They are selected such that they minimize the function.

$$\sum_{r=1}^{r=27} \left\{ \left(\frac{M}{M_{\sigma_0, P_t}^P} \right)_r C_1 \left[1 + C_2 \left(\frac{t}{OD} \right)_r \right] \left[1 + C_3 \left(\frac{P_{tot}}{P_y} \right)_r \right] \left[1 + C_4 \left(\frac{\sigma_h}{\sigma_y} \right)_r \right] - 1 \right\}^2$$

where the summation is performed over the 27 FEA runs, and the subscript r denotes the number of the run.

The minimization process was performed using the Solver utility in the program package Microsoft Excel 5 and the function f determined accordingly. Using the expression of function f , Equation 5.16 can be written as

$$M_{cap} = 1.20 \left[1 - \left(\frac{7.3t}{OD} \right) \right] \left[1 - 0.038 \left(\frac{P_{tot}}{P_y} \right) \right] \left[1 - 0.195 \left(\frac{\sigma_h}{\sigma_y} \right) \right] M_{\sigma_0, P_t}^P \quad (5.37)$$

The values of M_{cap} as computed from Equation 5.36 using the form in Equation (5.37) are given in the last column of Table 5.1. Equation (5.36) has an average value of $M_{cap}/M_{\sigma_0, P_t}^P$ of 1.0 and a standard deviation 0.05. This indicates that the scatter in the results based on Equation (5.36) is less than that based on the equation $M_{cap} = M_{\sigma_0, P_t}^P$, with M_{σ_0, P_t}^P evaluated from Equation 3.10 that has a standard deviation of 0.09. On the

other hand, the most unconservative estimate of Equation 5.36 is $0.80M_{\sigma,P}^p$ rather than $0.85M_{\sigma,P}^p$. This will probably make equation 5.36 less appealing to designers than Equation 3.10.

5.5 Deformation Limit State Equations

Using the deformation criteria defined in Section 5.3 deformation limits are proposed in this section. The results of the finite element parametric runs are presented in Table 5.2 and the proposed equations are obtained by regression analysis of these results. Where equations are devised to approximate the finite element results, an assessment of the quality of agreement between the two sets of values is presented. The assessment is based on the average value and the standard deviation of the error. A measure of the correlation in the obtained equation is provided by the coefficient of determination r^2 (Wesolowsky, 1976) defined as

$$r^2 = 1 - \frac{\sum_{i=1}^{i=27} (\epsilon_i^{FEA} - \epsilon_i)^2}{\sum_{i=1}^{i=27} (\epsilon_i^{FEA} - \bar{\epsilon})^2} \quad (5.38)$$

where each value of the subscript i denotes one of the 27 loading conditions investigated in the parametric runs, ϵ_i^{FEA} is the longitudinal strain for loading condition number i as determined by finite element runs, ϵ_i is the longitudinal strain for loading condition number i as determined by the predicting equation, and $\bar{\epsilon}$ is the average strain as obtained from finite element results. A value of r^2 of unity indicates perfect ability of the proposed function to represent the values ϵ_i^{FEA} . On the other hand, a value of zero indicates a poor correlation between ϵ_i^{FEA} and ϵ_i .

5.5.1 Limit Point Strain Criterion

The relationship of the limit point strains vs. the axial load ratio is presented in Figure 5.13. It can be noticed that the limit point strains increase with an increase in the tensile force and with a decrease in the diameter to thickness ratio. No clear trend is apparent relating the effect of the hoop stress ratio and the limit point strain.

5.5.1.1 General Form

In this sub-section, an equation that passes through the values of each of the 27 values of strains based on the limit point criterion as obtained from the finite element analysis is fitted. The proposed design equation has 27 constants. A polynomial function is assumed for this purpose. The resulting equation is

$$\begin{aligned}
 \epsilon_{lim} = & 0.04068 - 6.683 \times 10^{-4} x + 9.115 \times 10^{-2} y + 0.1327z + 3.246 \times 10^{-6} x^2 \\
 & - 1.849 \times 10^{-3} xy - 0.2663y^2 - 0.7705yz - 0.1099z^2 - 3.069 \times 10^{-3} zx \\
 & + 5.816 \times 10^{-3} xy^2 + 9.841 \times 10^{-6} x^2y + 3.411 \times 10^{-3} xz^2 + 1.726 \times 10^{-5} x^2z \\
 & + 0.8795y^2z + 0.9726yz^2 + 1.777 \times 10^{-2} xyz - 3.229 \times 10^{-5} x^2y^2z \\
 & - 2.154 \times 10^{-5} x^2z^2 - 1.038 \times 10^{-4} x^2yz - 1.483 \times 10^{-2} xy^2 - 2.579xyz^2yz^2 \\
 & - 1.478 \times 10^{-2} xy^2z^2 + 0.3103y^2z^2 + 6.514 \times 10^{-5} x^2y^2z + 1.625 \times 10^{-4} x^2 \\
 & + 1.165 \times 10^{-4} x^2y^2z^2
 \end{aligned}
 \tag{5.39}$$

where $x = OD/t$, $y = P_t/P_y$, and $z = \sigma_h/\sigma_y$.

Two groups of curves for the longitudinal compressive strain at limit points as predicted by Equation 5.34 are provided in Figures 5.14 and 5.15. In each figure, the strain at the limit point is plotted against the outside diameter to thickness ratio. The first group of curves (Figure 5.14) is for a hoop stress ratio of zero and the second group of curves

(Figure 5.15) is for a hoop stress ratio of 0.80. Each group of plots consists of a series of curves for axial load ratios P_t/P_y ranging from 0.2 (tension) up to 0.30 (compressive).

5.5.1.2 Simplified Form

Equation 5.39 is too complex to use for design calculations. For this purpose, a simplified equation is suggested, although the simplification results in a penalty in the accuracy of the solution, as will be demonstrated. For simplicity, the function is assumed to consist of the product of three functions. The argument of each function is only one of the variables OD/t , σ_h/σ_y , and P_t/P_y .

$$\epsilon_{lim} \left(\frac{OD}{t}, \frac{P_t}{P_y}, \frac{\sigma_h}{\sigma_y} \right) = f_1 \left(\frac{\sigma_h}{\sigma_y} \right) \times f_2 \left(\frac{P_t}{P_y} \right) \times f_3 \left(\frac{OD}{t} \right) \quad (5.40)$$

In the examination, for a given value of OD/t and P_t/P_y there are three parametric runs as the parameter σ_h/σ_y is varied. Based on the results of the three runs, the relationship between ϵ_{lim} and the parameter σ_h/σ_y is quadratic, in general. Therefore, function f_1 is assumed to take a quadratic form. (A more elaborate form of the proposed relationship necessitates a larger number of parametric runs). Using the same argument, the function f_2 is assumed to take also a quadratic form.

The same argument could be extended to function f_3 . However, it was noticed that a nearly linear relationship exists between $\log(\epsilon_{lim})$ and $\log(OD/t)$. This observation suggests that a good representation of the relationship between ϵ_{lim} and OD/t can be achieved if the function f_3 is assumed to take a power form. The assumption of a power function for function f_3 reduces the number of regression constants by one as compared to an assumed quadratic function, leading to a simpler form. The proposed simplified is

$$\epsilon_{lim} = \left[C_1 + C_2 \left(\frac{\sigma_h}{\sigma_y} \right) + C_3 \left(\frac{\sigma_h}{\sigma_y} \right)^2 \right] \times \left[1.00 + C_4 \left(\frac{P_t}{P_y} \right) + C_5 \left(\frac{P_t}{P_y} \right)^2 \right] \times \left(\frac{OD}{t} \right)^{-C_6} \quad (5.41)$$

where constants C_1 through C_6 are to be determined by regression analysis such that they minimize the function $\sum_{r=1}^{27} (\epsilon_{lim} - \epsilon_{lim}^{FEA})^2 w_r$, subject to the conditions

$$\left(\frac{\epsilon_{lim} - \epsilon_{lim}^{FEA}}{\epsilon_{lim}^{FEA}} \right)_r \leq \frac{0.04}{w_r} \quad (5.42)$$

Each value of subscript r denotes one of the 27 finite element runs presented in Table 5.2. The ϵ_{lim}^{FEA} is the longitudinal compressive strain corresponding to the limit point as predicted by finite element runs, and w is a weighting function defined by

$$w_r = \frac{\phi_{lim}}{\phi_{0.95}} \quad (5.43)$$

where ϕ_{lim} is the local curvature at the limit point, and $\phi_{0.95}$ is the local curvature at the point of 0.95% moment capacity in the post-buckling range of deformation.

The purpose of the constraints given by inequality 5.42 is to force the resulting design equation to yield more conservative results in the case where the post-buckling slope of the moment curvature diagram is steep and to tolerate more error on the unconservative side when the post-buckling slope is mild. The numerator of the right-hand side of the constraint in (5.42) is a measure of the average error on the unconservative side that is to be tolerated. Its value is arbitrary. However, for a feasible solution, its magnitude has to be increased as the number of constants in the suggested approximate equation is decreased.

In the function $\sum_{r=1}^{27} (\epsilon_{lim} - \epsilon_{lim}^{FEA})^2 w_r$, the coefficients w_r place more weight in the regression analysis on loading cases with steep moment vs. curvature slopes. Performing the required minimization, the result is

$$\epsilon_{lim} = \left[1.63 + 0.456 \left(\frac{\sigma_h}{\sigma_y} \right) + 1.21 \left(\frac{\sigma_h}{\sigma_y} \right)^2 \right] \times \left[1.00 + 0.962 \left(\frac{P_t}{P_y} \right) - 4.44 \left(\frac{P_t}{P_y} \right)^2 \right] \times \left(\frac{OD}{t} \right)^{-1.20} \quad (5.44)$$

where the error (defined as $\frac{\epsilon_{lim} - \epsilon_{lim}^{FEA}}{\epsilon_{lim}^{FEA}}$) has an average value of -0.21, and a standard deviation of 0.23 (refer to Table 5.3).

Equation 5.40 has a coefficient of determination of 0.25. The low value of the coefficient of determination can be attributed to two facts. These are; (a) the simplicity of the form of the assumed function; and (b) the imposition of the constraints in Equation 5.42 forces the resulting equation to yield conservative results in most cases rather than yielding the best fit curve. The scatter in the relationship between the limit point strains as predicted by the finite element results and those based on the results of Equation 5.44 is presented in Figure 5.16.

5.5.1.3 Range of Applicability

Both Equations 5.39 and 5.44 are based on the finite element results on pipe segments of a diameter to thickness ratios ranges of 51 to 100, a hoop stress ratio range of 0.00 to 0.72, an axial load corresponding to a temperature differential range of +30 to -45 C°, and hardening properties consistent with X52 steel (n=12). The equations are therefore applicable to any combination of parameters inside or close to the borders of the domain defined by the stated ranges.

5.5.2 Strain at 95% Moment Capacity

The relationship of the strains at 95% moment capacity vs. the axial load ratio is presented in Figure 5.17. It can be noticed that the strains at 95% moment capacity increase with an increase in the tensile force and with a decrease in the diameter to thickness ratio. No clear trend is apparent relating the effect of the hoop stress ratio and the strain at 95% moment capacity.

5.5.2.1 General Form

Following the same procedure as that used to obtain Equation 5.39, but with values of longitudinal compressive strains corresponding to a local moment value of 95% of the moment capacity in the post-buckling range, the equation for predicting strains is

$$\begin{aligned}
 \epsilon_{0.95} = & 0.06145 - 9.118 \times 10^{-4} x + 9.806 \times 10^{-2} y + 0.1600 z + 3.940 \times 10^{-6} x^2 \\
 & - 2.140 \times 10^{-3} xy - 0.1524 y^2 - 0.9619 yz - 6.331 \times 10^{-2} z^2 - 3.353 \times 10^{-3} zx \\
 & + 3.089 \times 10^{-3} xy^2 + 1.221 \times 10^{-5} x^2 y + 2.785 \times 10^{-3} xz^2 + 1.779 \times 10^{-5} x^2 z \\
 & + 1.267 y^2 z + 1.027 yz^2 + 1.974 \times 10^{-2} xyz - 1.789 \times 10^{-5} x^2 y^2 + 1.267 y^2 z \\
 & + 1.027 yz^2 + 1.974 \times 10^{-2} xyz - 1.764 \times 10^{-5} x^2 z^2 - 9.346 \times 10^{-5} x^2 yz \\
 & - 2.352 \times 10^{-2} xy^2 z - 2.620 \times 10^{-2} xyz^2 + 0.3803 y^2 z^2 + 7.885 \times 10^{-5} x^2 y^2 z \\
 & + 1.167 \times 10^{-4} x^2 yz^2 - 1.483 \times 10^{-2} xyz^2 z + 2.301 \times 10^{-4} x^2 y^2 z^2
 \end{aligned}
 \tag{5.45}$$

Equation 5.45 is plotted in Figures 5.18 and 5.19 for σ_h/σ_y values of 0.00 and 0.80, respectively. For the case of no internal pressure, the plotted strain varies from 0.008 to 0.028. For fully pressurized cases ($\sigma_h/\sigma_y = 0.80$), the strain varies from 0.016 to 0.116. In the two cases, the general trend of the 95% moment capacity strain is to drop as the diameter to thickness ratio increases.

5.5.2.2 Simplified Form

Following the rationale explained in justifying the form of Equation 5.41, the same simplified form may be used for an approximate equation that predicts strains based on the 95% moment capacity criterion. When the function $\sum_{r=1}^{27} (\epsilon_{0.95} - \epsilon_{0.95}^{FEA})^2 w_r$ is minimized subject to the constraints (5.42), the following equation is obtained

$$\epsilon_{0.95} = \left[4.87 + 15.6 \left(\frac{\sigma_h}{\sigma_y} \right) + 3.75 \left(\frac{\sigma_h}{\sigma_y} \right)^2 \right] \times \left[1.00 - 1.05 \left(\frac{P_t}{P_y} \right) - 1.042 \left(\frac{P_t}{P_y} \right)^2 \right] \times \left(\frac{OD}{t} \right)^{-1.41} \quad (5.46)$$

The average error in Equation 5.42 is -0.20 with a standard deviation of 0.21 (refer to Table 5.4). The coefficient of determination is 0.70 and the scatter between the finite element results as predicted from Equation 5.46 is shown in Figure 5.20. The range of applicability of Equations 5.45 and 5.46 is the same as that of Equations 5.39 and 5.44.

5.5.3 Ovalization Criterion

As mentioned in Section 5.3.9.5, the ovalization criterion is relevant only for design and assessment of unpressurized pipes, where it can reach magnitudes of 15% or higher. The longitudinal compressive strain corresponding to an ovalization of 15% can be used as a deformation limit state. Referring to Table 5.5, multiplying the strains at 15% ovalization as determined by finite element analyses by the diameter to thickness ratio and plotting this result against P_t/P_y , one finds the relationship between the two variables is found to be nearly linear. Therefore, an equation of the form

$$\epsilon_{15\%} = \frac{t}{OD} \left(C_1 + C_2 \frac{P_t}{P_y} \right) \quad (5.47)$$

is assumed to yield an appropriate representation of the relationship between OD/t , P_t/P_y , and $\epsilon_{15\%}$.

Through regression analysis of the nine finite element runs presented in Table 5.5, the following equation is obtained

$$\epsilon_{15\%} = \frac{t}{OD} \left(1.76 + 3.66 \frac{P_t}{P_y} \right) \quad (5.48)$$

where the average error in the prediction of $\epsilon_{0.15}$ is nearly zero, with a standard deviation of 0.066 and a coefficient of determination of 0.99 (refer to Table 5.5). Equation 5.48 is both simple and accurate and can be used for design and assessment calculations based on the 15% ovalization criterion. A group of curves of $\epsilon_{15\%}$ as computed from Equation (5.48) versus OD/t at different values of P_t/P_y is presented in Figure 5.21. It is observed that the strains at 15% have a maximum value of 0.058 and a minimum value of 0.01. Equation 5.21 is valid for unpressurized pipes with a OD/t value ranging from 51 to 100 and a P_t/P_y value ranging from 0.20 (tension) to 0.30 (compression). The scatter of the strains corresponding to 15% ovalization as determined by equation 5.48 in relation to those predicted by finite element analyses is presented in Figure 5.22.

5.5.4 Hoop Strain Criterion

The hoop strain criterion is of interest in the design of pressurized pipes. For pressurized pipes, only two values of hoop stress ratio σ_h/σ_y were investigated. These are 0.36 and 0.72. It is observed that the magnitude of hoop stress ratio (at least in the 0.36 to 0.72 range) does not significantly affect the magnitude of the longitudinal compressive strain corresponding to a hoop strain value of 0.08. Also, no significant effect of the axial load ratio P_t/P_y is observed (Table 5.6).

The elimination of these two parameters leads to considerable simplification in the form of the proposed equation. It is noticed that the lowest value of the longitudinal compressive strain at 8% hoop strain, $\epsilon_{0.08}$, is in the neighborhood of 0.03. The longitudinal strain corresponding to 8% increases as the t/OD ratio increases. The maximum value of strain attained is 0.046.

A proposed function of the form

$$\epsilon_{0.08} = C_1 + \left(\frac{C_2 t}{OD} \right)^{C_3} \quad (5.49)$$

is assumed. It should provide a minimum value of predicted strain of C_1 (in the neighborhood of 0.03) and an additional value that is proportional to $(t/OD)^{C_3}$ that is nearly zero for an OD/t value of 100 and a maximum value (in the neighborhood of 0.016) at a OD/t value of 51. These conditions are achieved by varying the constants C_2 and C_3 .

Through regression analysis, the following equation is obtained.

$$\epsilon_{0.08} = 0.034 + \left(\frac{32.7t}{OD} \right)^{10.8} \quad (5.50)$$

The average error of the strains predicted by Equation (5.50) is nearly zero (refer to Table 5.6), with a standard deviation magnitude of 0.066 and a coefficient of determination of 0.727. The relationship between $\epsilon_{0.08}$ and OD/t as given by Equation 5.50 is plotted in Figure 5.23.

Equation 5.50 is valid for OD/t values ranging from 50 to 100, P_t/P_y values from 0.20 (tension) to 0.30 (compression), and σ_h/σ_y values ranging from 0.25 to 0.80. The suggested limits for σ_h/σ_y are based on engineering judgment, rather than on analytical

results. More runs in the range of σ_h/σ_y value of 0.0 to 0.36 are needed in order to determine the bounds of applicability of Equation 5.50. The scatter of the strains corresponding to 8% hoop strains as determined by equation 5.50 in relation to those predicted by finite element analyses is presented in Figure 5.24.

5.5.5 Comparison Between Different Deformation Criteria

Three of the design criteria presented are relevant in the design of unpressurized pipelines. These are the longitudinal compressive strains that corresponding to the limit point, the point of 95% moment capacity, and the point of 15% ovalization. With reference to Table 5.2 and Figures 5.14, 5.18, and 5.21, the limit point criterion yields the least strain values and the 15% ovalization the highest strain values.

The three criteria that are relevant to the design of pressurized pipelines are the longitudinal compressive strains corresponding to the limit point, the point of 95% moment capacity, and the point of 8% hoop strain. The strains based on the first criterion are the most conservative (Table 5.2). No such clear observations can be made for the two other criteria. In some instances, the 95% moment capacity yields smaller values of strains than does the 8% hoop strain criteria, and in other instances the reverse is true.

5.6 Deformed Configurations

5.6.1 Buckled Length

Figures 5.25 to 5.27 are the wire mesh plots of the deformed configurations of the 27 specimens of the parametric finite element runs. It is observed that, with the exception of 77C45H72 and 100C7.5H00, each specimen exhibits a buckle near each end of the specimen. The buckles are symmetric with respect to a horizontal plane passing through the specimen mid-height.

The application of equal and opposite rotations to the ends of Specimens 77C45H72 and 100C7.5H00 resulted in two identical buckles near the center of the specimen. The two buckled zones interfered with each other. It was judged that such a case, which is unlikely to occur in the field, is not of practical importance. In order to force only one buckle to occur in these two cases, unequal rotations were applied to the ends of the specimens.

It was also observed that, as the end rotation progressed, the buckles that initially formed near the ends of the specimens were amplified and no additional local buckles formed in the specimens.

All pressurized cases considered exhibited outward bulging buckles. For these cases, the buckled length to outside diameter ratio ranged between 0.38 and 0.53 (refer to Table 5.7). All unpressurized cases considered exhibited inward buckling patterns with a buckled length to diameter ratio ranging from 0.53 to 0.75. Seven of the unpressurized cases exhibited a Brazier mode of buckling, while the remaining two cases (77C45H00 and 100C45H00) exhibited diamond buckling patterns. This observation suggests that diamond shape buckling is more likely to occur for unpressurized pipes having a high diameter to thickness ratio subjected to high axial compressive loads.

5.7 Effect of Boundary Conditions

The loading conditions and cross section geometry of Specimens UGA324, HGA324, and DGA324 of the experimental program (see Chapter 2) are similar to those of the parametric runs 51C45H00, 51C45H36, and 51C45H72. The difference between the two groups lies in the type of boundary conditions imposed at the top and bottom ends. A comparison of the limit point strains obtained by the two groups is given in Table 5.8. It is noticed that the strains based on test results are either slightly higher (Specimens UGA324 and HGA324), or equal (Specimen DGA324) to those based on the corresponding parametric runs. This may be caused by the fact that the end boundary

conditions in the tests provides more stiffness to the specimens than provided by the boundary conditions in the parametric runs.

5.8 Summary and Conclusions

In this chapter, the parameters affecting the local buckling behaviour of pipes were identified. The number of parameters that need to be studied was reduced through dimensional analysis. A parametric study was conducted using a finite element model similar to the one devised in chapter 4. The non-dimensional parameters varied are D/t , P_{imp}/P_y , and σ_h/σ_y . The parametric study consists of twenty-seven combinations of loading conditions and pipe geometry. Four definitions for deformation limiting criteria for pipelines were proposed. Equations for predicting longitudinal compressive strains corresponding to each of the proposed deformation limiting criteria are provided.

The parametric study was carried out using the true stress vs. true strain relationship for X52 Steel as obtained from coupon tests. Therefore, the results of the study are limited to pipes made of gradual yielding steel having a plasticity exponent in the neighborhood of 12. The parametric study needs to be expanded to cover other values of the plasticity exponent of practical importance.

The buckling modes obtained consisted of outward bulges for all pressurized pipes and either diamond shape or Brazier modes for unpressurized pipes. The boundaries separating the three modes of buckling are not clearly identified. Further finite element runs are needed for this purpose.

Table 5.1 Moment Capacity Ratios

Identifier	Dimensionless Parameters			Moment Ratios	
	OD/t	P_{tot}/P_y	$\sigma_{\text{tr}}/\sigma_y$	$\frac{M}{M_{\sigma_o, P.}^P}$	$f \frac{M}{M_{\sigma_o, P.}^P}$
51T30H00	51	-0.195	0.00	0.95	0.98
77T30H00	77	-0.195	0.00	0.93	1.01
100T30H00	100	-0.195	0.00	0.95	1.05
51C7.5H00	51	0.049	0.00	0.94	0.97
77C7.5H00	77	0.049	0.00	0.93	1.00
100C7.5H00	100	0.049	0.00	0.94	1.03
51C45H00	51	0.293	0.00	0.95	0.96
77C45H00	77	0.293	0.00	0.91	1.00
100C45H00	100	0.293	0.00	0.92	1.04
51T30H36	51	-0.301	0.36	1.03	1.00
77T30H36	77	-0.301	0.36	0.99	1.00
100T30H36	100	-0.301	0.36	1.02	1.05
51C7.5H36	51	-0.057	0.36	1.00	0.96
77C7.5H36	77	-0.057	0.36	0.96	0.96
100C7.5H36	100	-0.057	0.36	0.97	1.00
51C45H36	51	0.188	0.36	1.03	0.98
77C45H36	77	0.188	0.36	0.94	0.96
100C45H36	100	0.188	0.36	0.93	0.98
51T30H72	51	-0.406	0.72	1.15	1.03
77T30H72	77	-0.406	0.72	1.09	1.02
100T30H72	100	-0.406	0.72	1.00	0.96
51C7.5H72	51	-0.162	0.72	1.15	1.02
77C7.5H72	77	-0.162	0.72	1.07	0.99
100C7.5H72	100	-0.162	0.72	1.05	1.00
51C45H72	51	0.082	0.72	1.29	1.13
77C45H72	77	0.082	0.72	0.85	0.79
100C45H72	100	0.082	0.72	1.07	1.03
Average				1.00	1.00
St. Dev.				0.09	0.05
Min.				0.85	0.79
Max.				1.29	1.13

Table 5.2 Summary of Strain Values for Different Design Criteria

Identifier	Longitudinal Compressive Strain @				Dimensionless Parameters				Geometry		Loading Variables					
	Limit	0.95Mom Capacity	15% Ovalization	8% Hoop Strain	OD/t	P _t /P _y	P _{tot} /P _y	σ_t/σ_y	OD (mm)	t (mm)	Pressure (MPa)	Δt	P _{imp} (kN)	P _{pres} (kN)	P _{tot} (kN)	P _y (kN)
51T30H00	0.0086	0.020	0.021		51	-0.195	-0.195	0.00	324	6.35	0.00	-30	-444	0	-444	2275
51T30H36	0.0280	0.055		0.046	51	-0.195	-0.301	0.36	324	6.35	5.27	-30	-444	-240	-684	2275
51T30H72	0.0440	0.103		0.044	51	-0.195	-0.406	0.72	324	6.35	10.55	-30	-444	-480	-924	2275
51C7.5H00	0.0160	0.026	0.040		51	0.049	0.049	0.00	324	6.35	0.00	8	111	0	111	2275
51C7.5H36	0.0230	0.041		0.042	51	0.049	-0.057	0.36	324	6.35	5.27	8	111	-240	-129	2275
51C7.5H72	0.0330	0.062		0.041	51	0.049	-0.162	0.72	324	6.35	10.55	8	111	-480	-369	2275
51C45H00	0.0170	0.028	0.056		51	0.293	0.293	0.00	324	6.35	0.00	45	667	0	667	2275
51C45H36	0.0220	0.034		0.041	51	0.293	0.188	0.36	324	6.35	5.27	45	667	-240	427	2275
51C45H72	0.0320	0.055		0.040	51	0.293	0.082	0.72	324	6.35	10.55	45	667	-480	187	2275
77T30H00	0.0067	0.012	0.014		77	-0.195	-0.195	0.00	610	7.92	0.00	-30	-1051	0	-1051	5378
77T30H36	0.0130	0.032		0.038	77	-0.195	-0.301	0.36	610	7.92	3.45	-30	-1051	-567	-1618	5378
77T30H72	0.0270	0.082		0.034	77	-0.195	-0.406	0.72	610	7.92	6.89	-30	-1051	-1135	-2185	5378
77C7.5H00	0.0088	0.0147	0.026		77	0.049	0.049	0.00	610	7.92	0.00	8	263	0	263	5378
77C7.5H36	0.0110	0.021		0.035	77	0.049	-0.057	0.36	610	7.92	3.45	8	263	-567	-305	5378
77C7.5H72	0.0190	0.039		0.032	77	0.049	-0.162	0.72	610	7.92	6.89	8	263	-1135	-872	5378
77C45H00	0.0097	0.014	0.034		77	0.293	0.293	0.00	610	7.92	0.00	45	1576	0	1576	5378
77C45H36	0.0110	0.018		0.036	77	0.293	0.188	0.36	610	7.92	3.45	45	1576	-567	1009	5378
77C45H72	0.0120	0.022		0.031	77	0.293	0.082	0.72	610	7.92	6.89	45	1576	-1135	441	5378
100T30H00	0.0051	0.0080	0.0096		100	-0.195	-0.195	0.00	711	7.11	0.00	-30	-1103	0	-1103	5644
100T30H36	0.0090	0.021		0.037	100	-0.195	-0.301	0.36	711	7.11	2.64	-30	-1103	-595	-1698	5644
100T30H72	0.0160	0.079		0.033	100	-0.195	-0.406	0.72	711	7.11	5.28	-30	-1103	-1191	-2293	5644
100C7.5H00	0.0065	0.010	0.022		100	0.049	0.049	0.00	711	7.11	0.00	8	276	0	276	5644
100C7.5H36	0.0076	0.016		0.035	100	0.049	-0.057	0.36	711	7.11	2.64	8	276	-595	-320	5644
100C7.5H72	0.0130	0.026		0.030	100	0.049	-0.162	0.72	711	7.11	5.28	8	276	-1191	-915	5644
100C45H00	0.0070	0.0098	0.027		100	0.293	0.293	0.00	711	7.11	0.00	45	1654	0	1654	5644
100C45H36	0.0073	0.012		0.037	100	0.293	0.188	0.36	711	7.11	2.64	45	1654	-595	1059	5644
100C45H72	0.0130	0.020		0.034	100	0.293	0.082	0.72	711	7.11	5.28	45	1654	-1191	463	5644

Table 5.3 Longitudinal Compressive Strains at Limit Point

Identifier	Dimensionless Parameters			Strain at Limit Point		Error	Weight	Upper Limit for Error
	OD/t	P/P_y	σ_H/σ_y	FEA	Eq. 5.44			
51T30H00	51	-0.195	0.00	0.0086	0.0095	0.10	0.39	0.10
77T30H00	77	-0.195	0.00	0.0067	0.0058	-0.13	0.55	0.07
100T30H00	100	-0.195	0.00	0.0051	0.0042	-0.17	0.60	0.07
51C7.5H00	51	0.049	0.00	0.0160	0.0153	-0.04	0.59	0.07
77C7.5H00	77	0.049	0.00	0.0088	0.0094	0.06	0.63	0.06
100C7.5H00	100	0.049	0.00	0.0065	0.0068	0.05	0.76	0.05
51C45H00	51	0.293	0.00	0.0170	0.0133	-0.22	0.65	0.06
77C45H00	77	0.293	0.00	0.0097	0.0081	-0.16	0.67	0.06
100C45H00	100	0.293	0.00	0.0070	0.0059	-0.15	0.74	0.05
51T30H36	51	-0.195	0.36	0.0280	0.0114	-0.59	0.63	0.06
77T30H36	77	-0.195	0.36	0.0130	0.0069	-0.47	0.44	0.09
100T30H36	100	-0.195	0.36	0.0090	0.0051	-0.44	0.34	0.12
51C7.5H36	51	0.049	0.36	0.0230	0.0183	-0.20	0.59	0.07
77C7.5H36	77	0.049	0.36	0.0110	0.0112	0.02	0.54	0.07
100C7.5H36	100	0.049	0.36	0.0076	0.0082	0.08	0.52	0.08
51C45H36	51	0.293	0.36	0.0220	0.0159	-0.28	0.67	0.06
77C45H36	77	0.293	0.36	0.0110	0.0097	-0.12	0.63	0.06
100C45H36	100	0.293	0.36	0.0073	0.0071	-0.03	0.62	0.06
51T30H72	51	-0.195	0.72	0.0440	0.0151	-0.66	0.47	0.09
77T30H72	77	-0.195	0.72	0.0270	0.0092	-0.66	0.37	0.11
100T30H72	100	-0.195	0.72	0.0160	0.0067	-0.58	0.24	0.17
51C7.5H72	51	0.049	0.72	0.0330	0.0243	-0.26	0.57	0.07
77C7.5H72	77	0.049	0.72	0.0190	0.0148	-0.22	0.50	0.08
100C7.5H72	100	0.049	0.72	0.0130	0.0109	-0.16	0.50	0.08
51C45H72	51	0.293	0.72	0.0320	0.0211	-0.34	0.60	0.07
77C45H72	77	0.293	0.72	0.0120	0.0129	0.07	0.53	0.07
100C45H72	100	0.293	0.72	0.0130	0.0094	-0.27	0.66	0.06
Average Error						-0.21		
Coef. of. Det.						0.25		
Standard Deviation						0.23		

Table 5.4 Longitudinal Compressive Strains at 95% of the Moment Capacity

Identifier	Dimensionless Parameters			Strains at 95% Mom. Capacity		Error	Weight	Upper Limit for Error
	OD/t	P_y/P_y	σ_h/σ_y	FEA	Eq. 5.46			
51T30H00	51	-0.195	0.00	0.0200	0.022	0.05	0.39	0.10
77T30H00	77	-0.195	0.00	0.0120	0.012	0.00	0.55	0.07
100T30H00	100	-0.195	0.00	0.0080	0.009	0.05	0.60	0.07
51C7.5H00	51	0.049	0.00	0.0260	0.018	-0.37	0.59	0.07
77C7.5H00	77	0.049	0.00	0.0147	0.010	-0.36	0.63	0.06
100C7.5H00	100	0.049	0.00	0.0100	0.007	-0.34	0.76	0.05
51C45H00	51	0.293	0.00	0.0280	0.011	-0.58	0.65	0.06
77C45H00	77	0.293	0.00	0.0140	0.006	-0.57	0.67	0.06
100C45H00	100	0.293	0.00	0.0098	0.004	-0.57	0.74	0.05
51T30H36	51	-0.195	0.36	0.0550	0.050	-0.10	0.63	0.06
77T30H36	77	-0.195	0.36	0.0320	0.028	-0.12	0.44	0.09
100T30H36	100	-0.195	0.36	0.0210	0.019	-0.06	0.34	0.12
51C7.5H36	51	0.049	0.36	0.0410	0.040	-0.06	0.59	0.07
77C7.5H36	77	0.049	0.36	0.0210	0.023	0.05	0.54	0.07
100C7.5H36	100	0.049	0.36	0.0160	0.016	-0.03	0.52	0.08
51C45H36	51	0.293	0.36	0.0340	0.026	-0.27	0.67	0.06
77C45H36	77	0.293	0.36	0.0180	0.014	-0.22	0.63	0.06
100C45H36	100	0.293	0.36	0.0120	0.010	-0.18	0.62	0.06
51T30H72	51	-0.195	0.72	0.1030	0.082	-0.21	0.47	0.09
77T30H72	77	-0.195	0.72	0.0820	0.046	-0.44	0.37	0.11
100T30H72	100	-0.195	0.72	0.0790	0.032	-0.59	0.24	0.17
51C7.5H72	51	0.049	0.72	0.0620	0.066	0.02	0.57	0.07
77C7.5H72	77	0.049	0.72	0.0390	0.037	-0.07	0.50	0.08
100C7.5H72	100	0.049	0.72	0.0260	0.026	-0.03	0.50	0.08
51C45H72	51	0.293	0.72	0.0550	0.042	-0.26	0.60	0.07
77C45H72	77	0.293	0.72	0.0220	0.024	0.05	0.53	0.07
100C45H72	100	0.293	0.72	0.0200	0.016	-0.19	0.66	0.06
Average Error						-0.20		
Coef. of. Determination						0.70		
Standard Deviation						0.21		

Table 5.5 Longitudinal Compressive Strains at 15% Ovalization

Identifier	Dimensionless Parameters		Strain at 15% Ovalization		Error
	OD/t	P_x/P_y	FEA	Eq. 5.48	
51T30H00	51	-0.195	0.021	0.021	-0.023
77T30H00	77	-0.195	0.014	0.014	-0.030
100T30H00	100	-0.195	0.0096	0.010	0.083
51C7.5H00	51	0.049	0.040	0.038	-0.052
77C7.5H00	77	0.049	0.026	0.025	-0.032
100C7.5H00	100	0.049	0.022	0.019	-0.134
51C45H00	51	0.293	0.056	0.056	-0.008
77C45H00	77	0.293	0.034	0.037	0.076
100C45H00	100	0.293	0.027	0.028	0.047
Average Error					-0.008
Coef. of. Determination					0.99
Standard Deviation					0.068

Table 5.6 Longitudinal Compressive Strains at 8% Hoop Strain

Identifier	Dimensionless Parameters			Strain at 8% Hoop Strain		Error
	OD/t	P_x/P_y	σ_h/σ_y	FEA	Eq. 5.50	
51T30H36	51	-0.195	0.36	0.046	0.042	-0.084
77T30H36	77	-0.195	0.36	0.038	0.034	-0.104
100T30H36	100	-0.195	0.36	0.037	0.034	-0.083
51C7.5H36	51	0.049	0.36	0.042	0.042	0.003
77C7.5H36	77	0.049	0.36	0.035	0.034	-0.028
100C7.5H36	100	0.049	0.36	0.035	0.034	-0.030
51C45H36	51	0.293	0.36	0.041	0.042	0.028
77C45H36	77	0.293	0.36	0.036	0.034	-0.055
100C45H36	100	0.293	0.36	0.037	0.034	-0.083
51T30H72	51	-0.195	0.72	0.044	0.042	-0.042
77T30H72	77	-0.195	0.72	0.034	0.034	0.001
100T30H72	100	-0.195	0.72	0.033	0.034	0.029
51C7.5H72	51	0.049	0.72	0.041	0.042	0.028
77C7.5H72	77	0.049	0.72	0.032	0.034	0.064
100C7.5H72	100	0.049	0.72	0.03	0.034	0.131
51C45H72	51	0.293	0.72	0.04	0.042	0.054
77C45H72	77	0.293	0.72	0.031	0.034	0.098
100C45H72	100	0.293	0.72	0.034	0.034	-0.002
Average Error						-0.004
Coef. of. Determination						0.727
Standard Deviation						0.066

Table 5.7 Buckled Lengths and Buckling Modes

Identifier	Buckled Length to Diameter Ratio	Buckled Shape
51T30H00	0.53	Brazier
51T30H36	0.45	Outward Bulge
51T30H72	0.53	Outward Bulge
51C7.5H00	0.60	Brazier
51C7.5H36	0.53	Outward Bulge
51C7.5H72	0.53	Outward Bulge
51C45H00	0.75	Brazier
51C45H36	0.45	Outward Bulge
51C45H72	0.53	Outward Bulge
77T30H00	0.53	Brazier
77T30H36	0.45	Outward Bulge
77T30H72	0.45	Outward Bulge
77C7.5H00	0.60	Brazier
77C7.5H36	0.38	Outward Bulge
77C7.5H72	0.45	Outward Bulge
77C45H00	0.75	Diamond Shape
77C45H36	0.38	Outward Bulge
77C45H72	0.45	Outward Bulge
100T30H00	0.53	Brazier
100T30H36	0.38	Outward Bulge
100T30H72	0.45	Outward Bulge
100C7.5H00	0.60	Brazier
100C7.5H36	0.38	Outward Bulge
100C7.5H72	0.45	Outward Bulge
100C45H00	0.75	Diamond Shape
100C45H36	0.38	Outward Bulge
100C45H72	0.45	Outward Bulge

Table 5.8 Limit Point Strains based on Experimental and Finite Element Results

Experimental Results		Corresponding Parametric Results	
Identifier	Limit Point Strain	Identifier	Limit Point Strain
UGA324	2.00%	51C45H00	1.70%
HGA324	2.30%	51C45H36	2.20%
DGA324	3.20%	51C45H72	3.20%

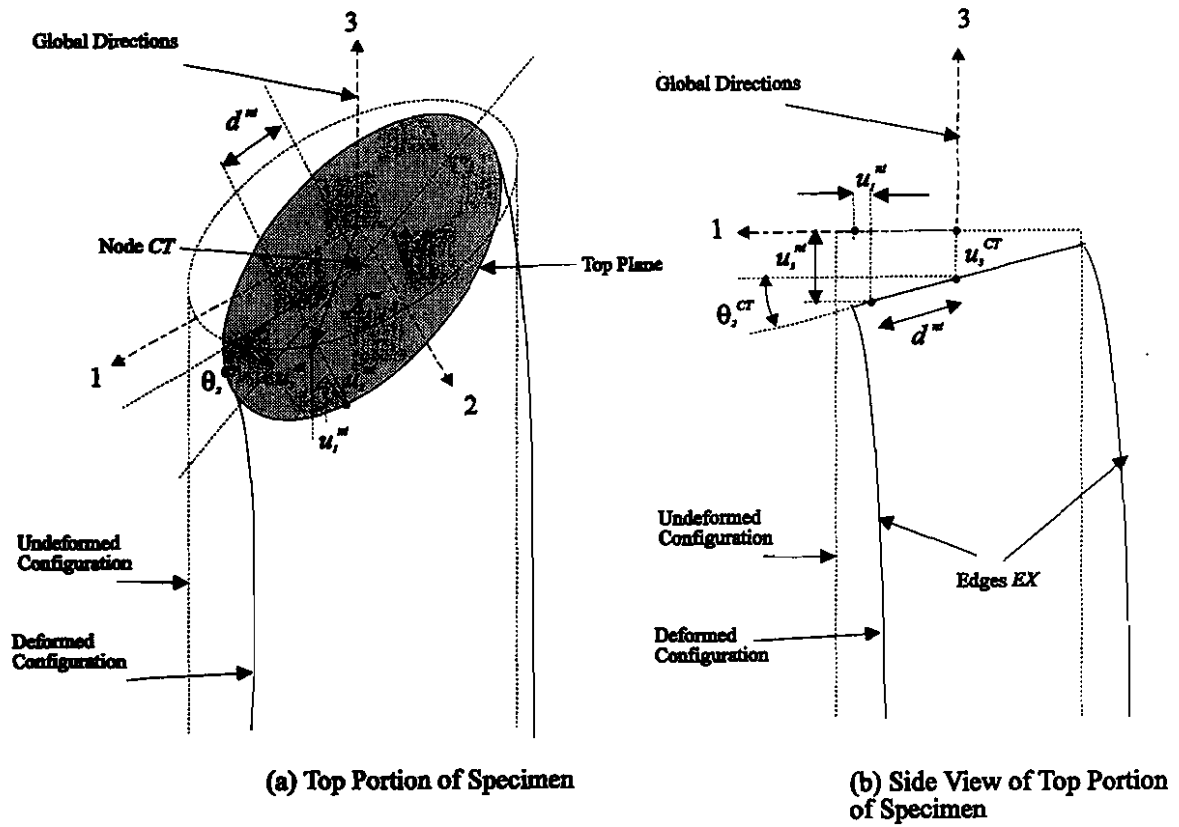


Figure 5.1 Boundary Conditions

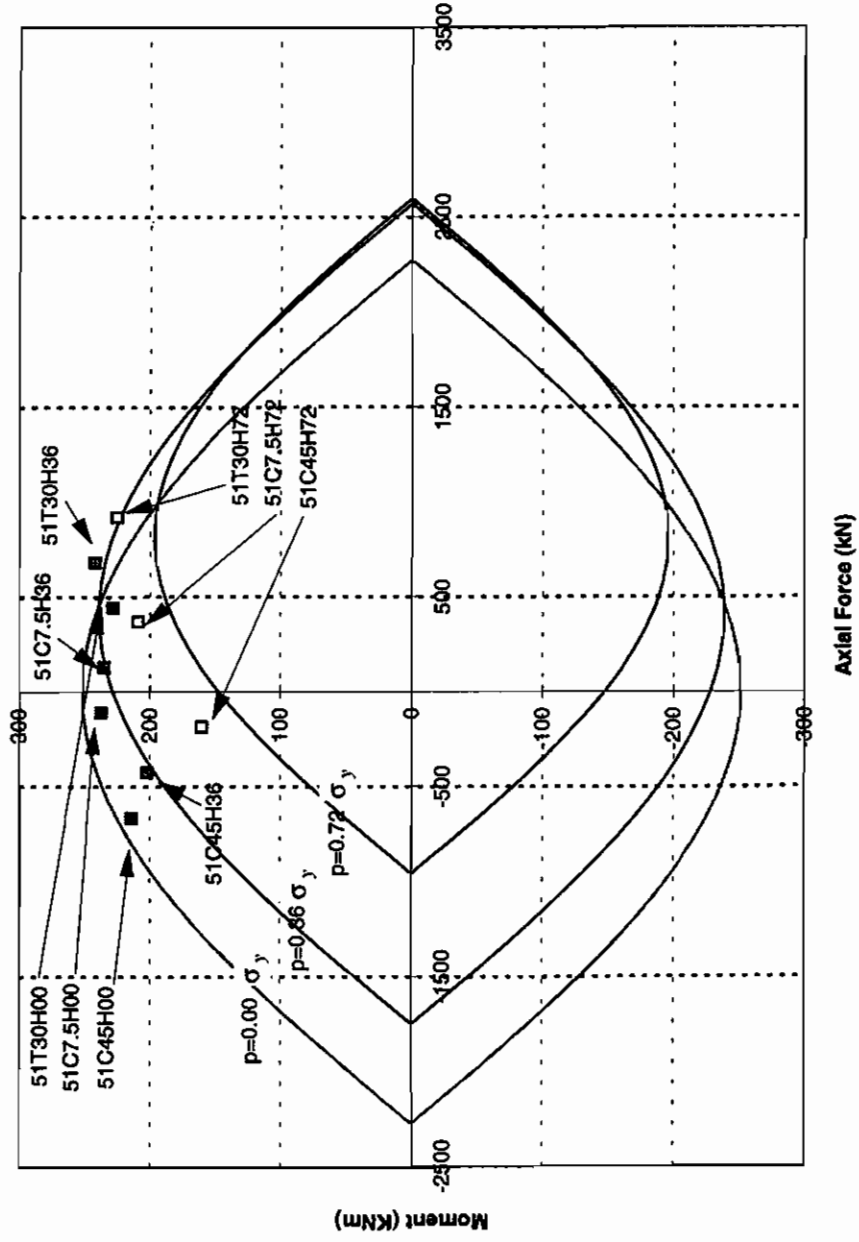


Figure 5.2 Interaction Diagrams for 324 mm OD x 6.35 mm Cross Section

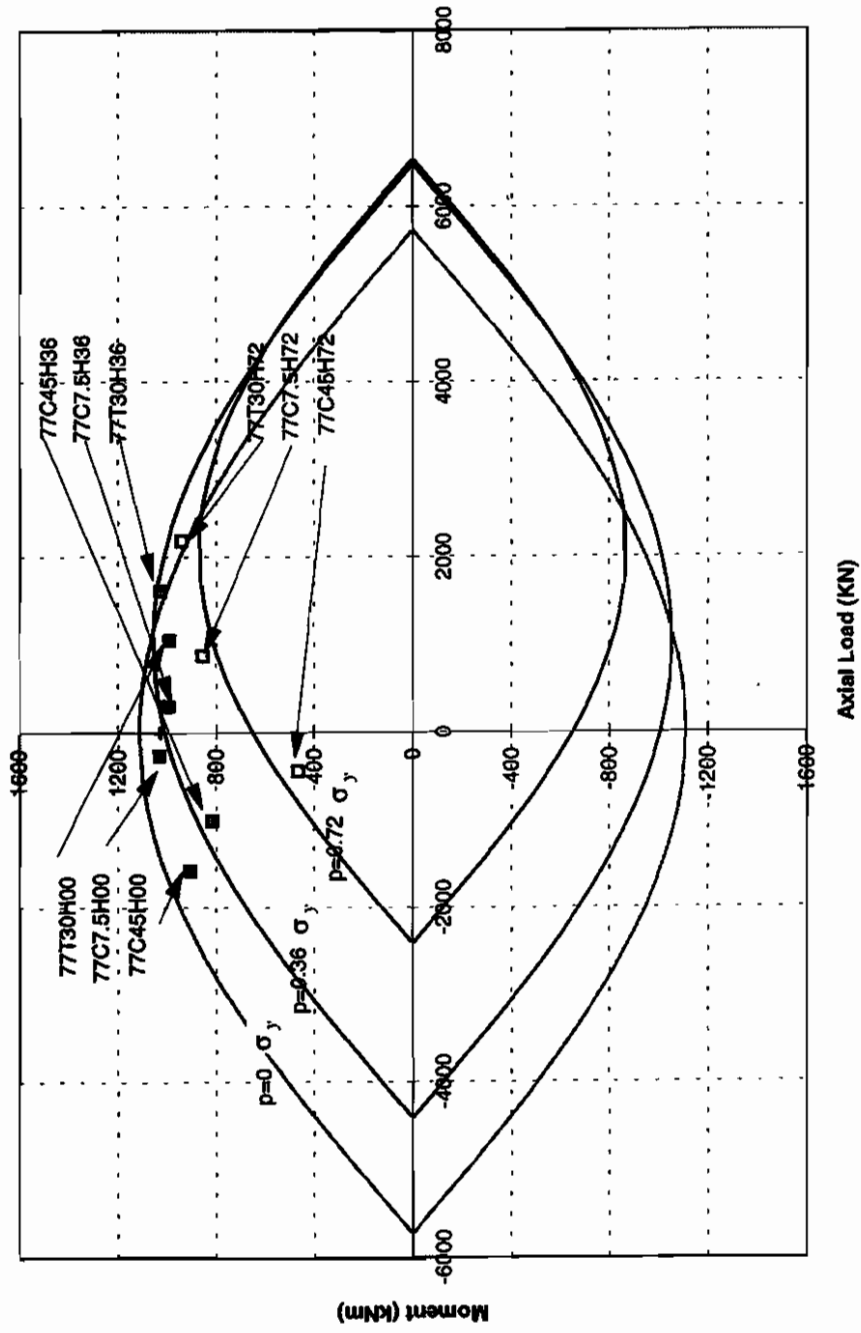


Figure 5.3 Interaction Diagrams for 610 mm OD x 7.92 mm Cross Section

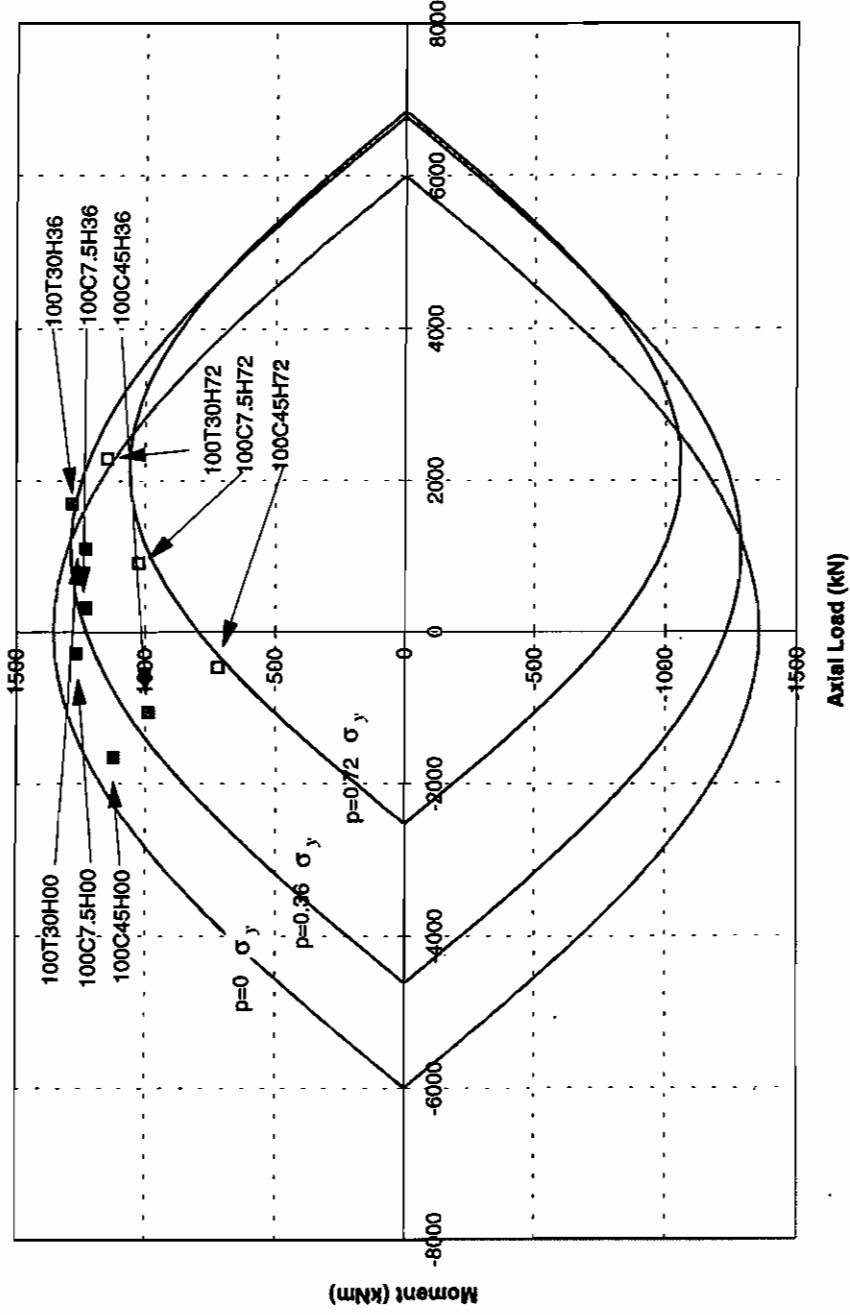


Figure 5.4 Interaction Diagrams for 711 mm OD x 7.11 mm Cross-Section

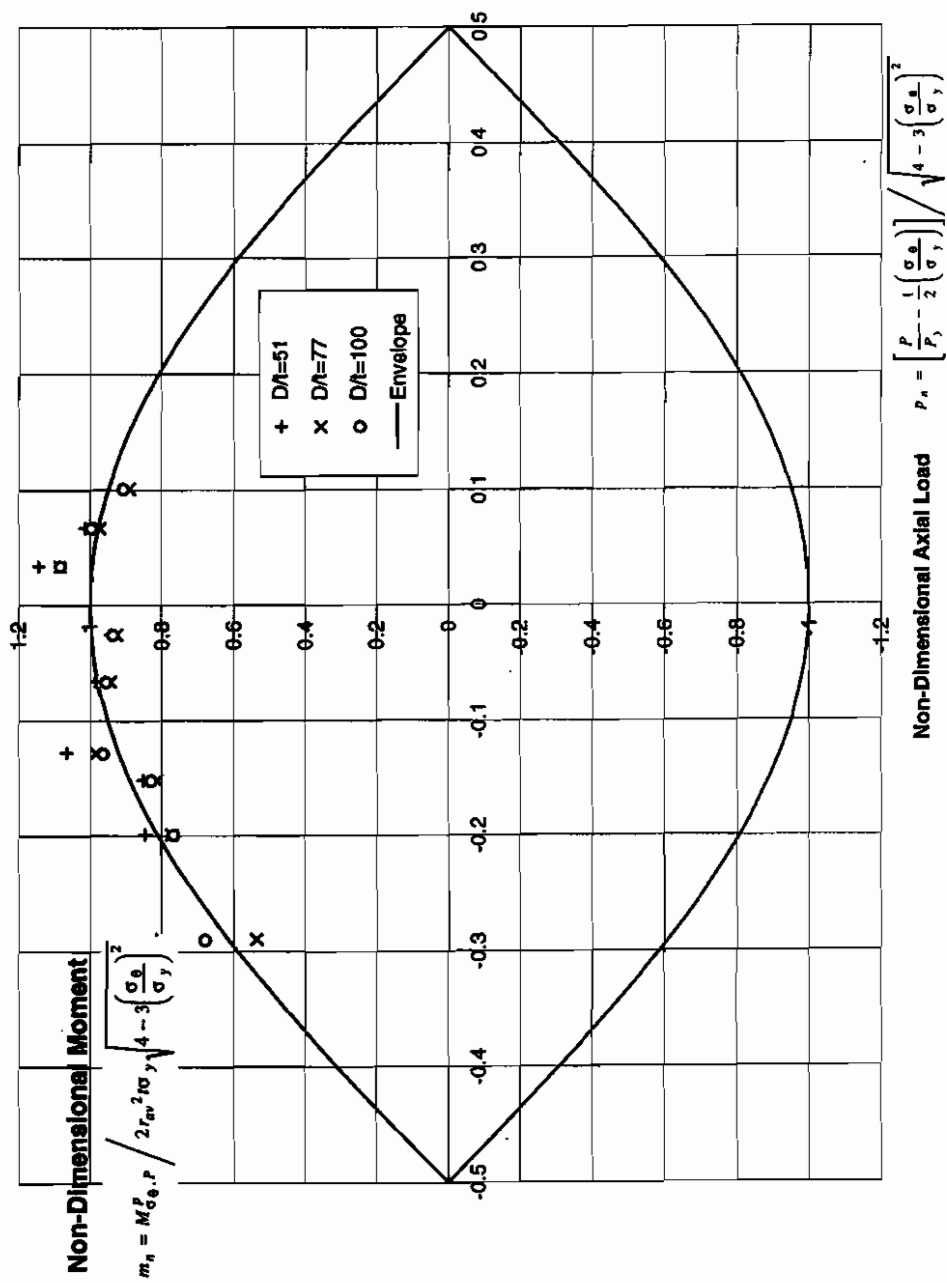


Figure 5.5 Non-Dimensional Interaction Diagram

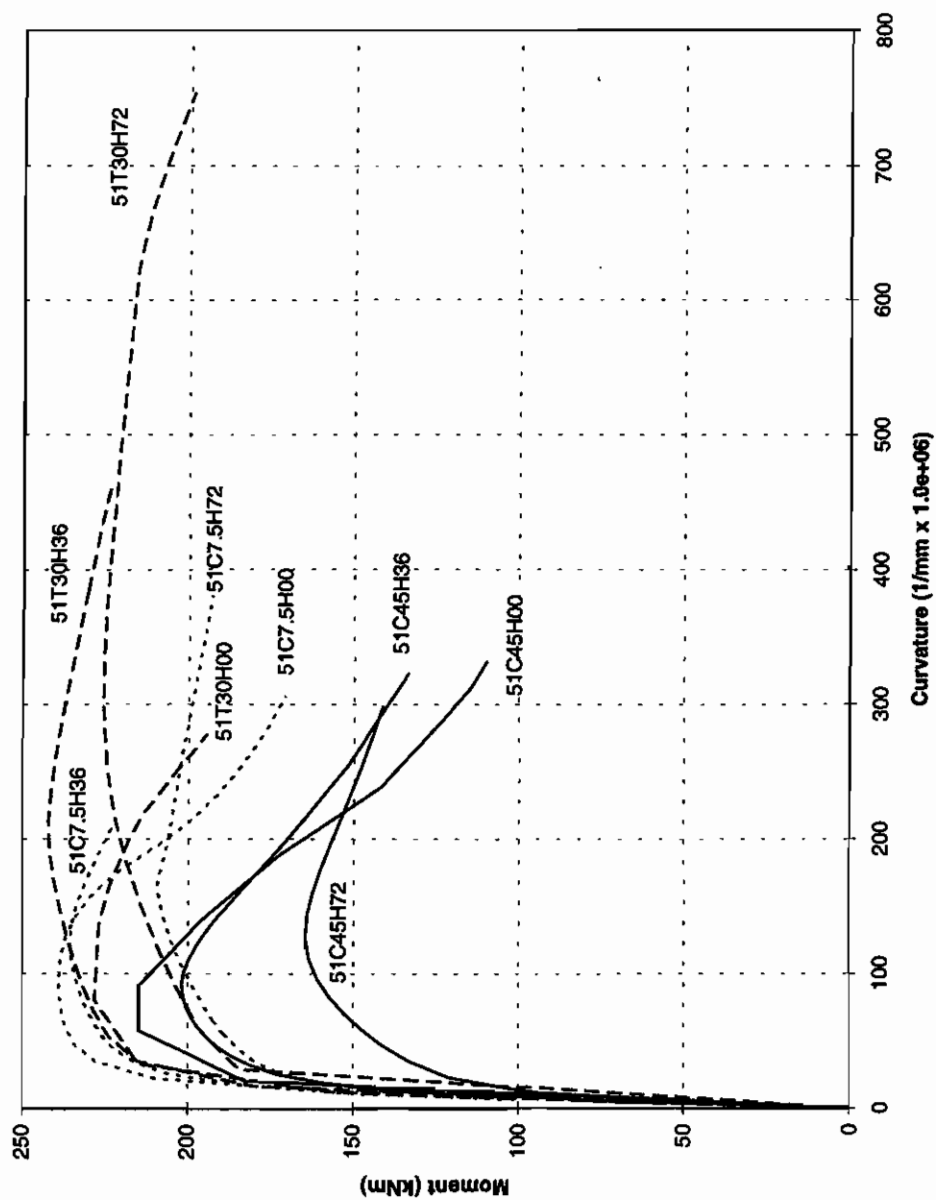


Figure 5.6 Local Moment vs. Local Curvature Diagrams for 324 mm OD x 6.35 mm Cross Section

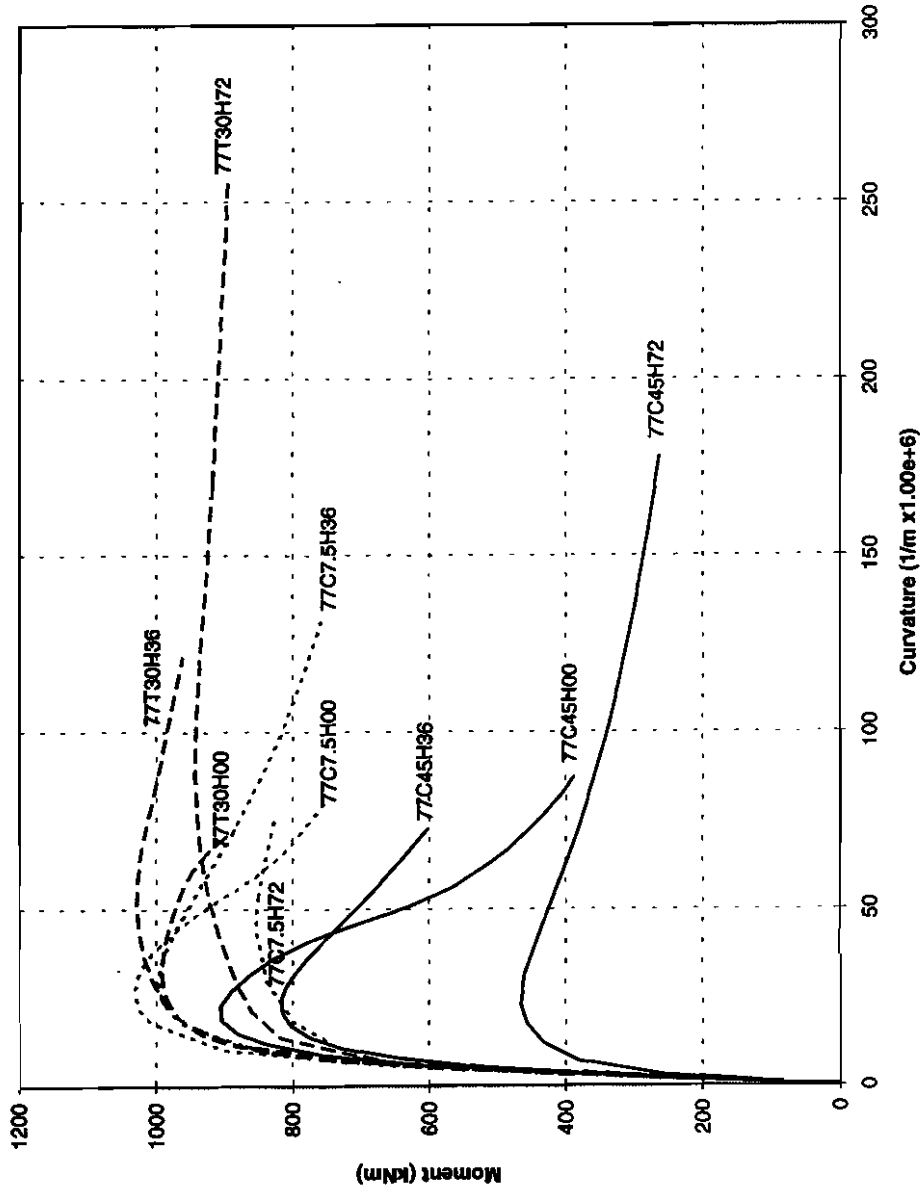


Figure 5.7 Local Moment vs. Local Curvature Diagrams for 610 mm OD x 7.92 mm Cross Section

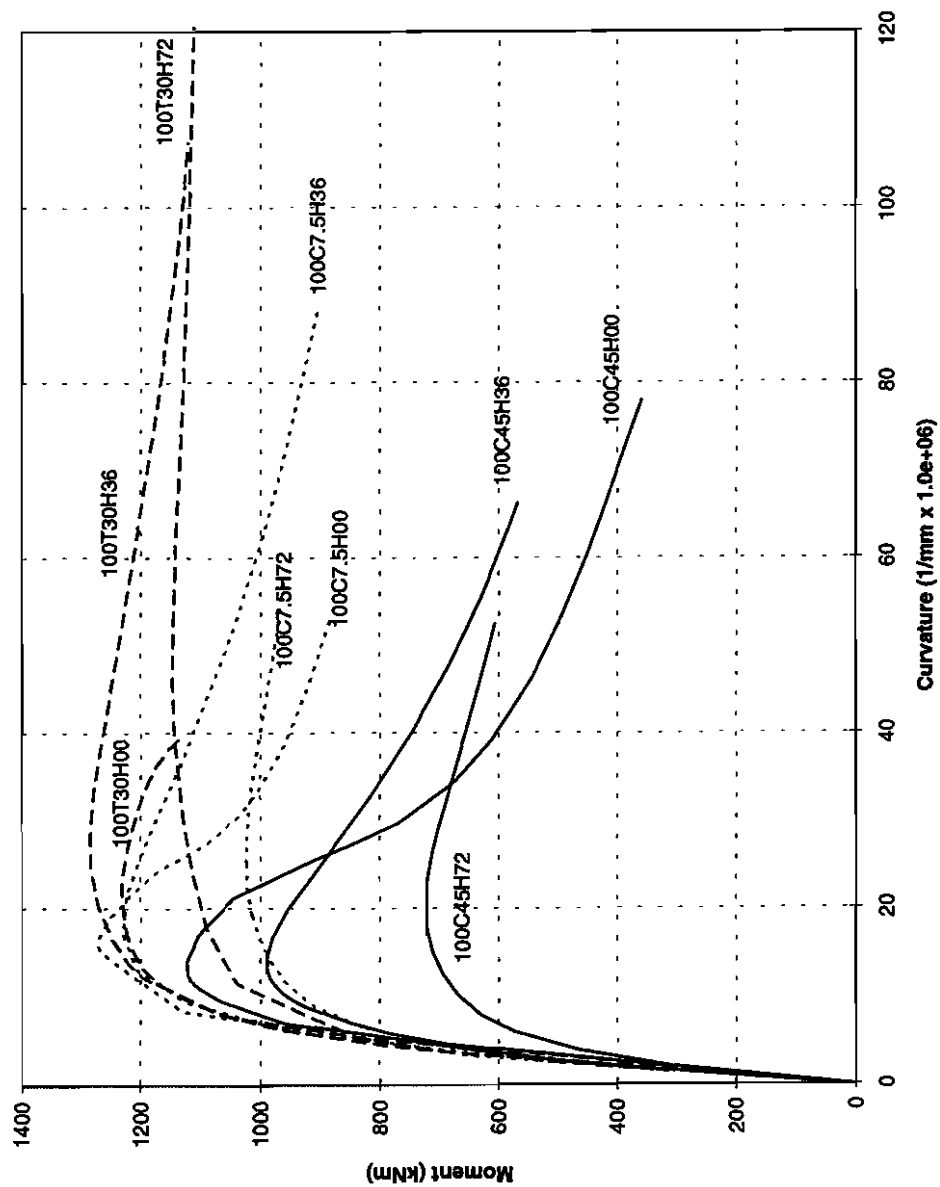


Figure 5.8 Local Moment vs. Local Curvature Diagrams for 711 mm OD x 7.11 mm Cross Section

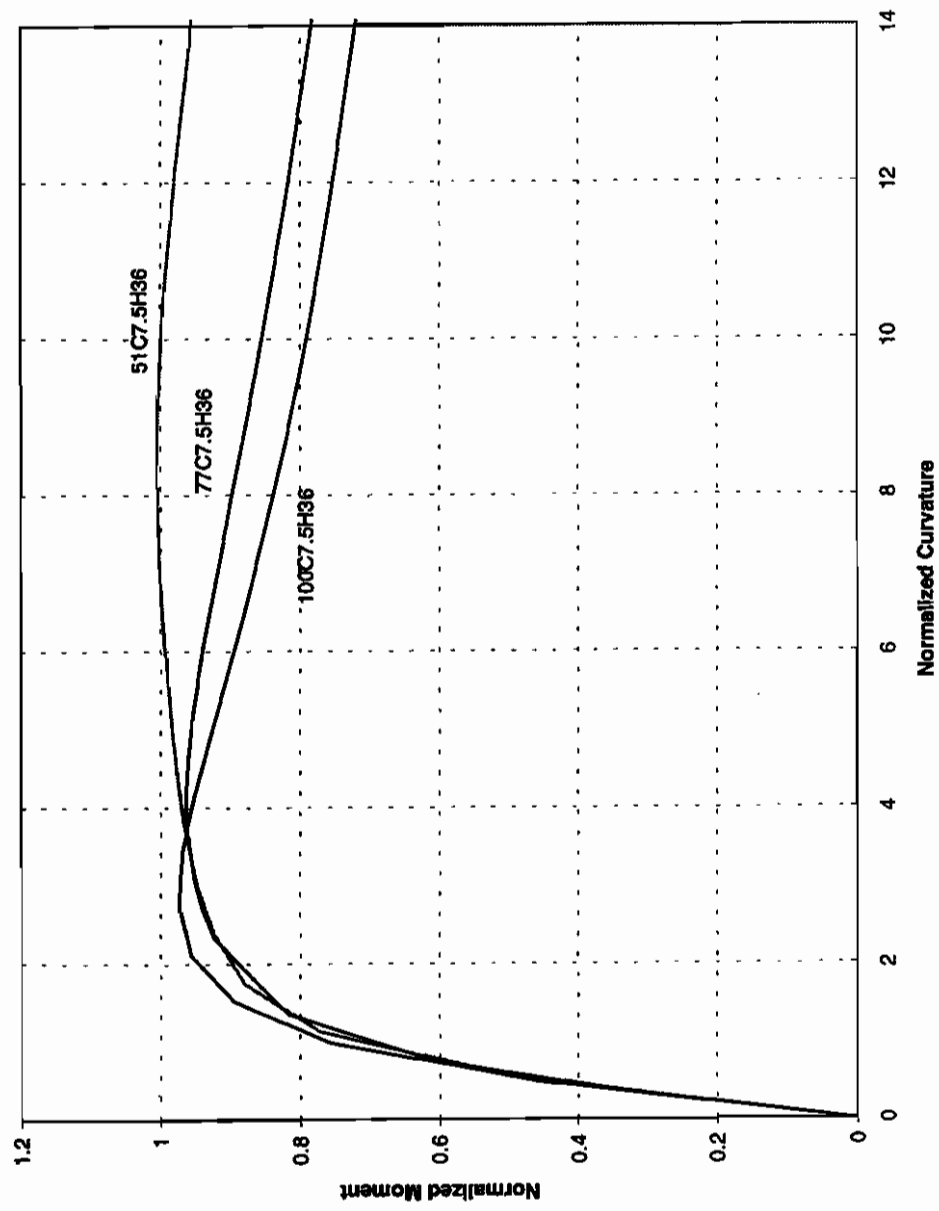


Figure 5.9 Non-Dimensional Moment vs. Curvature Diagrams for xxC7.5H36

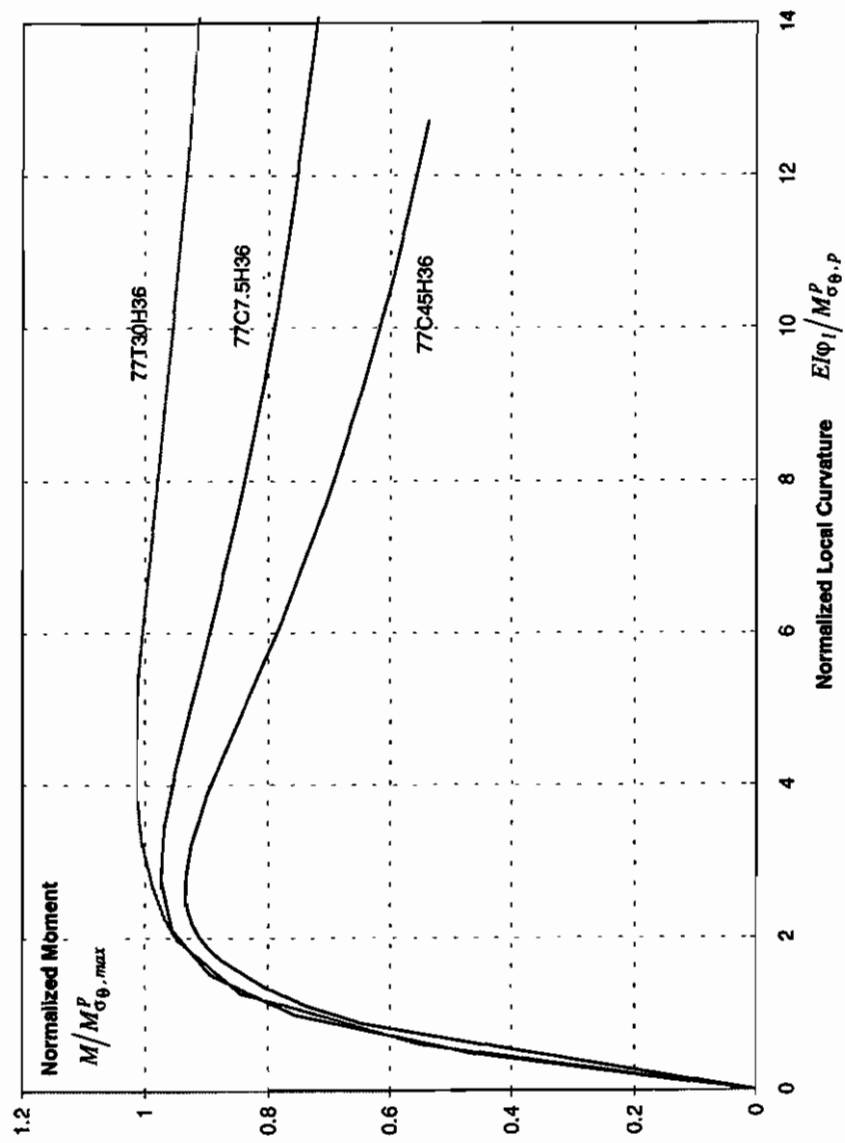


Figure 5.10 Non-Dimensional Moment vs. Curvature Diagrams for 77CxxH36

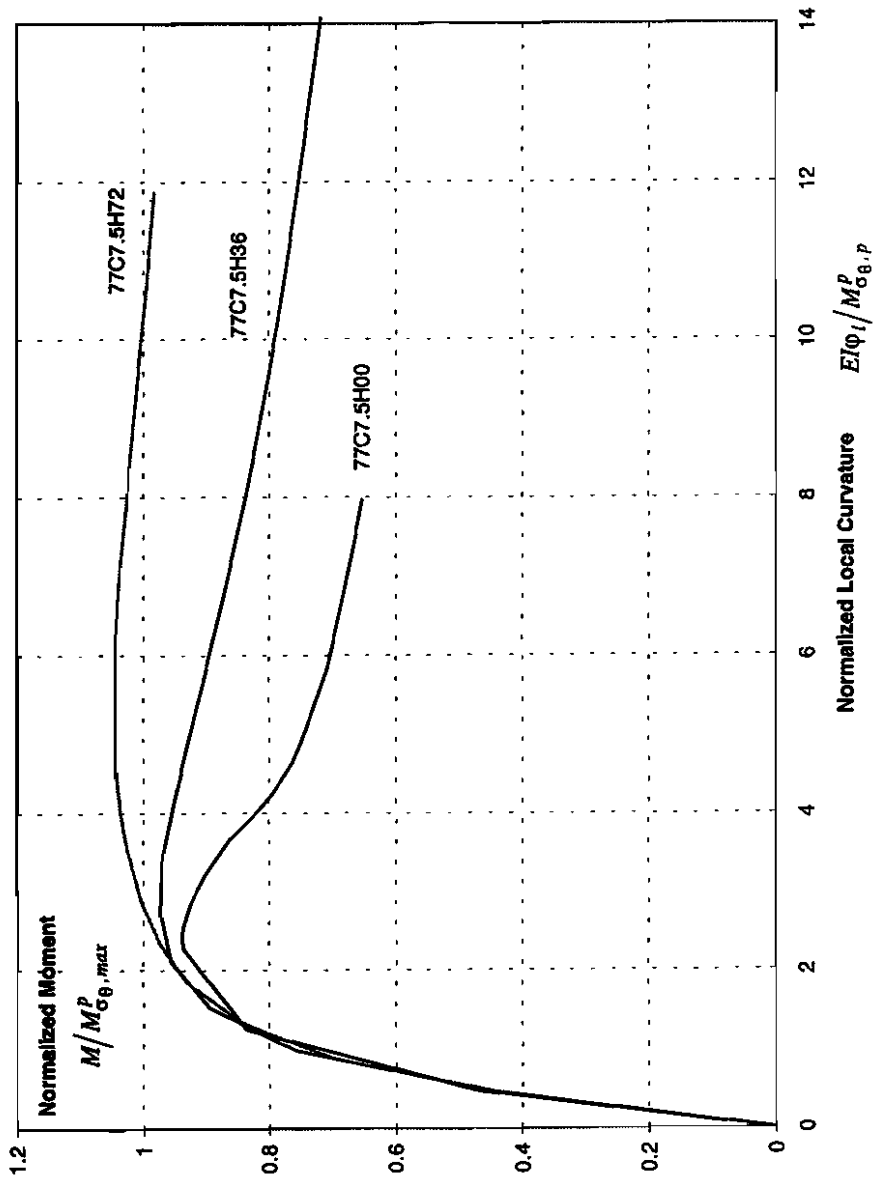


Figure 5.11 Non-Dimensional Moment vs. Curvature Diagrams for 77C7.5Hxx

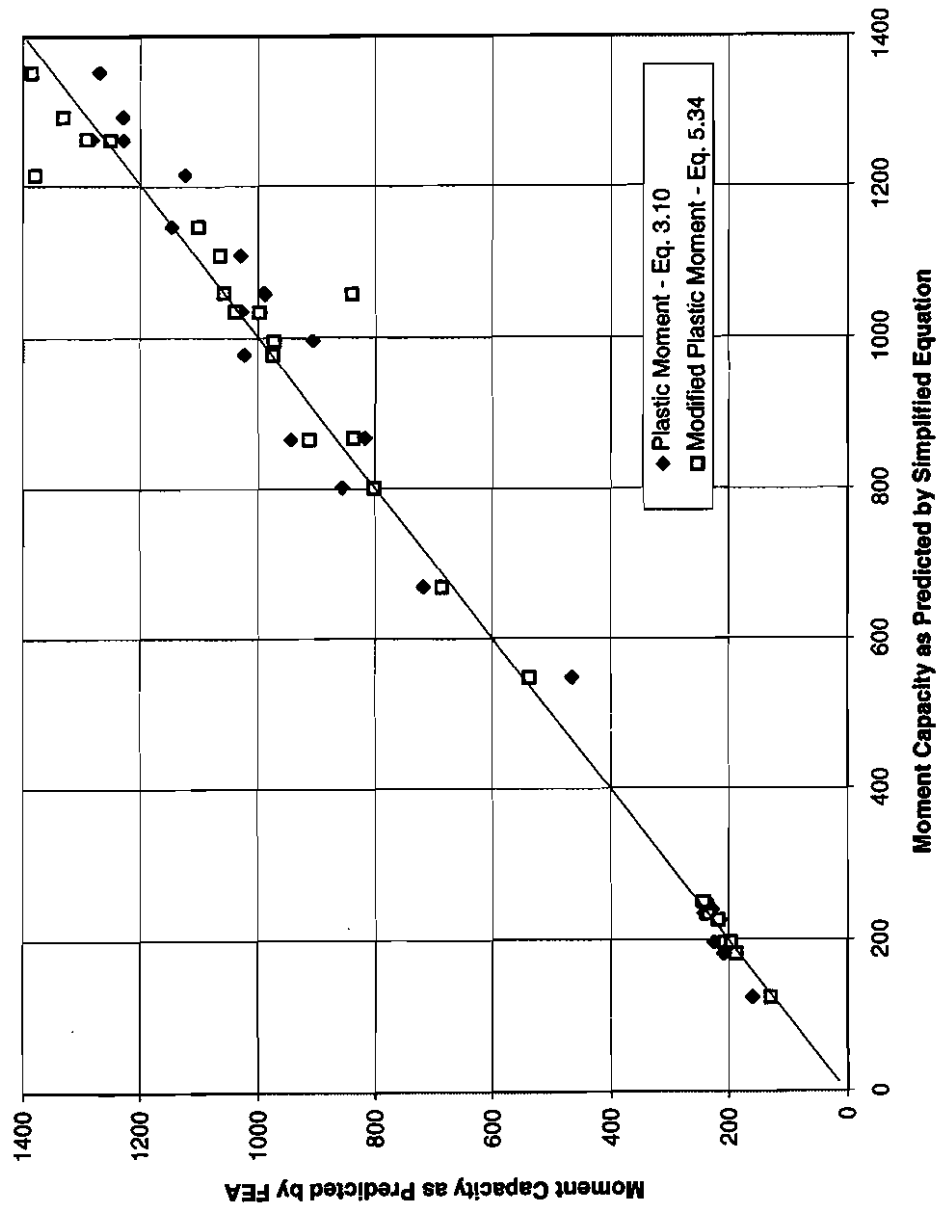


Figure 5.12 Scatter of Predicted Plastic Moment in Relation to Finite Element Results

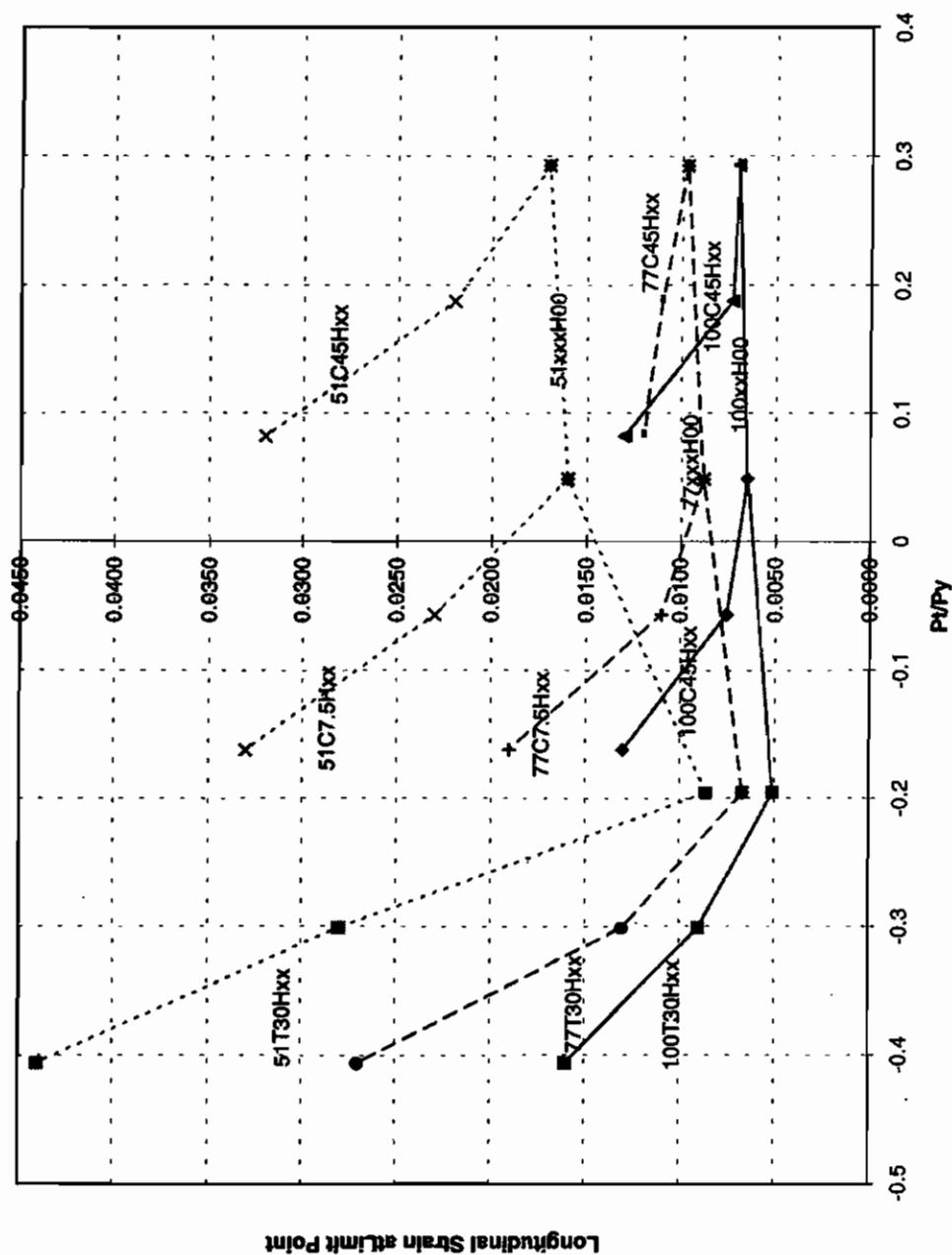


Figure 5.13 Limit Point Strains vs. Axial Load Ratios

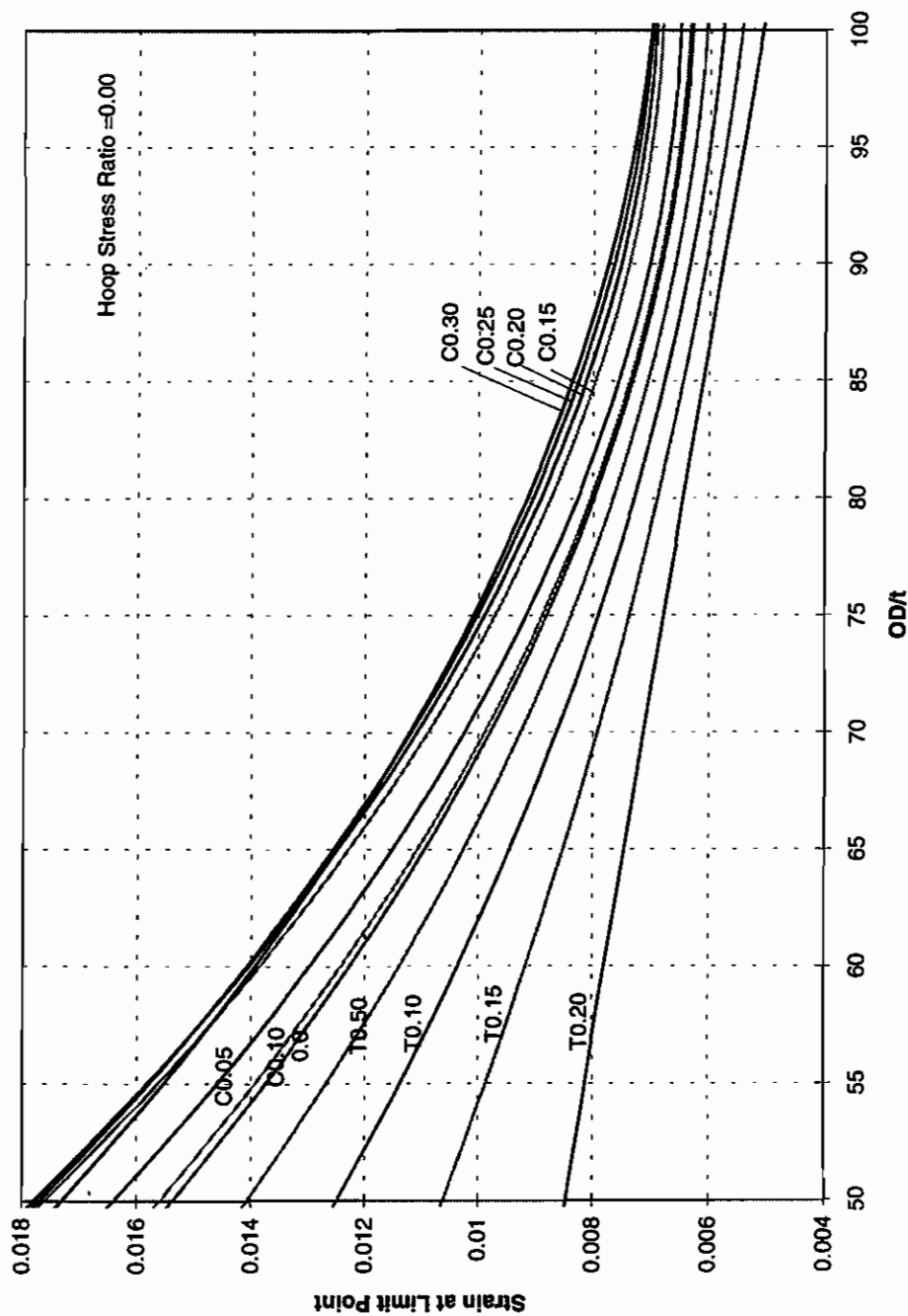


Figure 5.14 Longitudinal Compressive Strain at Limit Point (Hoop Stress Ratio = 0.00)

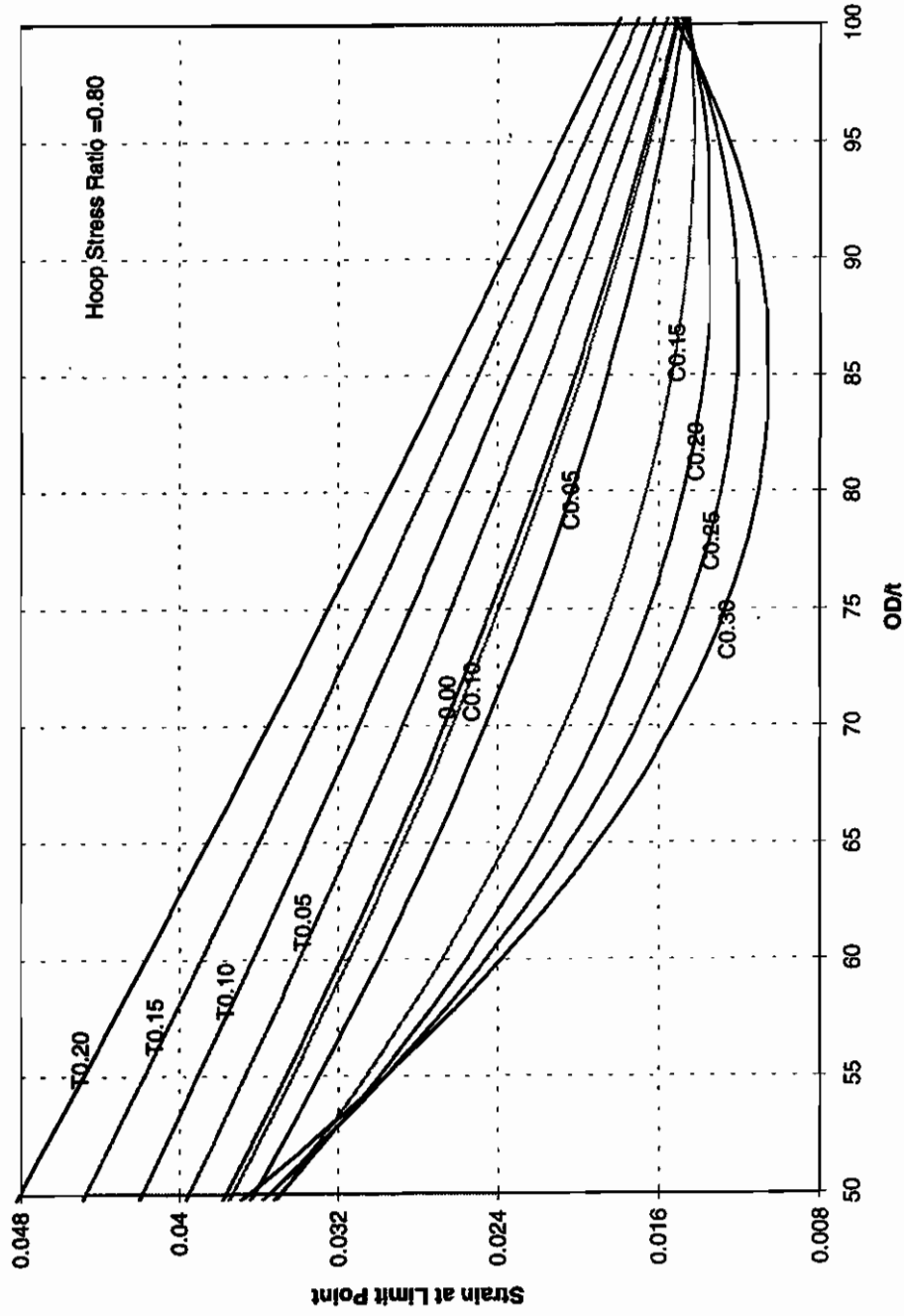


Figure 5.15 Longitudinal Compressive Strain at Limit Point (Hoop Stress Ratio = 0.80)

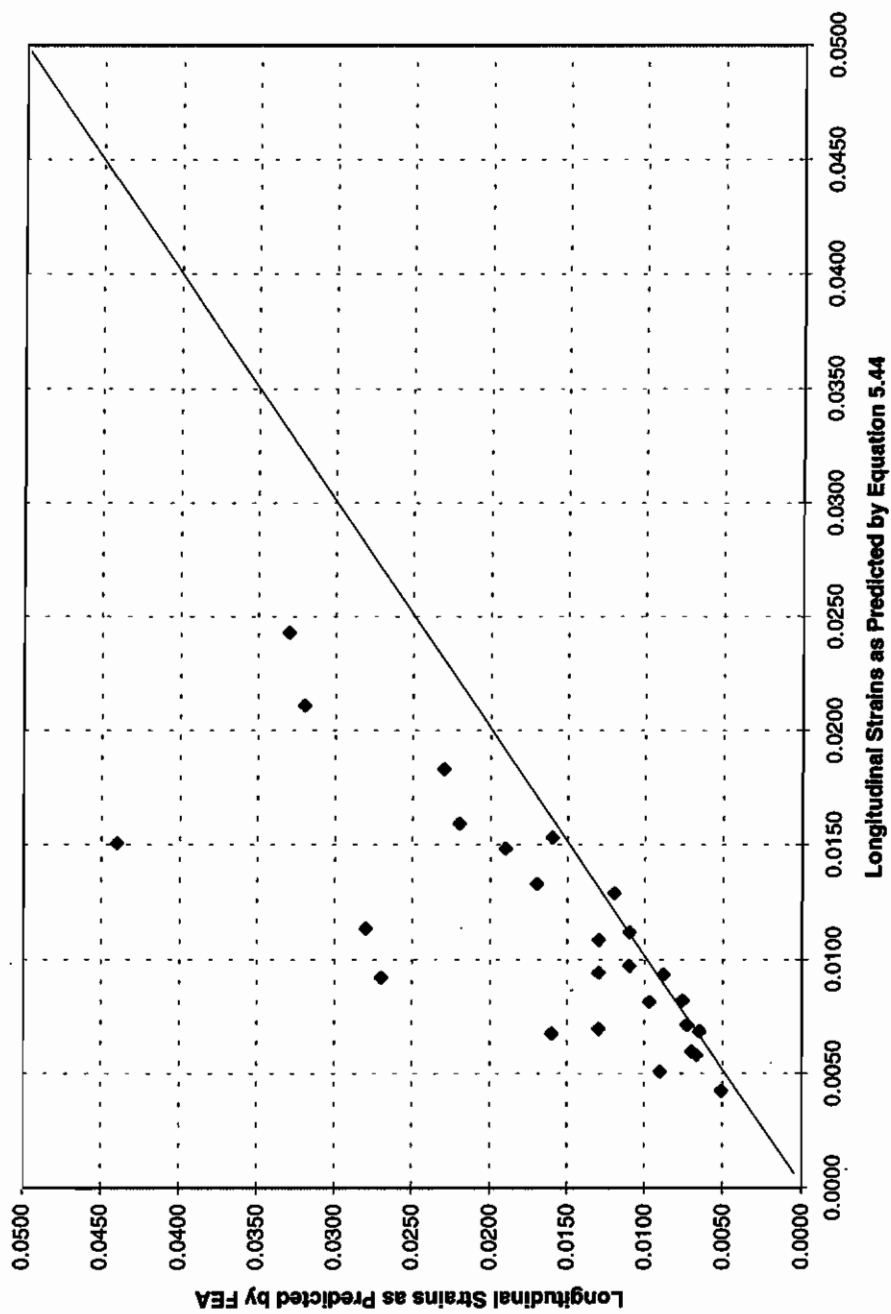


Figure 5.16 Scatter of Limit Point Strains: Finite Element Results vs. Equation 5.44

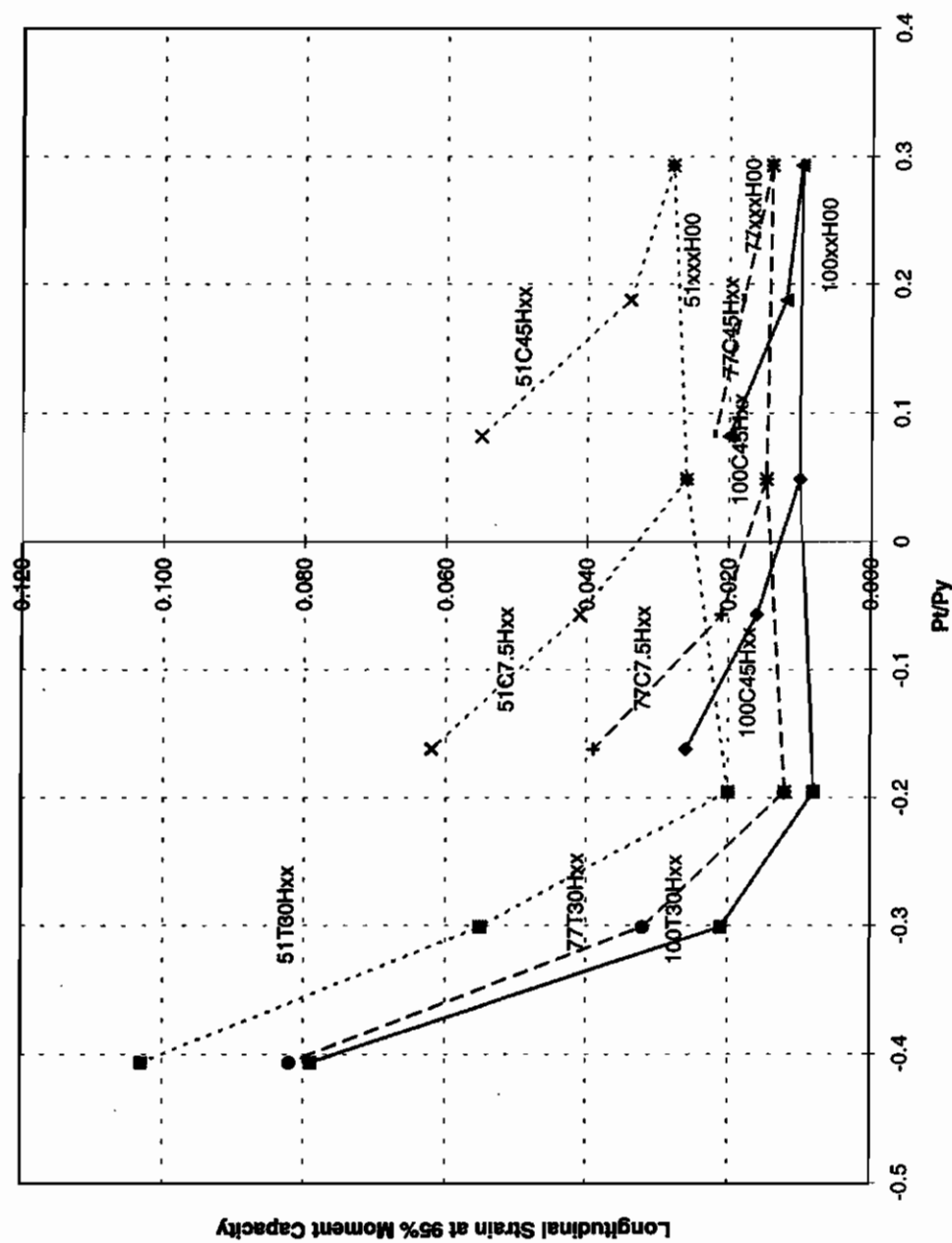


Figure 5.17 The 95% Moment Capacity Strains vs. Axial Load Ratios

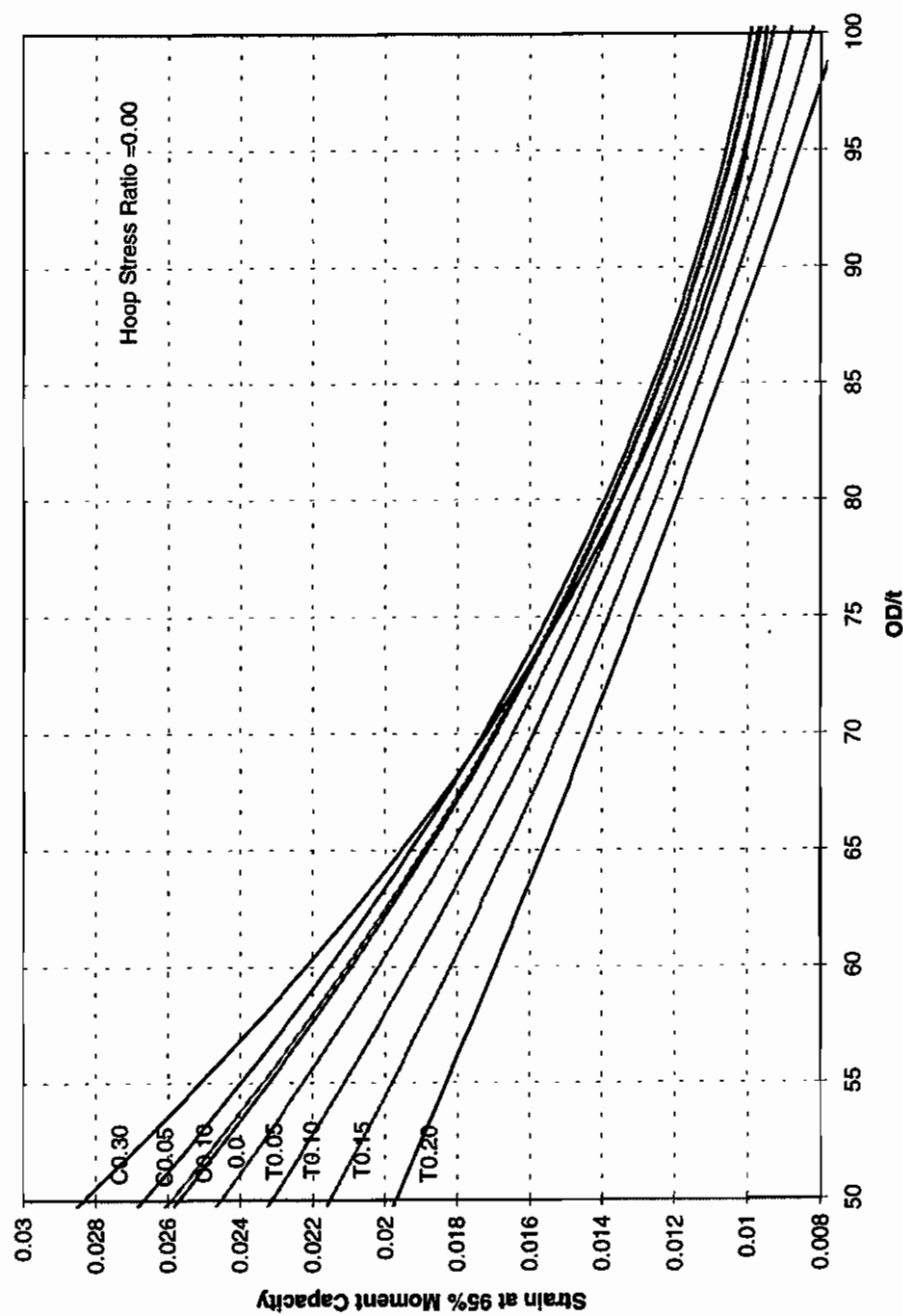


Figure 5.18 Longitudinal Compressive Strains at 95% Moment Capacity (Hoop Stress Ratio = 0.00)

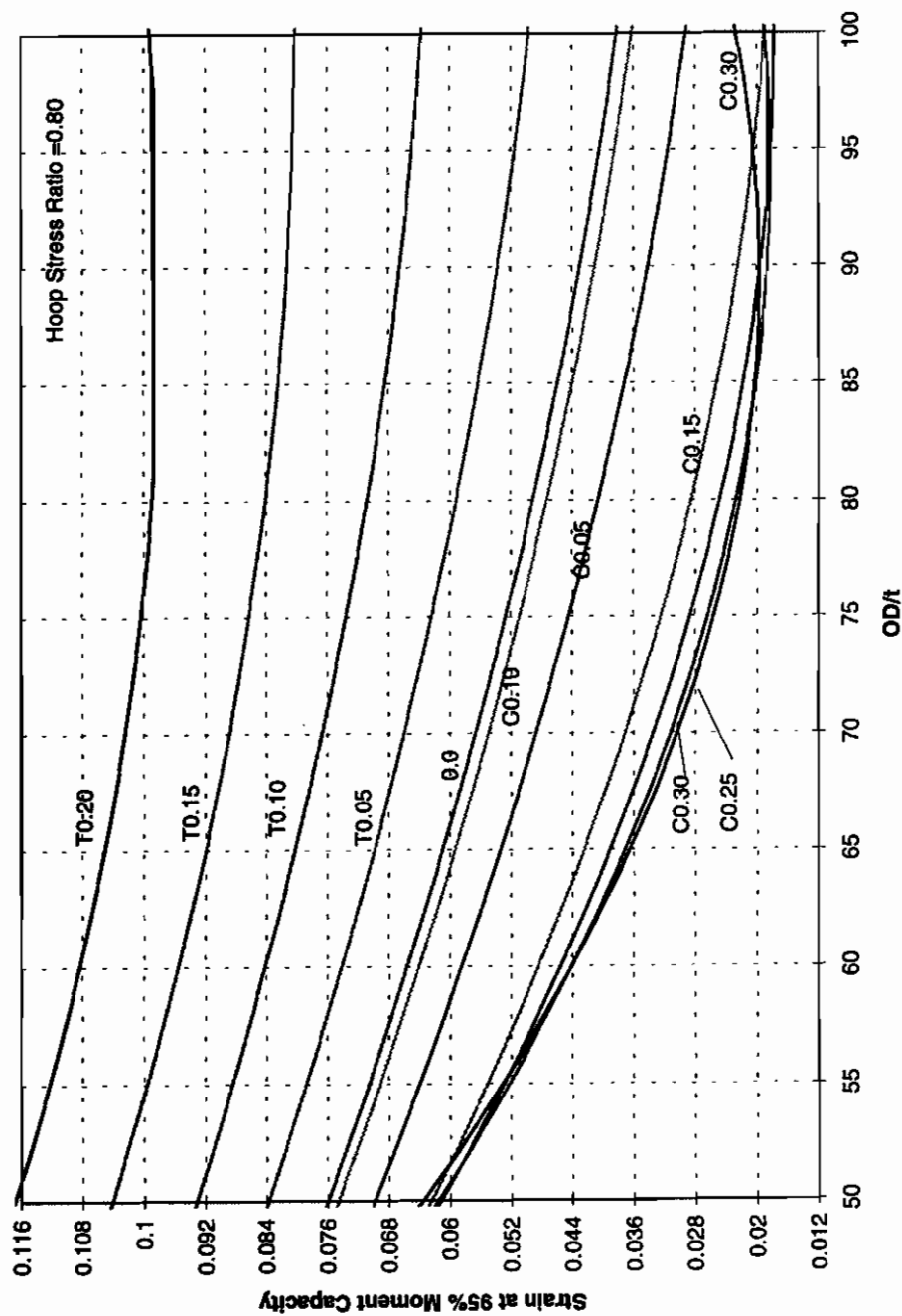


Figure 5.19 Longitudinal Compressive Strain at 95% Moment Capacity (Hoop Stress Ratio = 0.80)

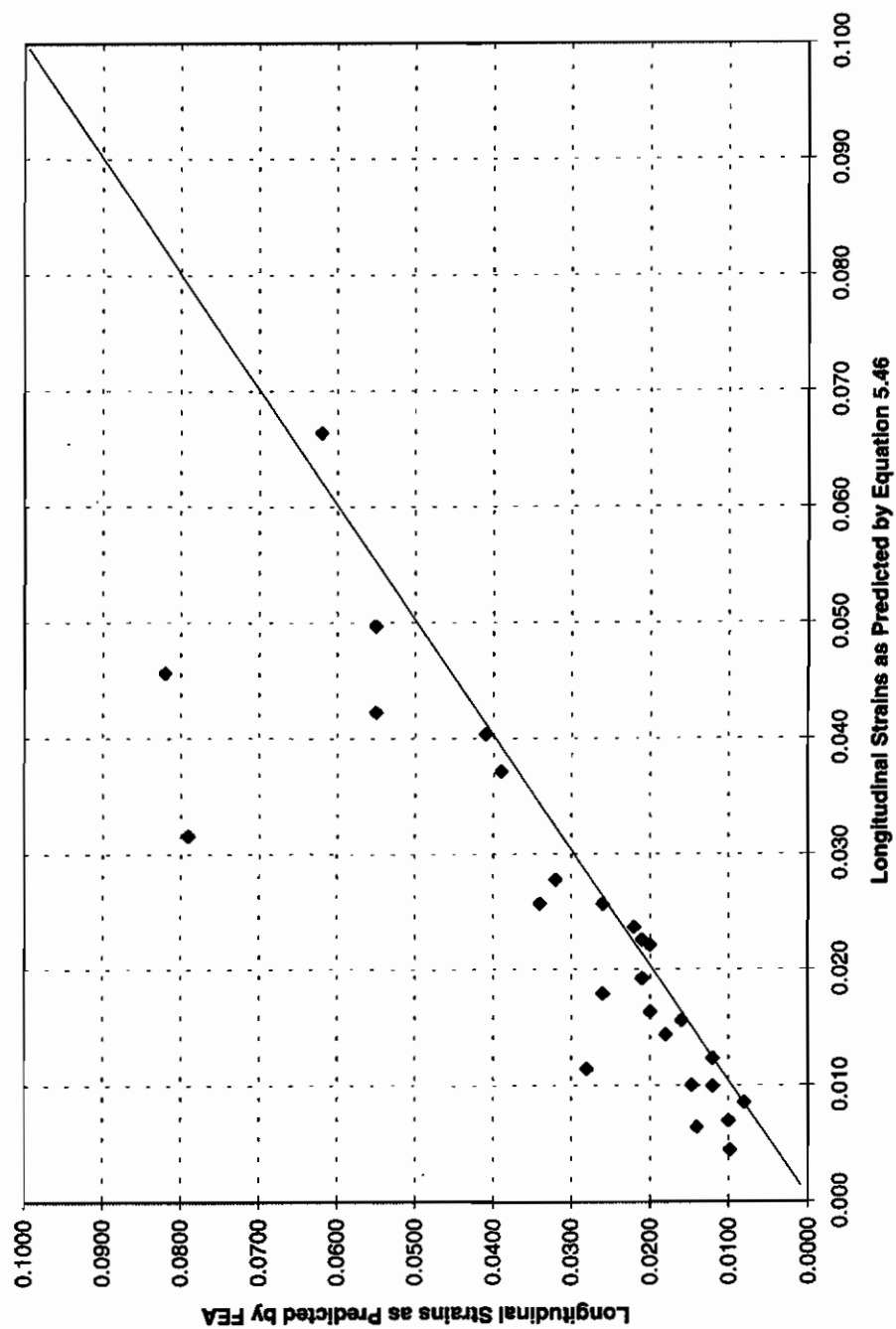


Figure 5.20 Scatter of 95% Moment Capacity Strains: Finite Element Results vs. Equation 5.46 Results

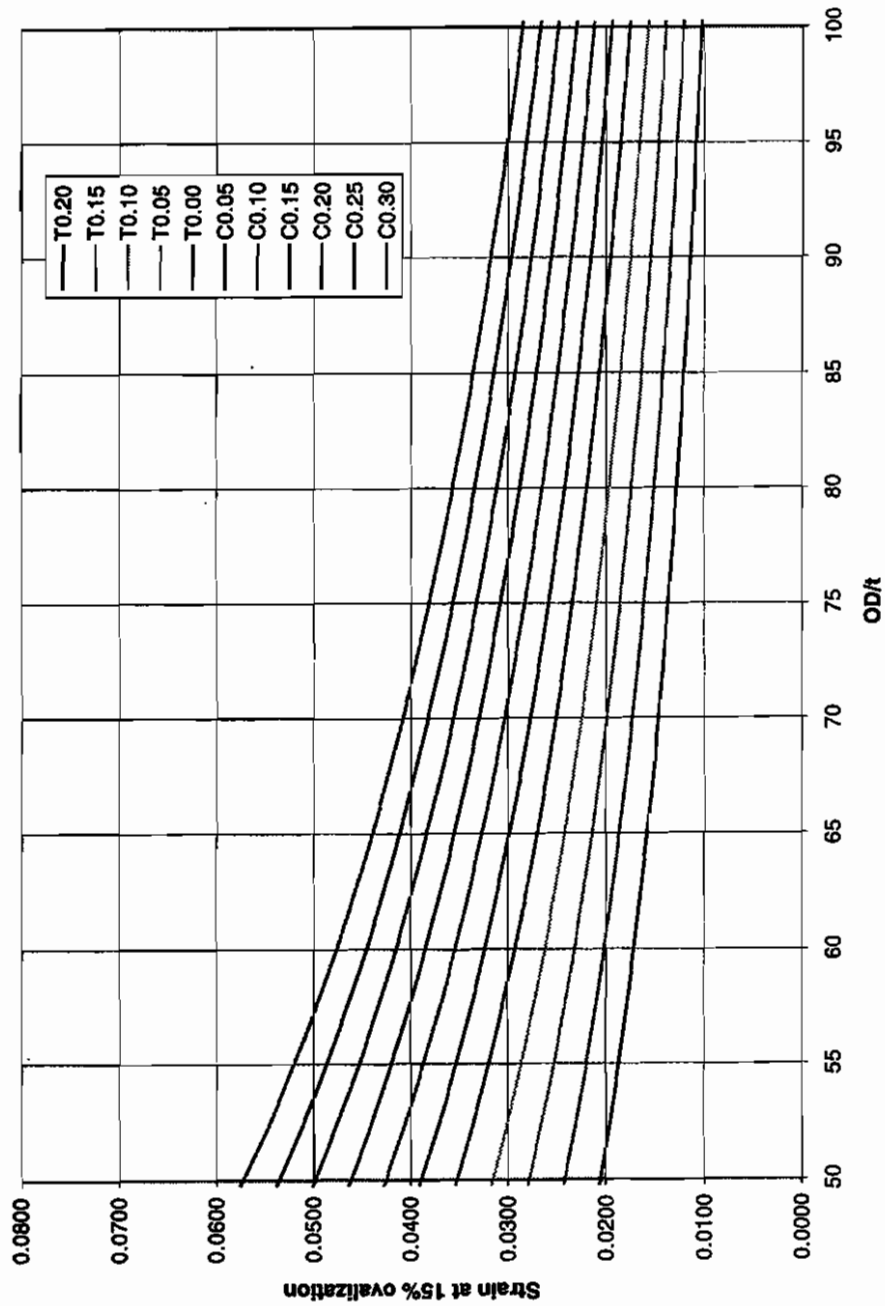


Figure 5.21 Longitudinal Compressive Strain at 15% Ovalization (Internal Pressure =0.00)

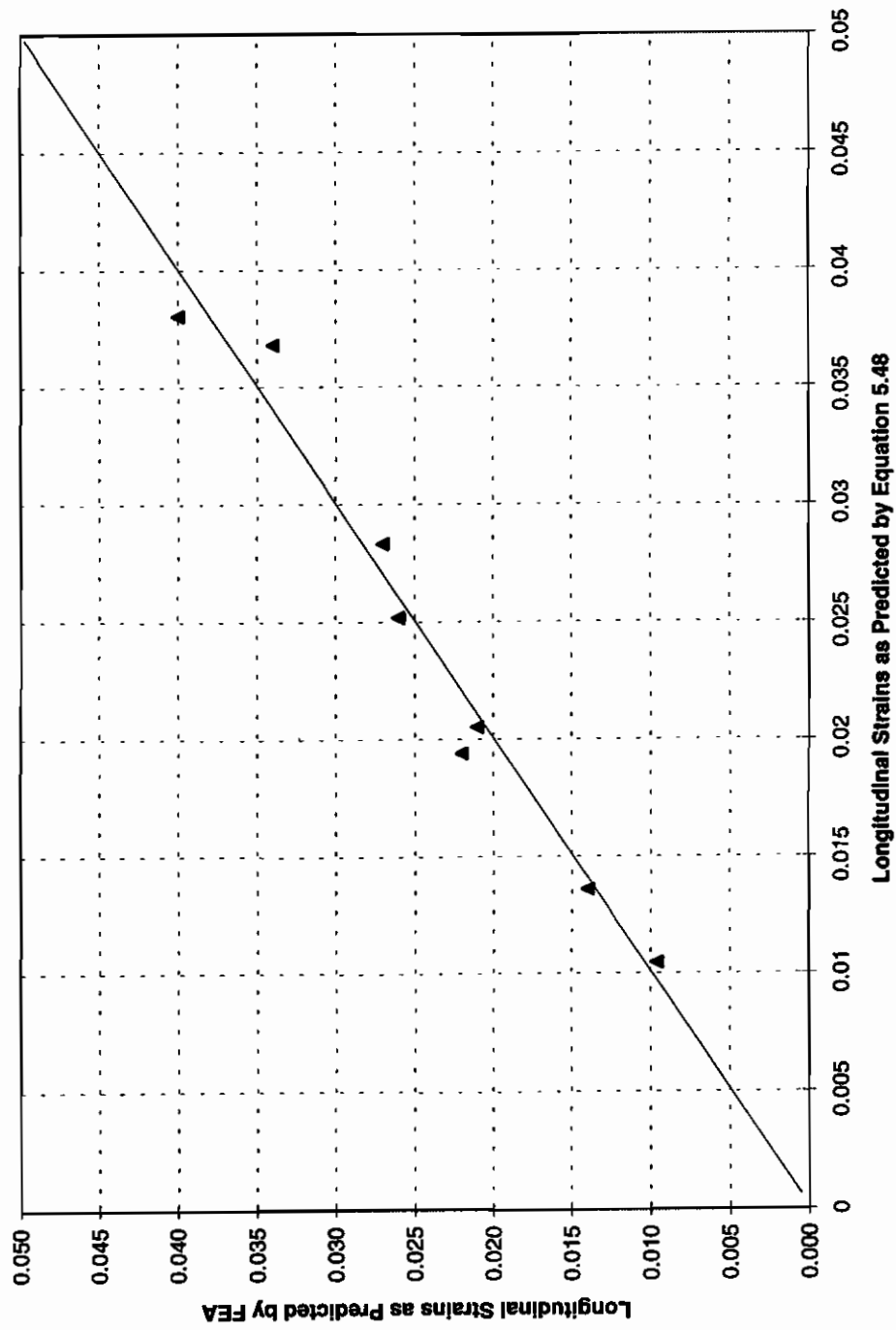


Figure 5.22 Scatter of 15% Ovalization Strains: Finite Element Results vs. Equation 5.48

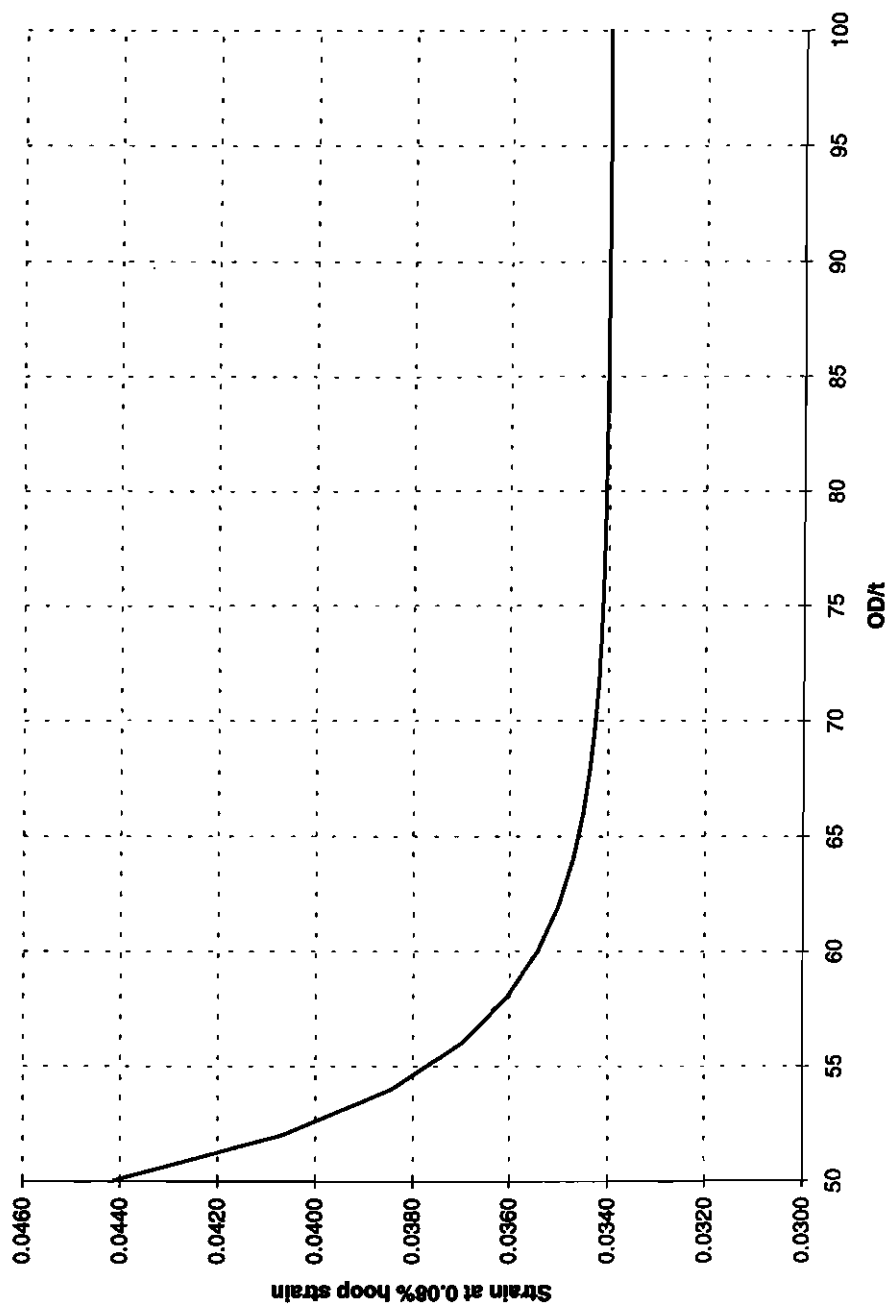


Figure 5.23 Longitudinal Compressive Strain at 8% Hoop Strain

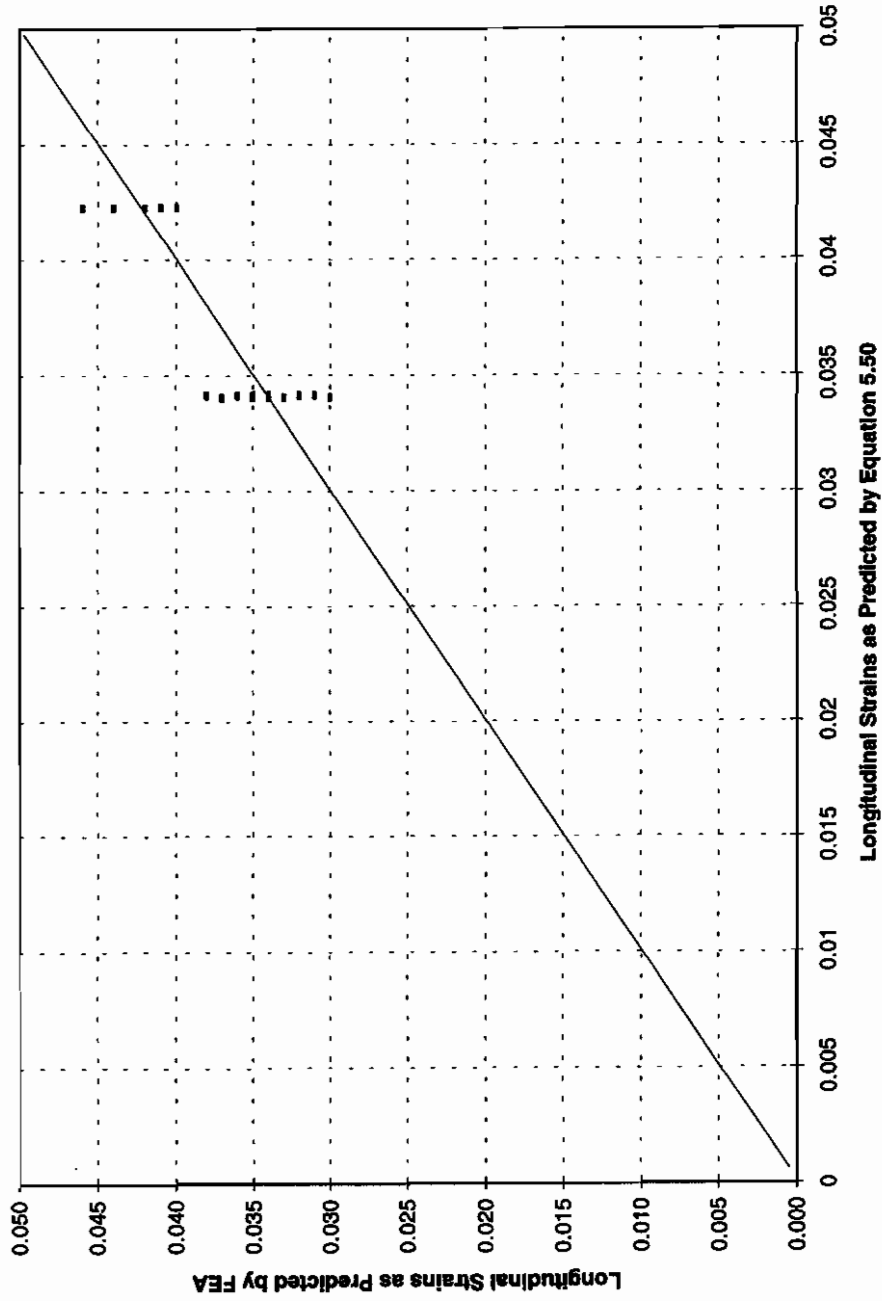


Figure 5.24 Scatter of Longitudinal Strains at 8% Hoop Strains: Finite Element Results vs. Equation 5.50

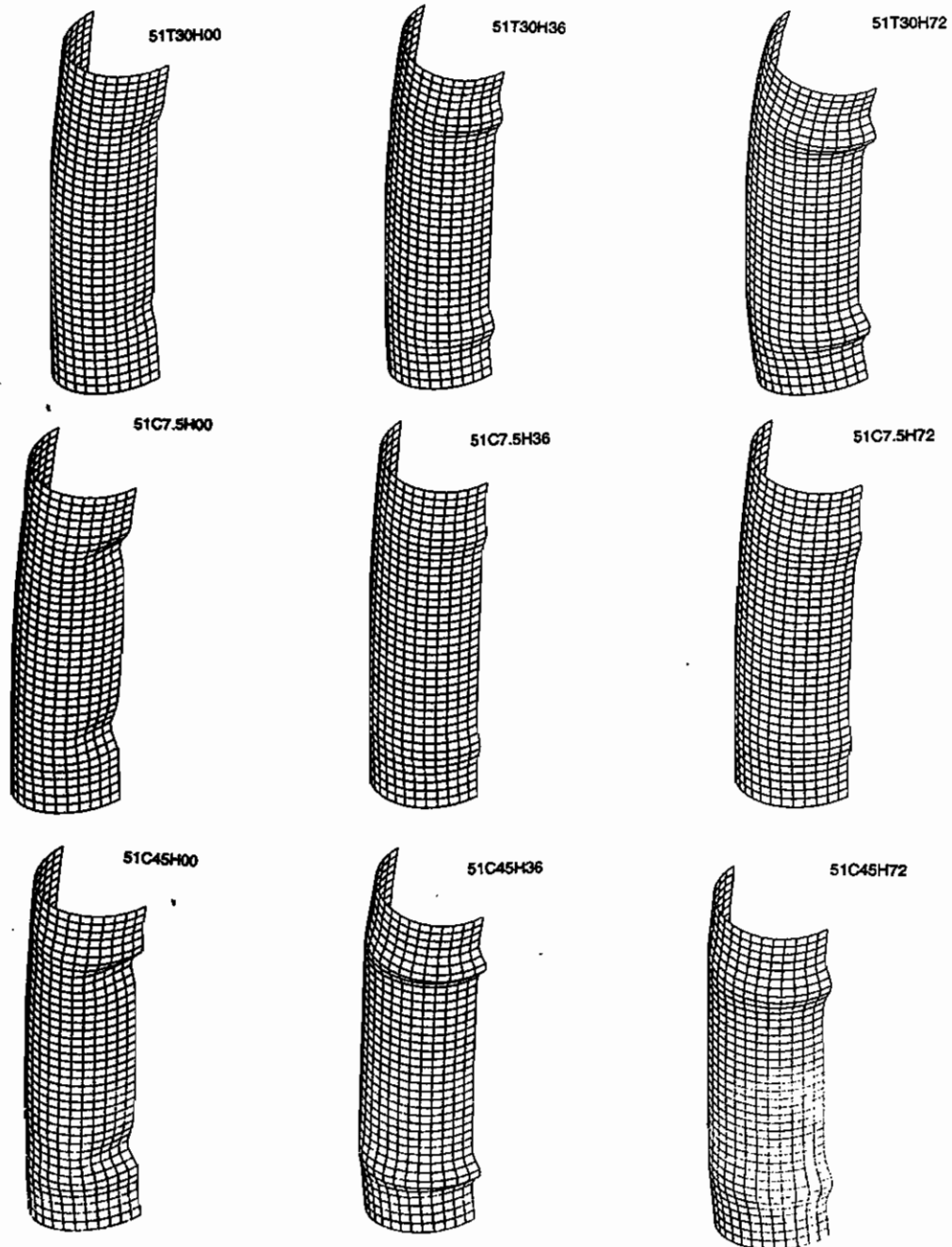


Figure 5.25 Deformed Configurations for Parametric Runs ($OD/t = 51$)

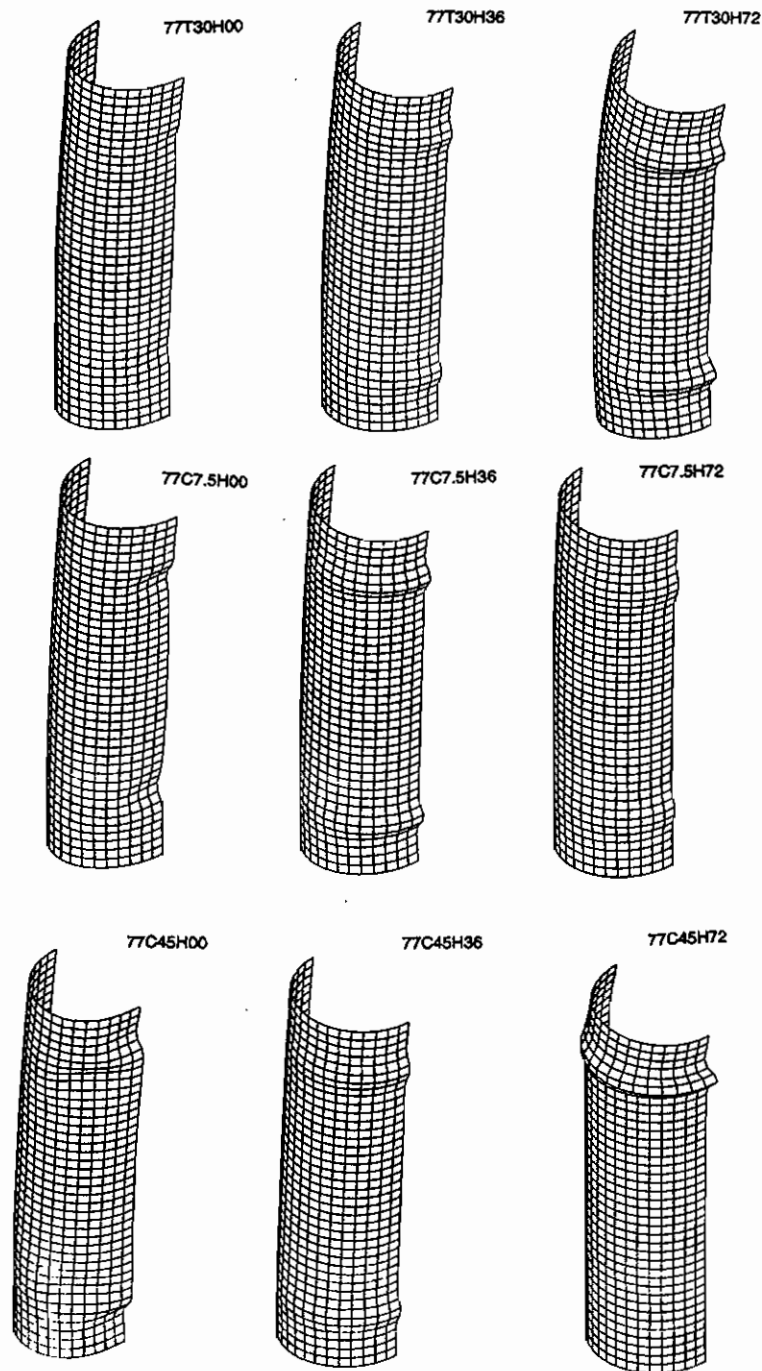


Figure 5.26 Deformed Configurations for Parametric Runs ($OD/t = 77$)

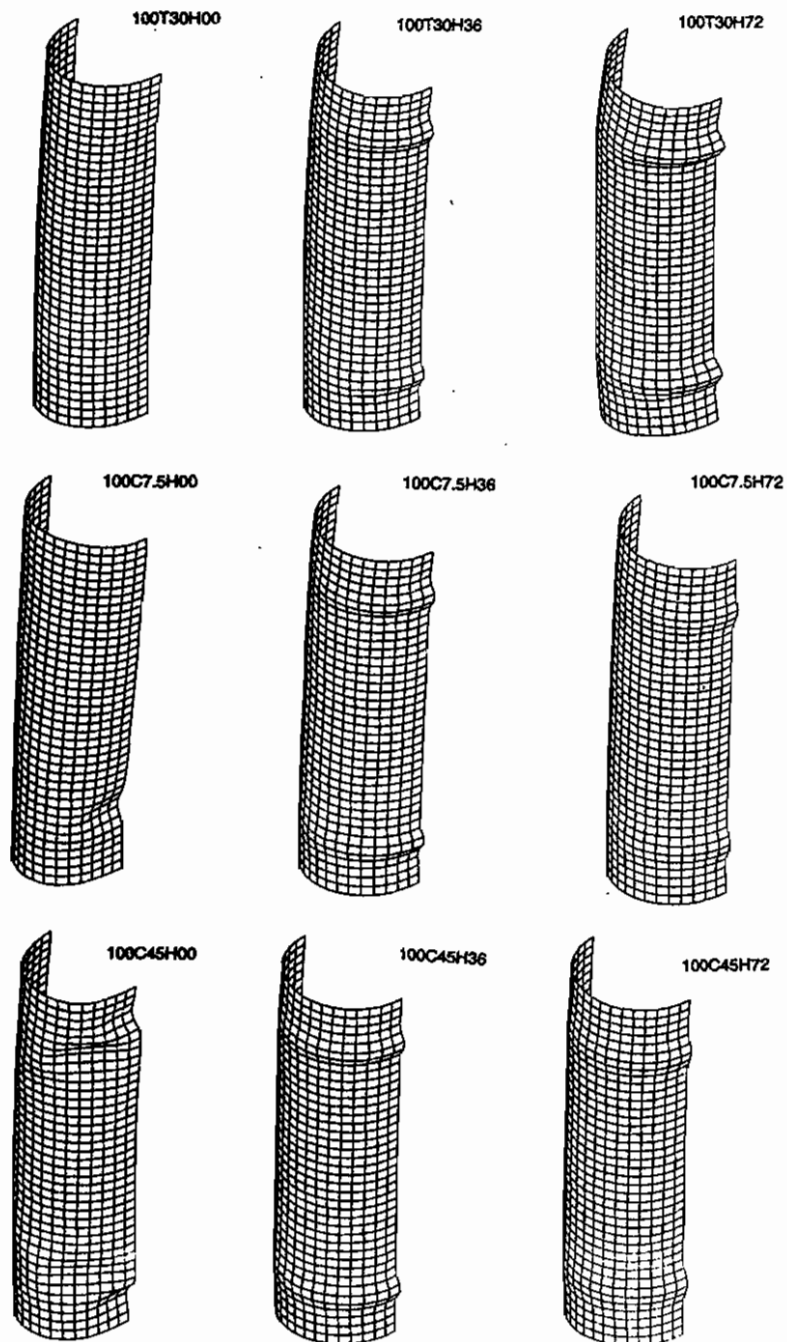


Figure 5.27 Deformed Configurations for Parametric Runs ($OD/t = 100$)

6. SUMMARY AND CONCLUSIONS

6.1 *Summary of Research*

This research focused primarily on the deformational behavior of pipelines. The following is a summary of the tasks performed.

1. An experimental program consisting of the testing of seven full scale pipes was carried out. The pipes were subjected to internal pressure, axial loading, and imposed curvatures of magnitudes comparable to those that might occur in the field.
2. A numerical finite element model was devised for the ABAQUS program in order to predict the deformational behaviour of the specimens tested. The model includes the effects of material elasto-plasticity, large displacements, large rotations, and finite strains.
3. A comparison between the experimental results and those based on the finite element analyses was performed. The comparison was based on the global moment vs. global curvature relationship and on the deformed configuration of the specimens. The model was found to be capable of reasonably predicting the moment vs. curvature response and the deformed configurations of the specimens considered. The agreement between the two sets of results established the ability of the analytical model to predict the behaviour of pipe for similar problems.
4. The boundary conditions of the finite element model devised in step two were modified in order to yield a closer resemblance to those expected in the field. The modified numerical model was used in analyzing pipe for 27 combinations of loading and cross-sectional geometries. Dimensional analysis

was used to reduce the number of parameters that needed to be considered in the study. The study focused on the effect of the non-dimensional parameters D/t , P_{imp}/P_y , and σ_h/σ_y on local buckling of pipes.

5. Attempts were made to define rational deformation limit criteria for pipelines. The deformation limit criteria proposed were the limit point, the point of 95% post-peak moment capacity, the point of 15% ovalization (for unpressurized pipes), and the point of 8% hoop strain (for highly pressurized pipes). The deformation limits corresponding to each of the proposed criteria were related to longitudinal compressive strains for design purposes. Based on the proposed deformation limit state criteria, equations for predicting the longitudinal compressive strains corresponding to each of the suggested criteria were proposed. The equations were based on the results of the parametric finite element runs.

6.2 Critique and Recommendations

6.2.1 Testing Procedure

The tests reported in this research were performed on pipe with seam welds. However, in all the tests, the seam weld was placed on the extreme tension fiber of the specimens. Therefore, the effect of longitudinal welds on the deformational behavior of pipes was not studied. In the field of course, local buckling can take place at the location of the longitudinal weld. Therefore, an experimental study on the effects of longitudinal welds on the pipe deformational behaviour is needed. Future tests are also needed for spirally welded pipes. An experimental program on the effect of girth welds on the deformational response of the pipe has recently been completed at the University of Alberta (see Yoosef-Ghodsi et al., 1994).

6.2.1.1 Material Properties

Workman (1987) performed an experimental study on the material properties of steel pipes, that included a number of steel grades. He observed that the mechanical properties of the pipe steel in the longitudinal direction are different from those in the circumferential direction. In the test program described herein, only the longitudinal material properties were obtained. A more complete description of the mechanical properties of the pipe steel would necessitate obtaining the stress vs. strain relationship of the pipe material in the circumferential direction as well. Based on the full description of the orthotropic behaviour of the pipe material, a more elaborate material model that accounts for the material orthotropy could be devised and used in the finite element parametric runs.

6.2.1.2 Test Set-up

In the test setup, the frictional horizontal force P_H (see Figure 3.18) was not measured. In the design stage of the experiment, it was assumed that the magnitude of the force P_H would be close to zero throughout the test. This assumption was based on an assumed deformation pattern approximately symmetric with respect to a horizontal plane passing through the mid-height of the specimen. As it turned out, this was true only in the pre-buckling range of deformation of the tested specimens. It was found from the finite element runs described in Chapter 4 that the magnitude of the force P_H is large enough to significantly affect the end moment values as computed by Equation 3.4. Therefore, in the computation of experimental end moments, values of force P_H were obtained from the finite element analysis.

The strain gage readings on the compression side of the specimen were of little importance since their readings were highly dependent on the location of the gages with respect to the location of the local buckles. The strain readings based

on the Demec gages provided a better measure of longitudinal compressive strains.

The tensile strains recorded were based on strain gage readings. Demec gage readings along the maximum tension fibers might have been appropriate in determining both tensile strains and curvatures based on segments of the tested specimens.

The radial displacement measurements for the tested specimens were based on the electronic readings of LVDTs. The resolution of the mesh traced by the LVDTs was too coarse to allow a reconstruction the pipe surface to be performed. However, the LVDT readings provide a data-base against which displacements determined by other means (e.g., photogrammetry) could be compared.

The elongation of the specimens was recorded through longitudinal LVDTs placed along the specimen. The reading of the longitudinal elongation was particularly important in controlling the reactive tests (Specimens UGR508 and DLR508). In these tests, it was intended that the specimens be maintained at a constant length throughout the deformation process. This condition was achieved only approximately because of the high sensitivity of the applied axial load (as determined by the controlling program) on any errors in the readings for specimen elongation.

In general, the end rotations applied to the specimens tested were unequal. It was not possible to impose equal rotations to the end of the specimens, since the rotation of both the top and bottom loading arms were controlled by only one force, that of the eccentric jack (i.e., force F in Figure 3.18). Applying equal end rotations to a specimen would necessitate controlling each of the loading arm rotations by a separate jack. An advantage that would be gained by applying equal end rotations to the specimens is that local buckling would be forced to occur at

the center of the specimen. This could not be achieved for Specimens DGA508 and DLR508 with a one eccentric jack setup.

Another way to force local buckles to occur in the middle of the specimen is to increase the $P-\Delta$ effect of the concentric axial load P (see Figure 3.18). This can be achieved by using relatively long specimens. The $P-\Delta$ effect was large enough to force local buckles of all 324 mm OD specimens to occur near the center of the specimens. For two of the 508 mm OD specimens, however, the buckles occurred near the bottom ends of the specimens. For these tests, longer specimens might have been more appropriate.

6.2.2 Deformation Limiting Criteria

Four deformation limiting criteria for buried pipelines are proposed as an outcome of this research. Although criteria based on moment capacity have considerable acceptability in the current pipeline industry, the criteria proposed herein, which are based on maximum ovalization and maximum hoop strains, provide a more rational basis in the design of buried pipelines.

Although the ovalization deformation limit state as defined in this research is a suitable limiting deformation criterion, the proposed 15% limit on ovalization is arbitrary. Better allowable limits on ovalization need to be obtained from the industry. These could be based on the through-flow capacity of ovalized pipes or on the dimensions of pigging devices used in the inspection of pipelines.

For the maximum hoop strain criterion, the 8% limit is suitable for longitudinally welded pipes. For seamless pipes, this limit may be significantly increased in accordance with the thickness of the pipe and its steel grades. Nevertheless, the 8% value remains a conservative limit for the design of seamless pipe.

6.2.3 Parametric Study

The parametric study presented in Chapter 5 was based on the finite element runs that used the material properties of X52 Steel. A comprehensive set of design rules should include the steel grade as a design parameter. The stress vs. strain characteristics of other steel grades need to be experimentally determined and more parametric runs based on the properties of these steel grades should be performed.

No attempts were made to study weld effects on the deformational behavior of pipes. It is possible that the residual stresses caused by the welding processes may significantly affect the pipe deformation limits. More research is needed in this area.

The effect of depressurization on pipe deformational behaviour has been outside the scope of this study, although it might be of practical interest to designers. Research in this area is needed.

More numerical studies are needed in the pressure ratio ranging between 0 and 36% so that the border between inward buckles and outward bulge buckles can be delineated.

6.3 Impact of Research

It is the writer's opinion that the results of this research will have a significant impact in the design philosophy and practice of buried pipelines. It is hoped that the current design practices based on elastic criteria (being overly conservative) will be abandoned in favour of the proposed deformation limit states that recognize the ability of buried line pipes to deform well into the plastic range while remaining fully operational. If the proposed deformation limits based on ovalization and hoop strain limits are adopted by the industry, they will result in a

significant economic impact. Also, by relaxing the design rules on buried pipelines, it is expected that the pipeline industry will be able to avoid the more expensive alternative of constructing elevated pipelines.

REFERENCES

Bouwkamp, J. G., and Stephen, R. M., (1973) "Structural Behaviour of a Large Diameter Pipeline Under Combined Loading," ASCE Journal of Transportation Division, Vol. 99, pp 521-536.

Bouwkamp, J. G., and Stephen, R. M., (1974) "Full Scale Studies on Structural Behavior of Large Diameter Pipes Under Combined Loading," Report No. UC-SESM 74-1, University of California, Berkeley, January.

Batterman, S. C., (1965) "Plastic Buckling of Axially Compressed Cylindrical Shells," AIAA Journal, Vol. 3, No. 2, pp. 316-325.

Canadian Standards Association (1990), "CAN/CSA-Z183-M90 Oil Pipeline Systems".

Canadian Standards Association (1984), "CAN/CSA-Z183-M84 Oil Pipeline Systems".

Canadian Standards Association (1993), "CAN/CSA-Z245.1-M84 Steel Line Pipe - Oil & Gas Industry Systems and Materials," March.

Ellinas C. P., Raven, P. W. J., Walker, A. C., and Davies, P., (1987) "Limit State Philosophy in Pipeline Design," ASME, Proceedings of the 6th International Offshore Mechanics and Arctic Engineering Symposium, January.

Gellin S., (1980) "The Plastic Buckling of Long Cylindrical Shells Under Pure Bending," International Journal of Solids and Structures, Vol. 16, pp 397-407.

Gresnigt, A. M., (1986) "Plastic Design of Buried Steel Pipelines in Settlement Areas," Heron.

Hibbit, H. D., Karlson, B. I., and Sorensen, P., (1993), "ABAQUS Version 5.3- Theory Manual," Pawtucket, RI.

Kim, H. O., (1992) "Plastic Buckling of Pipes under Bending and Internal Pressure," Proceedings of the Second International Offshore and Polar Engineering Conference, San Francisco, USA, June 14-19.

Kim, H. O., and Velasco P., (1988) "Review of Pipe Buckling For Arctic Pipeline Design," The Seventh International Conference on Offshore Mechanics and Arctic Engineering, Houston, Texas, February.

Langhaar, H. L., (1951), "Dimensional Analysis and Theory of Models," John Wiley & Sons, Inc., New York.

Langner, C. G., (1984) "Design of Deepwater Pipelines," TNO-IWECO 30th Anniversary Symposium on Underwater Technology, The Hague, May.

Lara, P. F., (1987) "Revisiting Failure Criteria of Buried Pipelines," ASME Pipeline Engineering Symposium, ETCE, Dallas, Texas.

Murphey, C. E. and Langner, C. C., (1985) "Ultimate Pipe Strength Under Bending, Collapse and Fatigue," ASME, Proc. 4th International Offshore Mechanics and Arctic Engineering Symposium, Dallas, February.

Peterson, A. E., (1992) "Photogrametric Mapping of a Pipe Under Axial Loading," 85th Annual Meeting of the Canadian Institute of Surveying and Mapping, June 23-26, Whitehorse, Yukon.

Popov, E. P., Sharifi, P., and Nagarajam, S., (1974), "Inelastic Buckling Analysis of Pipes Subjected to Internal Pressure, Flexure and Axial Loading," in Pressure Vessels and Piping: Analysis and Computers, edited by I. S. Tuba, R. A. Selby and W. B. Wright, ASME Symposium, pp 11-23.

Popov, E. P., (1973), "Theoretical Buckling Criterion for 48 Inch Steel Pipe," Report to the Alaska Pipeline Service Company, April.

Price, P. St. J. and Barnette, J. A., (1987) "Pipeline Codes and Structural Criteria for Pipelines in Arctic and Earthquake Regions," Sixth International Symposium and Exhibit on Offshore Mechanics and Arctic Engineering, Houston, March 1-6.

Price, P. St. J. and Anderson H. A., (1991) "Integrity Monitoring and Maintenance Criteria for New and Existing on Land and Marine Pipelines," Proceedings on the First International Offshore and Polar Engineering Conference, Edinburgh, United Kingdom, 11-16 August.

Prion, H. G. L., and Birkemoe, P. C., (1988) "Experimental Behaviour of Unstiffened Fabricated Tubular Steel Beam-Columns," University of Toronto, Department of Civil Engineering, Publication No. 88-03, ISBN 07-7727-7096-4.

Reddy B. D. (1979) , "An Experimental Study of the Plastic Buckling of Circular Cylinders in Pure Bending," International Journal of Solids and Structures, Vol. 15, pp 669-683.

Ramberg, W. and Osgood, W. B., (1943), "Description of Stress-Strain Curves by Three Parameters," Technical Note 902, National Advisory Committee for Aeronautics, Washington, D. C.

Row, D. G., Powell, C. H. and Morris, G. R., (1983) "Local Buckling Analysis of Pipelines," Proceedings of the Second International Offshore Mechanics and Arctic Engineering Symposium, ASME.

Row, D. G., Hollings, J. P., Sause R., and Der Kiureghian, A., (1987) "Limit State Probabilistic Design on Offshore Arctic Pipelines," The Sixth International Symposium on Offshore Mechanics and Arctic Engineering, Houston, Texas, March 1-6.

Seide, P., and Weingarten, V. I., (1961), "On the Buckling of Circular Cylindrical Shells Under Pure Bending," Journal of applied Mechanics, Vol. 28, pp 112-116.

Souza, L. T., PostSYNAS (1995) - A system for nonlinear analysis of shells - Post-Processing, User's Manual v. 1.0, (to be published).

Timoshenko, S. P. and Gere, J. M., (1961) "Theory of Elastic Stability," 2nd edition, McGraw-Hill.

Vol'mir, A. S., (1966) "Stability of Elastic Systems," Gosudarstvennoye, Izdatel'stve, Fiziko-Matematicheskoye Koy, Literatoy, Moskova, 1963, available in English, WPAFB, Foreign Tech. Div., AD628508.

Wesolowsky, G. O., (1976) "Multiple Regression Analysis of Variance, an Introduction for Computer Users in Management and Economics," Wiley, Interscience Publication.

Workman, G. H., (1988) "Manufacturing Residual Stress Effects on Buried Pipeline Structural Response," the Seventh International Conference on Offshore Mechanics and Arctic Engineering, Houston, Texas, February 7-12.

Workman, G. H., (1981) "Pipe wall stability analysis of 12.75 in. O. D. \times 0.25 in W. T. Grade 52 Pipe," Summary report to Canuck Engineering Ltd., March.

Yoosef-Ghodsi, N., Kulak, G. L., and Murray, D. W., (1994), "Behaviour of Girth-Welded Line Pipe," Structural Engineering Report No 203, Department of Civil Engineering, University of Alberta, Edmonton, AB, T6G 2G7

Zhou, Z. and Murray, D. W., (1993) "Numerical Structural Analysis of Buried Pipelines," Department of Civil Engineering, University of Alberta, Structural Engineering Report No. 181.

